University College London

Computational Modelling of $SmCoO_3$-based Cathode Materials for Solid Oxide Fuel Cells

Thesis submitted for the degree of Doctor of Philosophy (PhD) by

Emilia Olsson

Supervised by

Prof. Nora H. de Leeuw

University College London

Department of Chemistry

June 2017

Declaration

I, Emilia Olsson, confirm that the work presented in this thesis is my own. Where information has been derived from other sources, I confirm that this has been indicated in the thesis.

Emilia Olsson

Abstract

This thesis presents the results of a computational study of bulk $SmCoO_3$-based perovskites for use as Intermediate Temperature Solid Oxide Fuel Cell (IT-SOFC) cathode. Using both Density Functional Theory with on-site Coulomb corrections (DFT+U), with correction applied to the transition metal *d*-electrons, and Molecular Dynamics (MD), the properties of this material, and the effects of an array of dopants on these, is investigated, all in relation to cathode efficiency.

Firstly, a bulk characterisation using DFT+U of $SmCoO_3$ is conducted. Two crystal structures of $SmCoO_3$ are modelled; cubic and orthorhombic, and both crystal structures are semiconductors at 0 K. The experimentally observed semiconductor-to-metal transition is then investigated by studying different magnetic orders at different temperatures, with C-type antiferromagnetic ordering in the cubic structure being identified as responsible for this transition. Importantly, the spin transition is directly linked to changes in the Co-O bond lengths and distortions in the CoO_6-polyhedra.

Secondly, the oxygen and metal vacancy formation in $SmCoO_3$ is investigated, as these can directly influence the IT-SOFC cathode efficiency. To put the $SmCoO_3$ results into context, a comparison with $LaMnO_3$ is performed, as this is the current state of the art SOFC cathode parent-material. $LaMnO_3$, and its doped form $La_{1-x}Sr_xMnO_{3-d}$ (LSM), are the benchmarks for this study, as the aim of this thesis is to identify a material with more favourable cathode properties than LSM. It is shown that oxygen vacancies strongly alter the electronic and magnetic structure of $SmCoO_3$, but barely affect $LaMnO_3$. The intrinsic concentration of oxygen

vacancies in both $SmCoO_3$ and $LaMnO_3$ is very low by virtue of the high oxygen vacancy formation energy. Oxygen vacancies are typically induced by doping in these materials. Studying the cation vacancy shows that the formation of cation vacancies is less energetically favourable than oxygen vacancies (typically more than 3 eV higher in energy), and would thus not markedly influence the performance of the cathode.

Thirdly, substitutional doping of Ca^{2+}, Sr^{2+}, and Ba^{2+} on the Sm-site in $SmCoO_3$ is investigated. DFT+U calculations are employed to investigate dopant configurations at two different dopant concentrations: x=0.25 and 0.50, with two different charge compensation mechanisms; oxygen vacancies, and electronic holes. Comparing hole, and oxygen vacancy formation energies, we conclude that oxygen vacancy charge compensation is the preferred mechanism to maintain electroneutrality of the system. Furthermore, the increase in electronic conduction is not a direct consequence of the appearance of electron holes, but a result of the distortion of the Co-O bonds. Finally, MD is employed to model ionic conduction and thermal expansion coefficients (TEC). All dopants at both concentrations show high ionic conduction comparable, but too high TEC to match IT-SOFC electrolytes, with Ca^{2+}-doping showing the combined most preferable properties. Fourthly, Co-site doping with Fe^{3+}, Mn^{3+}, Ni^{3+}, and Cu^{3+} is investigated, as this has been shown to reduce TEC in similar materials. Again, doping introduces distortion into the system, inducing different electron occupations of the Co *d*-orbitals, thus altering the electronic and magnetic structure. From these calculations, the 0 K electronic conductivity (σ_e) is obtained, with $SmMn_xCo_{1-x}O_3$ showing the highest σ_e, and $SmFe_xCo_{1-x}O_3$ lowest. From calculations of the oxygen vacancy formation energy,

no direct impact on the ionic conductivity is expected from Co-site doping. Mn^{3+}-doping show the lowest TEC at low x. Thus, the subject of our final study is $Sm_{0.75}Ca_{0.25}Mn_xCo_{1-x}O_{2.88}$ x=0.125, and 0.25. With the effect of Mn-doping at both x being negligible around the valence band maximum, and mainly being observed 2 eV below the Fermi level and 1 eV above in the conduction band, the electronic conduction is mediated by the Co d-bands. This, together with the presence of an oxygen vacancy, results in lower electronic conduction than observed in Chapter 6, but sufficiently high for IT-SOFC purposes. The limiting factor for IT-SOFC cathodes, and the factor making LSM unsuitable as a cathode material at lowered operating temperatures, is the ionic conduction. Ionic conduction and oxygen diffusion calculations show that $Sm_{0.75}Ca_{0.25}Mn_xCo_{1-x}O_{2.88}$ are good oxygen conductors, with higher ionic conduction than LSM. x=0.25 shows the lowest TEC, and is thus concluded to be the most favorable Mn-doping concentration. Thus, from this work, we present $Sm_{0.75}Ca_{0.25}Mn_{0.25}Co_{0.75}O_{2.88}$ as an IT-SOFC cathode material that offers significant performance benefits when compared to LSM.

Acknowledgements

Firstly, I would like to thank my supervisor Professor Nora H de Leeuw, for giving me the opportunity to do my PhD in your group and for giving me the chance to be involved in an exciting and important part of science. I am grateful for your support, guidance, and cheerfulness all through my PhD and Masters.

Secondly, I am grateful to Dr Xavi Aparicio-Anglès for all your help, supervision, discussion, and guidance all the way through this project, not at least when it comes to scrutinising, editing and reading all my work. I like to think you have succeeded in limiting my use of thus, even if I have managed to include it here and there.

I would also like to take this opportunity to thank everyone in the de Leeuw group. Zhimei, thank you for always being helpful with everything. For the people in my office, you always made it a treat coming in to work, and I will miss the lively discussions, laughs, and food.

I also wish to acknowledge the UCL Doctoral Training Centre in Modelling and Materials Science for funding my PhD, and the computing facilities which made the work presented in this thesis possible; Archer, Legion, Grace, Huygens, and Hartree.

Finally, I want to thank mamma, pappa, Fredrica, and Dolton for all the love, and support. Jag älskar er. Jon, I love you, thank you for always being there for me and for making every single second wonderful.

Table of Contents

List of Publications

The work described in this thesis is based upon the following papers

Olsson, E.; Aparicio-Anglès, X.; De Leeuw, N. H. Ab Initio Study of Vacancy Formation in Cubic LaMnO3 and SmCoO3 as Cathode Materials in Solid Oxide Fuel Cells. *J. Chem. Phys*. 2016, 145 (1), 14703.

Olsson, E.; Aparicio-Anglès, X.; de Leeuw, N. H. A DFT + U Study of the Structural, Electronic, Magnetic, and Mechanical Properties of Cubic and Orthorhombic SmCoO3. *J. Chem. Phys.* 2016, *145* (22), 224704.

Olsson, E.; Aparicio-Anglès, X.; de Leeuw, N. H. A Computational Study of the Electronic Properties, Ionic Conduction, and Thermal Expansion of $Sm_{1-x}A_xCoO_3$ and $Sm_{1-x}A_xCoO_{3-x/2}$ (A=Ba^{2+}, Ca^{2+}, Sr^{2+}, and x=0.25, 0.5) as Intermediate Temperature SOFC Cathodes. *Phys. Chem. Chem. Phys.*, 2017, *19*, 13960-13969

Olsson, E.; Aparicio-Anglès, X.; de Leeuw, N. H. Computational Investigation of Thermal Expansion, Electronic Properties, and Oxygen Vacancy Formation in $SmB_xCo_{1-x}O_3$ (B=Fe^{3+}, Cu^{3+}, Ni^{3+}, Mn^{3+}, and x=0.125, 0.25, 0.5, 0.75, 1.0) SOFC Cathodes. Paper to be submitted

Olsson, E.; Aparicio-Anglès, X.; de Leeuw, N. H. Combined Density Functional Theory and Molecular dynamics Study of $Sm_{0.75}Ca_{0.25}Co_{1-x}Mn_xO_{2.88}$ (x=0.125, 0.25) as Potential Intermediate Temperature Solid Oxide Fuel Cell Cathode. Letter to be submitted

List of Abbreviations

AIM: Atoms in Molecules

CG: Conjugate Gradient

DFT: Density Functional Theory

DFT+U: Method combining a DFT Hamiltonian with a Hubbard Hamiltonian for the description of on-site Coulomb interactions

DOS: Density of States

GGA: Generalised Gradient Approximation

IT-SOFC: Intermediate Temperature Solid Oxide Fuel Cell

KS: Kohn-Sham

LDA: Local Density Approximation

LPAW: Linear Augmented Plane-Wave

NCPP: Norm-Conserving Pseudopotentials

PAW: Projector Augmented Wave

PBE: Generalised gradient approximation density functional developed by Perdew, Burke, and Ernzerhof

PDOS: Projected Density of States

SD: Steepest descent

SOFC: Solid Oxide Fuel Cell

TEC: Thermal Expansion Coefficient

USPP: Ultrasoft pseudopotentials

VASP: Vienna *Ab-Initio* Simulation Package

VSEPR: Valence Shell Electron Pair Repulsion

List of Tables

List of Figures

Chapter 1

Introduction

1.1 Introduction

One of the most pressing issues in today's society is the development of clean and sustainable energy sources as viable alternatives to fossil based fuels. As natural resources are becoming limited, and the effects of global warming are becoming more concerning, widespread efforts are made to reduce carbon dioxide and other greenhouse gas emissions. This has led to a huge scientific interest in energy materials, with a wide range of alternative energy conversion, storage, and generation technologies. Such electrochemical devices, such as lithium batteries, solar cells, thermoelectrics, and fuel cells are already important in the current energy economy. They are predicted to become even more important in the future, when the research effort has made these technologies commercially viable. Before this potential can be realized it is critical that the mechanisms that govern the functionality of these materials are understood. This understanding will guide the improvement and development of new materials to enhance device performance.

In this thesis, computational modelling methods are employed to study such energy materials, in the subset of solid oxide fuel cell materials, with the intention to act as a predictive tool and guide for experimental study.

1.2 Fuel Cells

Fuel cells are electrochemical devices that convert chemical energy in a fuel into electrical energy, and their main advantage over traditional fuel-to-energy devices, such as combustion engines, is their low pollutants emissions. [1–5] Additionally, fuel cells are quiet and modular in their physical design, which make them suitable for a variety of applications. These applications range from stationary grid-scale electricity generation to portable ones for transport applications.[6] In fuel cells, the fuel is continuously supplied from an external source, and thus, in theory, a fuel cell could continue to produce electricity for as long as a fuel is supplied.

During the more than 170 years that have passed since William Grove first introduced the fuel cell concept in 1839, a wide array of fuel cell types have been developed. [7] Common for all fuel cells are that they have three main components; cathode, anode, and electrolyte. At the anode side, a fuel, normally hydrogen, is oxidized, whilst at the cathode oxygen is reduced. [7] These then react to form water, at which side this reaction occurs is cell type dependent. The main difference between cell types lies in the electrolyte material. The electrolyte can be either oxide ion or proton conducting. The electrolyte should be ion/proton conducting, but electronically insulating. Electric power is generated by an electron flow around an external circuit. [7]

There are five main classes of fuel cells; alkaline fuel cells (AFC), molten carbonate fuel cells (MCFC), phosphoric acid fuel cells (PAFC), polymer electrolyte membrane fuel cells (PEM), and solid oxide fuel cells (SOFC). A summary of electrolytes, electrodes, and fuels is included in Table 1.1. As can be seen from this summary, most fuel cell electrolytes are corrosive liquids. This, together with having platinum

based electrodes (AFC, PAFC, and PEM), which are expensive and can be corroded by the corrosive electrolyte, have limited their use. Thus, SOFC are widely regarded as being one of the most practically viable fuel cell technologies, as they are made up entirely of ceramic components. However, platinum and other expensive materials are still used in SOFC, but are sought to be replaced with other more low-cost materials. [3,7–9]

Table 1.1. Fuel cell types and their electrolytes, electrodes, fuels, and operating temperatures. [5,7,10]

Type	Electrolyte	Fuel	Electrodes	Temperature (°C)
AFC	Aqueous sodium or potassium hydroxide	H_2	Carbon with Pt electrocatalyst	100-250
MCFC	Molten potassium lithium carbonate	H_2/CO	Non-precious metals	500-700
PAFC	Phosphoric acid	H_2	Carbon with Pt electrocatalyst	150-250
PEM	Proton conducting membrane	H_2	Carbon with Pt electrocatalyst	70-110
SOFC	Solid ceramic inorganic oxide	H_2/CO /Hydrocarbons	Solid ceramic inorganic oxide	700-1000

1.3 Solid Oxide Fuel Cells

SOFC are an effective, promising, and low CO_2-emission alternative to traditional power sources. These electrochemical cells ideally convert H_2 and O_2 present in air into water, generating electrical power (schematic picture of the SOFC process is presented in Figure 1.1.). [1–4] However, one of the main advantages of SOFC is their fuel flexibility. This means that modern SOFC can run on hydrocarbons, due to internal reforming, making the application less dependent on the production of hydrogen gas, but on the other hand leaving more by-products, such as CO_2. [1–4] However, these possible by-products levels of CO_2 are much reduced in comparison

to those of traditional power sources, and there are no emission at all of NO_x, SO_x, or hydrocarbons. [7]

A schematic picture of a SOFC is presented in Figure 1.1. In SOFC, air is let into the cathode where the oxygen is reduced (equation 1.1), whereas the fuel is let into the anode (equation 1.2). The electric power produced by the SOFC is coming from the electrons liberated at the anode (equation 1.2), which are propelled around an external circuit (Figure 1.1). After oxygen reduction, the anions migrate through the electrolyte to the anode, where they react with hydrogen to form water (1.3). [7,11]

$$\text{Cathode} \qquad \frac{1}{2}O_2 + 2e^- \rightarrow O^{2-} \qquad (1.1)$$

$$\text{Anode} \qquad H_2 + O^{2-} \rightarrow H_2O + 2e^- \qquad (1.2)$$

$$\text{Overall} \qquad \frac{1}{2}O_2 + H_2 \rightarrow H_2O \qquad (1.3)$$

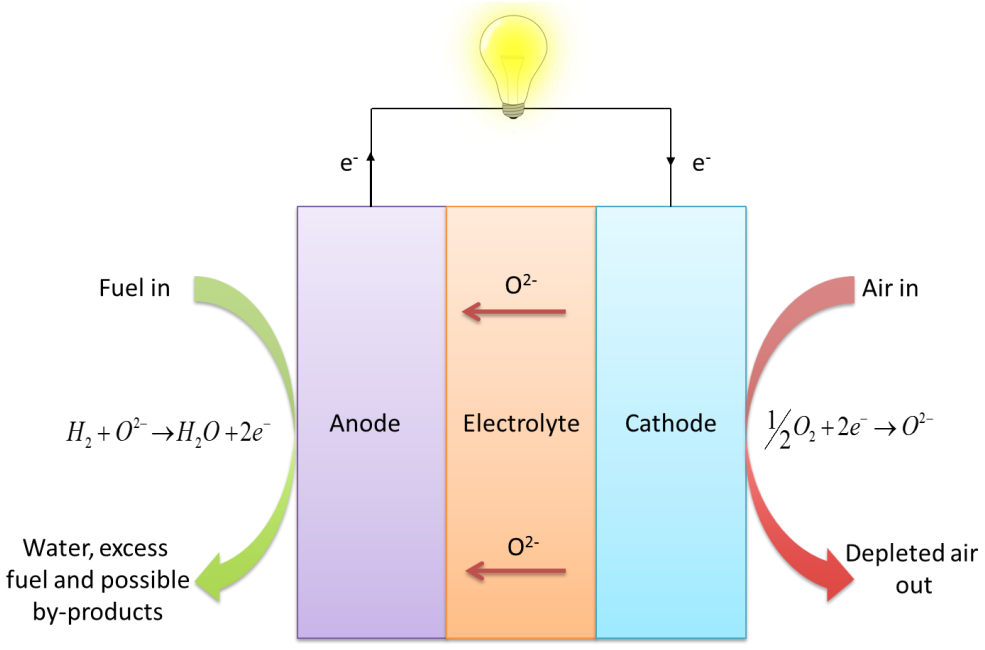

Figure 1.1. Schematic representation of a SOFC with ideal electrode reactions noted.

In the SOFC, the electrolyte is, as the name indicates, a solid oxide. The electrolyte should provide a gas diffusion barrier between the anode and the cathode, whilst having high ionic conductivity, and none or negligible electronic conductivity. Furthermore, the electrolyte should be chemically stable under both oxidizing (anode side) and reducing (cathode side) conditions. Traditional SOFC electrolyte materials are yttria-stabilised zirconia (YSZ), and gadolinium doped ceria (GDC). [5] As for the electrodes, these must both be porous, so as to enable gas diffusion to and from the electrode electrolyte interfaces, and be chemically stable at the SOFC operating temperatures and redox conditions. Both electrodes are also required to be good electronic conductors, and be chemically and physically compatible with the electrolyte. This compatibility is expressed in terms of matching thermal expansion coefficients (TEC), as this allows mechanical stress between the different components during cell operation to be minimised. The anode material, specifically, should have excellent catalytic activity for hydrogen oxidation and hydrocarbon reforming reactions (when running on non-pure hydrogen fuel). Normally, anodes are made of the same material as the electrolyte, in order to minimise the mechanical strain on the system, but with metal particles adsorbed at its surface, which are catalytically active. Typically, this metal is nickel, but other metals, such as platinum and copper, have been tested. Furthermore, the use of double perovskite and perovskite anodes have gained increased attention in recent years, in search of materials that can act both as anode, electrolyte, and cathode. [5,12–16]

Another important component of SOFC, are interconnects. The interconnects provide electrical connections between cells in a SOFC stack, and to the external circuit. Suitable interconnect materials are limited as they need to be stable under SOFC

conditions and high temperatures. Interconnect materials used are for example platinum and chromium. These interconnects are far from perfect, being both expensive, and at SOFC operating temperatures Cr-diffusion poisons the cell. [17]

1.4 SOFC Cathodes

Traditionally, SOFC operate at high temperatures, 800-1000°C. However, to decrease material cost (especially by using mild-steels instead of expensive alloys as interconnects), gain better long-term stability, increase SOFC material compatibility, and thus improve the fuel cell life time, efforts are made to reduce these temperatures to the intermediate range of 500-700°C, which leads to the concept of Intermediate Temperature SOFC (IT-SOFC). In IT-SOFC, the limiting factor is the cathode, which is the focus of this thesis. [1–4] A good cathode material should have (i) a small thermal expansion coefficient (TEC) that is compatible with its coupled electrolyte, (ii) high surface area to increase the active site concentration for the oxygen reduction reaction (ORR), (iii) high oxygen reduction catalytic activity at the operating temperature, and (iv) high oxygen ion bulk diffusion. [1] Hence, the main task for the SOFC cathode is to provide an efficient pathway for the reduced oxygen *via* the electrode to the electrolyte, through both bulk diffusion and surface exchange. [18,19] Koep *et al.* (2005) suggested that the ORR could follow three pathways in SOFC cathodes. [20]

1. The oxygen reduction can take place at the triple-phase boundary (TPB) where the oxygen gas, electrolyte, and oxygen meets, *via* direct electrochemical reduction. However, it is worth mentioning here that the importance of the TPB is decreasing as new cathode materials for IT-SOFC,

such as cobaltates and ferrites, have reactive sites over the entire cathode surface. [21,22]

2. A surface adsorption step, involving the adsorption and partial reduction of oxygen, with the breaking of the O-O bond, before the oxygen is transported through the electrode to the TPB.
3. Oxygen incorporation into the electrode through the surface of the cathode material, through surface exchange, and subsequent transport through the cathode bulk to the electrolyte. [20,23]

In the surface exchange rate-limiting proposal, it is suggested that the oxygen gas is incorporated at the surface through an adsorption step, followed by dissociation and charge transfer before entering the bulk, with one or more of the steps being rate limiting. [18–20,24] Under operating conditions, the preferred pathway is envisaged to be dependent on the electrode geometry and porosity, such as surface composition, vacancy concentration, and surface morphology. [20,25]

Another property influencing the cathode efficiency, is the area specific resistance (ASR), with lower ASR values being more favourable than high. ASR is related to the activation energy of the oxygen evolution process (*i.e.* ORR and the subsequent oxygen diffusion through the cathode to the electrolyte), and this activation energy can be obtained from Arrhenius plots of ASR. [26] High ASR indicates low ionic conduction, which in turn could be linked to low oxygen surface exchange rates and high polarisation resistances in the cell. These are all unfavourable properties, and hence low ASR are desired. Unfortunately, direct computational modelling of ASR is currently not possible, as it is dependent of the full cell setup and conditions. [26] To measure ASR, the cathode material is deposited onto an electrolyte material, and

properties such as layer thickness, cathode-electrolyte adhesion, and even cell preparation influence measurements. [26] Studies have found that ASR is linked to the oxygen *p*-band centre, which in turn is dependent on the oxygen vacancy formation energy, a property which is obtainable through computational methods. Lee *et al*. suggested in 2011 that log(ASR) decreases with decreasing negative O *p*-band centres, and that the bulk oxygen vacancy formation energy does so as well. [27] Hence, the study drew the conclusion that high log(ASR) leads to high bulk oxygen formation energy, and *vice versa*.

The efficiency of IT-SOFC cathodes is governed by the catalytic activity with respect to the oxygen reduction reaction, which depends on both the surface oxygen reduction and oxygen bulk diffusion. These reactions are oxygen vacancy assisted, whereby high oxygen vacancy concentrations are favourable. The main task of the IT-SOFC cathode is then to provide an efficient pathway for the reduced oxygen through the cathode bulk to the electrolyte. At the same time, the cathode should be able to transport electrons in the opposite direction, in other words having both ionic and electronic conductivity. [3] Furthermore, it is critical that the cathode is chemically and mechanically compatible with the electrolyte. Thus, the cathode material should have a thermal expansion coefficient (TEC) similar to that of its coupled electrolyte. If these are too different, the cell will break down, and the cathode efficiency in itself will not matter.[6,28,29] Normal TEC values are in the range of $10\text{-}13\times10^{-6}$ K^{-1}, and cathodes with TEC < 15×10^{-6} K^{-1} have been suggested to be suitable for electrolyte-coupling. However, efficient IT-SOFC cathode materials are often found to have TEC above 20×10^{-6} K^{-1} [30], which leads to the need of finding cathode materials with both high conductivity and low TEC.

Several studies have found that the ionic and electronic conductivity need to be increased in cathode materials in order to lower the operating temperature without losing cathode efficiency. [31,32] This has given rise to a new class of cathode materials with ambipolar conductivity, *i.e*. both electronic and ionic, classed as Mixed Ionic and Electronic Conductors (MIEC). [15,18] Traditional SOFC cathode materials are typically $LaMnO_3$-based perovskites, which will be further discussed below, and are mainly electronic conductors with low ionic conductivity. However, these materials lose its oxygen diffusion efficiency at lowered operating temperatures, thus leading to the need for materials with higher ionic conduction.

In the context of IT-SOFC, cathode materials are typically oxide perovskites. Depending on the combination of cations used, strain is introduced into the lattice, the cation-anion interatomic distances can be manipulated, and a variety of physical and chemical properties can be obtained. [33,34] For example, thermal stability is influenced by the combination of the cations, as well as redox properties being influenced mainly by the transition metal cation. [33–35] The ability to tune the chemical and physical properties of the perovskites, as well as their thermal stability, make them ideal for applications in fuel cells and catalysis. [33,36,37] Doping of the perovskite structure, widely utilised in solid oxide fuel cell components, does furthermore increase the possibilities to property enhancement and manipulation. [36]

1.4.1 Perovskites

The uses of perovskite materials are widespread, with applications ranging from methane combustion to catalysis. [34] The perovskite structure allows for a large variety of element combinations, and thereby highly tuneable materials properties.

Structurally, a wide range of defects can be accommodated, whilst still retaining structural stability. Ideal perovskites have chemical formula ABX_3, which has the same structure as its namesake, the mineral calcium titanate, $CaTiO_3$. Perovskites consist of two cations, A, traditionally lanthanides or alkaline earth metals, and B, usually transition metals, and anions, normally oxygen, forming corner sharing BO_6 octahedra. [36,38,39] Ideal perovskites possess a cubic structure with space group *Pm-3m,* [37] but other phases for perovskites are also possible, and highly abundant, *e.g.* rhombohedral and orthorhombic (Figure 1.2). [37] In the ideal cubic perovskite structure, *A* has a 12-fold coordination with respect to *O* and sits at the cuboctahedral sites at the cube corner positions (0 0 0), whilst *B* has a 6-fold coordination with respect to *O*, positioned in the middle, body centred position (½ ½ ½), of an octahedron with *O* in the corners, *i.e.* face centred positions (½ ½ 0). [2,34,37,40,41] The main focus in this thesis will be the cubic structure, as this is the phase commonly found for cathode materials at SOFC working temperatures [37].

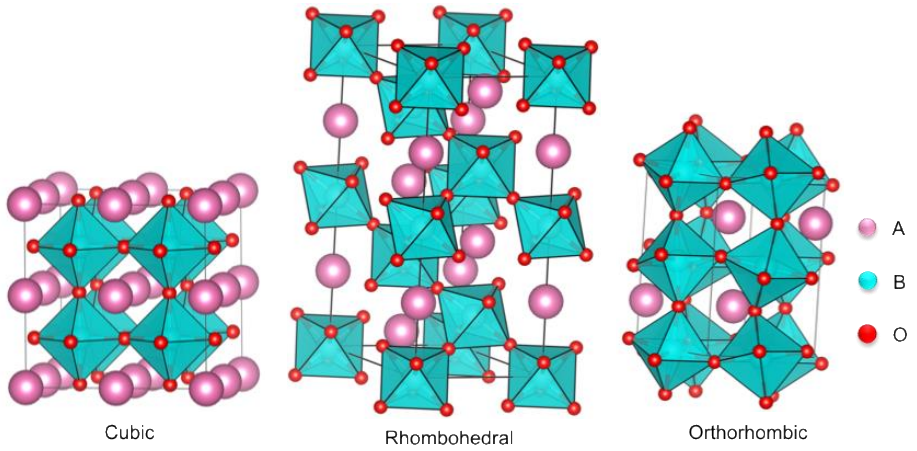

Figure 1.2. The different perovskite space groups. Pink spheres are A, blue B, and red O.

1.4.1.1 Structural Distortions in Perovskites

As mentioned above, one of the main advantages of perovskite materials is their ability to accommodate distortions. These distortions commonly arises from differences in A and B atomic or ionic radii, or from magnetic and electronic effects, and are typically observed as distortions to the BO_6 octahedra. To determine a certain element composition's formability as a perovskite structure, one can use the Goldschmidt Tolerance Factor (t), which is defined as

$$t = \frac{r_A + r_O}{\sqrt{2}(r_B + r_O)} \tag{1.4}$$

where r_A, r_B, and r_O, are the ionic radii of A, B, and O, respectively. Ideally, t=1 for perovskites. [42,43] Experimental studies have showed that perovskites are formed when 0.75<t<1.13, and that cubic structures are obtained for 0.89<t<1.00. At t<0.89, rhombohedral or orthorhombic structures are formed, whereas at values closer to 1.13, a hexagonal structure is observed. [44] *t* for systems in this thesis are provided in Appendix A.

1.4.1.2 Jahn-Teller Distortions and Crystal Field Splitting

Jahn-Teller (JT) distortions arise in perovskites when there is an increased separation in energy between occupied and unoccupied d-orbitals, and is especially occurring if B is an open shell transition metal. [45] In the ideal cubic perovskite structures, the regularity and non-distortion of the BO_6 octahedra results in the splitting of the B d-orbitals into three degenerate t_{2g} (lower in energy), and two degenerate e_g (higher in energy) orbitals, this is referred to as crystal field splitting (Figure 1.3). However, upon distortion of the BO_6 octahedra, t_{2g} or e_g orbitals split, moving away from the ideal

picture in Figure 1.3, and if these states are occupied, or partially occupied, this distorted structure could become more stable than the ideal cubic. For these pseudocubic structures, a portion of the B-O bonds normally elongate, whilst the other portion shortens. Furthermore, these distortions could lead to spin transitions, something that is very common in cobaltates. In cobaltates, the crystal field splitting energy of the Co *d*-states are comparable to the exchange energy from Hund's rule, leading to the energy gap between the e_g- and t_{2g}-states being small, and different cobalt spin states being possible. [46,47] The effect of this, and the spin states of cobalt, will be further discussed in Chapter 3, and as a running theme throughout this thesis.

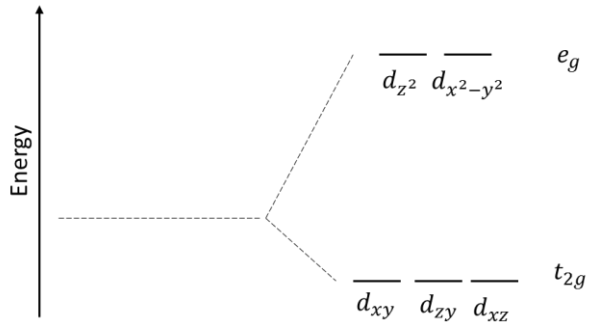

Figure 1.3. Crystal field splitting in an octahedral environment.

1.4.1.3 Defects in Perovskites

Moving away from the ideal theoretical picture of perovskites, it is important to consider the effect of defects on the perovskite structure and properties. Defects in crystals influence the structure, stability, material chemistry, and conductivities. Intrinsic defects, such as vacancies or interstitials, also increase with temperature (see chapter 4 for a complete discussion), and are thus of high importance in SOFC cathode materials. In cubic perovskites, vacancies are the main intrinsic defects, whilst interstitial defects are suppressed by the large ionic radii of the cations. [48]

Hence, Frenkel, and anti-site defects are not considered to be important for these perovskites. [48] Furthermore, it is worth mentioning that Schottky defects will not be considered in this work, due to the difference in valence between cations and anions. Schottky defects are vacancy pairs that form in a way so that the overall system remains charge neutral. However, in the systems investigated in this thesis, this would lead to the creation of 2 cation vacancies and 3 oxygen vacancies. This type of defect is furthermore only expected to exist in systems with an oxygen excess and at high temperatures (>1000°C), [49] which are higher than the IT-SOFC operating conditions, and hence only the individual vacancies will be discussed in this thesis.

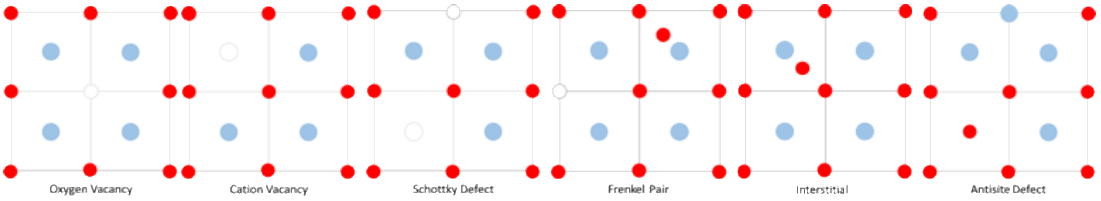

Figure 1.4. Schematic representation of different types of intrinsic defects. Red spheres are anions, blue are cations, and white with grey border is oxygen vacancy.

Extrinsic defects, such as substitutional dopants, are used to tune material properties, as will be explored in Chapters 5, 6 and 7. Doping can also lead to additional intrinsic defects, for example by charge compensation when substituting a +3-charged cation with a +2-charged one. Charge compensation then occurs either *via* a hole compensating mechanism, or an oxygen vacancy mechanism. This is essential for SOFC cathode materials, and is used to increase ionic conductivity. A further study of these mechanisms is presented and discussed in Chapter 5.

1.4.1.4 Oxygen Migration and Diffusion

Within perovskite SOFC cathode materials, the ion conduction is thought to follow a vacancy-hopping mechanism (Figure 1.5), with the oxygen anions migrating between oxygen vacancies on the edges of the BO_6-octahedra. The coexistence in these materials of different sub-lattices, restricts the diffusion paths of both oxygen and anions to their respective sub-lattice. Furthermore, oxygen self-diffusion is significantly faster in these materials than cation self-diffusion, which for the oxide materials investigated in this work can be assumed to be negligible in relation to the oxygen diffusion. [50] In crystalline materials, three migration paths are generally considered; interstitial, interstitialcy, and vacancy mechanisms. As interstitials are expected to be non-existent, or of negligible concentration, in cubic and pseudocubic perovskites with large cations, the first two migration paths are not normally considered for the ionic conductivity in SOFC cathodes. [48,50] The vacancy assisted mechanism involves an oxygen ion diffusing by jumping to a neighbouring vacancy (Figure 1.5), and is commonly known to direct oxygen transport in SOFC perovskites. Thus, it is of utmost importance that SOFC cathode materials have high oxygen vacancy concentrations, and low oxygen vacancy formation energies, as well as low oxygen migration energies. It is commonly seen that the barrier to oxygen migration is limiting to IT-SOFC cell performance, and governs at how low temperatures the cells are able to operate. Hence, this property has gained a lot of attention, and is seen as an important variable to reduce in IT-SOFC cathodes. Furthermore, the activation energy for oxygen diffusion is dependent on both the association energy and migration energy. Association energy is described as the electrostatic interaction between oxygen vacancies and dopants (see Chapter 4). Normally, the association

energy is easy to overcome at high temperatures, and hence, the activation energy is assumed to be equal to the migration energy. [51,52]

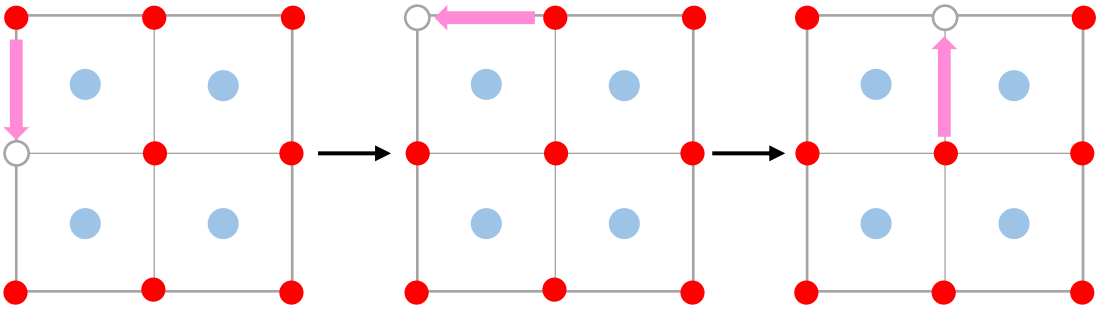

Figure 1.5. Schematic illustration of ionic conduction through vacancy-hopping mechanism in cubic crystal, with ion migration through vacancy filling by same type neighbouring species. For illustration purposes, oxygen vacancy around BO_6-octahedra has been chosen. Here blue dots are B, red oxygen, and white with grey border is oxygen vacancy.

1.4.2 Perovskite Materials for SOFC Cathodes

One important class of perovskite materials is the metal oxides perovskites, ABO_3 [38,39,53,54]. These materials have mixed ionic and covalent character, and it has been shown that the size of the *A*-cation strongly influences the *B*-O-*B* bond angle and distortion. [38,39] The *B*-O bonds are polar covalent and crystal field splitting is observed for the *B d*-orbitals. [55] Structural distortion, normally a consequence of doping, affects the electronic structure and the electron transport [38].

Controlling ionic and electrical conductivity, in addition to catalytic properties, for the ABO_3-type materials is of crucial importance for the enhancement of IT-SOFC performance. [53] The phenomenon controlling these properties is thought to be the oxygen diffusion, which is the limiting factor for IT-SOFC cathode efficiency, improved by the introduction of dopants and other defects, such as anion vacancies. [53] Thus, a large number of studies have been reporting on the oxygen diffusion in doped perovskite materials. [53]

In conjunction with experimental investigations, computational studies have been carried out, predominantly modelling the oxygen bulk diffusion, and how this is influenced by the dopant cation. By introducing differently charged dopants on the cation sites, the ionic conductivity can be increased as a consequence of increasing the number of oxygen vacancies through oxygen vacancy compensation schemes. Electronic conductivity can also be increased, but as a results of the mixed valence in the system and metallic electronic structure. [56] This has mainly been put down to the nature of the transition metal, which can induce metallic or semiconducting behaviour which in turn can increase the electronic conductivity. [35] Studies have also been performed regarding the substitution of *A*-site metals by both lanthanides and non-lanthanides. [57] Successful incorporation of the dopant is dependent on the dopant radii in respect to the original cation. [58]

1.4.2.1 Traditional Cathode Materials

Lanthanum manganate, $LaMnO_3$, is the current state of the art SOFC cathode parent material. [37,53,59–61] $LaMnO_3$ exhibits a plethora of favourable cathode properties, which have been assigned to the large number of variables relating to its charge, magnetism and structural interplay. [37] $LaMnO_3$ is orthorhombic at room temperature with an *A*-type antiferromagnetic magnetic structure [62,63]. However, at SOFC working temperature, $LaMnO_3$ is cubic, with a ferromagnetic ordering of the Mn *3d*-electrons. [37,54,63–68]

Sr-doped $LaMnO_3$, LSM, with general formula $La_{1-x}Sr_xMnO_{3-d}$, is the most important and current state-of-the-art SOFC cathode materials due to its high electronic conductivity, good ORR catalytic performance, low production cost, and good thermal

and chemical fit with the common SOFC electrolyte yttria-stabilised zirconia. [19,20,24,61,69–71] Substitution of La^{3+} with Sr^{2+} has been shown to increase the conductivity, [61] an effect assigned to charge compensation due to the different ionic charge of La^{3+} and Sr^{2+} and the many possible oxidation states of manganese. [53] However, lowering the operation temperature strongly influences the performance of the LSM cathode negatively, with lowered ORR efficiency and ionic conductivity. New cathode materials are hence sought by doping and combining LSM with other species, as well as exploring new perovskites. [71,72]

LSM cathodes also degrade at high temperatures owing to: (i) thermal stress at the grain boundaries with the electrolyte, leading to crack generation;[55] (ii) delamination of the electrode from the electrolyte, owing to the thermal stress and oxygen bubbling; [32,73] and (iii) migration of dopants and impurities to grain boundaries and dislocations, which reduces the effectiveness of the material as the oxygen migration from cathode to electrolyte becomes limited. [6,74] Therefore, it seems logical that to avoid these problems the operating temperature is reduced, but LSM has been shown to be less efficient under these conditions, with decreased ionic and electronic conductivity, leading to the need for now cathode materials. [3,6,7,25,69]

1.4.3 $SmCoO_3$-based SOFC Cathode Materials

Cobalt-based perovskites have attracted attention owing to their good performance at intermediate temperatures, with high ionic conductivity, and electronic conductivity sufficient for IT-SOFC cathode efficiency. It is well known that lanthanum cobaltates has higher ionic conductivity than LSM, [75] and more recently samarium cobaltate, $SmCoO_3$, has been reported to show excellent cathode potential at intermediate

temperatures. [1,3,15,18,71,76–82] Replacing La with Sm as the A-site cation can further prevent the formation of insulating phases from electrolyte-cathode interface reactions. La is known to react with electrolytes, especially YSZ, to form insulating pyrochlores such as $La_2Zr_2O_7$, with a substitution with the smaller ion Sm^{3+} not showing this reaction. It was also reported that this modification improve electronic conductivity. [83]

Through doping on either the Sm- or Co-site, or both, the ionic and electronic conduction can be enhanced in $SmCoO_3$, [1,15,71,76,80,81] and $SmCoO_3$-based materials (SCOs) are proposed to have higher oxygen diffusion than LSM. [82] The charge carrier (oxygen ions and electron holes) concentration in SCOs is typically increased as compared to $SmCoO_3$, leading to increased ionic and electronic conductivity. [71,76–79,82,84]

$SmCoO_3$ can exist in more than one phase, orthorhombic and cubic. [33,77,85] Due to the application of $SmCoO_3$ as a cathode material in this project, the focus lies on the cubic structure, as it is the stable structure at SOFC operating temperatures. [77,86] Apart from perovskite, $SmCoO_3$-based cathode materials could also have a spinel structure. The spinel gives better thermal expansion properties, but has shown worse electrochemical performance than perovskites, and thus, the perovskite structure has been selected for further study within this thesis. [87]

Electronically, $SmCoO_3$ is a semiconductor that possesses temperature-induced insulator-to-metal transitions as well as non-magnetic properties. [33,77,78,85,88–90] To enhance its electronic conductivity, $SmCoO_3$ is normally doped on the Co site in order to induce metallic behaviour. [35] Doping the Co-positions with dopants of

the same charge does not generate oxygen vacancies, but induces a change of the electronic structure, inducing electronic conductivity. [26]

Co-site doping with same period transition state metals can also decrease the thermal expansion coefficient, whereas Sm-site doping (with alkaline earth metals) typically increases TEC due to the increase of oxygen vacancies from the charge-compensation. [26] High thermal expansion coefficients in cobalt-based perovskites have been attributed to the increase in ionic radius of Co^{3+} during the aforementioned insulator-to-metal transition, which cobalt undergoes at elevated temperatures, whose effect can be reduced by the introduction of transition state metals with more stable spin states. [26] Co^{3+} can exist in different spin states, which will be discussed further in chapter 3, which are coupled to the transition, and these spin states alter the ionic radius of cobalt. [26] Introducing Fe^{3+} to the Co-site has been shown to increase the perovskite's thermoelectric properties by distortion of the lattice parameters, due to Fe^{3+} larger ionic radius as compared to Co^{3+}. [78] The same argument holds for the mixed valence Sm-site doping, but here the aim is to increase the ionic conductivity through charge compensation. [78] By doing this, the charge-transfer gap decreases, thus reducing $SmCoO_3$'s insulating properties. [78] This experimental study also showed that SCOs have good electrical conductivity at the SOFC operating temperatures. [78] A more thorough discussion on $SmCoO_3$-based cathodes is included in chapter 3 and onwards.

1.5 Motivation

The aim of this thesis is to investigate, through computational methods, novel IT-SOFC cathode materials based on $SmCoO_3$ and to compare those to the current

state-of-the-art SOFC cathode LSM. This will be done by doping the parent compound $SmCoO_3$, and modelling these systems using density functional theory (DFT) and molecular dynamics (MD). MD gives an insight into the oxygen diffusion, and thermal expansion, whereas DFT allows for the understanding of electronic and magnetic structures, as well as lattice structures and bulk chemistry. Computational techniques provide powerful tools with which to analyse and understand cathode efficiency at the atomistic level, and can also be used to complement and guide experimental study. To accomplish this, firstly, a bulk characterisation of $SmCoO_3$ is conducted, calculating physical and chemical properties. Secondly, different dopant schemes are evaluated in terms of improvement to IT-SOFC cathode properties such as thermal expansion coefficient, ionic and electronic conduction. Finally, on the basis of these results, a new cathode material is proposed, with enhanced properties compared to LSM and $SmCoO_3$ itself.

The thesis is divided into the following sub-sections. In Chapter 3, a bulk characterisation of $SmCoO_3$ is presented, and its magnetic, electronic, and mechanical properties are evaluated. As $LaMnO_3$ is very well studied in literature, it is used to benchmark results for $SmCoO_3$, and to serve as a direct comparison in Chapter 4. In Chapter 4, the influence of intrinsic defects in $SmCoO_3$ is studied, as defects influence the diffusion rate and reactivity of the cathode materials. Three defects are studied; oxygen vacancy and cation vacancies, all in their possible charge states. Building on from this, dopants are introduced to $SmCoO_3$, evaluating the effect of dopants on each cation site separately (Chapter 5 and 6), through different dopant schemes. Finally, the two dopant schemes are combined in the final part of this thesis to account for a possible practical IT-SOFC cathode material (Chapter 7).

Chapter 2

Methodology

2.1 Introduction

To understand and model SOFC cathode materials, it is important to appreciate the atomistic properties of the material such as electronic and magnetic structure, defect chemistry, and diffusion, as they influence the effect of dopants and the rate of oxygen reduction. Two different methodologies have been employed throughout this thesis: density functional theory (DFT), and molecular dynamics simulations (MD). DFT has been used, as this is a well-utilised and proven technique, for modelling the ground-state electronic structure of many-body systems in the solid state. It has further been shown useful for modelling transition metals, and complex metal oxides.[91] MD, on the other hand, allows for simulation of temperature dependent properties and atomic motion, such as thermal expansion coefficients and ionic conductivity. Most importantly, these two methods have successfully been used to model perovskite cathode materials in the past. [19,27,31,75]

Three simulation codes have been used in this thesis; the Vienna *Ab Initio* Simulation Package (VASP) [92–95], DL_POLY [96], and the General Utility Lattice Program (GULP) [97–99]. VASP was used for static-lattice DFT calculations, GULP for interatomic potential evaluation for use in the MD calculations, and finally DL_POLY was employed for MD simulations.

In this chapter, we introduce the theory behind these methods, first presenting the time-independent non-relativistic Schrödinger equation, and the Born-Oppenheimer approximation for explaining the motion of many electrons in a static nuclei field. Different approaches to solve the Schrödinger equation through the Hohenberg-Kohn theorems, and their applications through the Kohn-Sham equations are then presented together with a discussion of different exchange-correlation functionals, and the Hubbard parameter for Coulombic term improvement. Secondly, MD methods are introduced discussing Newton's equations of motion, finite difference methods, and how to control temperature and pressure during simulations utilising thermostats and barostats. Finally, interatomic potential models are discussed, and their implementation in this work indicated.

2.2 Schrödinger Equation

The Schrödinger equation was postulated by Erwin Schrödinger in 1926, and is a mathematical expression that allows for the determination of a given property (in this case the energy) for a given system. For a chemical system with *M* nuclei and *N* electrons, the interaction of the *M+N* particles can be expressed through the time-independent Schrödinger equation (2.1).

$$\hat{\mathcal{H}}\Psi = \mathrm{E}\Psi \tag{2.1}$$

where $\hat{\mathcal{H}}$ is the Hamiltonian operator, Ψ the electron wavefunction, and *E* the particle energy. Ψ contains all information of the studied system for a given quantum state, and the square of Ψ is the probability density that the studied particle is found in a given region of space. This can then be expanded to process interactions between multiple particles in a system, which forms the basis of electronic structure methods.

Electronic structure methods consider explicit *M* nuclei and *N* electrons forming a chemical system, and describe the interaction of the *M+N* particles through the non-relativistic time-independent Schrödinger equation 2.2

$$E\Psi = (E_{T,e} + E_{T,n} + E_{V,en} + E_{V,ee} + E_{V,nn})\Psi \quad (2.2)$$

The content of the parentheses on the right hand side of equation 2.2 represents i) kinetic energy of the electrons ($E_{T,e}$), ii) the nuclei kinetic energy ($E_{T,n}$), iii) the Coulomb attraction between nuclei and electrons ($E_{V,en}$), and iv) the Coulomb repulsion in-between electrons ($E_{V,ee}$) and in-between nuclei ($E_{V,nn}$), respectively. Unfortunately, due to the nature of equation 2.2 of being dependent on two sets of related variables (in terms of nuclei and electrons) and requiring the calculation of the electron-electron interaction term, a solution is not possible to find with the current available mathematical tools. Thus, an assumption based on the relative masses of the particles is employed, in order to simplify the problem.

2.2.1 Born-Oppenheimer Approximation

In 1927, Max Born and J. Robert Oppenheimer assumed that the motions of nuclei and electrons could be separated. The mass of a proton is ~1830 times larger than that of an electron, leading to the assumption that the relative velocity of an electron is much higher than that of the nuclei. This formed the basis of the Born-Oppenheimer Approximation. [100]

The Born-Oppenheimer Approximation, by neglecting nuclei kinetic energy (term ii in 2.2) and assuming constant nucleic repulsion (term iv in 2.2), separates electronic and nuclear coordinates in the many-body wavefunction, and thus simplifies equation

2.2. This simplified Schrödinger equation (2.3) then describes the electron motion within a static nuclei arrangement.

$$E\Psi = \left[-\sum_{i=1}^{N} \frac{1}{2} \nabla_i^2 - \sum_{i=1}^{N} \sum_{A=1}^{M} \frac{Z_A}{r_{iA}} + \sum_{i=1}^{N-1} \sum_{j>i}^{N} \frac{1}{r_{ij}} \right] \Psi \qquad (2.3)$$

Here, the first summation is the electron kinetic energy, the second summation is the electron nuclear attraction, and the third summation represents the electron-electron repulsion. ∇ is the Laplace operator, which represents the second derivative of a nucleus or electron with respect to the spatial coordinates, Z_A is the atomic number of nucleus A, r_{iA} is the distance between electron *i* and nucleus *A*, whereas r_{ij} is the distance between electron *i* and electron *j*. However, the exact solution for equation 2.3 can only be obtained for hydrogen like atoms, *i.e.* atoms consisting of a nucleus and only one electron. For multi-electron and multi-atom systems, further simplifications are necessary.

For multi-electron systems, the Coulomb repulsion (term iv in 2.2) becomes challenging to evaluate as there are no mathematical tools to do so, and thus further approximations are necessary. Early approaches included to reduce the multi electron problem to a single electron problem, which led to the foundation of Hartree-Fock theory. Hartree-Fock theory assumes that every electron in a system interacts with a mean-field of all the other electrons in the system. However, Hartree-Fock theory has a major disadvantage in its total energy solution. The total energy obtained from Hartree-Fock methods differs by the correlation energy from the exact total energy of the system. This discrepancy arises from the correlation of parallel electron motions. Methods have been developed to improve this difference (post-Hartree-Fock

methods), but for solid state modelling, density functional theory (DFT) remains the preferred method and is the one used for the electronic structure simulations in this thesis.

2.3 Density Functional Theory

2.3.1 Hohenberg-Kohn Theorems

Density functional theory (DFT) has its basis in the two Hohenberg-Kohn theorems. Presented by Walter Kohn and Pierre Hohenberg in 1964, the first theorem states that ground state electron density $n(\mathbf{r})$ provides a unique solution to the Hamiltonian, and hence all the properties of a multiple electron system, and its total energy, can be exactly calculated from its ground state. [101] The second Hohenberg-Kohn theorem state that a universal functional $F[n(\mathbf{r})]$ exists such that the total energy of a system $E[n(\boldsymbol{r})]$ of electrons can be calculated from its corresponding electron density following equation 2.4. [101]

$$E[n(\boldsymbol{r})] = F[n(\boldsymbol{r})] + \int n(\boldsymbol{r})V(\boldsymbol{r})d\boldsymbol{r} \tag{2.4}$$

where $F[n(\boldsymbol{r})]$ contains the inter-electronic Coulomb repulsion, exchange and correlation energies in addition to kinetic energy, and $V(\mathbf{r})$ is the Coulomb attraction between nuclei and electrons for atomic systems. To solve equation 2.4, the variational principle was applied, by minimizing $E[n(\boldsymbol{r})]$ to obtain the system ground state energy, and therefrom the exact $n(\mathbf{r})$ and properties. However, difficulties in solving the Hamiltonian electron-electron term still persists, and the exact form of $F[n(\boldsymbol{r})]$ remains unknown.

2.3.2 Kohn-Sham Equations

A scheme to solve equation 2.4 was published the following year, 1965, by Kohn and Lu Jeu Sham. [102] Here, a fictional system with non-interacting electrons is introduced with the same density as the real system of interacting electrons, with the energy of the fictional system being able to be split into the following terms:

$$E[n(\boldsymbol{r})] = E_T[n(\boldsymbol{r})] + E_V[n(\boldsymbol{r})] + E_H[n(\boldsymbol{r})] + E_{XC}[n(\boldsymbol{r})] \tag{2.5}$$

$E_T[n(\boldsymbol{r})]$ is the Kohn-Sham kinetic energy of the fictional system of non-interacting electrons, $E_V[n(\boldsymbol{r})]$ is the potential energy, $E_H[n(\boldsymbol{r})]$ is the Hartree energy relating to the Coulomb repulsion between all electrons, and $E_{XC}[n(\boldsymbol{r})]$ is the exchange correlation energy, which is a correction to the kinetic energy and the non-classical inter-electronic repulsion due to exchange and correlation. As the kinetic energy term is now expressed in terms of a non-interacting system, the wave-function can be written as a Slater determinant (equation 2.6).

$$\Psi_{SD}(\boldsymbol{r}_1, \dots, \boldsymbol{r}_N) = \frac{1}{\sqrt{N!}} \begin{bmatrix} \psi_1(\boldsymbol{r}_1) & \cdots & \psi_N(\boldsymbol{r}_N) \\ \vdots & \ddots & \vdots \\ \psi_N(\boldsymbol{r}_N) & \cdots & \psi_N(\boldsymbol{r}_N) \end{bmatrix}, \tag{2.6}$$

$\psi_1(\boldsymbol{r}_1)$ are the single particle orbitals. A Slater determinant describes wavefunctions of multi-fermionic systems. Using the Born interpretation of the wave function, which states that the probability of finding a given particle at a given point is proportional to the square modulus of the wavefunction, the electron density can then be written as

$$n(r) = \sum_i^N |\psi_i(r)|^2 = |\Psi|^2 \tag{2.7}$$

Building from this, the total system energy can be expressed in terms of an expectation value of the wavefunction's Hamiltonian. To reproduce the ground state density, an external potential v_{eff} is chosen such that the ground state energy (E_{gs}) can be written as

$$E_{gs} = \langle \Psi_{gs}[n] | \hat{H} | \Psi_{gs}[n] \rangle \tag{2.8a}$$

where

$$\hat{H} = \frac{\hbar \nabla^2}{2m} + v_{eff} \tag{2.8b}$$

$$v_{eff} = v_{ext}(\boldsymbol{r}) + v_{Hartree}(\boldsymbol{r}) + v_{xc}(\boldsymbol{r}) = v_{ext}(\boldsymbol{r}) + \int d\boldsymbol{r}' \frac{n(\boldsymbol{r})}{|\boldsymbol{r} - \boldsymbol{r}'|} + \frac{\delta E_{xc}[n]}{\delta n(\boldsymbol{r})}, \tag{2.8c}$$

In equation 2.8, v_{ext} is the electron-ion interaction, $v_{Hartree}$ is the electron-electron potential, and v_{xc} is the exchange-correlation potential. Using the Kohn-Sham formulation of the Schrödinger equation, the single particle orbitals can be determined as

$$\left(-\frac{\hbar \nabla^2}{2m} + v_{eff}(\boldsymbol{r}) \right) \psi_i(\boldsymbol{r}) = \varepsilon_i \psi_i(\boldsymbol{r}), \tag{2.9}$$

$v_{eff}(\boldsymbol{r})$ is the effective potential, $\psi_i(\boldsymbol{r})$ is the Kohn-Sham orbital, and ε_i is the Kohn-Sham orbital eigenvalue. Equation 2.9 forms the basis of Kohn-Sham DFT, and are a system of equations that are solved self-consistently from an initial electron density guess until convergence. However, an exact solution to $E_{XC}[n(\boldsymbol{r})]$ is not currently available, and hence this approach does not solve the ground state of a many-body system exactly. Approaches have been proposed to approximate the exchange-

correlation functional, such as the local density approximation and generalised gradient approximation presented below.

2.3.3 Exchange Correlation Functionals

2.3.3.1 Local Density Approximation

The local density approximation (LDA) is a rough approximation of E_{XC}, calculating the exchange-correlation from the electron density at each point in space through a homogeneous electron gas, a jellium, as

$$E_{XC}^{LDA}[n(\mathbf{r})] = \int d^3\mathbf{r} n(\mathbf{r})\, \varepsilon_{XC}^{LDA}\big(n(\mathbf{r})\big) \tag{2.10}$$

where ε_{XC} is the exchange-correlation energy for each particle in the jellium. This can be further extended to spin-polarised systems by calculating the spin up (α) and spin down (β), electron density separately, leading to the local-spin-density-approximation (LSDA).

$$E_{XC}^{LSDA}\big[n_\alpha, n_\beta\big] = \int d^3\mathbf{r} n(\mathbf{r})\, \varepsilon_{XC}\big(n_\alpha, n_\beta\big) \tag{2.11}$$

LDA has shown good results, accurately calculating bond lengths. However, LDA has also shown poor reproducibility of van der Waals interactions and underestimation of band gaps, leading in some cases to the prediction of metallic behaviour for semiconductors. The method also fails to describe atomic core levels, and *d*- and *f*-orbitals.[19,103,104]

2.3.3.2 General Gradient Approximation

The shortcomings of LDA can be improved by introducing gradient corrections to the exchange-correlation energy for each particle in the jellium. This approach is referred to as the general gradient approximation (GGA) and expressed as

$$E_{XC}^{GGA}[n(\mathbf{r})] = \int d^3\mathbf{r}\left(n(\mathbf{r}), \nabla n(\mathbf{r})\right) \tag{2.12}$$

GGA has shown many improvements compared to LDA, such as more accurate bond lengths, lattice constants (although for noble metals LDA tends to give better agreement with experiment) and bond angles, improved atomic and binding energies and band gaps.[104] Thus, this approach has been chosen for this project over LDA, by the implementation of Perdew-Burke-Ernzerhof (PBE) functionals.[105–108] However, GGA does still underestimate band gaps in semiconductors, which leads to the need for corrected GGA to be applied to the system investigated here. [19]

The DFT+U method aims to be an improvement on GGA techniques by implicitly taking into account the electron self-interaction error, and is described in more detail in the next section. Other approaches commonly includes Meta-GGA and hybrid functionals. Meta-GGA are based on GGA functionals, but also includes the second derivative of the electron density and depends on the kinetic energy density.[104] Hybrid functionals includes an exact exchange part, obtained from Hartree-Fock theory, which acts as a self-interaction cancellation in some extent. Hartree-Fock theory does not experience self-interaction errors, as the diagonal terms in the exchange and Coulomb integrals cancel, and hence, DFT calculations are proposed to be improved by mixing in Hartree-Fock exchange. Normally, 25% Hartree-Fock

exchange is used (PBE0), but the exact amount, and calculated results, are in VASP dependent on a pre-converged PBE calculation.[104] These methods whilst useful have been rejected in this work though, as they would induce a too high computational cost, preventing a meaningful study of dopant types and concentrations. As this is of critical importance for the understanding of SOFC cathode performance, the DFT+U method was chosen.

2.3.4 DFT+U Method

The electron self-interaction problem inherent in DFT arises from the electron interacting with an average of all the electrons, including itself. [109] This leads to DFT favouring delocalised solutions, and failing when modelling transition metals that got localised *d*- and *f*-states. It is well documented that DFT usually fails when describing the electronic structure of transition metal perovskites, and that normal exchange correlation functionals cannot correct the electron self-interaction problem, leading to a metallic description of perovskites and/or an underestimation of their band gaps. [65,110,111] The DFT+U method seeks to reduce the overlapping of orbitals that arises from the delocalisation of DFT by introducing a penalty energy for the hybridisation of *d*- or *f*-orbitals. [112] The method introduces a Hubbard parameter, or U parameter, which penalises double *d*-band occupation, thus enhancing the on-site Coulomb repulsion between electrons in the same *d*-band.

The U-parameter is fitted empirically so that the model reproduces existing experimental data. There are different implementations of the DFT+U approach. The one used in this work is Dudarev's approach (equation 2.13). [109]

$$E_{DFT+U} = E_{DFT} + \frac{U_{eff}}{2} \sum_{\sigma} r[n^{\sigma} - n^{\sigma} n^{\sigma}] \quad (2.13)$$

Here, n^{σ} is the on-site density matrix of the *d*-electrons with spin σ, and U_{eff} is the difference between the Coulomb, *U*, and the exchange, *J,* interactions between the electrons. This approach has been chosen as it is widely used for perovskites, and only one parameter, U_{eff}=*U*-*J,* has to be fitted empirically. *J*=1 has been applied throughout this thesis. [19]

In this work, U_{eff} is introduced for the cobalt 3*d*-electrons. To the best of our knowledge, no U_{eff} parameter had been previously reported for Co *d*-electrons in $SmCoO_3$. We performed an empirical fitting with respect to its geometric parameters, but results were inconclusive, with increasing U-values giving decreasing lattice parameter and increasing band gap (see Table 2.1). Hence, we decided to use U_{eff} = 3 eV, with Co PBE potential, as this value has been previously used for other cobalt-based perovskites and fitted to experimental data for $LaCoO_3$. [19,113] Furthermore, this *U*-value gives good structural agreement, and a band gap within the range previously observed for cobalt perovskites. [113,114]

Table 2.1. Comparison of cobalt PBE functionals and cobalt U_{eff} values for $SmCoO_3$ in terms of lattice parameter (a), interatomic distances, and band gap (E_g). Co pseudopotentials have their semi core states frozen, whereas Co_pv pseudopotentials have *p*-electrons treated as valence electrons. [115]

		U_{eff}	a (Å)	Sm-O (Å)	Co-O (Å)	E_g (eV)
Experimental			3.751	2.652	1.875	
Co	PBE	N/A	3.757	2.653	1.876	0
	PBE+U	2	3.754	2.654	1.877	0.24
		3	3.754	2.654	1.877	0.68
		4	3.752	2.653	1.876	1.02
		5	3.751	2.652	1.875	1.16
		6	3.750	2.651	1.875	1.26
Co_pv	PBE	N/A	3.759	2.658	1.880	0
	PBE+U	2	3.757	2.657	1.879	0.27
		3	3.756	2.656	1.878	0.69
		4	3.757	2.656	1.878	1.04
		5	3.755	2.656	1.878	1.19
		6	3.756	2.656	1.878	1.29

2.3.5 Electronic Structure Problem in Periodic Solids

Applying these methods to crystalline solids, the number of atoms and electrons in the simulation cell can be reduced by taking into account symmetry elements. Within this thesis, this has been applied though the use of plane-wave basis sets.

2.3.5.1 Bloch's Theorem

The wavefunction of a free electron is described by a plane wave, $\psi \sim e^{i\mathbf{k}\cdot\mathbf{r}}$, where a perpendicular plane to vector **k** is made from points with constant value. The one electron wavefunction ($\psi_{i,\mathbf{k}}(\mathbf{r})$) moving in a periodic potential is furthermore similar to the wavefunction of a free electron $e^{i\mathbf{k}\cdot\mathbf{r}}$, and is described by the function $f_{i,\mathbf{k}}(\mathbf{r})$ through equation 2.14. [116]

$$\psi_{i,\mathbf{k}}(\mathbf{r}) = f_{i,\mathbf{k}}(\mathbf{r})e^{i\mathbf{k}\cdot\mathbf{r}} \tag{2.14}$$

$f_{i,\mathbf{k}}(\mathbf{r})$ has the periodic character of the crystal, which means that whether the input argument is **r** or any other translational vector (**T**) within the same crystal periodicity, the value of $f_{i,\mathbf{k}}(\mathbf{r})$ will be the same. $f_{i,\mathbf{k}}(\mathbf{r})$ can be expanded as a Fourier series of vectors **G** in the reciprocal lattice, where **G** is defined as $e^{i\mathbf{G}\cdot\mathbf{T}} = 1$.

$$f_{i,\mathbf{k}}(\mathbf{r}) = \sum_{\mathrm{G}} c_{i,\mathbf{k},\mathbf{G}}\, e^{i\mathbf{G}\cdot\mathbf{r}} \tag{2.15}$$

Equation 2.14 and 2.15 give that wavefunctions with index **k** have the same solutions as those with index **k+G**. Thus, it is sufficient to find the solutions for **k**-points in the first Brillouin zone, *i.e.* the primitive cell in reciprocal space. Not solving these equations in reciprocal space would result in a finite number of equations with an infinite number of variables, whereas solving these problems in reciprocal space gives the reverse, and thus the **k**-points are those points in which the wavefunction is evaluated.

In this work, two methods for **k**-point sampling have been used; the improved tetrahedron method, and the Monkhorst-Pack method. [117,118] The improved tetrahedron method breaks up the simulation cell in reciprocal space into tetrahedra, whereas the Monkhorst-Pack method generates a grid of **k**-points in the Brillouin zone.

2.3.5.2 Plane-wave expansion of the wavefunctions

Substituting equation 2.15 into equation 2.14, each wavefunction can be expressed as a basis set plane-wave expansion, according to equation 2.16.

$$\psi_{i,\mathbf{k}}(\mathbf{r}) = \sum_{\mathrm{G}} c_{i,\mathbf{k},\mathbf{G}}\, e^{i(\mathbf{G}+\mathbf{k})\cdot\mathbf{r}} \tag{2.16}$$

Exact description of the electronic wavefunction is only possible to obtain from an infinite plane-wave basis set. Practically though, $c_{i,\mathbf{k+G}}$ tend to 0 for high kinetic energy plane-waves, and is thus commonly truncated to only take into account plane-waves with kinetic energy below this cut-off. This plane-wave cut-off is established through convergence testing for the specific system in interest. Furthermore, as $\psi_{i,\mathbf{k}}(\mathbf{r})$ is dependent on plane-wave coefficient $c_{i,\mathbf{k+G}}$, finding a solution to the Kohn-Sham equation is reduced to finding a set of $c_{i,\mathbf{k+G}}$ such that this set minimizes the energy.

However, the wavefunction size (determined by the plane-wave cut-off) is still large for multi-body systems, and thus it is necessary to introduce approximations, such as pseudopotentials.

2.3.5.3 Basis sets

Solving the single-particle Kohn-Sham equations, the single-electron wavefunctions need to be expanded in terms of a basis. By doing this, one transforms the single-particle Schrödinger equations into a matrix equation. This matrix equation can then in turn be efficiently solved computationally. In modern electronic structure techniques, two broad classes (with the suitability being dependent on the expansion of the valence orbitals and the charge densities) of this solution are defined; atomic orbitals (AO) and plane-wave basis sets. For molecular systems, AO have been applied to solve the Kohn-Sham equations, by composing a basis of a finite number of atomic orbitals, each centred at the individual atomic nuclei within the molecule. Plane wave basis sets are not localised on an atom and the forces are directly

calculated from the Hellmann-Feynman theorem.[119,120] Plane wave basis sets utilises Fourier transforms to move between k- and real space, which increases computational efficiency. Plane waves are orthogonal across the system, and thus basis superposition errors are avoided.

In theory, a basis set would be complete enough to be a representative of any wave function if an infinite number of plane waves (or AO) were considered. However, this is computationally impractical, and thus the basis set needs to be truncated at such a point that the kinetic energy is sufficiently converged to converge the total energy calculation.

2.3.5.4 Pseudopotentials

Pseudopotentials reduce the wavefunction size problem, and thus calculation complexity, by just considering the valence electrons of the investigated system explicitly, treating the core electrons as a punctual charge. The interaction between the pseudopotential and the valence electrons is simulated by introducing a potential term acting on the valence electrons, which replaces the Coulomb potential for the nucleus and core electrons. Core electrons are thus assumed to have low chemical reactivity, an assumption which forms the basis of norm-conserving pseudo-potentials (NCPP). Within the NCPP methodology, the atom core region is replaced by a soft nodeless pseudo-wavefunction having the same charge as the all-electron wavefunction for this region, where before application of NCPP core wavefunctions would be oscillating rapidly. [121] Building on from the NCPP approach, the ultrasoft pseudopotentials (USPP) were developed. For these, the core electrons charge is

not kept fixed, but instead allowed to vary. The variation in charge is then compensated by localized atom-centred augmentation charges. [122]

2.3.5.4.1 Projector Augmented-Wave Method

The projector augmented-wave (PAW) method [123] is the most robust pseudopotential method and is inspired by the all-electron linear augmented plane-wave (LAPW) method. [124] Within the PAW approximation, one can express the wavefunction per equation 2.17.

$$\psi(\mathbf{r}) = \tilde{\psi}(\mathbf{r}) + \sum_{\Lambda} \left[\phi_A(\mathbf{r}) - \widetilde{\phi_A}(\mathbf{r})\right] \langle \widetilde{p_\Lambda} | \tilde{\psi} \rangle \qquad (2.17)$$

Here, ψ is the wavefunction, $\tilde{\psi}$ the pseudo-wavefunction, $\widetilde{p_\Lambda}$ are projector functions, and ϕ_A and $\widetilde{\phi_A}$ are the one-electron Schrödinger equations for the isolated atom partial waves and auxiliary pseudo-partial waves, respectively. Within this framework, ψ adapts atom-like behaviour within the atomic (augmentation) regions, whereas outside (interstitial regions) ψ is identical to $\tilde{\psi}$. The solutions to ϕ_A forms the basis set in the augmentation region and have nodal behaviour. Expanding $\widetilde{\phi_A}$, such that ϕ_A=$\widetilde{\phi_A}$ in the interstitial region, within the augmentation region, $\tilde{\psi}$ is cancelled out. Equation 2.16 is exact if one can perform a complete expansion of ϕ_A. However, in practice, this expansion is truncated to allow fast convergence. Because of this, the augmentation regions will have some $\tilde{\psi}$ contributions. Furthermore, in this method, the core electrons are considered frozen for atomic solutions, and the full all-electron wavefunction is used to allow for the calculation of properties which are dependent on the spin density and full charge. Finally, PAW enables faster $\tilde{\psi}$ convergence

compared to NCPP and USPP, and is the method used in this method, as implemented in VASP. [125]

2.3.6 Geometry Optimization Techniques

To optimise atomic positions and cell parameters, a variety of methods are available. The methods do not only aim to find the minimum electronic energy, but do also minimize the inter-nuclear Coulomb energies at 0 K. By combining these two energies, the total energy is obtained.

2.3.6.1 Conjugate Gradient Method

The conjugate gradient method (CG) is used to optimise ionic positions. [126] For an ionic system, the CG method calculates the energy function $E(\mathbf{R})$ and its gradient with respect to the ion's (or nuclei) coordinates, **R**. The gradient, $-\partial E(\mathbf{R})/\partial \mathbf{R}$, is defined as the force (**F**) acting on the ions. It is calculated by solving the Hellman-Feynman theorem for a given system.

CG uses the steepest descent algorithm (SD) to find optimised ionic positions. In SD, the atoms are moved in the direction of **F**, and the evaluation of $E(\mathbf{R})$, is initially carried out at regular intervals along two points. For any initial position $\mathbf{R}_1$, the new position $\mathbf{R}_2$, can be expressed as

$$\mathbf{R}_2 = \mathbf{R}_1 + b_1 \mathbf{F}(\mathbf{R}_1) \tag{2.18}$$

where b_1 is picked so that $\mathbf{F}(\mathbf{R}_2)\cdot\mathbf{F}(\mathbf{R}_1)=0$. The new gradient ($\mathbf{F}(\mathbf{R}_2)$) should be perpendicular to the previous line. The procedure is then repeated from this new point along the direction of $\mathbf{F}(\mathbf{R}_2)$ until such a time as a minimum is located. This is a

disadvantage of the SD method, as only directions which are perpendicularly related are allowed, and it leads to a larger number of required iterations before convergence.

The first step of the CG and SD methods is the same. However, in the CG method, the successive displacements, which were restricted in SD, can take any direction. This is expressed in equation 2.19.

$$\mathbf{R}_{m+1} = \mathbf{R}_m + b_m \mathbf{S}_m \tag{2.19}$$

$\mathbf{S}_m$ is a search vector, and contains gradient and search direction information from the previous step.

$$\mathbf{S}_m = \mathbf{F}(\mathbf{R}_m) + \gamma_m \mathbf{S}_{m-1} \tag{2.20}$$

In equation 2.20 the scalar coefficient γ_m is 0 when m=1. For m>1, γ_m is defined as

$$\gamma_m = \frac{\mathbf{F}(\mathbf{R}_m)\cdot\mathbf{F}(\mathbf{R}_m)}{\mathbf{F}(\mathbf{R}_{m-1})\cdot\mathbf{F}(\mathbf{R}_{m-1})} \tag{2.21}$$

The CG method, in relation to SD, thus readily reduces the number of iterations needed to find the energy function minimum. The search directions are independent (conjugate) from each other, which enables the minimum to be found from a quadratic function of *M* variables in *M* steps.

The CG method is implemented in VASP. Firstly, the ions and cell shape, dependent on calculation type, are changed using SD. Secondly, a line minimization is required in the CG method. This is done in several steps;

(i) a trial step in the search direction is performed whereby the energy and forces are recalculated.

(ii) approximate total energy minimum is obtained from a cubic or quadratic interpolation using the change in energy and forces from the previous step. Following this, a corrector step is included so that the ionic positions corresponds to the newly calculated minimum.

(iii) Following the corrector step, energy and forces are re-evaluated for the new ionic positions. The VASP code then checks if the new forces contain any significant component that is parallel to the search direction in the previous step. If so, additional corrector steps are performed to improve the line optimisation.

This outline assumes that only a single minimum is present in the energy function. For an energy function with several minima, this method will find the minimum within the basin of the initial sampling point.

2.3.6.2 Pulay Stress and Equation of State Method – Cell Parameter Relaxation

To optimise cell parameters, and not only ionic positions, Pulay stress can arise. [127] This originates from the plane wave basis set not being complete with respect to volume changes. The number of base functions are determined by the energy cut-off and the reciprocal lattice cell size. During lattice parameter optimisation, the crystal cell volume will vary, which in turn will change the number of plane waves in the basis set for the same cut-off. This relates to a pressure larger than zero or in other words stress, which has a tendency to decrease volume. This can be prevented by choosing an energy cut-off ~30% higher than necessary for energy convergence. Disadvantageously though, this increases computational expense. However, such a

cut-off should be sufficient for converging the stress tensor and will thus justify the increase in computational time.

Another method to avoid Pulay stress is to perform volume conserving calculations, whereby one only allow the ion coordinates and cell shape to relax. In this type of calculation, the basis set remains constant, and the Pulay stress is kept to a minimum as it is mainly volume dependent. To find the equilibrium cell volume, an energy versus volume graph can be plotted, with a cubic equation of state fitted to the points, wherefrom a minimum can be localised.

2.3.7 DFT Optimised Structure Analysis

To analyse our DFT results, vibrational frequencies, density of states, and Bader charges have been used to obtain properties and to characterise steady states.

2.3.7.1 Vibrational Frequencies

For an optimised structure, the gradient of each individual vibrational mode should be zero. Both local and global minima on a potential energy surface have positive second derivatives, giving all real vibrational frequencies. For a transition state however, one vibrational frequency will be imaginary, as one of its secondary derivatives is negative. This is implemented in VASP by calculating the second derivative of the energy gradient numerically from small atomic displacements at each Cartesian coordinate. Furthermore, the Hessian matrix, which is the second derivative of the energy with respect to atomic positions, can be determined from forces, leading to convergence of forces to find optimised structures important. The vibrational

frequencies are then the eigenvalues in the Hessian matrix, and the vibrational normal modes are the eigenvectors.

2.3.7.2 Bader Charge Analysis

Bader charge analysis is a methodology that partitions atomic charges based upon electron density and its gradient, which can be readily obtained from DFT calculations and is convenient for condensed matter use. This methodology was proposed by Richard Bader who introduced the Atoms in Molecules (AIM) theory for topological analysis of electron density and based it on the Lewis model and Valence Shell Electron Pair Repulsion (VSEPR). [128–131] The electron density in a chemical bond between two atoms is highest between the two nuclei which is where the electron density gradient vectors start and end. Here, electron density can be divided into subsystems that are further separated by zero-flux surfaces of electron density, and in AIM theory, an atom is defined as bound by a cavity with a zero flux gradient vectors surface. The atomic charge is then evaluated over the Bader basin, which is the volume enclosed by the zero-flux surface. Over this space, a number of atomic properties, for example spin and charge density, could be integrated to give a non-basis set sensitive result. [132–134] A drawback of this method is however that Bader charges underestimates ionic charges as a consequence of the electron delocalisation inherent in DFT. Importantly though, this method allows for comparative studies to be made, and for general trends within a system to be explored.

2.3.7.3 Density of States

Periodic solid systems consisting of a large number of atoms has individual discrete energy levels very close together, and these form continuous bands. To characterise these bands, density of states (DOS) plots can be used. DOS show the number of available states that electrons can occupy at a given energy. Furthermore, it contains information regarding the site-projected DOS (PDOS) and the α (upwards direction) and ß (downwards direction) electron states, which are DOS projected onto atomic orbitals. PDOS can be used to examine what bands are involved in chemical bonds, and changes in intensity and energy position can indicate charge transfer and/or ionic or covalent interactions.

2.4 Molecular Dynamics

Molecular dynamics (MD) is a technique utilised to study the time evolution of interacting particles, by integrating the interacting particles' equations of motion. [135,136] Within classical MD, the time evolution is calculated based on the following assumptions:

(i) The atomic nuclei move according to Newton's second law, and are treated as classical particles. This assumption is valid for the motion of non-light atoms and whilst vibrations with frequencies (v) fulfil $hv>k_BT$. This relation is true at high temperatures.

(ii) No electrons are explicitly included. The interaction between particles is instead computed by a potential energy function. This assumption is dependent on the applied force-field models utilised to account for the intra- and inter-molecular interactions between the particles.

2.4.1 Newton's Equation of Motion Integration

For a classical particle with mass *m* that is moving under the influence of a force **F**(**r**)

$$m\frac{d^2\mathbf{r}}{dt^2} = \mathbf{F}(\mathbf{r}) \tag{2.22}$$

and the classical equations of motion are expressed though equation 2.23.

$$\frac{d\mathbf{r}(t)}{dt} = \frac{\mathbf{p}(t)}{m} = \mathbf{v}(t) \tag{2.23a}$$

$$\frac{d\mathbf{p}(t)}{dt} = \mathbf{F}(\mathbf{r}) \tag{2.23b}$$

$$\frac{d\mathbf{v}(t)}{dt} = \frac{\mathbf{F}(t)}{m} \tag{2.23c}$$

p is the particle's momentum (**p**=*m***v**(*t*), **v**(t) is the particle's velocity), and *t* is time. From the integration of equations 2.23a-c, the particle trajectory dependent on the external force-field **F**(**r**) is defined, giving the position **r**(t), and momentum **p**(t) at each time. For a moving particle influenced by a constant force, such that **F**(**r**)=*F*, the evolution of a particle's momentum and position with time is given by

$$\mathbf{p}(t) = Ft + \mathbf{p}_0 \tag{2.24a}$$

$$\mathbf{r}(t) = \frac{1}{2}\frac{F}{m}t^2 + \frac{\mathbf{p}_0}{m}t + \mathbf{r}_0 \tag{2.24b}$$

$\mathbf{r}_0$ and $\mathbf{p}_0$ are the particle's initial position and momentum. The knowledge of these defines the particle's trajectory.

A more realistic simulation is a system consisting of *N* interacting particles where the force acting on a particle changes with changing particle position $\mathbf{F}_i = \mathbf{F}_i(\mathbf{r}_1, \mathbf{r}_2, \ldots, \mathbf{r}_N)$, either induced by the particle moving on its own or when any of the other particles in the system interact with it and thus makes the particle change position. To describe the motion of *N* interacting particles, a set of *N* equations are used (equation 2.25).

$$m_i \frac{d^2\mathbf{r}}{dt^2} = \mathbf{F}_i(\mathbf{r}_1, \mathbf{r}_2, \ldots, \mathbf{r}_N), i = 1, N \qquad (2.25)$$

with the equations of motion for each of the *N* particles being

$$\frac{d\mathbf{r}_i}{dt} = \frac{\mathbf{p}_i}{m} \qquad (2.26a)$$

$$\frac{d\mathbf{p}_i}{dt} = \mathbf{F}_i \qquad (2.26b)$$

Equation 2.26 cannot be analytically solved due to the complicated form of the force acting on the particles. To solve these differential equations, MD simulation techniques utilises a finite difference approach by breaking down the calculation in short time steps (Δt). At each time step, the forces acting on the particles are calculated and then combined with the current particle positions and velocities to give new positions and velocities. The particle is then moved to this new position and the forces are updated. The force acting on a particle is assumed to be constant during each time step. Repeating this procedure for a set simulation time generates a dynamical trajectory, which is describing the time evolution of $\mathbf{p}_i$ and $\mathbf{r}_i$ for each particle on a time grid (equation 2.27)

$$\{\mathbf{r}_i(t_0), \mathbf{r}_i(t_0 + \Delta t), \mathbf{r}_i(t_0 + 2\Delta t), \dots\} \quad (2.27a)$$

$$\{\mathbf{p}_i(t_0), \mathbf{p}_i(t_0 + \Delta t), \mathbf{p}_i(t_0 + 2\Delta t), \dots\} \quad (2.27b)$$

Thus, MD allows the microscopic dynamics of a system, in terms of a trajectory for each individual particle in the system, to be computed. It is also a deterministic technique, which means that given an initial set of positions and momenta the time evolution is defined completely. Furthermore, the configuration of the interacting particles at each time *t* is completely defined by

$$\{\mathbf{x}_1(t), \mathbf{x}_2(t), \dots, \mathbf{x}_N(t)\} \quad (2.28)$$

where, $\mathbf{x}_i=(\mathbf{r}_i,\mathbf{p}_i)$ and defines the position and momentum of particle *i*.

2.4.2 Total Energy Conservation

A system's total energy (*E*) can be written as the sum of its kinetic (*K*) and potential (*V*) energies.

$$E = K + V \quad (2.29)$$

If it is assumed that these components are time independent, then from the equations of motions $\frac{dE}{dt} = 0$, *i.e.* the total energy is a constant of motion. For this to be true, no explicitly time-independent or velocity-dependent forces may act on the system. Thus, in MD calculations of systems with *N* interacting particles, the particles follow Newton's equations of motion and conserve *E*.

2.4.3 Finite Difference Methods

MD simulations require time integration algorithms that integrate the equations of motion to obtain trajectories. These integration algorithms are based on finite difference methods. Finite difference methods introduce time as a discrete variable on a finite grid by defining the time-step (Δt) as the distance at the time grid between two consecutive points. Thus, by knowing the atomic positions and the derivative of these at time t, the chosen integration scheme can give the atomic positions at a later point in time ($t+\Delta t$), and by repeating this for $n\Delta t$, the time evolution for the system can be obtained. The most commonly used MD integration schemes are based on the Verlet algorithm. In this work, we have employed the velocity Verlet algorithm, with a more detailed outline presented below.

2.4.3.1 Verlet Algorithm

The Verlet algorithm is based on third order Taylor expansions of $\mathbf{r}(t)$, with one going forward in time and one going backwards. If $\mathbf{v}$ is the velocity, *i.e.* the first time derivative of $\mathbf{r}(t)$, $\mathbf{a}$ is acceleration, *i.e.* the second time derivative of $\mathbf{r}(t)$, and $\mathbf{b}$ is the third time derivative of $\mathbf{r}(t)$, one can write

$$\mathbf{r}(t+\Delta t) = \mathbf{r}(t) + \mathbf{v}(t)\Delta t + \frac{1}{2}\mathbf{a}(t)\Delta t^2 + \frac{1}{6}\mathbf{b}(t)\Delta t^3 + O(\Delta t^4) \quad (2.30a)$$

$$\mathbf{r}(t-\Delta t) = \mathbf{r}(t) - \mathbf{v}(t)\Delta t + \frac{1}{2}\mathbf{a}(t)\Delta t^2 - \frac{1}{6}\mathbf{b}(t)\Delta t^3 + O(\Delta t^4) \quad (2.30b)$$

$O(\Delta t^4)$ is the truncation error of the algorithm. Adding equation 2.30a and 2.30b together, one obtains the basic form of the Verlet algorithm (equation 2.31).

$$\mathbf{r}(t+\Delta t) = 2\mathbf{r}(t) - \mathbf{r}(t-\Delta t) + \mathbf{a}(t)\Delta t^2 + O(\Delta t^4) \tag{2.31}$$

a(*t*) is the force divided by the mass, and the force is a function of **r**(*t*):

$$\mathbf{a}(t) = -\frac{1}{m}\mathbf{F} = -\frac{1}{m}\nabla_{\mathbf{r}} V(\mathbf{r}_1, \mathbf{r}_2, \ldots, \mathbf{r}_N) \tag{2.32}$$

One issue with this basic form of the Verlet algorithm is that **v**(*t*) is not directly calculated, and whilst they are not required for modelling the time evolution of a system, it is necessary for calculating *K*. *K* is furthermore necessary to confirm the conservation of total energy (equation 2.29). **v**(*t*) can be obtained from equation 2.33.

$$\mathbf{v}(t) = \frac{\mathbf{r}(t+\Delta t) - \mathbf{r}(t-\Delta t)}{2\Delta t} \tag{2.33}$$

However, the truncation error for equation 2.33 is $O(\Delta t^2)$ instead of $O(\Delta t^4)$. Thus, the velocity Verlet algorithm has been introduced as an improvement of the basic Verlet algorithm (equation 2.34). Here, **r**(*t*+Δ*t*), **v**(*t*+Δ*t*), and **a**(*t*+Δ*t*) are calculated simultaneously at *t*.

$$\mathbf{r}(t+\Delta t) = \mathbf{r}(t) + \mathbf{v}(t)\Delta t + \frac{1}{2}\mathbf{a}(t)\Delta t^2 \tag{2.34a}$$

$$\mathbf{v}(t+\Delta t/2) = \mathbf{v}(t)\Delta t + \frac{1}{2}\mathbf{a}(t)\Delta t \tag{2.34b}$$

$$\mathbf{a}(t+\Delta t) = -\frac{1}{m}\nabla_{\mathbf{r}} V\big(\mathbf{r}(t+\Delta t)\big) \tag{2.34c}$$

$$\mathbf{v}(t+\Delta t) = \mathbf{v}(t+\Delta t/2) + \frac{1}{2}\mathbf{a}(t+\Delta t)\Delta t \tag{2.34d}$$

The half-step velocities (2.34b) are used to advance atomic positions by a full time-step. This leads to less memory requirements and higher computational efficiency than the basic Verlet algorithm, whilst generating identical trajectories and properties. From the above, it is clear that the choice of time-step is crucial. If the chosen time step is too small, only a portion of the trajectory will be covered, and if it is too large, instabilities in the integration algorithm might arise as a consequence of high energy overlap between atoms.

2.4.4 Temperature and Pressure Control

The complete collection of all possible systems with different microscopic states but same thermodynamical state is referred to as an ensemble. Dependent on simulation type, different ensembles are possible. The simplest of these is the NVE ensemble, *i.e.* microcanonical ensemble. In the NVE ensemble, all states have the same number of atoms (*N*), same cell volume (*V*), and same total energy (*E*). Within this ensemble, *P* and *K* are allowed to vary, but must always obey equation 2.29. However, this does not correspond to the majority of actual systems.

For more realistic simulations, one has to take into account temperature (*T*) and pressure (*p*). This is done in the NVT (canonical) ensemble and the NPT (isobaric isothermal) ensemble. *T* and *p* can be controlled by mathematical thermostats and barostats, which allow for dynamical system responses to *T* or *p*, and represent a way to study non-equilibrium systems where it is necessary for *E* to vary. [137,138] In these calculations, *T* is the instantaneous kinetic energy [139] of the system that can be directly related to atomic velocities (*v*). [138]

$$T \propto \sum_{i=1}^{N} \frac{1}{2} m_i v_i^2 \tag{2.35}$$

A simple thermostat was defined by Berendsen *et al.* [137] In this thermostat, a hypothetical external heat bath of fixed temperature is coupled to the simulation cell. The practical implication of this is frequent collisions of the simulated particles with light particles forming an ideal gas at the fixed temperature. This is realised by introducing a velocity scaling factor (λ), with a value of λ such that the change of temperature with time is proportional to the temperature difference between external bath and simulation cell (equation 2.36). Equation 2.36 gives an exponential decay of the simulation cell temperature with respect to time.

$$\frac{dT(t)}{dt} = \frac{1}{\tau}(T_0 - T(t)) \tag{2.36}$$

Here, $T(t)$ is temperature at time t for the simulation cell, T_0 is the fixed temperature of the external bath, and τ is the empirical parameter rise time that allows for control of speed of the exponential system temperature decay to the wanted temperature. [137,140] Depending on the choice of τ, the effect of the Berendsen thermostat varies. For small τ-values, the bath and cell are very tightly bound together, leading to unrealistically small temperature fluctuations. Reversely, for very large τ ($\tau \to \infty$), the effect of the thermostat is lost, and a return to NVE sampling is seen. [138]

Unfortunately, this thermostat have weaknesses, even though it is efficient to relax the system into the desired temperature and is easy to implement computationally. To start with, equation 2.36 is time irreversible, and secondly, the effect of this in the atomic motions does not lead to accurate solutions belonging to the canonical

ensemble. However, last disadvantage might be improved by increasing the number of atoms in the system. Thus, other thermostats have been designed based on the Berendsen thermostat.

The Nosé-Hoover thermostat [139,141] does just as the Berendsen thermostat link the simulation cell to an external heat bath, but the effect of this external heat bath on the system is accounted for by including an additional degree of freedom in the determination of *E*. The Nosé-Hoover algorithm use modified Newton's equations of motion by adding a friction coefficient (χ) to equation 2.23 as

$$\frac{d\mathbf{r}(t)}{dt} = \mathbf{v}(t) \tag{2.37a}$$

$$\frac{d\mathbf{v}(t)}{dt} = \frac{\mathbf{F}(t)}{m} - \chi(t)\mathbf{v}(t) \tag{2.37b}$$

$$\frac{d\chi(t)}{dt} = \frac{2K(t) - 2\sigma}{q_{mass}} \tag{2.37b}$$

Here, σ is the target thermostat energy, and $q_{mass}=2\sigma\tau_T^2$ is the thermostat mass which is directly dependent on the specified time constant τ_T. This term is normally in the range of 0.5-2 ps. This leads to direct implications on the atomic motions, which produces time-reversible, smooth, and deterministic trajectories, which are all part of the canonical ensemble. Please note that these thermostats can also be used as barostats.

2.4.5 Periodic Boundary Conditions

Periodic boundary conditions (PBC) are applied so that a finite system can imitate an infinite system. Without such conditions, the simulation box would effectively be

enclosed by surfaces, and would more resemble a cluster of atoms. Thus, to model realistic materials, particles are enclosed by a simulation box that is then replicated infinitely by translation in all three (x, y, z) Cartesian directions. For the more specific example of solid state systems, the simulation box is normally made up of the unit cell or a supercell. Using PBC, if a particle or atom is located at position **r** within the simulation box, the same particle represents an infinite set of particles such that

$$\mathbf{r} + l\mathbf{a} + m\mathbf{b} + n\mathbf{c}, (l, m, n = -\infty, +\infty) \tag{2.38}$$

l, m, and, *n* are integers, and **a**, **b**, and **c**, are the edge vectors of the simulation box. A graphical representation is included in Figure 2.1.

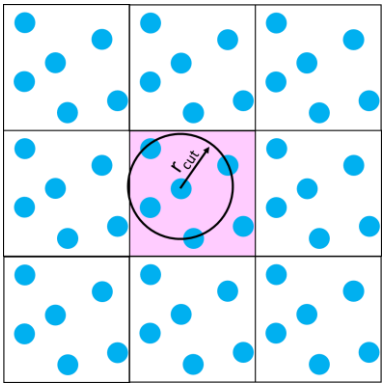

Figure 2.1. Graphical representation of periodic boundary conditions. Pink box is simulation box, and the white boxes are the periodic images of this, *i.e.* exact images of the simulation box. Blue dots are atoms. Please note that the simulation box does not have to be cubic, and that a cubic cell has only been used here for ease of visualisation.

From Figure 2.1 it is seen that as an atom leaves the simulation box, it is folded back into the opposite side of the box. This implies that the number of atoms in the system is conserved. It is also important to note that the atoms are not experiencing any surface forces as these through PBC are completely eliminated. r_{cut} in Figure 2.1

represents the cut-off radius for calculating the interaction between two atoms. Implementing a cut-off radius, leads to the interaction calculated are always within the closest image, a technique normally referred to as the minimum image convention. r_{cut} cannot be larger than the half width of the simulation cell, *i.e.* $L_{box}>2r_{cut}$, and thus atoms can only interact with one image of any atom. However, to model atomic interactions, there needs to be a way of mathematically define these. In MD, this is done through interatomic potential models.

2.4.6 Interatomic Potential Models

MD, as opposed to *ab initio* techniques, is based on empirical observations of interatomic interactions, and are suitable for large systems and long simulation time that will result in good statistical data from MD runs. To accomplish this, interatomic potentials are used to describe the energetics of interatomic interactions. The form of the interatomic potential is dependent on the type of interaction that one seeks to model. Interatomic potentials are parameter-based, which allows for them to be changed dependent on what chemical properties and factors, such as bonding nature or atomic radius, are involved in the system. In this work, the Born model of solids have been used as the basis of the atomistic technique used. [142]

The Born model of solids is based on the lattice energy (E_L) only containing a pairwise term, which then in turn is sub-divided into a term describing the long-range Coulombic interactions and one term describing the short-range jellium cloud interactions. E_L is the energy that would be released when the ions in the crystalline lattice are put at the lattice sites/positions taken from an infinite distance. It is assumed that ions within the crystal are only interacting *via* long-range electrostatic

forces and short-range forces. This includes repulsion and van der Waals attractions between neighbouring ions' electron clouds. E_L is expressed as [99]

$$E_L = \sum_{i=1}^{N} \sum_{j>i}^{N} \frac{q_i q_j}{4\pi\varepsilon_0 r_{ij}} + \sum_{i=1}^{N} \sum_{j>i}^{N} \phi_{ij}(r_{ij}) \tag{2.39}$$

where q is the charge of atom i and j, r_{ij} is the interatomic distance between i and j, and ε_0 is the free space permittivity. The first summation term in equation 2.39 is the long-range Coulomb interaction, and ϕ_{ij} is the short-range term. The Coulomb term can be directly calculated for non-periodic systems, but for periodic systems this is not practical (see section 2.4.6.1). The second term is the short-term interactions and will be discussed in section 2.4.6.2.

2.4.6.1 Long-range interaction – Ewald Summation

The impracticality of directly calculating the Coulomb term for an infinite number of atoms lays in the increase of interactions with distance. The Coulomb term is conditionally convergent, which leads to slow convergence and long calculation times. A solution to this problem was proposed by Ewald [143], by rewriting the Coulomb term as a sum of two convergent series. To speed up convergence, a transformation is subjected on the Coulomb term, which is subsequently separated into two components. One of these is rapidly convergent in real space, and the second one is quickly decaying in reciprocal space. This method is commonly described as adding and subtracting Gaussian charge distributions, each which are centred on an ion. This results in the energy term being divided into terms for real, reciprocal, and self-energy, as expressed in equation 2.40.[99]

$$E^{electrostatic} = E^{real} + E^{reciprocal} + E^{self} \quad (2.40)$$

E^{self} is a correction term and cancels out the self-interactions of the artificial counter charges. As a consequence of the Ewald summation method to calculate the Coulomb term, calculations are only possible to make on systems that are charge neutral and that has a dipole moment of zero.

In the DL_POLY programme, Ewald summation is implemented through the smooth particle mesh Ewald algorithm (SPME), which requires less computational time and memory than the original Ewald algorithm. In SPME, the interaction potential ($\varphi(\boldsymbol{r})$) is divided into two terms, and the direct summation of point particle interaction energies is changed to two summations

$$E_{total} = E_{short-range} + E_{long-range} \quad (2.41a)$$

$$E_{short-range} = \sum_{i,j} \varphi_{short-range}(\boldsymbol{r}_j - \boldsymbol{r}_i) \quad (2.41b)$$

$$E_{long-range} = \sum_{i,j} \widetilde{\Phi}_{long-range}(\boldsymbol{k})|\tilde{\rho}(\boldsymbol{k})|^2 \quad (2.41c)$$

Equation 2.40b represents the particle part of SPME, and equation 2.41c is a Fourier transform summation representing the Ewald summation part. $\widetilde{\Phi}_{long-range}(\boldsymbol{k})$ is the Fourier transform of the potential, whereas $\tilde{\rho}(\boldsymbol{k})$ is the same, but for the charge density. Equation 2.41c converges quickly in Fourier space, and equation 2.41b converges rapidly in real space. $\tilde{\rho}(\boldsymbol{k})$ is calculated through a fast Fourier transform on a discrete lattice, *i.e.* the mesh. The smooth part of SPME comes from the energy

function (equation 2.41) being smooth so that the derivative of it can be analytically obtained, which in turn improves energy conversation. [144] To implement this in DL_POLY, periodic boundary conditions are required, as described above.

2.4.6.2 Short-Range Interactions

Continuing to the second term in equation 2.39, this represents the short-range interactions, and includes repulsive forces arising from the overlap of ion charge clouds, and van der Waals attractive forces between neighbouring electron charge clouds. $\phi_{ij}(r_{ij})$ is the two-body contribution to the short-range energy. This term varies only with distance (r_{ij}) between ions, and is the most dominant component of the short-range energy.

2.4.6.2.1 Buckingham Potential

The Buckingham potential ($V_{i,j}$) is a two-body potential that has been widely applied to ionic solids and other solid state systems. $V_{i,j}$ is expressed as

$$V_{i,j}(r_{ij}) = A\exp\left(\frac{-r_{ij}}{\rho}\right) - \frac{C}{r_{ij}^6} \tag{2.42}$$

where r_{ij} is the interatomic distance between ion *i* and *j*, and *A*, ρ, and *C* are empirically fitted parameters. *A* is a measure of electrons within an ion and is atomic size dependent, ρ is the electron density, and *C* is the polarizability of the ion. This model has been successfully used in many oxide systems, and the use of this interatomic potential on perovskites has been widely justified. [53,75,145–147]. However, to properly model these systems, and especially the oxygen diffusion, electronic

polarizability needs to be taken into account, as the polarizability of the oxygen ions will have a significant impact. [75] Thus, a shell model is implemented as well.

2.4.6.2.2 Shell Model

In the shell model, an ion is described as having a massless shell, as opposed to every ion being a point charge (which is how they were described before). Only including point charges in a simulation where the system contains defects, such as oxygen vacancies, could lead to polarisation of ions in the lattice, and thus inclusion of this in the model is crucial. [148] In the shell model, every polarisable atom is represented by a core (nucleus and core electrons) that is coupled to a massless shell (representing the valence electrons) by an isotropic harmonic spring. This can be expressed as

$$\alpha = \frac{Y^2}{k} \tag{2.43}$$

where α is the electronic polarizability of the atom, *Y* is the charge of the massless shell, and *k* is the force constant for the harmonic spring. The core and shell charges should be assigned such that their sum equals the total formal ion charge. *Y* and *k* are obtained from the interatomic potential fitting. Furthermore, the ion polarizability is related to *C* in equation 2.42.

Upon implementation of an electric field on the ion, the shell moves relative to the core, such that a dipole is developed, and as such dielectric polarizability is simulated in the system. Implementing the shell model in MD simulations, and specifically in DL_POLY, the shell is given a mass. This shell mass should be negligible in

comparison to the core mass, such that no energy exchange between the core and shell is possible.

2.4.6.3 Interatomic Potential Fitting

To perform MD simulations, an interatomic potential set is required to describe the interatomic interactions. Interatomic potential parameters can be derived empirically from experimental or *ab initio* data. By fitting interatomic potential parameters, one means the process of finding parameters such that a good fit to this data is obtained. What data the model is fitted too depends on what data is available and application. For example, one could fit the parameter set to crystallographic data, physical properties (*eg.* elastic constants), and/or phonon frequencies. This makes the quality of results obtained with the interatomic potential method limited, as they are all dependent on the quality of the interatomic potential and how well the interatomic potential reproduces the physics of the system of interest. To overcome this, it is important and necessary to use interatomic potentials that are derived for the same class of materials and applications. [99]

In a fitting process, such as that implemented in GULP and used in this work, the fitting of the parameters is judged by the sum of squares (*F*) [99]

$$F = \sum_{i=1}^{N} w_i \left(f_{i,calc} - f_{i,obs}\right)^2 \tag{2.44}$$

where *N* is number of observable parameters being fitted to, f_n the value of the observable parameter from calculation ($f_{i,calc}$) and the data being fitted to ($f_{i,obs}$). w_i is a weighing factor that adjusts for the magnitude of the data and its reliability. In the

ideal scenario and a perfect fit, *F*=0. However, in practice, fitting in GULP utilises a minimisation algorithm. Traditionally, fitting would be carried out statically, keeping the structural and experimental data constant, and just minimising the forces acting on atoms during the fitting algorithm. In GULP, however, one can employ relaxed fitting, which results in better structural and ionic position fits. Relaxed fitting lets the system relax at every fitting step before F is calculated, thus adjusting the fitting parameters according to the relaxed structure and not a static un-optimised one in every step. This method leads to a more reliable potential set (within the applied approximations). [99]

2.4.6.4 Interatomic Potential Set

The interatomic potentials used in this work are taken from the Cherry *et al.* library, as they have previously been used to model ionic conductivity in this class of perovskites and for SOFC materials and purposes. [53,147,149,150] The Sm^{3+}-O^{2-}, Ni^{3+}-O^{2-}, and Cu^{3+}-O^{2-} interatomic potential parameters had to be derived separately since they were not available for this potential model. To that end, we have used the GULP code [97–99,151] to fit them according to the structural data for cubic and orthorhombic $SmCoO_3$, as well as Sm_2O_3. Ni^{3+}-O^{2-}, and Cu^{3+}-O^{2-} in turn were perfectly fitted to the calculated $SmNiO_3$ and $SmCuO_3$ DFT lattice parameters, respectively. The full set of interatomic potentials used is presented in Table 2.2. The fitting results for $SmCoO_3$ and Sm_2O_3 are presented in Table 2.3, which show that the derived model well replicates the structural properties of all different phases and materials considered. Additionally, mechanical properties calculated with this potential set is provided in Appendix B.

Table 2.2. Interatomic potential parameters. Potential cut-off was set to 12 Å.

	Short range interactions			Shell Model			
Interaction	A (eV)	ρ (Å)	C (eVÅ^{-6})		Y (e)	k (eVÅ^{-2})	ref
Sm^{3+}-O^{2-}	1252.94	0.3590	0.00	Sm^{3+}	-0.250	173.90	
Co^{3+}-O^{2-}	1329.82	0.3087	0.00	Co^{3+}	2.040	196.30	[53]
O^{2-}-O^{2-}	22764.30	0.1490	43.00	O^{2-}	-2.389	42.00	[53]
Ba^{2+}-O^{2-}	4818.42	0.3067	0.00	Ba^{2+}	1.831	34.05	[147]
Ca^{2+}-O^{2-}	1090.40	0.3437	0.00	Ca^{2+}	3.135	110.20	[150]
Sr^{2+}-O^{2-}	959.10	0.3721	0.00	Sr^{2+}	3.251	71.70	[150]
Fe^{3+}-O^{2-}	1156.36	0.3299	0.00	Fe^{3+}	4.970	304.70	[53]
Mn^{3+}-O^{2-}	1267.50	0.3214	0.00	Mn^{3+}	3.000	95.00	[53]
Ni^{3+}-O^{2-}	1947.47	0.2882	0.00	Ni^{3+}	3.344	193.70	
Cu^{3+}-O^{2-}	5888.83	0.2427	0.00	Cu^{3+}	4.001	99.00	

Table 2.3. Calculated and experimental lattice parameters (a, b, c) in Å for cubic and orthorhombic $SmCoO_3$, as well as Sm_2O_3 using interatomic potentials from Table 2.2. For cubic systems, only a is given as a=b=c.

	Calculated a, b, c	Experimental a, b, c	Difference (%)
Cubic	3.75(0)	3.75(1) [152]	0.0
Orthorhombic	5.30, 5.34, 7.51	5.28, 5.35, 7.50 [153]	0.37, 0.19, 0.09
Sm_2O_3	10.68	10.85 [154]	1.53

2.4.7 MD Data Analysis

From MD and atomistic techniques, one can calculate temperature dependent properties such as diffusion and thermal expansion.

2.4.7.1 Mean Square Displacement

From atomistic techniques and through MD calculations, diffusion in bulk materials can be calculated from Mean Square Displacement (MSD) graphs. D_i is the self-

diffusion coefficient for species *i*, which obtainable from the gradient of the MSD plot through equation 2.45.

$$\langle r^2(t)\rangle = 6D_i t + B_i \tag{2.45}$$

where $\langle r^2(t)\rangle$ is the time-dependent MSD, t is time, and B_i is the thermal factor associated with atomic vibrations. The MSD represents the displacement of atoms or ions within a simulation, in respect to their initial positions. Thus, calculating the MSD gives insight into ion transport with respect to time for different materials. This is extra important for SOFC cathode materials, as their efficiency is proposed to be directly proportional to its bulk oxygen diffusion.

From D_i, one can then calculate the diffusion activation energy of species *i,* from equation 2.46

$$D_i = D_0 \exp\left({}^{-E_a}/_{kT}\right) \Leftrightarrow \ln D_i = \ln D_0 - \frac{E_a}{kT} \tag{2.46}$$

D_0 is the temperature-independent pre-exponential, which could also be described as the diffusion coefficient at infinite T, E_a is the diffusion activation energy, k_B Boltzmann's constant, and T temperature. E_a is thus obtained from the gradient of ln(D_i) against 1/T Arrhenius plots.

2.4.7.2 Thermal Expansion Coefficient

The thermal expansion coefficient (TEC) relates to a system's volume expansion with temperature. The TEC (α_T) is thus related to the lattice parameters and can be calculated through equation 2.47. [155]

$$\alpha_T = \frac{1}{V_0}\frac{dV}{dT} \tag{2.47}$$

where V is the lattice volume, V_0 is the reference lattice volume, and T is temperature.

Chapter 3

$SmCoO_3$ Bulk Characterisation

Abstract

In this chapter, we present a bulk characterisation of $SmCoO_3$, as despite experimental studies, some of its chemical and physical properties have remained unknown due to the complexity of the material. It is known from experimental evidence that this perovskite exists in two different space groups, cubic and orthorhombic, and that at low temperatures both structures are semiconductors. However, when temperature increases, a semiconductor-to-metal transition, linked to a change in Co spin state, has been reported, and the material becomes conducting. Little is known about the mechanism that induces $SmCoO_3$ to alter its magnetic structure or the actual magnetic structure that causes the metallic behaviour. Here, we therefore present a systematic DFT+U study on the electronic and magnetic properties of $SmCoO_3$ in order to determine the possible reasons behind the magnetic transition, by studying the different magnetic orders exhibited by both crystal structures at different temperatures. Taking advantage of these calculations, we have also evaluated the mechanical properties of $SmCoO_3$, which are difficult to measure experimentally, leading to lack of data for its two different polymorphs. Hence, we have calculated the elastic constants, finding that both polymorphs exhibits similar ductility and brittleness, but that the cubic structure is harder than the orthorhombic phase.

3.1 Introduction

$SmCoO_3$ is found in two different phases; orthorhombic and cubic (Figure 3.1). The orthorhombic structure is the most stable phase at low temperatures, whereas the cubic structure is stabilized when the material is doped and/or at high temperatures. [156] The temperature also influences the electronic and magnetic properties of $SmCoO_3$. The electronic behaviour has been studied experimentally, and a semiconductor-to-metal transition is reported at temperatures higher than 500 K, [33,157,158] with the transition being suggested to be due to a change in the cobalt spin state. [33,157–160] At the same time, the Co^{3+} spin state is heavily influenced by the local structure, dopant substitution, and applied external pressure, and it is normal to find different spin domains or co-existence of two spin states in the same sample. To add further complexity, the spin state can consequently affect the magnetic structure, and *vice versa*, [160] which at the same time influences the chemistry of $SmCoO_3$. Thus, there is a clear interest in understanding which spin state is coupled to a certain magnetic structure, and which magnetic structure is the most likely to be responsible for the metallic state observed at high temperatures.

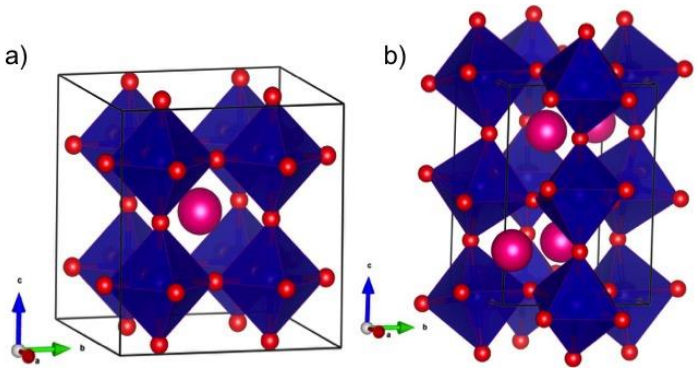

Figure 3.1. Graphical polyhedral representation of a) cubic and b) orthorhombic $SmCoO_3$. Pink spheres are Sm, blue Co and red O. Sm atoms are also placed in the centre of the edges and faces, but are not shown here for clarity.

Mechanical stability of SOFC cathodes is of importance for the performance and stability of the fuel cell, especially for industrial scalability, a fact that is often overlooked in fundamental studies. [161] SOFC materials should have thermal compatibility with the electrolyte, good mechanical strength, and be tough. [5,28] It is further undesirable to have large mechanical deformation at operating temperatures, and an understanding of the mechanical properties such as bulk and Young's moduli is useful. [5,28,161] To the best of our knowledge, there are no reported experimental values for the mechanical properties or elastic constants of $SmCoO_3$, neither for the cubic or the orthorhombic structure. For the determination of the elastic constants, large single crystals with very high purity are required, and this is difficult to achieve for many perovskites. [77,162]

Despite the availability of some experimental data on $SmCoO_3$, detailed information is lacking, including the antiferromagnetic arrangement and the Co spin state at high temperatures, or the precise values of the main mechanical properties. *Ab initio* calculations represent a powerful tool to provide insight into these properties and,

here we have used density functional theory (DFT) calculations to study the magnetic structure and the mechanical properties for the two polymorphs of $SmCoO_3$, taking into account the effect of temperature by simulating the thermal expansion of the material.

3.2 Computational Details

The VASP code has been used for all calculations. [92–95] We have used DFT+U to perform spin-polarized simulations with the PBE functional to describe the correlation-exchange interaction.[107,108] The project-augmented wave method (PAW) was used to describe the ion-electron interaction,[123] and we considered the following valence electrons for the atomic species involved: Sm ($5s^2 5p^6 6s^2$), Co ($4s^2 3d^7$), and O ($2s^2 2p^4$), with La ($5s^2 5p^6 6s^2 5d^1$), Mn ($3p^6 3d^6 4s^1$) for the included $LaMnO_3$ calculation. Sm *f*-electrons were included in the pseudopotential as core electrons as the samarium ion in $SmCoO_3$ is +3 charged. The kinetic energy cut-off for the plane-wave basis set was converged at 500 eV (600 eV for $LaMnO_3$) after testing it for both crystal structures. Structure optimizations were performed with the conjugate gradient method, considering electronic and ionic convergence criteria of 1×10^{-5} eV and 1×10^{-3} eV $Å^{-1}$, respectively. The tetrahedron method was used for the smearing,[117] and was applied together with a 4x4x4 and 8x8x6 Γ-centred Monkhorst-Pack grid for the cubic and orthorhombic models respectively, to describe the reciprocal space.[118] The bulk models used throughout this chapter are the 2x2x2 *Pm-3m* cubic cell and the 2x1x1 *Pnma* orthorhombic cell, both containing 40 atoms (Figure 3.1). Finally, in order to properly describe the electronic and magnetic structures of $SmCoO_3$, the Hubbard approximation was employed as described in the

Dudarev approximation [109] and U_{eff} = 3 eV was applied to the Co d-electrons, with U_{eff}=4 eV for Mn d-electrons.[19]

3.3 Results and Discussion

3.3.1 Structural Properties

From the two reported crystal structures of $SmCoO_3$, the orthorhombic phase (*Pnma*) is known to be more stable than the cubic phase (*Pm-3m*) at low temperatures. [81,152,163] However, when $SmCoO_3$ is used for SOFC (normally doped and operating at high temperatures (<500°C)), the cubic phase becomes stabilised. [86,164] Calculations made in this work indicate that, as observed experimentally, the orthorhombic phase is 0.64 eV·(formula unit)$^{-1}$ lower in energy than the cubic phase at 0 K (it is worth noting that these DFT calculations do not include the effect of temperature). Both structures show good agreement with the experimental structural data, as shown in Table 3.1. The only noticeable difference with experiment is the lattice parameter *b* for the orthorhombic system, which is ~1.7% larger than the experimental value. This discrepancy has been seen in previous theoretical work on orthorhombic cobalt perovskites. [113] However, this larger *b* parameter induces deviations in the bond lengths that are parallel to the *b*-direction. Fortunately, the largest elongation for the Co-O bonds is only 0.03 Å, whereas the Sm-O bonds are stretched by a maximum of 0.14 Å.

Table 3.1. Calculated lattice parameters (a, b, and c), and Sm/Co-O bond lengths for the cubic and orthorhombic $SmCoO_3$. Experimental data are included in brackets, cubic structure obtained from Wold *et al*. [152], whereas orthorhombic experimental data were obtained from Perez-Cacho *et al*. [153] All data is expressed in Å.

Structure	a	b	c	Sm-O	Co-O
Cubic	3.75(4) (3.75)			2.65 (2.65)	1.88 (1.88)
Orthorhombic	5.29 (5.28)	5.44 (5.35)	7.53 (7.50)	2.30 (2.27) 2.34 (2.35) 2.37 (2.41) 2.50 (2.53) 2.64 (2.61) 3.06 (3.05) 3.37 (3.23)	1.94, 1.95, 1.96 (1.93)

3.3.2 Electronic and Magnetic Structures

The magnetic properties of lanthanide cobaltate perovskites are attributed to the Co^{3+} atoms. [158,159] Co^{3+} is a d^6 centre, which is 6-coordinated by O^{2-} anions in an octahedral configuration in the cubic structure, and in a distorted octahedron in the orthorhombic structure. According to crystal field theory (CFT), the octahedral crystal field splits the five d-orbitals between the t_{2g} (d_{xy}, d_{yz}, and d_{xz}) and the e_g (d_{x2-y2}, and d_{z2}), with the former being lower in energy than the latter. Depending on the occupancy of these orbitals, we distinguish between three different spin states for Co^{3+}; (i) low spin state (LS, $t_{2g}^6 e_g^0$) with S = 0; (ii) intermediate spin state (IS, $t_{2g}^5 e_g^1$) with S = 1; and (iii) high spin state (HS, $t_{2g}^4 e_g^2$) with S = 2, all of them schematically represented in Figure 3.2. [33,157] It is assumed that the occupation of these orbitals will obey Hund's rule, *i.e.* that the most stable configurations should be those that maximize the spin multiplicity. For example, HS is S=2 if and only if all unpaired electrons are either α or β. However, due to the nature of DFT, it becomes complicated to determine pure intermediate or high spin states, and they normally

appear as a combination. In the HS case, we can have three α electrons and one β, which means S = 1, or two α and two β, which describes a singlet state, which explains why in Table 3.2, cobalt magnetization can be found between 0 and 4 μ_B, depending on the spin state.

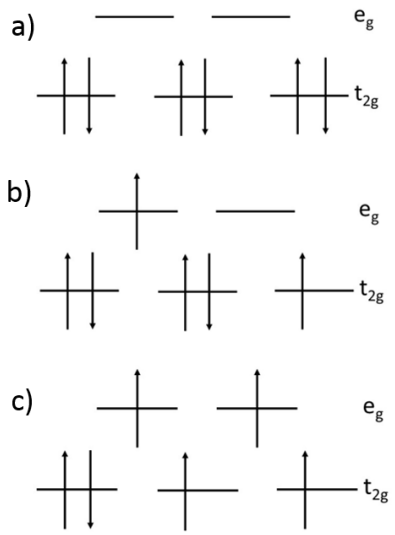

Figure 3.2. Schematic representation of the three possible spin states for Co $3d^6$ a) low, b) intermediate, and c) high spin state, assuming maximum multiplicity.

For LS states, the system becomes diamagnetic. However, when Co^{3+} centres are found in IS or HS, we can distinguish four different paramagnetic structures, as shown in Figure 3.3: three antiferromagnetic (AFM) structures, A-type (AAFM), C-type (CAFM), and G-type (GAFM), and one ferromagnetic (FM).[165,166]

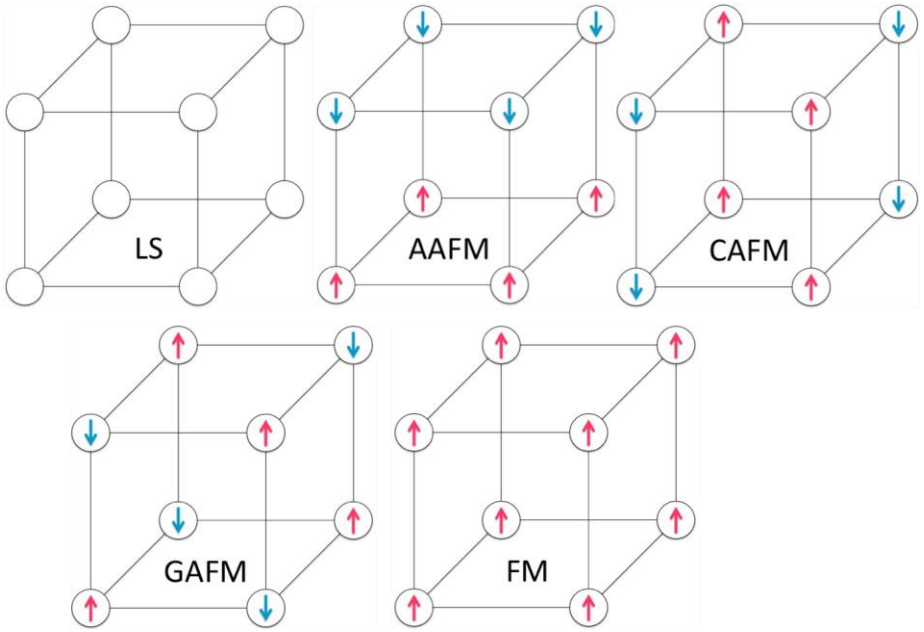

Figure 3.3. Graphical representation of the different magnetic structures. For simplicity, each sphere represents a Co atom in the cubic phase, with this scheme being transferable to the orthorhombic phase. Pink up-arrows represent α-spin, whereas blue down-arrows represent β-spin, regardless of the spin state of the cobalt centres.

Magnetic moments for samarium and oxygen ions are negligible in relation to their cobalt neighbours and thus, they do not influence the magnetic structure of the perovskite. The Bader charges (Table 3.2) on Sm and O show negligible variance with magnetic moment. Analysis shows that the magnetic structure seems to have little to no impact on the charge of the different atoms in the material. Noticeably though, the orthorhombic phase shows higher charges compared to the cubic phase throughout, which could imply that the orthorhombic phase is more ionic than the cubic phase (Table 3.2).

Table 3.2. Bader charges (q), and band gap (E_g) in eV.

	LS/DM	AAFM	CAFM	GAFM	FM
q^{Sm}_{Cubic}	2.00	2.02	2.05	2.06	1.95
$q^{Sm}_{Orthorhombic}$	2.15	2.14	2.14	2.15	2.15
q^{Co}_{Cubic}	1.31	1.30	1.38	1.32	1.22
$q^{Co}_{Orthorhombic}$	1.44	1.61	1.61	1.45	1.47
q^{O}_{Cubic}	-1.10	-1.10	-1.14	-1.12	-1.06
$q^{O}_{Orthorhombic}$	-1.19	-1.27	-1.25	-1.20	-1.20
E_g^{Cubic}	0.68	0	0	0	0
$E_g^{Orthorhombic}$	1.2	0	0	0.79	0.82 (β)

Spin density plots for the calculated magnetic structure for the cubic and orthorhombic systems are provided below (Figure 3.4 and Figure 3.5). Examining these, it can be seen that the spin ordering presented in Figure 3.3 has been preserved in the calculations.

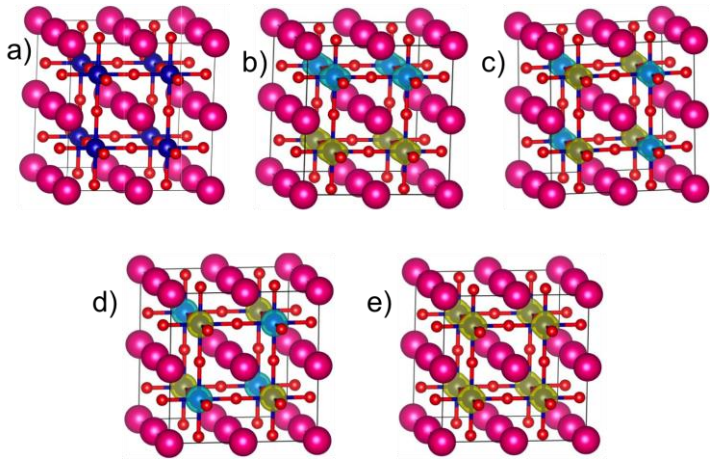

Figure 3.4. Spin density plots of a) diamagnetic, b) AAFM, c) CAFM, d) GAFM, and e) FM cubic magnetic structures. Pink spheres are samarium, blue cobalt, and red oxygen. Yellow spin density represents α-spin, and light blue β-spin. Surface isovalue is 0.05 for all systems.

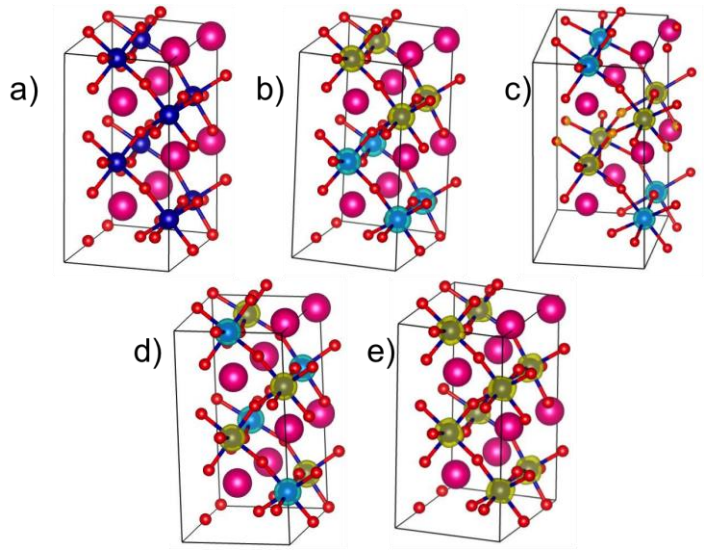

Figure 3.5. Spin density plots of a) diamagnetic, b) AAFM, c) CAFM, d) GAFM, and e) FM orthorhombic magnetic structures. Pink spheres are samarium, blue cobalt, and red oxygen. Yellow spin density represents α-spin, and light blue β-spin. Surface iso-value is 0.05 for all systems.

3.3.2.1 Diamagnetic Structures

From the projected density of state (PDOS), we observe that for the $SmCoO_3$ diamagnetic (DM) cubic structure, (Figure 3.6a) the Co t_{2g}-orbitals describe the valence band in combination with the O *2p* orbitals, whereas the conduction band is defined by the Co e_g orbitals. The band-gap between the conduction and valence bands is 0.68 eV. This picture agrees with the crystal field theory prediction for the LS state of Co ions and with reported experimental information about the $SmCoO_3$ magnetic behaviour, although no precise data regarding its bandgap were available. [78,88] However, it has been reported that the band gap of the related perovskite $LaCoO_3$ is 0.6 eV, [167] which suggests that the obtained results are consistent with those of other lanthanide cobalt oxide perovskites. On the other hand, the orthorhombic structure also gives rise to an insulator material, but with a larger band-gap of 1.20 eV (Figure 3.6b). In this case, however, CFT cannot be used to describe

the electronic structure as t_{2g} and e_g appear at the same energies, suggesting a distortion of the octahedral environment of the cobalt centres. Therefore, both valence and conduction bands are described by a combination of t_{2g} and e_g-orbitals, and the O *2p* band. For the diamagnetic structures, both materials show $\mu_{Co} = 0\ \mu_B$.

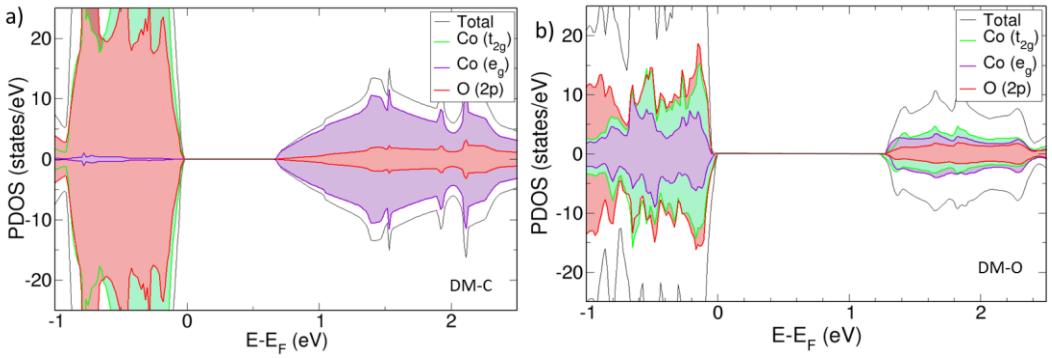

Figure 3.6. PDOS for (a) cubic and (b) orthorhombic diamagnetic $SmCoO_3$. The Fermi level is at 0 eV, and negative E-E_F represent the occupied bands and positive the virtual bands. Positive PDOS are associated with the α-spin, whereas negative PDOS are associated with β-spin. For PDOS including Sm, please see Appendix C.

3.3.2.2 Antiferromagnetic Structures

In the antiferromagnetic structures, the formal splitting of the Co^{3+} d-orbitals is not as clear as it was for the diamagnetic systems (Figure 3.7). One fact that is common for almost all structures regardless of the crystallographic phase, is that $SmCoO_3$ becomes metallic, as there is no band gap at the Fermi level. This behaviour has previously been observed in related perovskites. [113] Specifically, the orthorhombic phase becomes metallic when it has an AAFM or CAFM structure, but it remains a semiconductor when it has a GAFM structure. This suggests that the experimentally observed insulator to metal transition would not involve the GAFM magnetic structure. Furthermore, since all three magnetic structures show non-split t_{2g}- and e_g-orbitals, electronic conduction goes through the *d*-metal band, without orbital preference.

Conversely, all cubic antiferromagnetic systems show metallic behaviour. The electronic structures for AAFM and GAFM show that conduction is mainly through the t_{2g} Co orbitals, whereas for the CAFM it is mainly through the e_g, with a small contribution of the t_{2g} as well.

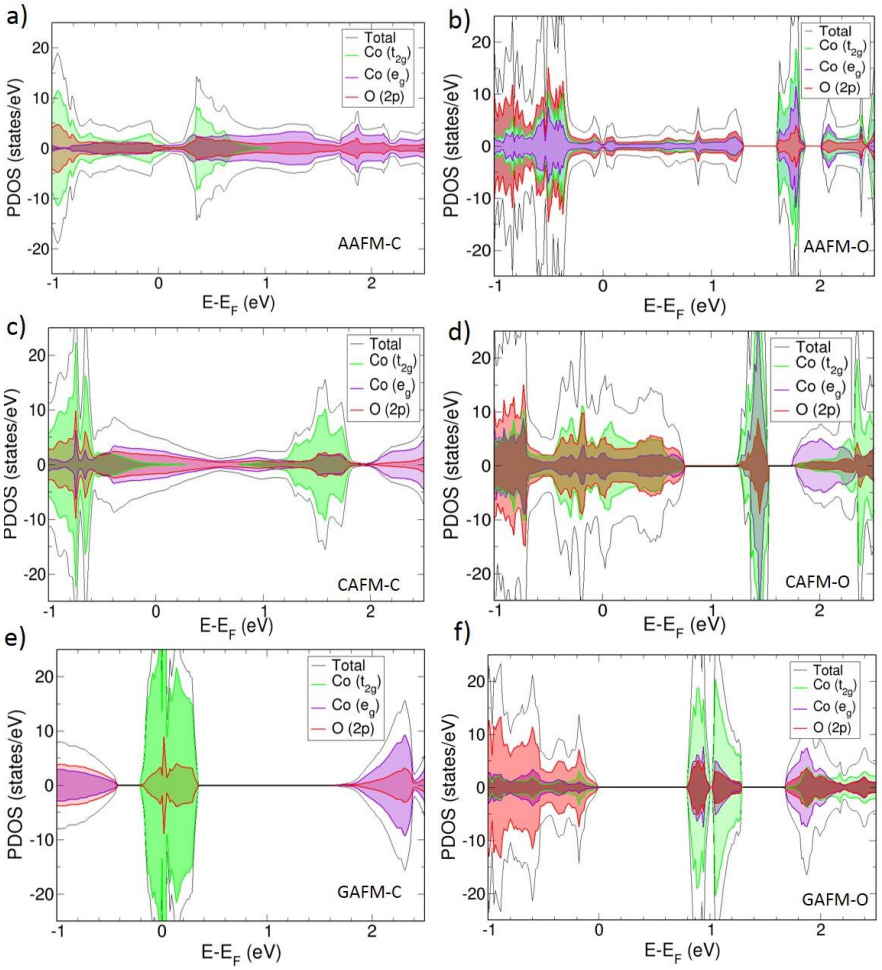

Figure 3.7. PDOS for a) cubic AAFM, b) orthorhombic AAFM, c) cubic CAFM, d) orthorhombic CAFM, e) cubic GAFM, and f) orthorhombic GAFM. The Fermi level is at 0 eV, and negative $E\text{-}E_F$ represent the occupied bands and positive the virtual bands. Positive PDOS are associated with the α-spin, whereas negative PDOS are associated with β-spin.

3.3.2.3 Ferromagnetic Structures

Since the ferromagnetic structure has a non-zero total spin, α and β PDOS are not symmetric. The cubic FM structure has metallic behaviour (figure 3.8a), where the t_{2g} Co orbitals combined with the O *2p* orbitals define the β conduction and valence band, and the Co e_g orbitals with the O *2p* orbitals describe the α bands. For orthorhombic FM, a pure half-metallic structure was found (figure 3.8b), agreeing with previous experimental results found for other perovskites, such as FM $LaCoO_3$. [19,65,113] Again, Co d-states are mixed t_{2g} and e_g, but the occupied α states at the Fermi level are mainly O *2p*, with a Co d band gap of 0.82 eV in the β spin.

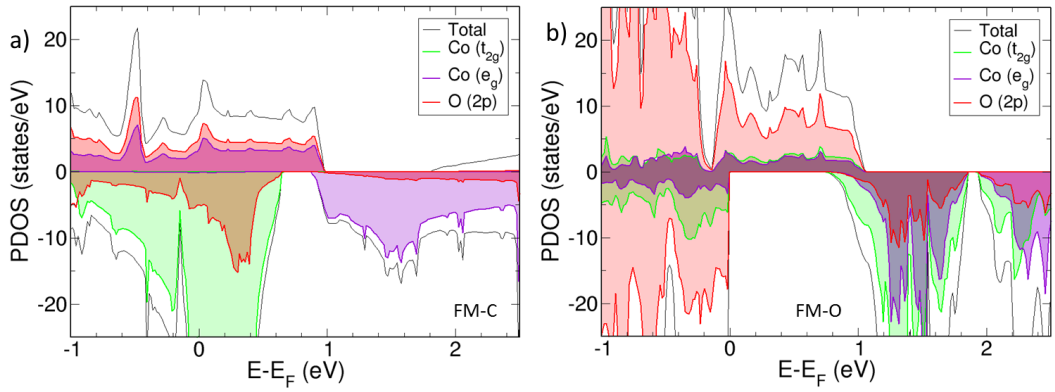

Figure 3.8. PDOS for (a) cubic, and (b) orthorhombic FM $SmCoO_3$. The Fermi level is at 0 eV, and negative $E-E_F$ represent the occupied bands and positive the virtual bands. Positive PDOS are associated with the α-spin, whereas negative PDOS are associated with β-spin.

3.3.2.3.1 $LaMnO_3$

This is the same structure that the traditional SOFC cathode material, $LaMnO_3$, shows at its operating temperatures. To benchmark our results, and to be able to provide a direct comparison to this material in Chapter 4, we also calculated this cubic FM phase of $LaMnO_3$ using the same method as above. The calculated geometry and

electronic structure of $LaMnO_3$ were compared to available experimental data, which shows excellent agreement with previous computational studies and with experimental data. Calculated lattice parameters and distances are available in Table 3.3, with variation of only 0.04-0.03 Å for La-O and Mn-O respectively.

Table 3.3. Calculated and experimental lattice parameter (*a*) in Å; metal–oxygen distances in Å, and band gap (E_g) in eV.

System		a	La-O	Mn-O	E_g
$LaMnO_3$	Experimental	3.90 [59]	2.74 [59]	1.94 [59]	1.7 [38]
	DFT+U	3.94	2.78	1.97	0 (α) 1.58 (β) 3.38 (β^{CBM}-β^{VBM})

The PDOS of $LaMnO_3$ shows a half-metallic ferromagnetic structure with an α-β band gap of 1.58 eV calculated from the Fermi level, and a β^{CBM}-β^{VBM} band gap of 3.38 eV (Figure 3.9), in agreement with previous studies. [19] The calculated magnetic moment of the Mn centres is 3.93 μ_B, indicating a high spin state ($HS,\ t_{2g}^3 e_g^1, S = 2$) in agreement with the PDOS, in which α-t_{2g} are fully occupied, α-e_g orbitals are half occupied, and β-t_{2g} and β–e_g are unoccupied. Furthermore, the O *2p*-orbitals in $LaMnO_3$ are degenerate with the Mn *3d*-states, which agrees well with the previously published literature. [37,110]

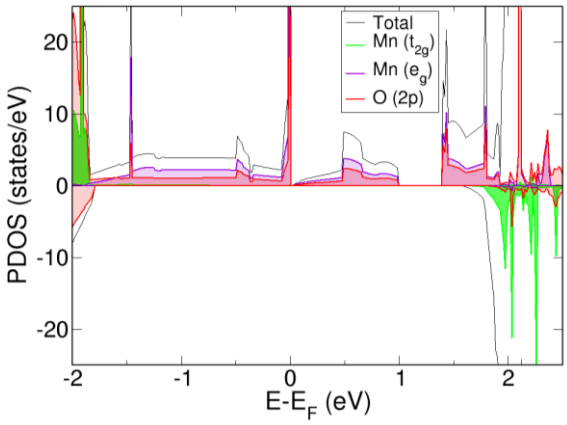

Figure 3.9. PDOS for cubic $LaMnO_3$. The Fermi level is at 0 eV, and negative $E-E_F$ represent the occupied bands and positive the virtual bands. Positive PDOS are associated with the α-spin, whereas negative PDOS are associated with β-spin.

3.3.2.4 Cobalt Magnetic Moments

Cobalt magnetic moments in the cubic structures are slightly lower compared to the orthorhombic structures (Table 3.4). The differences in different magnetic structures between the phases are between 0.6 and 0.7 μ_B for AAFM and CAFM, and nearly 1.0 μ_B for FM. As a consequence, for the AAFM, CAFM, and FM magnetic structures, the cubic phase presents Co centres in a mixed LS and IS state, whereas they are clear IS states for the orthorhombic phase. The most remarkable difference is found for the GAFM structure. In both phases, Co magnetization is between 0.6 and 1 μ_B higher compared to the rest of magnetic structures, and they are very similar for both polymorphs, 2.94 μ_B for the orthorhombic and 2.88 μ_B for the cubic phase. As a result, in the GAFM structure, Co spin states are mixed IS and HS.

Table 3.4. Cobalt magnetic moments (μ) in μ_B and relative energy difference (ΔE) in relation to DM in eV for cubic and orthorhombic $SmCoO_3$ in different magnetic structures.

	μ^{Co}_{Cubic}	ΔE cubic	$\mu^{Co}_{Orthorhombic}$	ΔE orthorhombic
DM	0.00	0.00	0.00	0.00
AAFM	1.28	1.48	2.01	1.25
CAFM	1.71	1.85	2.34	1.79
GAFM	2.88	6.53	2.94	0.68
FM	1.03	2.41	2.02	2.73

3.3.3 Insulator-to-Metal Transition

To evaluate the evolution of the magnetic structure with temperature (Figure 3.10), we have mimicked the temperature-dependent volume expansion using the experimental isotropic thermal expansion coefficient (α_T) for the orthorhombic $SmCoO_3$, $\alpha_T=2.17 \times 10^{-5}$ K^{-1}. [168] The linear thermal expansion coefficient is related to the lattice parameters, and thus supercell volume, through equation 2.47. The same thermal expansion coefficient was assumed for the cubic phase, since to the best of our knowledge, no experimental thermal expansion coefficient has been reported for this phase. In addition, we assumed that the thermal expansion was linear with respect to temperature.

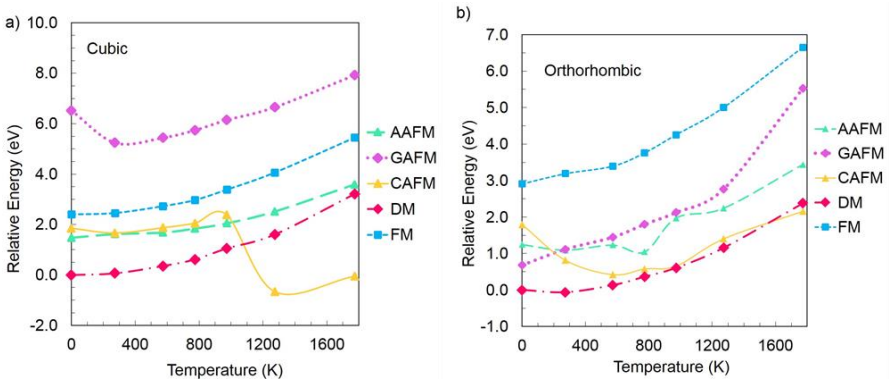

Figure 3.10. Relative energies of magnetic structures with respect to DM at 0 K versus temperature for (a) cubic, and (b) orthorhombic $SmCoO_3$.

Examining Figure 3.10, it can be seen that, as predicted experimentally, the diamagnetic structure is the ground state for both polymorphs, and the antiferromagnetic structures are higher in energy at low temperatures. At 500 K the CAFM and the DM states become nearly degenerated for the orthorhombic phase. However, due to the small relative energy differences, we believe that there would be a coexistence of both states. These results are in line with the experimental transition found above 500 K. For the cubic structure, however, a clear crossing between the DM and the CAFM is observed at around 1100 K, in which the latter becomes almost 1 eV more stable than the former. This behaviour is indeed in full agreement with the experimental results, which as previously noted, predicts an antiferromagnetic structure for the metallic state. It is important to highlight here that at these high temperatures, the phase transition from orthorhombic to cubic is known to occur, and according to our results, the insulator-to-metal transition is coupled with it. [156]

The stabilization of the CAFM structure seems to be related with the change in Co magnetic moment due to temperature. As depicted in Figure 3.11, the magnetic moment of cobalt is initially 1.72 μ_B, and slightly increases with temperature until 1000 K. After that point, we can observe a drastic change in the Co magnetic moment, which reaches 2.93 μ_B at 1273 K. This increase is related to the deformation of the system, which is now pseudo-cubic, in agreement with a previous high temperature synthesis of $SmCoO_3$. [156] The deformation of the Co-O bond induces a loss of the octahedral environment, which thus alters the orbital splitting allowing a different orbital occupation and electronic structure.

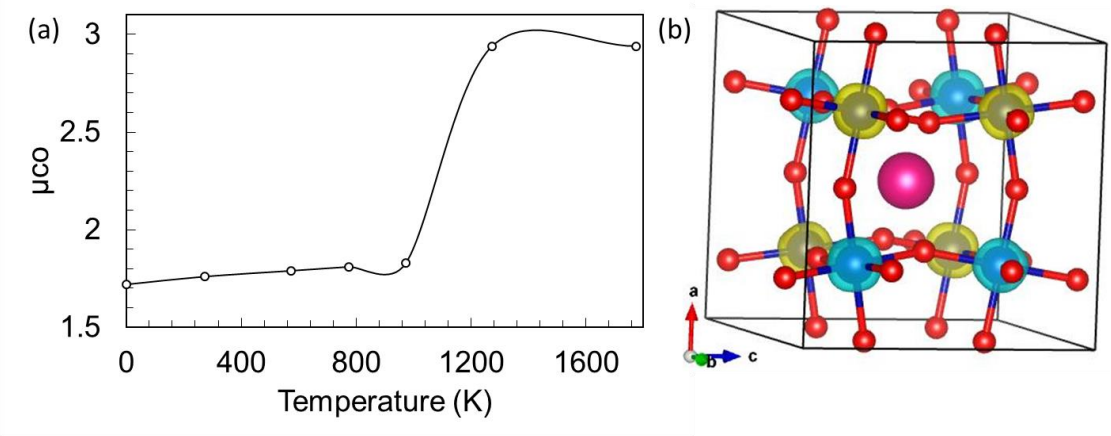

Figure 3.11. (a) Cobalt magnetic moment in the cubic CAFM magnetic structure as a function of temperature (K). (b) Structure of the pseudo-cubic CAFM structure $SmCoO_3$ at 1273 K.

3.3.4 Mechanical Properties

Mechanical properties are obtained from the elastic constants (C_{ij}). C_{ij} were computed in VASP, using the finite difference technique to calculate the Hessian matrix. In the finite difference technique, displacements of each ion are made in the direction of each Cartesian coordinate in the lattice, with the Hessian being determined from the atomic displacements. To reduce computational effort, only non-equivalent symmetry displacements are considered. The elastic tensor is then calculated by distorting the original lattice and derived using the strain-stress relationship, with the elastic constants calculated according to eq. 3.1. [162,169,170] Due to symmetry operations, cubic materials have three independent elastic constants, [171] whereas orthorhombic systems have nine [172].

$$C_{ij} = \frac{1}{V}\frac{\partial^2 E}{\partial \varepsilon_i \partial \varepsilon_j} \tag{3.1}$$

E is the total energy of the stressed simulation cell, ε is the applied strain component, and V the equilibrium volume. The calculated C_{ij} can be found in Table

3.5. Generally speaking, C_{ii} relates to a material's response to a uniform pressure that is applied perpendicularly to each cell face. A distortion affecting two non-equal axes is represented by C_{ij} and its equivalents. [169,173] Also, specifically for cubic materials, the Cauchy relation (C_{12}=C_{44}) should hold, [169] although real materials do not always obey it. [146,174] For example, in our cubic $SmCoO_3$, this violation is observed since C_{12}=75.89 GPa, and C_{44}=100.72 GPa (Table 3.5). This is in disagreement with previously published molecular dynamics-derived data, [77] this is understood as being due to short-comings in the interatomic potential model, as the core-shell model is known to favour solutions that do not violate the Cauchy relation. [146,175] In addition, the elastic constants have to adhere to the general rules for mechanical stability. These relations differ depending on the symmetry of the crystal. In the case of cubic crystals, C_{ij} should accomplish [169]: $C_{11} - C_{12} > 0$, $C_{11} + 2C_{12} > 0$, and $C_{44} > 0$, whereas for orthorhombic crystals [173]: $C_{11} + C_{22} > 2C_{12}$, $C_{22} + C_{33} > 2C_{23}$, $C_{11} + C_{33} > 2C_{13}$, $C_{ii} > 0$, and $C_{11} + C_{22} + C_{33} + 2C_{12} + 2C_{13} + 2C_{23} > 0$. The elastic constants obtained here fulfil these conditions for both materials.

Table 3.5. Elastic constants (expressed in GPa) for cubic and orthorhombic $SmCoO_3$.

	Cubic	Orthorhombic
C_{11}	461.60	244.84
C_{12}	75.89	86.09
C_{44}	100.72	99.82
C_{22}		154.40
C_{33}		300.65
C_{55}		105.38
C_{66}		85.62
C_{13}		84.76
C_{23}		49.21

From the elastic constants, mechanical properties were calculated using equations 3.2-3.12, and are collected in Table 3.6. [176] Equations 3.2, 3.4, 3.6, and 3.9 are valid for cubic systems since C_{11}, C_{12}, and C_{44} are the complete set of independent elastic constants. [171] Orthorhombic crystals, on the other hand, have a larger set of independent elastic constants, and their mechanical properties are calculated using equations 3.5, 3.7, 3.9, 3.10-3.12. [173] For clarity, superscripts *c* and *o* are used to indicate the cubic and orthorhombic crystal, respectively. Furthermore, the bulk and shear moduli have been calculated using the Voigt approximation. [169,171,173,177]

3.3.4.1 Bulk Modulus (B)

The bulk modulus (*B*) (eq. 3.2-3) is the material's ability to resist a uniform compression (*i.e.* fracture resistance). It has been shown experimentally that for ABO_3 perovskites, *B* is dependent on the lattice volume, with larger cell volumes leading to smaller *B* through an inverse relationship. [169] Our calculated bulk moduli follow this behaviour. B^O is 126.67 GPa, whereas B^C=204.46 GPa, with the volume for the orthorhombic cell being larger than the cubic. Comparison with an experimental study made on $LaCoO_3$ at room temperature, whose orthorhombic bulk modulus is 122 GPa, shows that our results show a good match with general cobaltate perovskites. [178] The scale of *B* can also be related to the material's hardness, with higher values indicating harder materials. [169] Therefore, our values imply that the cubic structure should be harder than the orthorhombic. However, the geometry of the structures has to be taken into account, and thus, the shear modulus (G) is required to make any comment on the relative hardness of the two materials.

$$B^c = \frac{C_{11} + 2C_{12}}{3} \tag{3.2}$$

$$B^o = \frac{C_{11} + C_{22} + C_{33} + 2(C_{12} + C_{13} + C_{23})}{9} \tag{3.3}$$

3.3.4.2 Shear Modulus (*G*)

G (eq. 3.4-5) is the relation between shear stress and shear strain (*i.e.* resistance to plastic deformation). *G* was found to be 137.58 GPa for the cubic, and 90.15 GPa for the orthorhombic phase. A large shear modulus is related to a larger resistance against elastic shear strain and surface penetration, which in turn is proportional to hardness. [169] According to our results, cubic $SmCoO_3$ is more resistant to surface penetration than the orthorhombic phase, reinforcing the suggestion that the cubic phase is harder than the orthorhombic one.

$$G^c = \frac{C_{11} - C_{12} + 3C_{44}}{5} \tag{3.4}$$

$$G^o = \frac{C_{11} + C_{22} + C_{33} - C_{12} - C_{13} - C_{23}}{15} + \frac{C_{44} + C_{55} + C_{66}}{5} \tag{3.5}$$

3.3.4.3 B/G Ratio

The B/G ratio gives empirical information on a material's plastic properties. A material with a B/G ratio larger than 1.75 is expected to be ductile, whereas a B/G smaller than 1.75 describes a brittle material. The B/G for $SmCoO_3$ calculated here is found to be 1.49 for the cubic structure and 1.41 for the orthorhombic phase, which puts both polymorphs in the brittle category. No previous reports on $SmCoO_3$'s brittleness

have been found, but a study on the related cobaltite perovskite, $LaCoO_3$, showed that it is brittle, [179] thus making it plausible that $SmCoO_3$ would be brittle as well.

3.3.4.4 Poisson Ratio (σ)

Poisson's ratio (σ) (eq. 3.6-7) is defined as the ratio of lateral to longitudinal strain in the elastic region while being under uniform uniaxial stress, and relates to the change in a material during uniaxial stress. [176] It could be used to provide information on interatomic forces. Covalent materials have σ < 0.1, whereas for ionic materials σ is higher than 0.25. [162] σ for the cubic structure is here calculated to be 0.14, whereas σ for the orthorhombic structure is 0.21, indicating that the latter structure is more ionic than the cubic phase, although each structure has both ionic and covalent character. [89]

$$\sigma^c = \frac{C_{12}}{C_{11} + C_{12}} \tag{3.6}$$

$$\sigma^o = \frac{\frac{3B^o}{2} - G^o}{3B^o + G^o} \tag{3.7}$$

3.3.4.5 Young's Modulus (*E*)

From *B* and *G*, Young's modulus (*E*), commonly known as the elastic modulus, can be obtained through equation 3.8. [171] *E* represents the slope of the elastic region in a stress-strain curve. The expression for *E* is the same for both structures, but their values differ. [171,173] Cubic $SmCoO_3$ was found to have an *E* of 337.11 GPa, whereas *E* for the orthorhombic phase was only 218.60 GPa. The smaller *E* for the orthorhombic system shows that this phase is more receptive to physical changes

than its cubic counterpart, which fits with the reasoning above regarding their relative hardness.

$$E = \frac{9BG}{3B + G} \tag{3.8}$$

3.3.4.6 Elastic Anisotropy (*A*)

Elastic anisotropy (A) is measured for the (100), (010), and (001) shear planes, which in the cubic symmetry (equation 3.9) are identical, but different in the orthorhombic structure (equation 3.10-12). [173] This property describes a material's tendency to form micro-cracks. [162] An elastic anisotropy value of 1 indicates an isotropic crystal, whereas deviation indicates shear anisotropy. Here, all $A \neq 1$, indicating that the behaviour of the two crystals will be dependent on the stress direction.

$$A^c = \frac{2C_{44}}{C_{11} - C_{12}} \tag{3.9}$$

$$A_1^o = \frac{4C_{44}}{C_{22} + C_{33} - 2C_{23}} \tag{3.10}$$

$$A_2^o = \frac{4C_{55}}{C_{11} + C_{33} - 2C_{13}} \tag{3.11}$$

$$A_3^o = \frac{4C_{66}}{C_{11} + C_{22} - 2C_{12}} \tag{3.12}$$

Table 3.6. Mechanical properties of $SmCoO_3$. Bulk modulus (B), shear modulus (G), Young's modulus (E), Poisson's ratio (σ), and anisotropy factor (A) are derived from the elastic constants, which in turn were calculated using DFT+U.

	Cubic	Orthorhombic
B (GPa)	204.46	126.67
G (GPa)	137.58	90.15
B/G	1.49	1.41
E (GPa)	337.11	218.60
$\boldsymbol{\sigma}$	0.14	0.21
A^c	0.52	
$\mathbf{A_1^o}$		1.12
$\mathbf{A_2^o}$		1.12
$\mathbf{A_3^o}$		1.51

From the elastic constants and calculated mechanical properties, it can then be concluded that the values of the cubic *B*, *G*, and *E* are higher than their orthorhombic counterparts, and that the orthorhombic $SmCoO_3$ is more sensitive to deformation than the cubic phase. These conclusions are in line with the hardness results, which indicate that the cubic polymorph is harder than its orthorhombic counterpart, with a lesser degree of anisotropy. However, comparing the ratio-dependent properties, σ and B/G, we found that both structures exhibits similar brittleness and ductility, which is expected considering that they have the same chemical composition. Consequently, both $SmCoO_3$ phases are prone to fracture, which should be taken into account for the development of SOFC devices.

3.4 Chapter Conclusions

In this chapter, a characterization using DFT+U of the magnetic and mechanical properties of the cubic and the orthorhombic $SmCoO_3$ material was presented. Special attention was paid to the magnetic and mechanical properties, which are important when considering them as practical SOFC materials. The electronic ground state for both phases was found to be diamagnetic, with the paramagnetic structures higher in energy at 0 K. In addition, the orthorhombic phase was lower in energy than the cubic one, agreeing with experimental evidence. In order to introduce the effect of temperature, we mimicked the effect of thermal expansion by increasing the lattice parameter of the bulk material, using the thermal expansion coefficient for orthorhombic $SmCoO_3$. Hence, we were able to determine the coexistence of both the CAFM and the DM structures for the orthorhombic phase at high temperatures, and a clear stabilization of the CAFM structure for the cubic phase around 1100 K, all in full agreement with the experimental data. These transitions were linked to a large increase in the Co spin state, as well as to a distortion of the Co octahedral environment that allowed a different Co d-orbital occupation.

The most important mechanical properties were evaluated based on calculated elastic constants. There were clear differences between the two $SmCoO_3$ polymorphs, relating to anisotropy, bulk, shear and Young's modulus. Orthorhombic $SmCoO_3$ exhibited lower hardness than the cubic phase, and that it also has a larger degree of anisotropy. Conversely, both phases showed the same ionic/covalent character (σ), and brittleness (B/G).

Chapter 4

Lattice Vacancies in Cubic $SmCoO_3$ and $LaMnO_3$

Abstract

In this chapter, the oxygen and metal vacancy formation in $SmCoO_3$ is investigated. As $LaMnO_3$ is the traditional SOFC cathode parent material, it has been included here for comparison. The main difference between these two cathode materials is that $SmCoO_3$ has been suggested to be a more efficient cathode material than $LaMnO_3$ at lower temperatures. In this chapter, we perform a comparative DFT+U study of the impact of oxygen and cation vacancies on the geometry, electronic and magnetic properties. Oxygen vacancies strongly alter the electronic and magnetic structure of $SmCoO_3$, but barely affect $LaMnO_3$. However, due to their high oxygen vacancy formation energy, oxygen vacancy concentration in the material is very low and need to be induced by doping. Studying the cation vacancy concentration shows that the formation of cation vacancies is energetically less favourable than oxygen vacancies, and would thus not markedly influence the performance of the cathode.

4.1 Introduction

It is well known that lanthanum cobaltites show higher ionic conductivities than LSM. As ionic conduction in these materials follows an oxygen vacancy migration path, and ease of forming oxygen vacancies is of crucial importance to cathode performance, a comparative study of the oxygen vacancy formation in $LaMnO_3$ and $SmCoO_3$ is instructive. Neutron diffraction analysis has shown that, particularly in the case of $LaMnO_3$, these perovskite materials can also contain cation vacancies and that these are fully ionized at SOFC operating temperatures. [59,180] Due to the inability of the cubic perovskite materials' to accommodate oxygen interstitials in the lattice, cation defects are formed to compensate for the space limitation under high concentrations of oxygen in the lattice, as a consequence of high oxygen partial pressures. [181–183] Furthermore, it has been shown microscopically that cation migration takes place in LSM cathodes, resulting in grain growth and electrode-electrolyte degradation. [59] In particular, the heat treatment and annealing techniques used during production can lead to the formation of these defects. [60,183] For example, manganese excess is often present in LSM cathodes where it has been shown to decrease electrolyte-electrode degradation. [184] In this chapter, three different lattice vacancies are thus studied; the oxygen vacancy, and the two cation vacancies.

4.2 Computational Methods

4.2.1 Calculation details

VASP was employed for all calculations. After convergence tests, energy cut-off for $LaMnO_3$ was set at 600 eV, whereas for $SmCoO_3$ it was set at 500 eV. To describe the ion-electron interaction, the projector-augmented wave method (PAW) was applied. [123] Spin-polarized calculations were performed, using the Perdew-Burke-Ernzerhof (PBE) [107,108] functional under electronic and ionic self-consistence, with convergence criteria of 10^{-5} eV and 10^{-3} eV·Å^{-1} respectively. We have considered the following valence electrons for the atomic species involved: La ($5s^2 5p^6 6s^2 5d^1$), Mn ($3p^6 3d^6 4s^1$), Sm ($5s^2 5p^6 6s^2$), Co ($4s^2 3d^7$), and O ($2s^2 2p^4$). Sm *f*-electrons were included in the pseudopotential. The tetrahedron method with Blöchl corrections for smearing [117] was applied together with a 4×4×4 Γ-centred Monkhorst-Pack grid. [118] Bader AIM (Atoms in Molecules) charges [130] were calculated using the Henkelman algorithm. [185] The on-site Coulombic interaction (DFT+U) has been used for the 3*d*-electrons in Mn and Co respectively. For $LaMnO_3$, U_{eff} = 4 eV has been applied to Mn *d*-orbitals according to the previous literature, [19] and for Co *d*-electrons in $SmCoO_3$ U_{eff} = 3 eV.

The structural model used throughout this chapter is the 2×2×2 *Pm-3m* pseudo cubic cell for both $LaMnO_3$ and $SmCoO_3$. Perovskites normally crystallize in an orthorhombic structure, but under SOFC and IT-SOFC working conditions, these materials are found in the cubic (*Pm-3m*) crystal structure, which is why we chose this one for the present study.

4.2.2 Defect Calculations

4.2.2.1 Vacancy Formation Energy

Following the method used for previous studies on perovskites such as $PbTiO_3$ [186], $SrTiO_3$ [187], $La_{1-x}Sr_xFeO_3$ [48], and $BaZrO_3$ [188], the formation of lattice vacancies in the cathode, both cationic and anionic, was evaluated by the defect formation energy at thermodynamic equilibrium. The defect formation energy is commonly calculated using the following formula: [189–191]

$$E_f(j,q) = E_{Defective,q} - E_{Bulk,q} + n_j\mu_j + q(E_v + \Delta E_F) \quad (4.1)$$

where $E_f(j,q)$ is the defect formation energy for a defect *j* in a system with charge *q*. $E_{Defective,q}$ is the total energy of the defective system with charge *q*, $E_{Bulk,q}$ is the total energy of the non-defective charged system; n_j is the number of removed species *j* from the bulk, and μ_j is the chemical potential of *j.*

It is well documented in the literature that the formation of vacancies may lead to stabilized charge states different from 0, which means that different defect charge states can be accessible. [186,188,191–193] To take this into account, we include the term $q(E_v + \Delta E_F)$, where E_v corresponds to the valence band maximum (VBM), which is the Fermi level (E_F), considered to be at 0 eV throughout this work. The term ΔE_F describes the possible positions of the Fermi energy, located between the VBM and the conduction band minimum (CBM), which can be accessible at different energies. Charged bulks were computed by changing the total number of electrons in the systems accordingly. In VASP, one can define the total number of valence electrons. A homogeneous background charge is added to account for the

charge, making the system totally neutral and avoiding a diverging Coulomb interaction. Furthermore, finite-size supercell correction schemes for charged defects can be taken into account. [194,195] However, due to the high dielectric constants of the investigated materials, 52.71 [59] for $LaMnO_3$, and 65.24 [77] for $SmCoO_3$, the electrostatic interaction energy between the charged supercells were found to be negligible when using finite-size correction schemes, as these are all inversely proportional to the dielectric constant (Appendix D). [195,196]

In the particular case of oxygen vacancies, it is known that when using DFT the oxygen binding energy is overestimated, and its degree of variation depends on several computational parameters. In order to obtain reliable values that can be compared with the experimental data, the oxygen overpotential correction term should be included in equation 4.1. [19] However, as this work intends to perform a comparative study, the absolute of this term becomes irrelevant. Finally, thermal, vibrational, and entropic contributions are neglected, as they are known to be smaller than the typical DFT error. [114,197]

4.2.2.2 Chemical Potentials

The chemical potential term in equation 4.1 refers to the species that is being removed from the unit cell to generate the vacancy. Chemical potentials are thermodynamic functions that describe the change in energy in a thermodynamic system when a species is added or removed. Given a perovskite with ABO_3 stoichiometry, the chemical potentials must satisfy the following condition:

$$g_{ABO_3}^{bulk} = \mu_A + \mu_B + 3 \cdot \mu_O \tag{4.2}$$

where $g_{ABO_3}^{bulk}$ is the free energy per formula unit for bulk ABO_3, and μ_i is the chemical potential of each species. In order to avoid the formation of the respective elementary crystals, each chemical potential must fulfil:

$$\Delta\mu_A = \mu_A - g_A^{bulk} \leq 0 \tag{4.3}$$

$$\Delta\mu_B = \mu_B - g_B^{bulk} \leq 0 \tag{4.4}$$

$$\Delta\mu_O = \mu_O - \frac{1}{2} g_{O_2}^{tot} \leq 0 \tag{4.5}$$

where $\Delta\mu_i$ is the chemical potential deviation, g_i^{bulk} is the free energy of element *i*, and $g_{O_2}^{tot}$ is the free energy of the oxygen molecule ($O_{2\,(g)}$). It is accepted that $g_{O_2}^{tot}$ can be substituted by the electronic energy of $O_{2\,(g)}$ (E_{O_2}). [188] This approximation can be made under the assumption that the bulk is in thermodynamic equilibrium with the surface, and the latter is in equilibrium with the gas phase.

The oxygen-rich situation will be determined by equation 4.5 when μ_o is at its maximum, *i.e.* $\mu_O = \frac{1}{2} E_{O_2}$. On the other hand, the oxygen-poor region will be determined by the formation of the elementary crystals A and B respectively. In this context, equation 4.2 can be rewritten as:

$$\mu_O \geq \frac{1}{3}\left[g_{ABO_3}^{bulk} - g_A^{bulk} - g_B^{bulk}\right] \tag{4.6}$$

and then, by combination of equations 4.5 and 4.6, the limits for the oxygen-poor situation are

$$\frac{1}{3}\Delta G_{ABO_3}^{f} \leq \Delta\mu_O \leq 0 \tag{4.7}$$

where $\Delta G^f_{ABO_3} = \left[g^{bulk}_{ABO_3} - g^{bulk}_A - g^{bulk}_B - \frac{3}{2}E_{O_2}\right]$. It is possible to consider the precipitation of intermediate oxides, *e.g.* AO_2, through their formation free energy:

$$\Delta G^f_{AO_2} > \Delta\mu_A + 2\Delta\mu_O \tag{4.8}$$

Solving the set of inequalities, a range for chemical potentials is obtained in which the investigated perovskites are stable. It is worth noting that throughout this work, we considered μ_o and μ_A as independent variables, whereas μ_B is a dependent variable of the previous two. For $LaMnO_3$ we have considered the formation of the following intermediate oxides: La_2O_3, MnO, MnO_2, Mn_3O_4, and Mn_2O_3, whereas for $SmCoO_3$ we have considered Sm_2O_3, CoO_2, CoO, and Co_3O_4. The detailed list of oxide formation energies is provided in Table 4.1. The here calculated formation energies provide excellent agreement with experimental sources, and show smaller errors between theory and experiment than previously published GGA+U studies [114,198] and within the same error as a study using hybrid functionals [199].

Table 4.1. Calculated and experimental formation energies for the oxides and metals expressed in eV.

Oxide	**Calculated ΔE^f**	**Experimental ΔH^f**	**Polymorph**
$LaMnO_3$	-14.90	-14.77 [200]	Pm-3m
$SmCoO_3$	-13.07	-12.95 [156]	Pm-3m
La_2O_3	-18.41	-18.54 [201]	P-3m1
MnO	-3.85	-3.99 [201]	Fm-3m
Mn_3O_4	-14.14	-14.38 [201]	I41/amd
Mn_2O_3	-9.76	-9.94 [201]	Ia-3
MnO_2	-5.27	-5.39 [201]	P42/mnm
Sm_2O_3	-18.68	-18.86 [201]	I213
CoO_2	-1.35	-1.47 [202]	C2/m
CoO	-2.40	-2.46 [201]	F43-m
Co_3O_4	-9.00	-9.23 [201]	Fd-3m
Metal	**Calculated ΔE^f**	**Experimental ΔH^f**	**Polymorph**
La	-4.89	-	P63/mmc
Mn	-4.76	-	I43-m
Sm	-4.66	-	P63/mmc
Co	-4.75	-	Fm-3m

After solving the set of inequalities for each system, a range of chemical potentials is obtained, as depicted in Figure 4.1.

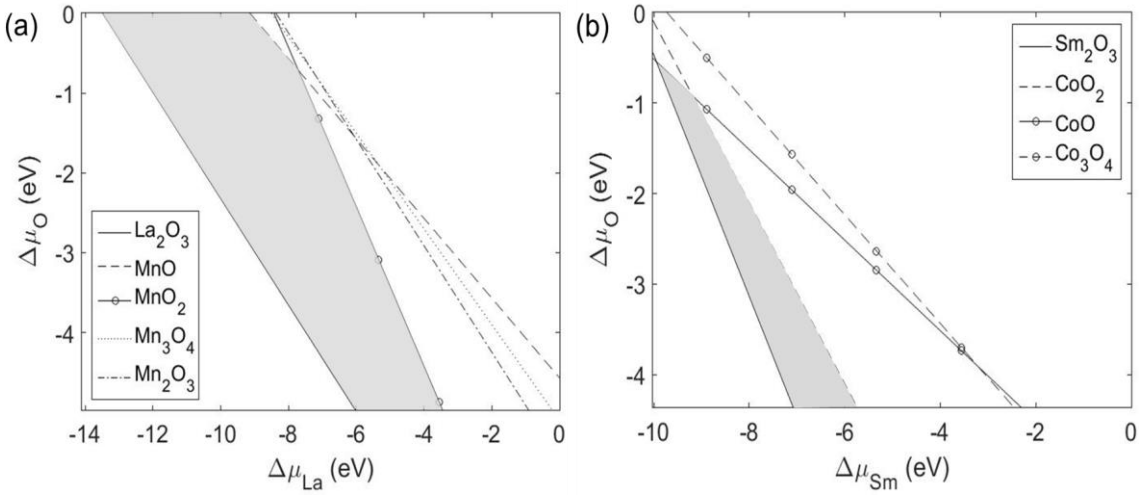

Figure 4.1. Chemical potential phase diagrams for a) $LaMnO_3$ and b) $SmCoO_3$. The grey areas represent the range of chemical potentials in which both perovskites are stable.

When we examine the calculated chemical potential phase diagrams, it can be seen that $SmCoO_3$ is unstable under oxygen-rich conditions, which favours the formation of CoO_2. This has also been noted experimentally, with cobalt-based SOFC cathodes known to be unstable at high oxygen pressures, which validates our model. [87] Therefore, according to Figure 4.1, the limits for each atomic species are as follows: $-14.10\ \text{eV} \leq \Delta\mu_{La} \leq 0\ eV$, $-10.02\ \text{eV} \leq \Delta\mu_{Sm} \leq 0\ eV$, $-4.97\ \text{eV} \leq \Delta\mu_O^{LaMnO_3} \leq 0\ eV$, and $-4.36\ \text{eV} \leq \Delta\mu_O^{SmCoO_3} \leq -0.5\ eV$.

Finally, oxygen chemical potentials can be related to the temperature and the partial oxygen pressure (*p*) according to equations 4.9-11. [187] This approximation relates the term $\Delta\mu_O(T,p)$ to an empirical expression that only considers experimental thermodynamic data. [114]

$$\Delta\mu_O(T,p) = \frac{1}{2}\left\{\Delta G_{O_2}(T,p^0) + k_B T \ln\left(\frac{p}{p^0}\right)\right\} + \delta\mu_O^0 \qquad (4.9)$$

with

$$\Delta G_{O_2}(T, p^0) = G_{O_2}(T, p^0) - G_{O_2}(T^0, p^0) \tag{4.10}$$

and

$$\delta\mu_O^0 = \frac{1}{n}\sum\left\{\frac{1}{y}\left(E_{M_xO_y} - xE_M - \Delta H_{M_xO_y}^{f,0}\right) - \frac{1}{2}\left(E_{O_2}^{tot} + T^0 S_{O_2}^{gas}(T^0, p^0)\right)\right\} \tag{4.11}$$

In these equations, $G_{O_2}(T, p^0)$ is the tabulated Gibbs free energy for O_2 at a given temperature (T) and standard pressure (p^0); k_B is the Boltzmann constant (8.6173 x 10^{-5} eV·K^{-1}), p is the pressure, T^0 is the standard temperature and $S_{O_2}^{gas}(T^0, p^0)$ is the tabulated entropy of O_2 gas.[203] The term $\delta\mu_O^0$ is a correction term that compensates the deviation between the experimental and the computational data.

4.3 Lattice Vacancies

Ionic conduction depends, among other factors, on the number of the oxygen vacancies, which in turn depends on the oxygen chemical potential. A low oxygen chemical potential enhances the creation of oxygen vacancies, whereas high oxygen chemical potentials may lead to the creation of cation vacancies. On the other hand, cation vacancies originate as a result of the fabrication process or as a consequence of the different chemical potentials. Figure 4.2 shows a schematic of the three types of vacancies investigated in this chapter.

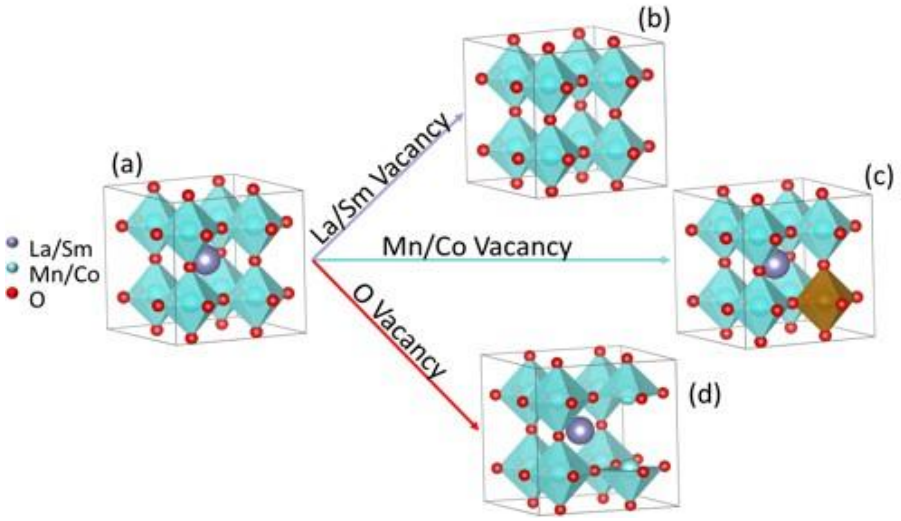

Figure 4.2. Polyhedral representation of the crystal structures of a both $LaMnO_3$ and $SmCoO_3$ in a) bulk, b) A-site cation vacancy, c) B-site cation vacancy, and d) oxygen vacancy. Grey spheres represent La and Sm, red spheres oxygen, and blue polyhedra have Mn and Co centred in them.

4.3.1 Oxygen Vacancies

The presence of oxygen vacancies leads to small distortions of both $LaMnO_{3-x}$ and $SmCoO_{3-x}$ lattices, mainly localised in the atoms neighbouring the vacancy, as shown in Table 4.2. In $LaMnO_3$, Mn-O bonds shorten by about 0.06 Å, whereas in $SmCoO_3$, Co-O bond changes are barely noticeable, with a lengthening of only 0.02 Å. We observe the same trends in the A-O distances. La-O bonds are lengthened by 0.13 Å whereas Sm-O only lengthen by 0.02 Å. It is commonly accepted that, for the same type of material, larger distortions indicate a more covalent bonding character, whereas minor distortions show a greater ionic contribution.

Table 4.2. Calculated metal-oxygen distances (in Å) next to vacancies for non-defective and defective $LaMnO_3$ and $SmCoO_3$. A is La or Sm, and B is Mn or Co, respectively.

Material	Vacancy Site	A-O distance	B-O distance
$LaMnO_3$	None	2.78	1.97
	O	2.57, 2.63, 2.66, 2.70, 2.77	1.91, 1.95, 1.96, 1.97, 1.99
	La	2.58, 2.69, 2.72	1.91, 1.94
	Mn	2.60, 2.72	1.86, 1.92, 1.93
$SmCoO_3$	None	2.65	1.88
	O	2.54, 2.56, 2.65	1.84, 1.87, 1.88, 1.89, 1.91
	Sm	2.49, 2.61, 2.65	1.86, 1.90
	Co	2.63, 2.65	1.79, 1.86, 1.87, 1.89, 1.90

The introduction of an oxygen vacancy induces changes, as well, in both the electronic and magnetic structure, as shown in Figure 3.9, as a consequence of the lattice distortions. In $LaMnO_3$, the presence of an oxygen vacancy does not significantly alter its electronic structure. The only noticeable difference is that the β band-gap is slightly reduced, as some states are now found at 2.6 eV. Moreover, Mn magnetic moments do not significantly differ from the non-defective bulk, although the Mn that are next nearest neighbours (NNN) of the oxygen vacancy show a slightly higher magnetic moment, as shown in Table 4.3, coinciding with a small decrease of charge shown by NNN Mn centres compared to those adjacent to the oxygen vacancy.

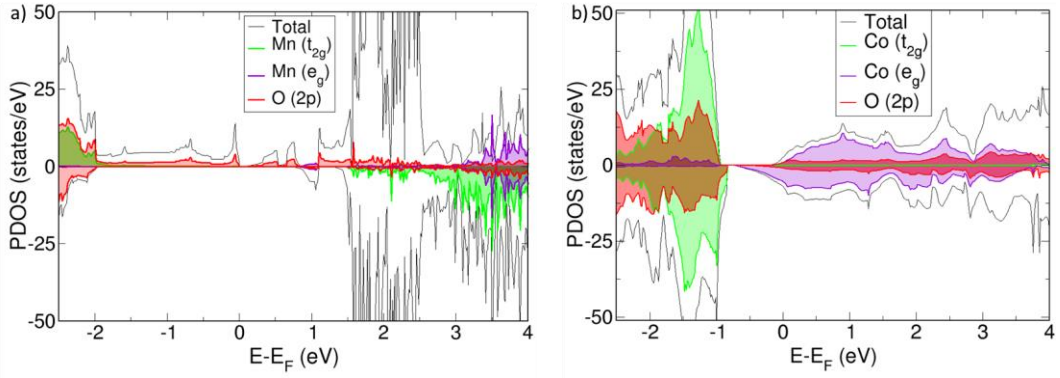

Figure 4.3. PDOS after introduction of oxygen vacancy in a) $LaMnO_3$, and b) $SmCoO_3$. The Fermi level is at 0 eV, and negative $E-E_F$ represent the occupied bands and positive the virtual bands. Positive PDOS are associated with the α-spin, whereas negative PDOS are associated with β-spin.

On the other hand, the presence of an oxygen vacancy in $SmCoO_3$ alters not only the electronic structure of the system but also the Co magnetic moment. The system now shows half-metallic behaviour, in which the valence band is described by the Co t_{2g} orbitals and the conduction band by the Co e_g orbitals. Secondly, the magnetic moments of Co centres that are nearest neighbours (NN) to the oxygen vacancy increase from 0 to 0.58, whereas the rest of the Co atoms are around 0.24. This agrees well with the calculated Bader charges, which are lower for NN Co compared to NNN Co atoms.

Table 4.3. Magnetic moments of the transition metal ion (μ_B) in μ_B and Bader charges (q) in e before and after the creation of lattice vacancies. * indicates ion adjacent to vacancy site. All other values are averaged over the number of species.

	$LaMnO_3$				$SmCoO_3$			
	Bulk	V_O	V_{La}	V_{Mn}	Bulk	V_O	V_{Sm}	V_{Co}
$\boldsymbol{\mu_B}$	3.93	4.05	3.61	3.52	0.0	0.24	0.02	0.84
$\boldsymbol{\mu_B^*}$		3.93	3.61	3.43		0.58	0.02	0.12
$\boldsymbol{q_B}$	+1.81	+1.60	+1.78	+1.89	+1.31	+1.26	+1.32	+1.40
$\boldsymbol{q_B^*}$		+1.54	+1.78	+1.80		+1.10	+1.32	+1.36
$\boldsymbol{q_A}$	+2.12	+2.10	+2.14	+2.09	+2.01	+2.07	+2.12	+2.09
$\boldsymbol{q_O}$	-1.31	-1.29	-1.24	-1.26	-1.11	-1.16	-1.05	-1.11

Magnetic moments and Bader charges suggest that, as stated in previous publications, [181] the generation of an oxygen vacancy is related to the reduction of two neighbouring Mn/Co atoms, which can be represented as:

$$O^{2-} + 2Mn^{3+} \rightarrow \frac{1}{2}O_2 + 2Mn^{2+} \tag{4.12}$$

Or according to the Kröger-Vink notation, it is represented as: [204]

$$O_O + 2Mn_{Mn}^{x} \rightleftharpoons V_O^{\cdot\cdot} + \frac{1}{2}O_2 + 2Mn_{Mn}^{\cdot} \tag{4.13}$$

Both equations note the formation of an Mn^{2+} – V_o – Mn^{2+} cluster, and equally applied to Co^{2+}. [181] We verified the existence of these clusters by calculating the spin density ($\Delta\rho^{\alpha-\beta}$) difference, defined as $\Delta\rho^{\alpha-\beta} = \rho_{ABO_{3-x}}^{\alpha-\beta} - \rho_{ABO_3}^{\alpha-\beta} - \rho_O^{\alpha-\beta}$, where $\rho_{ABO_3}^{\alpha-\beta}$ is the spin density for the bulk material, $\rho_{ABO_{3-x}}^{\alpha-\beta}$ is the spin density of the defective bulk, and $\rho_O^{\alpha-\beta}$ is the spin density of a single oxygen atom, calculated in its triplet state. It is worth noting that for both materials, the spin depletion

observed in the oxygen vacancy is owing to the fact that we calculated the single oxygen atom in its triplet state.

In the case of $LaMnO_{3-x}$, (Figure 4.4a) we observe a spin redistribution on the Mn that are NN to the oxygen vacancy, and a very small increase on the rest of the Mn, which fully agrees with the magnetic moments and Bader charges previously discussed. However, the formation of the Mn^{2+}-V_O-Mn^{2+} clusters is not quite evident. In $SmCoO_{3-x}$ (Figure 4.4b) we do see an increase in spin density in all Co centres, but with a larger isosurface in those that are NN to the oxygen vacancy, clearly showing the formation of the reduced Co – V_O clusters. Continuing the reasoning from Chapter 3, this increase in spin density is a consequence of the distortion in the Co-O bonds upon oxygen vacancy formation and the change in Co 3d-orbital occupation.

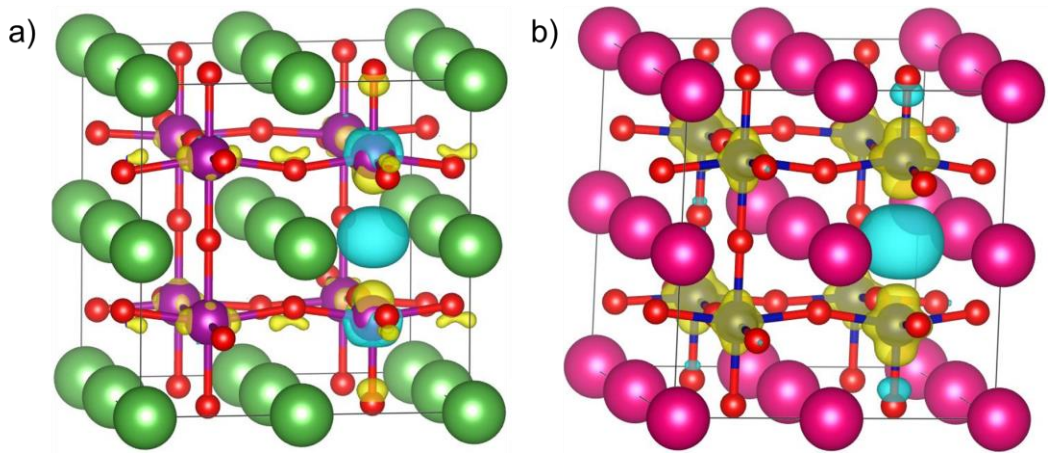

Figure 4.4. Spin density difference ($\Delta\rho^{\alpha-\beta}$) representation of a) $LaMnO_3$ and b) $SmCoO_3$ with oxygen vacancy in the neutral charge state. Yellow $\Delta\rho^{\alpha-\beta}$ isosurface represents an increase of spin density, whereas blue $\Delta\rho^{\alpha-\beta}$ isosurface represents a spin density depletion. Isosurface value is set at 0.02.

Oxygen vacancy formation energies ($E_f^{V_O}$) were calculated for five different defect charge states; 0, ±1, and ±2, under the O-rich regime (Table 4.4 and Figure 4.7). These charge states have been selected as the formal oxygen anion charge is -2. Likewise, the oxygen-rich regime was selected as experimental studies are performed at high oxygen partial pressure. For CBM, we have used the calculated band gap for $SmCoO_3$ and the β-direction band gap of 1.58 eV for $LaMnO_3$.

Table 4.4. Oxygen vacancy formation energies (in eV) for $LaMnO_3$ and $SmCoO_3$ for different charge states at the valence band maximum ($\boldsymbol{E_f^{VBM}}$) and at the conduction band minimum ($\boldsymbol{E_f^{CBM}}$) under oxygen rich conditions.

	$LaMnO_3$		$SmCoO_3$	
q	E_f^{VBM}	E_f^{CBM}	E_f^{VBM}	E_f^{CBM}
+2	3.15	6.31	0.30	1.65
+1	3.09	4.67	1.46	2.14
0	3.14	3.14	2.08	2.08
-1	3.24	1.66	2.64	1.96
-2	3.91	0.75	2.99	1.64

As expected, all formation energies are positive, clearly indicating that oxygen vacancies will not be formed spontaneously. However, the formation of oxygen vacancies in $SmCoO_3$ is slightly more favoured. For example, if we consider the neutral charge state, in $LaMnO_3$ $E_f^{V_O}$ = 3.14 eV, whereas in $SmCoO_3$ it is 2.08 eV, *i.e.* more than 1 eV smaller.

The influence of temperature and pressure on the oxygen vacancy formation energy was analysed for the non-charged states for $LaMnO_{3-x}$ and $SmCoO_{3-x}$,

according to equations 4.9-11. For $LaMnO_{3-x}$, the formation of oxygen vacancies is only spontaneous at temperatures higher than 1100 K, in combination with low oxygen partial pressure. On the other hand, for $SmCoO_{3-x}$ oxygen vacancies can be spontaneously generated at lower temperatures (>900 K) than $LaMnO_3$, but again at low oxygen partial pressure, which as we have stated already, are not the working conditions in SOFC.

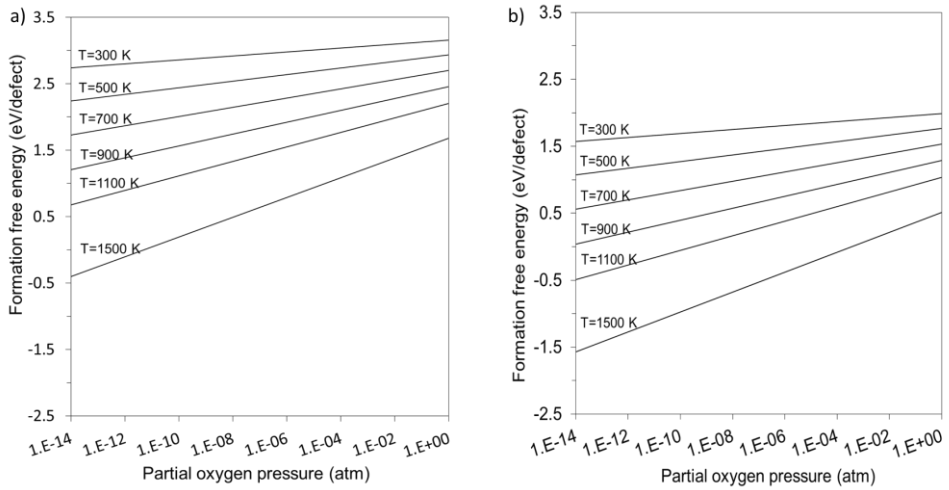

Figure 4.5. Oxygen vacancy formation energy as a function of partial oxygen pressure (atm) at different temperatures for a) $LaMnO_3$, and b) $SmCoO_3$.

Using the vacancy formation energy of the neutral charge state we can calculate the concentration of the oxygen vacancies (C_{V_O}) per mole of perovskite according to the following formula: [113,189,205]

$$C_V = N\exp\left(\frac{-E_f^{V_o}}{k_B T}\right) \tag{4.14}$$

where $E_f^{V_o}$ is the oxygen vacancy formation energy (Table 4.4), *N* is the concentration of atomic sites substituted by the defect, which for oxygen vacancies is $N=3-C_{V_O}$. [113,189] We calculated the concentration for both $LaMnO_{3-x}$ and

$SmCoO_{3-x}$, as shown in Figure 4.6. We observe that C_{V_O} under equilibrium conditions is higher in $SmCoO_3$ than in $LaMnO_3$, as it would be expected from their formation energies. However, vacancy concentrations in $SmCoO_{3-x}$ are still below 1×10^{-6} mol×(mol perovskite)$^{-1}$, and even smaller in $LaMnO_{3-x}$, where they are found below 1×10^{-11} mol×(mol perovskite)$^{-1}$. These results are expected, as it is known experimentally that V_O are obtained mainly by doping both materials. Nevertheless, we could also modify the oxygen chemical potential by means of reducing p_{O_2}.

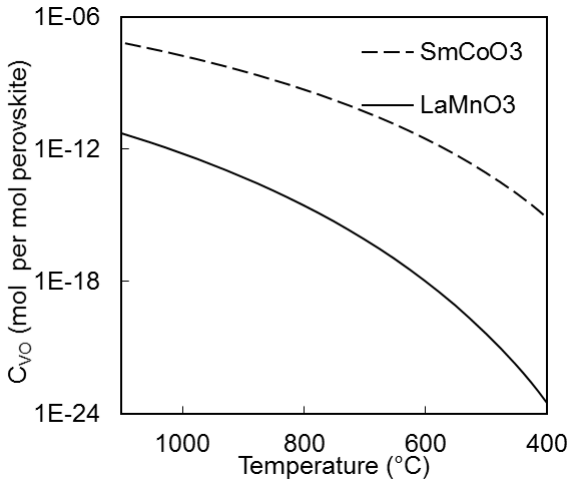

Figure 4.6. Oxygen vacancy concentration (mol per mol perovskite) as a function of temperature in $SmCoO_3$ (dashed line) and $LaMnO_3$ (full line), assuming oxygen rich conditions.

Considering the different charge states, collected in Table 4.4 and represented in Figure 4.7, we note that the +1 charge state for $LaMnO_3$ has the smallest $E_f^{V_o}$ for ΔE_F= 0 eV. Charge transitions occur when $E_f^{V_o}$ for different charge states intercross at a given energy. [206] The first charge transition is at ΔE_F = 0.05 eV and corresponds to the transition from +1 to 0, almost at the same ΔE_F in which

the transition from 0 to -1 occurs, 0.06 eV. The last observed transition happens at ΔE_F = 0.67 eV, from -1 to -2. To get an idea of the thermal cost of these transition energies, we can use the relation $\Delta E_F = k_B T$. Thus, the transition from +1/0 occurs at approximately 580 K, 0/-1 at 696 K, and the transition -1/-2 at 7775 K. The last transition is thermally inaccessible at working temperatures and far above the melting point of $LaMnO_3$. We can conclude that at working temperatures, the charge state that is stabilized is q=-1, although due to the small energy difference between +1/0 and 0/-1 charge transitions (only 0.01 eV), it is likely that the three charge states, +1, 0, and -1 coexist.

In contrast, in the equilibrium picture, $SmCoO_{3-x}$ shows a completely different trend, with a preferential charge state of +2, and no accessible charge transitions. This would indicate that $SmCoO_{3-x}$ does not prefer to accommodate the two electrons resulting from the oxidation of O^{2-}, *i.e.* $SmCoO_{3-x}$ will not act as an effective electron conductor at intermediate temperature SOFC working temperatures. This behaviour is in agreement with the literature. [82,87,153,207,208]

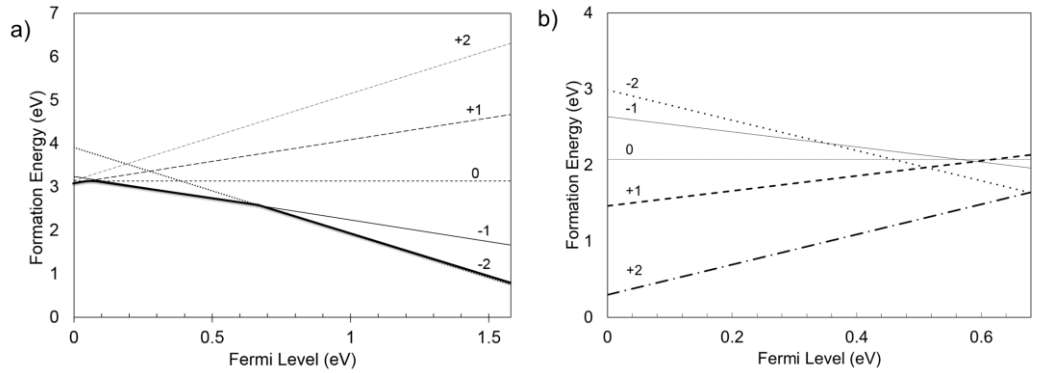

Figure 4.7. Oxygen vacancy formation energy in different charge states as a function of the Fermi level for a) $LaMnO_3$ and b) $SmCoO_3$. For the $LaMnO_3$, VBM, ΔE_F =0 eV and CBM, ΔE_F =1.58 eV, whereas for $SmCoO_3$, VBM, ΔE_F =0 eV and CBM, ΔE_F =0.68 eV.

4.3.2 Cation Vacancies

Finally, we also evaluated the cost of generating cation vacancies in both materials. To that end, and using equation 4.1, the cation vacancy formation energies for both cations in both materials for the charge states between -3 and +3 are calculated. E_f^V are listed in Table 4.5, assuming oxygen- and cation-rich conditions for all cases.

Table 4.5. E_f^V at the VBM and CBM respectively, E_f^{VBM} and E_f^{CBM} for the cation vacancies in different charge states (q). For V_{La} and V_{Mn}, VBM, ΔE_F =0 eV and CBM, ΔE_F =1.7 eV, and for V_{Sm} and V_{Co}, VBM, ΔE_F =0 eV and CBM, ΔE_F =0.68 eV.

	A-site				B-site		
	q	E_f^{VBM} (eV)	E_f^{CBM} (eV)		q	E_f^{VBM} (eV)	E_f^{CBM} (eV)
V_{La}	3+	10.18	14.08	V_{Mn}	3+	7.30	7.49
	2+	8.80	11.40		2+	6.30	8.90
	1+	7.73	9.03		1+	5.76	7.06
	0	6.95	6.95		0	5.74	5.74
	1-	6.30	4.99		1-	5.78	4.48
	2-	6.01	3.41		2-	6.13	3.53
	3-	6.22	2.32		3-	11.20	3.59
V_{Sm}	3+	10.17	12.20	V_{Co}	3+	4.86	6.88
	2+	10.0	11.35		2+	4.65	6.00
	1+	8.35	9.02		1+	4.79	5.46
	0	7.98	7.98		0	5.17	5.17
	1-	6.89	6.21		1-	3.56	2.89
	2-	6.39	5.04		2-	3.48	2.13
	3-	4.97	2.95		3-	1.93	-0.09

As expected, all vacancy formation energies are highly positive, although for the B position (Mn and Co respectively) they are between 1 and 2 eV smaller than the A position. In any case, all energies are higher than 5 eV, indicating that vacancies will not generate spontaneously. As to the charge states, all cation vacancies are negatively charged, as shown in table 4.6. For V_{La}, E_f^V shows only one charge transition, -2/-3 at 0.21 eV, which is thermally inaccessible. For V_{Sm}, the -3 charge state is most stable, with no observed charge transitions, agreeing with the previous literature. [180] Looking at V_B, only one charge transition is observed for V_{Mn}, -1/-2 at 0.36 eV. This transition is not thermally accessible during device operation, leaving the charge state of the system as -1. For V_{Co}, the most stable charge state is -3, a charge state that has also been calculated to be the most

stable for both cation vacancies in $SmCoO_3$. This is also the most probable cation vacancy, in comparison, to be present in $SmCoO_3$. However, the concentration of these defects is expected to be very low in comparison to oxygen vacancies.

Despite the possible influence of cation vacancies on the electronic conductivity, defect concentrations calculated from their vacancy formation energy indicate that in fact, these vacancies are very unlikely. As shown in Figure 4.8, and using equation 4.14 with N=1-C_V, cation concentrations under both rich and poor conditions are found below $1 \cdot 10^{-10}$ mol · (mol perovskite)$^{-1}$ in almost all cases. The only exception is observed for V_{Co} under Co-poor conditions, which are not found under experimental conditions. Hence, we can conclude that cation vacancies do not play any key role in the cathode properties, as their concentrations will be extremely low. Worth noting is as well that their impact on electronic structure, and magnetic moments is seen to be negligible (Appendix D and Table 4.3), except for Co-vacancies, which does alter the electronic structure of $SmCoO_3$ from semiconductor to half-metallic. This is not unexpected though as the major contributor to change in $SmCoO_3$ electronic structure is disorder in the CoO_6-polyhedra, and removing a cobalt from these does indeed induce disorder.

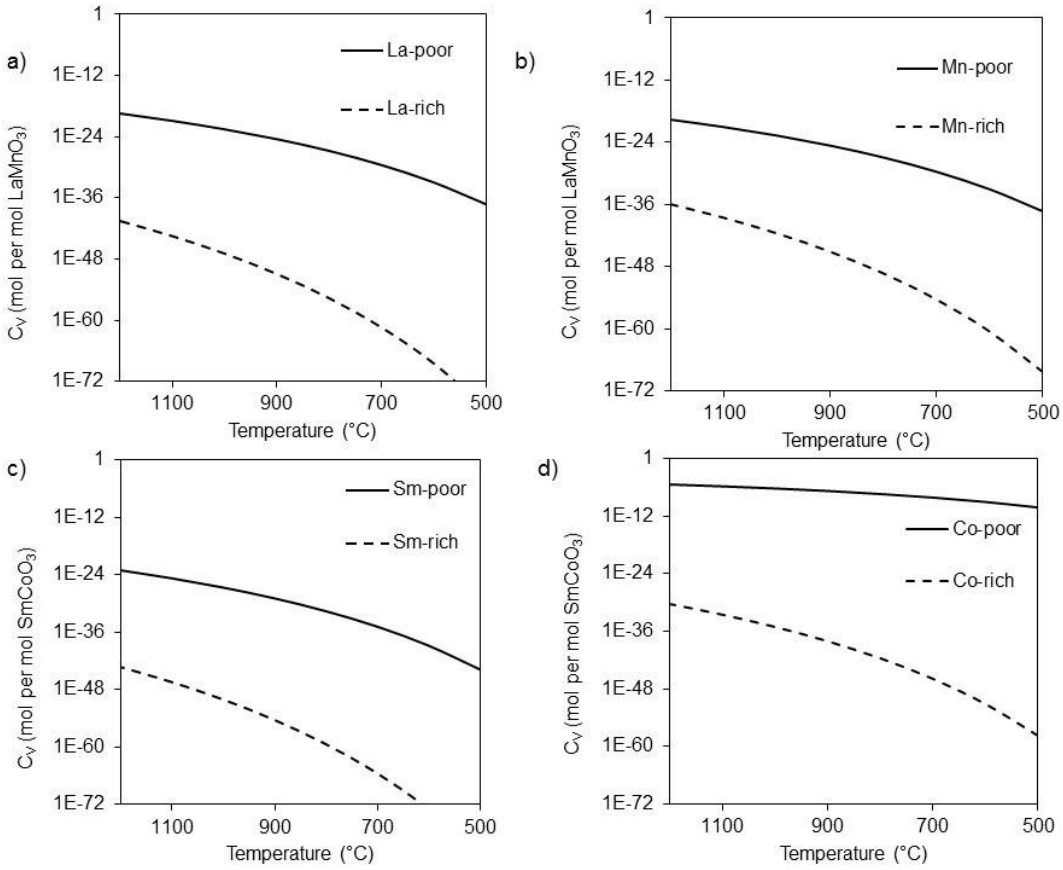

Figure 4.8. a) Lanthanum, b) manganese, c) samarium, and d) cobalt vacancy concentrations versus temperature.

4.4 Chapter Conclusions

In this chapter, we have used DFT+U techniques to investigate the impact of lattice vacancies in $SmCoO_3$, and to compare this to the well-known $LaMnO_3$. To model lattice vacancies, we calculated the range of chemical potentials in which the materials are stable, obtaining results in agreement with experimental evidence on stability. We found that the oxygen vacancy formation energy for $LaMnO_3$ is higher than for $SmCoO_3$, but that they are all positive, indicating that the formation of V_O is not spontaneous, unless we move into an oxygen-poor regime. The presence of V_O did not significantly affect the electronic structure of $LaMnO_3$, but it did alter the

electronic and magnetic properties of $SmCoO_3$. V_O in $SmCoO_3$ turned this semiconductor into a half-metallic material, with the formation of Co^{2+}-V_O-Co^{2+} clusters. In comparison, these clusters were not evident in $LaMnO_3$. Equilibrium C_{V_O} was calculated, showing as expected that it is very low, although $SmCoO_3$ shows C_{V_O}, related to its lower vacancy formation energy. The investigation of the charge states indicated that at SOFC working temperatures, $LaMnO_3$ showed stabilization of a negative charge whereas $SmCoO_3$ was not able to accept extra charge, which explained the different experimental behaviour observed for both materials regarding electronic conductivity.

Finally, the formation of cation vacancies was studied, and it was shown that they require very high energies to be formed.[1] Thus, it is expected that these will only exists in very small concentrations, and will have negligible impact on the electronic and ionic conduction in the materials.

[1] All defect formation energies calculated here are calculated from the same volume simulation cell as the defect free bulks, as per convention. Test calculations allowing the simulation cells with defects relax their volume were carried out, and it was found that the results presented here would not be changed by allowing these volumes to be relaxed. For comparison, the oxygen formation energy in $SmCoO_3$ in a relaxed supercell is 2.51 eV, samarium vacancy 8.14 eV, and cobalt vacancy 3.06 eV.

Chapter 5

Ba^{2+}, Ca^{2+}, and Sr^{2+} Substitutional Doping on Sm-site in $SmCoO_3$

ABSTRACT

The substitutional doping of Ca^{2+}, Sr^{2+}, and Ba^{2+} on the Sm-site in $SmCoO_3$ has been showed to improve both electronic and ionic conductivities for applications as solid oxide fuel cell (SOFC) cathodes. In this chapter we use DFT calculations to investigate dopant configurations at two different dopant concentrations: x=0.25 and 0.50. To preserve the electroneutrality of the system, we have studied two different charge compensation mechanisms; the creation of (i) oxygen vacancies, and (ii) electronic holes. After examining the electronic structure, charge density difference, and oxygen vacancy formation energies, we concluded that the charge is compensated by the generation of oxygen vacancies. Furthermore, we found that the improvement of the electronic conduction is not a direct consequence of the appearance of electron holes, but a result of the distortion of the material, more specifically, the distortion of the Co-O bonds, which leads to a different occupation of the Co 3d-orbitals, enabling electronic conductivity. Finally, MD simulations were employed to model ionic conduction and thermal expansion coefficients. It was found that all dopants at both concentrations showed high ionic conduction comparable to experimental results for other SOFC cathode materials.

5.1 Introduction

Unlike traditional cathode materials such as $La_{1-x}Sr_xMnO_{3-\delta}$ (LSM), which loses efficiency at these low temperatures due to polarization resistance, cobalt-based perovskites have shown better performance and have been suggested as suitable materials for IT-SOFC, [66] as their reported properties include better mixed ionic and electronic conduction, low polarization resistance, and lower overpotentials. [1,209] Their higher ionic conductivity is a consequence of the lower activation energies required for the oxygen to migrate *via* oxygen vacancies, which are induced when substituting Sm^{3+} by a divalent cation (A). [1,18,35,71,82,160,209,210]

Upon doping, the overall charge of the system can be compensated *via* two different charge compensation schemes. On the one hand, oxygen vacancies (V_O) can be generated, according to the Kröger-Vink notation, as described in equation 5.1: [204]

$$2AO \xrightarrow{SmCoO_3} 2A'_{Sm} + 2O_O^x + V_O^{\cdot\cdot} \quad (5.1)$$

On the other hand, the charge can be compensated with the creation of electron holes, as expressed in equation 5.2. [48,82,211,212]

$$AO \xrightarrow{SmCoO_3} A'_{Sm} + O_O^x + h^{\cdot} \quad (5.2)$$

While the oxygen vacancy compensation mechanism is widely used to explain the formation of oxygen vacancies, and thus the increase in the ionic conductivity, the hole compensation mechanism has been suggested to explain

the increase in the electronic conductivity. [48,212] Although there is no strong evidence, it is believed that both mechanisms coexist in the material. The increase in the electronic conductivity seems to be related with the spin transition observed in cobalt, from low spin to either high (HS, $t_{2g}^4 e_g^2$), intermediate (IS, $t_{2g}^5 e_g^1$), or mixed spin (LS/IS, IS/HS). [160] This leads to magnetic domains, metallic electronic structure, and the cobalt ions coexisting in different spin states. [160] Another improvement that doped $SmCoO_3$ cathodes present with respect to LSM, is that although they do not couple well with yttria-stabilized zirconia (YSZ) as the electrolyte material, they show better compatibility with ceria-based electrolytes such as gadolinium-doped ceria (GDC). [35,209] Although experimental studies conducted on $Sm_{1-x}A_xCoO_{3-x/2}$ indicate that they could be promising materials for IT-SOFC cathodes, questions remain why these materials show better performance than doped lanthanum manganite. [213]

In this chapter, we investigate three common $SmCoO_3$ dopants; Ca^{2+}, Sr^{2+}, and Ba^{2+}, at two different dopant concentrations (x); x=0.25, and 0.5. Using a combination of DFT and MD simulations, we have investigated two different charge compensation schemes, the electronic and magnetic structure, oxygen diffusion, and the thermal expansion coefficients. On the basis of these calculations, we then compare the different $Sm_{1-x}A_xCoO_{3-x/2}$ systems to gain an understanding of how the dopant species and its concentration influences the materials' properties. The results have been compared to experiment, and especially the compatibility with traditional electrolytes has been kept in mind when evaluating which dopant and concentration are most suitable for IT-SOFC cathode applications.

5.2 Computational Details

We have employed two different methodologies to model the $Sm_{1-x}A_xCoO_{3-x/2}$ systems; DFT has been used to study the energetics and the electronic structure of the different dopant configurations, whereas MD is used to study thermal properties and oxygen diffusion at different temperatures.

5.2.1 Density Functional Theory Calculations

DFT calculations were performed with VASP. The PAW method was applied to describe the ion-electron interaction. Based on convergence tests, the plane wave energy cut-off was set to 500 eV. Spin-polarized calculations were performed with the PBE functional under electronic and ionic self-consistence, with convergence criteria of 10^{-5} eV and 10^{-3} eV·Å^{-1} respectively. The following valence electrons for the atomic species involved were taken into account: Sm ($5s^25p^66s^2$), Sr ($4s^24p^65s^2$), Ba ($5s^25p^66s^2$), Ca ($3s^23p^64s^2$), Co ($4s^23d^7$), and O ($2s^22p^4$). The tetrahedron method with Blöchl corrections for smearing together with a 4×4×4 Γ-centred Monkhorst-Pack grid was applied. Bader charges were calculated using the Henkelman algorithm. [185] When non-stoichiometric bulk materials were modelled without charge compensation via oxygen vacancies, a homogeneous background charge was added to counteract the resulting charge. This makes the system overall charge-neutral and avoids a diverging Coulomb interaction.

To correct the electron self-interaction problem arising from the d-electrons of Co, [65,110,111] we have used the DFT+U, considering a Hubbard parameter of 3 eV using the Dudarev approximation. [109] Finally, the crystal structure and cell used

was the 2×2×2 *Pm-3m* pseudo cubic cell. These materials have average cubic structures at high temperatures, with local Jahn-Teller distortions on the CoO-octahedra. [114]

5.2.2 Molecular Dynamics Calculations

All MD simulations were performed using the DL_POLY 4.07 code, with a 20×20×20 supercell simulated under NPT conditions, using a Nosé-Hoover thermostat. All statistics were collected after a system equilibration of 13 ps, with an added 100 ps production phase. The time step for both phases was 0.5 fs. The Ewald summation was employed to account for the electrostatic interactions, whereas the Verlet algorithm evaluated the atomic motions. The Buckingham potential, within the Born model for ionic solids, was used to describe the short-range interactions between atoms, together with the shell model for the electronic polarizability. The interatomic potentials used in this work are presented in section 2.7.1.2.4.

5.3 Dopant Configurations

To evaluate the position of the A^{2+} and the V_O, we have used the Site-Occupancy Disorder program (SOD). [214] SOD uses the symmetry operations of the non-doped bulk system to determine all the non-equivalent substitutions. At this stage, we should then use SOD again to determine the non-equivalent positions for the oxygen vacancy in the doped system. However, due to the high number of resulting configurations (around 250 configurations in total), we first determined the most stable dopant configuration in doped $SmCoO_3$ without V_O. We found three inequivalent configurations for x=0.25, and six for x=0.50 (Figure 5.1).

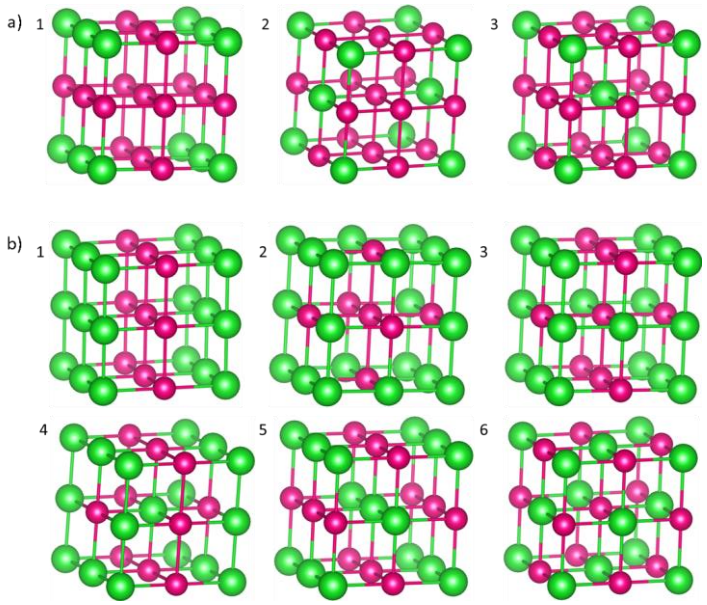

Figure 5.1. Ball-and-stick representation of the three non-equivalent configurations for a) $Sm_{0.75}A_{0.25}CoO_3$, and the six non-equivalent configurations for b) $Sm_{0.5}A_{0.5}CoO_3$ as calculated with SOD. O and Co have been omitted for clarity. Sm is coloured in pink whereas the dopant is coloured in green.

Since SOD does not provide any information about the relative stability of the different bulks, we optimized all the different distributions using VASP, for all the different dopants: Ca^{2+}, Sr^{2+}, and Ba^{2+}. After optimization, the most stable dopant distribution per dopant and concentration was used to determine the positions of the oxygen vacancies. We found that all systems with x=0.25 had the same most stable dopant vacancy configuration, whereas Sr- and Ba-doped systems for x=0.5 had different configurations from the Ca-doped system at the same concentration. The reason for this difference was attributed to size-effects, as Ca^{2+} is the smallest dopant. The final configurations for each cation and concentration are depicted in Figure 5.2.

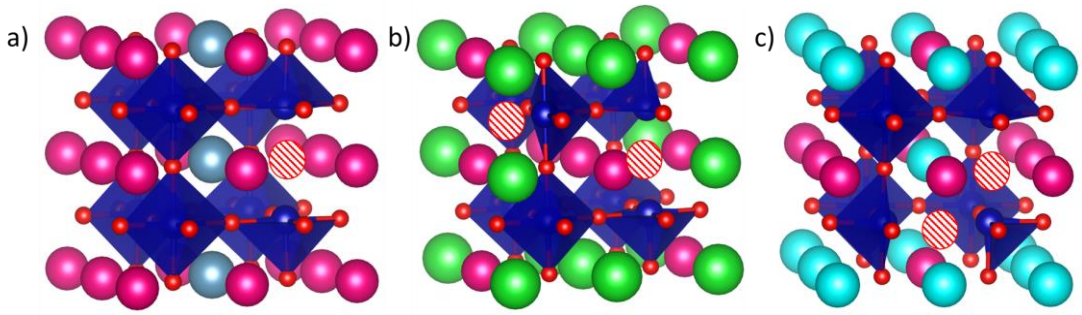

Figure 5.2. Dopant-vacancy configurations for a) $Sm_{0.75}A_{0.25}CoO_{2.88}$, b) $Sm_{0.5}A_{0.5}CoO_{2.75}$ (A=Ba, Sr), and c) $Sm_{0.5}Ca_{0.5}CoO_{2.75}$. The pink spheres are Sm^{3+}, whereas Co^{3+} are in the centre of the blue octahedra, and O^{2-} are red. V_O is represented by white and red circles. In a) grey spheres are Ca^{2+}, Sr^{2+}, or Ba^{2+}, whereas in b) green are Sr^{2+}, or Ba^{2+}, and in c) light blue spheres are Ca^{2+}.

Table 5.1. Energy differences (eV) for dopant configurations. Numbers refer to the different SOD configurations.

	Ca		**Sr**		**Ba**	
	x=0.25	x=0.5	x=0.25	x=0.5	x=0.25	x=0.5
1	0.0	1.6	0.0	0.7	0.0	0.4
2	0.4	3.5	0.9	1.7	0.9	1.4
3	1.1	0.5	1.2	0.0	0.8	0.0
4		0.0		0.5		0.8
5		1.4		0.7		0.7
6		4.3		4.0		5.2

More specifically, at x = 0.25, configuration 1 is the most stable for all three dopants, and the range of energies is about 1.0 eV, with the other configurations found at least 0.4 eV higher in energy than the most stable structure, regardless of dopant. On the other hand, for x=0.50, configuration 3 is the most stable for Ba^{2+} and Sr^{2+}, whereas for Ca^{2+} configuration 4 is the most stable. At this concentration, the range of energies is larger compared to x=0.25; for Ca^{2+} the range is 3.5 eV,

for Sr^{2+} 1.7 eV, and 5.2 eV for Ba^{2+}. The difference in energies between the most stable configuration and the next one is between 0.5 and 0.7 eV for the different dopants. A full list of relative energies is included in Table 5.1. Furthermore, introducing A on the Sm-site leads to increased lattice volume in the pseudocubic structure, as found from DFT+U calculations. Deviations from the perfect cubic lattice are observed, with disorder present in the Sm-O and Co-O bonds (Table 5.2).

Table 5.2. Volumes (Å^3), and interatomic distances (Å) in dopant systems for the most stable configuration (N) referring to Figure 5.1 and Figure 5.2. A refers to dopant.

System	N	Volume	Sm-O	Co-O	A-O
$SmCoO_3$		52.73	2.65	1.88	N/A
$Sm_{0.75}Ca_{0.25}CoO_3$	1	54.43	2.60-2.69	1.89, 1.91	2.74, 2.76
$Sm_{0.50}Ca_{0.50}CoO_3$	4	54.01	2.69-3.03	1.91-1.95	2.69-2.95
$Sm_{0.75}Sr_{0.25}CoO_3$	1	54.58	2.58-2.73	1.89-1.92	2.77, 2.80
$Sm_{0.50}Sr_{0.50}CoO_3$	3	55.59	2.57-2.72	1.91	2.69-2.83
$Sm_{0.75}Ba_{0.25}CoO_3$	1	56.33	2.56-2.77	1.91, 1.96	2.84
$Sm_{0.50}Ba_{0.50}CoO_3$	3	58.41	2.55-2.78	1.92-1.96	2.74-2.92

For the most stable dopant configurations we have explored the non-equivalent V_O positions with SOD and the remaining symmetry operations per system, leading to a total of 39 non-equivalent V_O distributions. Low V_O concentrations do not have a significant effect on the lattice parameters, [211] and the supercell volume can thus be kept constant when introducing V_O.

5.4 Electronic and Magnetic Structures

Projected density of states (PDOS) for the oxidized systems ($Sm_{1-x}A_xCoO_3$) with x=0.25 and 0.5 are collected in Figure 5.3. All materials, with the exception of $Sm_{0.50}Sr_{0.50}CoO_3$, show the same common features. Upon doping, the systems become half-metallic, thus indicating that they all become electronic conductors. This conduction mainly occurs through the Co e_g orbitals, which are hybridized with the O *2p*-orbitals. We modelled different magnetic structures (according to Chapter 3) for all the different systems, and in all cases the ferromagnetic ground state was the most stable. The ferromagnetic structure is evidenced in the PDOS by the fact that *α*- and *β*-densities are not symmetrical. The change in the magnetic structure is attributed to the LS to IS transition observed in the cobalt centres and listed in Table 5.3, where Co^{3+} magnetic moment increases from LS μ_{Co}=0 μ_B (LS) to μ_{Co}≈2 μ_B (IS). Cobalt charges (q_{Co}) do not vary markedly with increasing *x*, whereas q_O decreases by ≥0.04 *e* going from x=0.25 to x=0.5. This trend has also been observed for $La_{1-x}Sr_xFeO_3$, and was suggested to indicate hole delocalization on the oxygen sub-lattice, [48] although there is no clear evidence in the PDOS of the existence of this electronic hole near the Fermi level (E_F).

For the specific case of $Sm_{0.50}Sr_{0.50}CoO_3$, it is still a conductor since the cobalt t_{2g} orbitals are found both above and below E_F, but its electronic structure reveals that the t_{2g}/e_g crystal field splitting still applies for this material despite the doping (Figure 5.3d). Accordingly, the magnetic moment of cobalt atoms is around 0 and no significant change in the cobalt charge is observed.

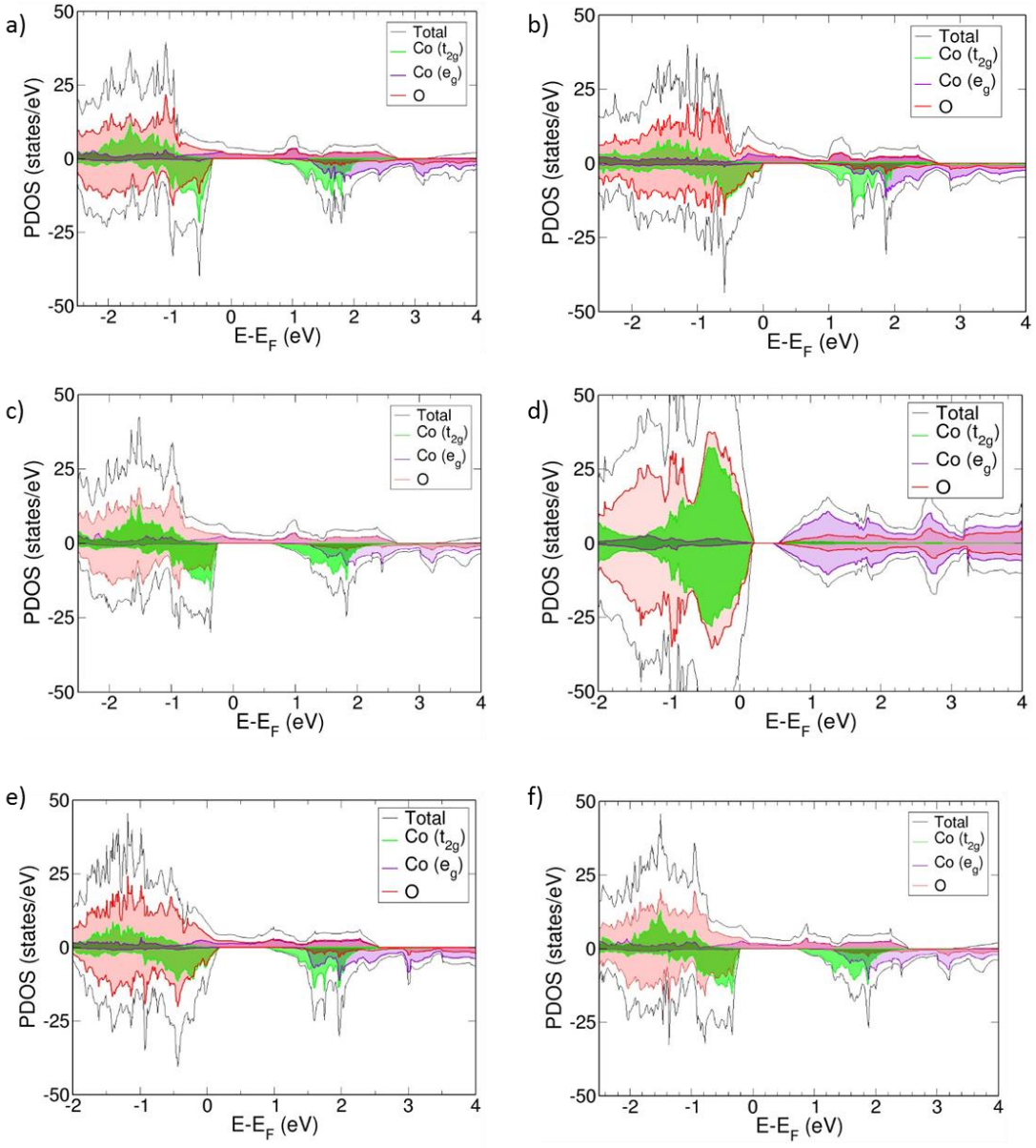

Figure 5.3. PDOS for a) $Sm_{0.75}Ca_{0.25}CoO_3$, b) $Sm_{0.50}Ca_{0.50}CoO_3$, c) $Sm_{0.75}Sr_{0.25}CoO_3$, d) $Sm_{0.50}Sr_{0.50}CoO_3$, e) $Sm_{0.75}Ba_{0.25}CoO_3$, and f) $Sm_{0.50}Ba_{0.50}CoO_3$. The Fermi level is at 0 eV, and negative $E-E_F$ represent the occupied bands and positive the virtual bands. Positive PDOS are associated with the α-spin, whereas negative PDOS are associated with β-spin.

For the V_O compensated systems, the PDOS are collected in Figure 5.4. Now, without exception, all systems become half-metallic, thus becoming electronic conductors. The VBM is a mixture of O 2*p*, Co t_{2g}, and Co e_g, as opposed to the

oxidized systems where Co e_g-states were mainly present at the CBM and above. Again, the conduction mainly occurs through the Co e_g-orbitals, which are hybridized with the O 2*p*-orbitals.

The presence of V_O induces different magnetic moments in the cobalt centres. Those who are next to the V_O keep the same magnetic moment observed in the oxidized systems, around 1.8 μ_B, whereas the rest of the cobalt atoms show different values, ranging from 0 to 2.2 μ_B. All Co magnetic moments are aligned, indicating that the doped systems with oxygen vacancies become ferromagnetic, (Table 5.3), and the mixing of μ_{Co} is in agreement with experimental results on doped $SmCoO_3$. [160]

The presence of V_O in the lattice gives different cobalt spin states within the system, but no difference in cobalt charge state, which has also been noted experimentally for x>0.2 (Table 5.3). [215] This finding would imply that the charge compensation is fully completed through V_O compensation, without negative charge remaining in V_O, similar to that demonstrated in chapter 4 for undoped $SmCoO_3$. However, the subtle difference in q_{Co} between the oxidized and V_O compensated systems is worth noting. The difference in total q_{Co} in the two different charge compensation schemes for the same A and x is, however, larger. $\Delta_{Ca,0.25}$=0.70 e, $\Delta_{Ca,0.50}$=0.91 e, $\Delta_{Sr,0.25}$=0.78 e, $\Delta_{Sr,0.50}$=0.33 e, $\Delta_{Ba,0.25}$=0.92 e, and $\Delta_{Ba,0.50}$=0.65 e. This could possibly indicate the presence of an electron hole on the cobalt atoms, but we would then expect charges closer to 2 e. Therefore, no clear conclusion can be drawn from the partition of the Bader charges.

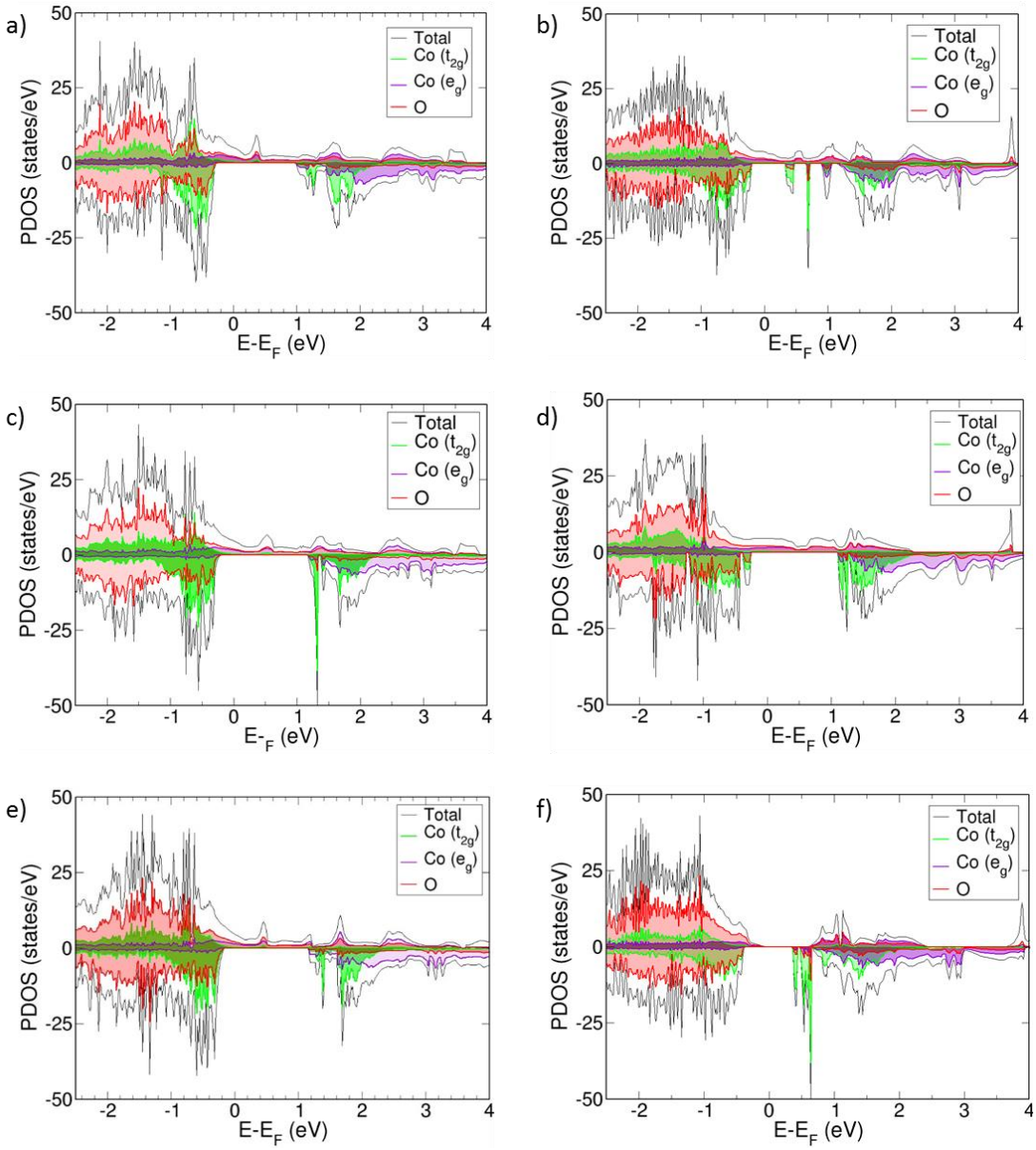

Figure 5.4. PDOS for a) $Sm_{0.75}Ca_{0.25}CoO_{2.88}$, b) $Sm_{0.50}Ca_{0.50}CoO_{2.75}$, c) $Sm_{0.75}Sr_{0.25}CoO_{2.88}$, d) $Sm_{0.50}Sr_{0.50}CoO_{2.75}$, e) $Sm_{0.75}Ba_{0.25}CoO_{2.88}$, and f) $Sm_{0.50}Ba_{0.50}CoO_{2.75}$. The Fermi level is at 0 eV, and negative E-E_F represent the occupied bands and positive the virtual bands. Positive PDOS are associated with the α-spin, whereas negative PDOS are associated with β-spin.

Table 5.3. Bader charges ($q_{Co,O}$ (e)), and cobalt magnetic moments ($\mu_{Co}(\mu_B)$) for $Sm_{1-x}A_xCoO_{3-x/2}$. A is dopant, * denotes ion next to V_O (nearest neighbor). Sm, A, and O magnetic moments were found to be negligible in comparison to cobalt and are thus not included. $\mu_{Co,SmCoO3} = 0\ \mu_B$, $q_{Co,\ SmCoO3}$=1.31 e, and $q_{O,\ SmCoO3}$=-1.11 e.

A		$Sm_{0.75}A_{0.25}CoO_3$	$Sm_{0.75}A_{0.25}CoO_{2.88}$	$Sm_{0.5}A_{0.5}CoO_3$	$Sm_{0.5}A_{0.5}CoO_{2.75}$
Ca	μ_{Co}	1.8	0.13, 2.1	1.7	0.1, 2.0, 2.1
	μ_{Co}^*		1.8		1.9, 2.0, 2.6
	q_{Co}	1.36	1.21-1.32	1.36	1.23-1.32
	q_{Co}^*		1.25		1.05-1.33
	q_O	-1.11±0.02	-1.13±0.1	-1.07±0.02	-1.11±0.07
Sr	μ_{Co}	1.8	0.1, 2.1	0.01, 0.03, 0.04, 0.05	1.8, 2.0, 1.9, 2.2
	μ_{Co}^*		1.8		1.9, 2.1
	q_{Co}	1.38	1.23-1.32	1.33	1.32-1.37
	q_{Co}^*		1.26		1.14-1.24
	q_O	-1.12±0.02	-1.13±0.06	-1.05±0.02	-1.14±0.06
Ba	μ_{Co}	1.9	0.1, 2.1, 2.2	1.9	2.4, 3.1, 2.1, 0.4
	μ_{Co}^*		1.7		2.3, 2.0
	q_{Co}	1.40	1.22-1.30	1.40	1.28-1.48
	q_{Co}^*		1.29		1.22-1.26
	q_O	-1.13±0.03	-1.14±0.1	-1.09±0.04	-1.15±0.1

Since the analysis of the density of states, and the variation of the cobalt magnetic moments and Bader charges do not provide clear evidence of the actual existence of an electron hole to compensate the charge of the system, we have examined their possible presence by calculating the charge density difference ($\Delta\rho$) according to equation 5.3.

$$\Delta\rho = \rho_{Sm_{1-x}A_xCoO_{3-x/2}} + n\rho_o - \rho_{Sm_{1-x}A_xCoO_3} \quad (5.3)$$

where ρ is the charge density and n the number of V_O in lattice. If there is an electronic hole, it should be represented as a depletion in the charge density plot. According to Figure 5.5, however, $\Delta\rho$ is mainly centered on the oxygen ions, indicating that the variation in charge density is located on the oxygen sub-lattice. Although we can observe charge depletion close to the cobalt centres, this is not enough to fully verify the presence of electron holes on the cobalt atoms. Furthermore, the charge density difference illustrates a rearrangement of charges rather than a proper electron hole. We also considered hole compensation in terms of the formation of O^-, by comparing the lattice relaxation around the oxygen nearest to the dopants. This formation energy can be obtained by calculating the difference in total energy between the fully relaxed localized polaron state, and the hole state in the perfect undistorted lattice, *i.e.* unrelaxed system.[216,217] From these calculations, we found that the hole polaron formation is 0.62 eV for x_{Ca}=0.25, 0.95 eV for x_{Ca}=0.50, 0.92 eV for x_{sr}=0.25, 0.78 eV for x_{Sr}=0.50, 1.06 eV for x_{Ba}=0.25, and 0.60 eV for x_{Ba}=0.50. These formation energies are significantly higher than the oxygen vacancy formation energy, as will be seen below in Table 5.4, and as such while hole formation could be expected to occur at SOFC operating temperature, it will always represent a minority reaction pathway when compared to vacancy formation.

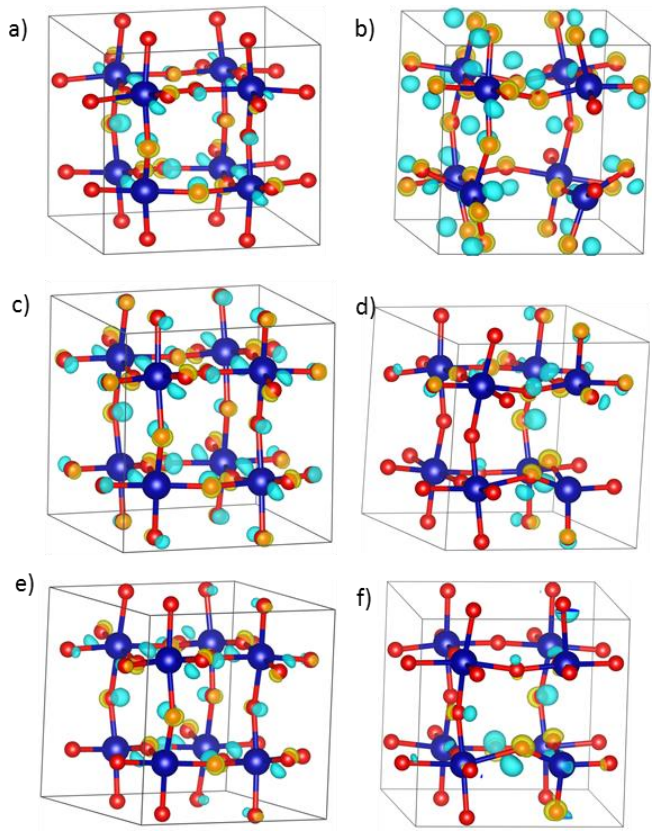

Figure 5.5. Charge density difference for a) x_{Ca}=0.25, b) x_{Ca}=0.5, c) x_{Sr}=0.25, d) x_{Sr}=0.5, e) x_{Ba}=0.25, and f) x_{Ba}=0.5. Isosurface value is 0.5. Yellow isosurface is positive $\Delta\rho$ (gain of charge), and blue is negative $\Delta\rho$ (depletion of charge).

The question still remains though, why A^{2+}-doped $SmCoO_3$ becomes an electronic conductor. The key to understand this behaviour can be seen in $Sm_{0.50}Sr_{0.50}CoO_3$, which is almost diamagnetic and still shows e_g/t_{2g} splitting. Examining the geometric structure of $Sm_{0.50}Sr_{0.50}CoO_3$, we realize that there are no distortions in the Co-O bond lengths (Table 5.2), and thus no CoO_6-octahedral distortions. Therefore, the crystal field theory splitting can still be applied, which explains why $Sm_{0.50}Sr_{0.50}CoO_3$ has not become at least half metallic. From this finding, we can conclude that any doping that induces structural distortion in $SmCoO_3$, will alter the electronic structure, *i.e*. will break the crystal field splitting, and the Co *d*-orbitals will be closer in energy, as well as more hybridized with O *2p*-orbitals,

turning the system into an electrical conductor. To prove this, hypothesis we calculated the 0 K electronic conductivity (σ_e) for all $Sm_{1-x}A_xCoO_3$, and plotted them as a function of Co-O bond length variance. The variance was set as the difference between the shortest and the longest Co-O distance, according to Table 5.2. The larger the spread in Co-O bond lengths, the higher the electronic conductivity. The trend is presented in Figure 5.6. Although it is not a perfect linear dependence, it is indicative enough to conclude that conductivity in Sm-site doped $SmCoO_3$ is a direct consequence of the distortion induced by doping the system, rather than being a consequence of any electron hole.

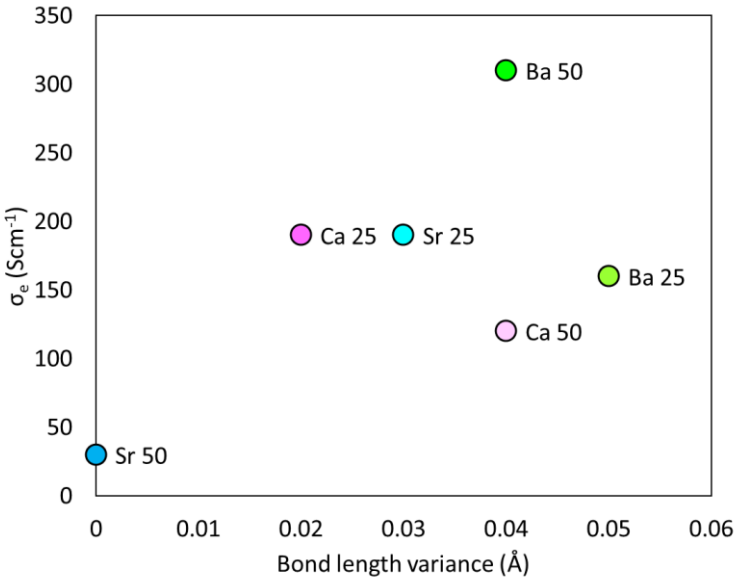

Figure 5.6. Electronic conduction plotted against Co-O bond length variance within the systems.

5.5 Oxygen Vacancy Formation Energy

To calculate $E_f^{V_O}$,we have again employed the method developed by Zhang and Northrup (eq. 5.4), which have been widely utilised to evaluate $E_f^{V_O}$ in similar systems. [48,211,218]

$$E_f = E_{Defective} - E_{Perfect} + \sum_i n_O \mu_O \quad (5.4)$$

where $E_{Defective}$ is the total energy of the defective system, $E_{Perfect}$ is the total energy of the non-defective system; n_o is the number of removed or added oxygen ions from the bulk, and μ_o is the oxygen chemical potential. For V_O we consider an O-rich situation, which for $SmCoO_3$ equals to $\mu_O = \frac{1}{2}E_{O_2}$-0.5. This approach has been successfully employed to perovskite systems in other computational studies. [211] It is worth noting that the introduction of dopants in the system is assumed to not affect the chemical potential for oxygen. Furthermore, DFT overestimates the oxygen binding energy, and with how much is dependent on several computational parameters.[19] Including the oxygen overpotential correction here, based on those corrections used in previous studies,[212] does not however influence the results presented, in terms of all oxygen vacancy formation energies being negative, and much lower in energy than the hole compensation scheme[19,219] Furthermore, we have neglected thermal, vibrational, and entropic contributions, as these are commonly known to be smaller than the typical DFT error.[114,197] Below follows a graphical summary of all the different vacancy configurations and their E_f.

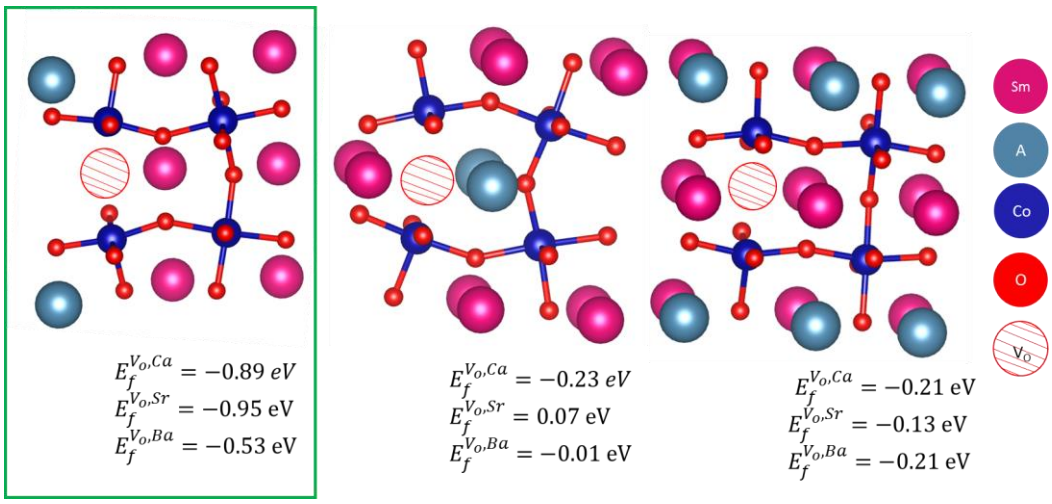

Figure 5.7. V_O configurations for $Sm_{0.75}A_{0.25}CoO_{2.88}$ with noted E_f. Green rectangle notes lowest E_f.

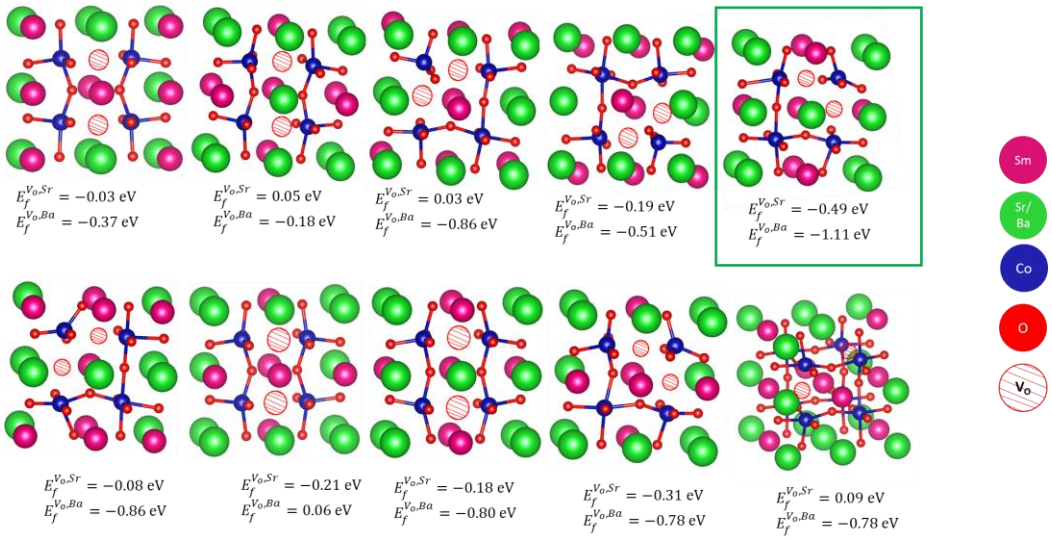

Figure 5.8. V_O configurations for $Sm_{0.5}A_{025}CoO_{2.75}$ (A=Sr, Ba) with noted E_f. Green rectangle notes lowest E_f.

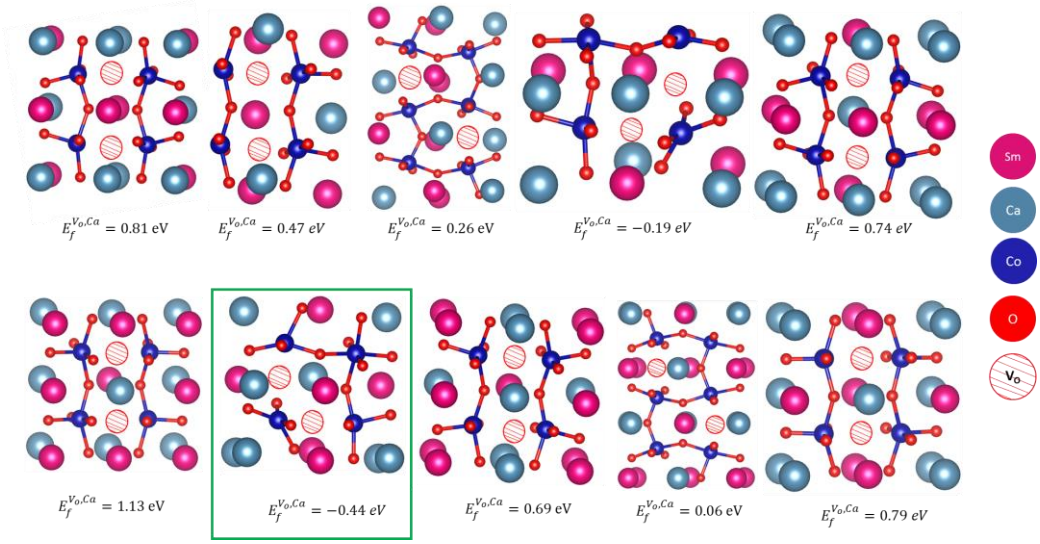

Figure 5.9. V_O configurations for $Sm_{0.5}Ca_{025}CoO_{2.75}$ with noted E_f. Green rectangle notes lowest E_f.

Table 5.4. Oxygen vacancy formation energy (E_f^{Vo}) for the most stable configuration.

System	E_f^{Vo}, x=0.25 (eV)	E_f^{Vo}, x=0.50 (eV)
$Ca_xSm_{1-x}CoO_{3-x/2}$	-1.39	-0.44
$Sr_xSm_{1-x}CoO_{3-x/2}$	-0.95	-0.49
$Ba_xSm_{1-x}CoO_{3-x/2}$	-0.53	-1.11

V_O formation in these doped materials is spontaneous, *i.e.* negative E_f^{Vo}, as expected considering the oxygen vacancy charge compensation scheme, and as mentioned for the hole compensation, there appear to exist dopant-size effects when the systems get more $ACoO_3$ character at the higher dopant concentration, leading to opposing trends in E_f^{Vo} at the higher concentration. This trend has previously been observed for $AMnO_3$, with E_f^{Vo} decreasing going from $CaMnO_3$, *via* $SrMnO_3$, and to $BaMnO_3$.[220] However, as all E_f^{Vo} are negative, the effect

would not be noticeably different between the different materials. The negative E_f^{Vo} does furthermore indicate that oxygen spontaneously could leave the lattice, which would eventually lead to material breakdown. The occurrence of this is previously known in literature to occur at high temperatures, but with these high temperatures being outside the IT-SOFC range.[87,168] It is also worth noting that the oxygen vacancy formation energies (corresponding to equation 1) are much lower in all cases than the hole formation energies (corresponding to equation 2), which indicates that oxygen vacancy formation is the most probable compensation scheme under equilibrium conditions.

Compared to $SmCoO_3$, which had an E_f^{Vo} =2.08 eV, we can conclude that doping clearly favours the formation of spontaneous vacancies. It is also worth mentioning that at high temperatures, $SmCoO_3$ has a C-type antiferromagnetic structure. Thus, we also calculated E_f^{Vo} for this high-temperature structure, and found this to be 1.43 eV. Furthermore, for comparison, we calculated E_f^{Vo} for the traditional high-temperature SOFC cathode material $La_{0.75}Sr_{0.25}MnO_{3-d}$ (LSM), which is 1.82 eV. We thus see that V_O formation in $Sm_{1-x}A_xCoO_{3-x/2}$ is energetically more favourable than in LSM. Thus, all of these systems show excellent potential as ionic conductors, but these results are not conclusive as to which x or A^{2+} leads to the highest oxygen conduction. Next, MD is used to evaluate the oxygen diffusion and ionic conduction. Please note that all the results below are for the systems in the V_O compensated scheme.

5.6 Dopant-Vacancy Association Energy

Another important property to assess is the dopant-V_O-cluster interaction energy (*E^{int}*), which is calculated (eq 5.5) as the difference in E_f of the defect cluster (E_f^{pair}), and the sum of E_f for the two individual defects ($E_f^{isolated\ defects}$). [188]

$$E^{int} = E_f^{pair} - \sum E_f^{isolated\ defects} \tag{5.5}$$

The individual components of equation 5.5 are comprised of equation 5.6-8.

$$E_f^{pair} = E_{Sm_{1-x}Ca_xCoO_{3-x/2}} + \frac{x}{2}\mu_O + x\mu_{Sm} - x\mu_A - E_{SmCoO_3} \tag{5.6}$$

$$E_f^{A_{Sm}} = E_{Sm_{1-x}Ca_xCoO_3} + x\mu_{Sm} - x\mu_A - E_{SmCoO_3} \tag{5.7}$$

$$E_f^{V_O} = E_{SmCoO_{3-x/2}} + \frac{x}{2}\mu_O - E_{SmCoO_3} \tag{5.8}$$

Negative values (*e.g.* -0.67 eV for Ca-doping) indicate an energetic benefit for the defects to be associated, whereas positive values (*e.g.* 0.06 eV for Sr-doping and 0.20 eV for Ba-doping) indicate the tendency for the defects to dissociate. Thus, trapping of V_O may occur near a Ca-dopant site at low temperatures, although at operating temperatures, either intermediate or high, this barrier will be easy to overcome and should not noticeably influence oxygen migration.

5.7 Oxygen Migration and Conduction

Diffusion in these materials have been calculated from the mean square displacements. According to the MSD representation depicted in Figure 5.10,

cation diffusion is limited and reaches equilibrium shortly after equilibration, whereas the oxygen MSD clearly increases with time. Only one example has been included here, as all systems showed the same characteristics, and a high temperature was chosen as to show that even at the higher temperatures, cation diffusion is negligible in relation to oxygen diffusion (D_O).

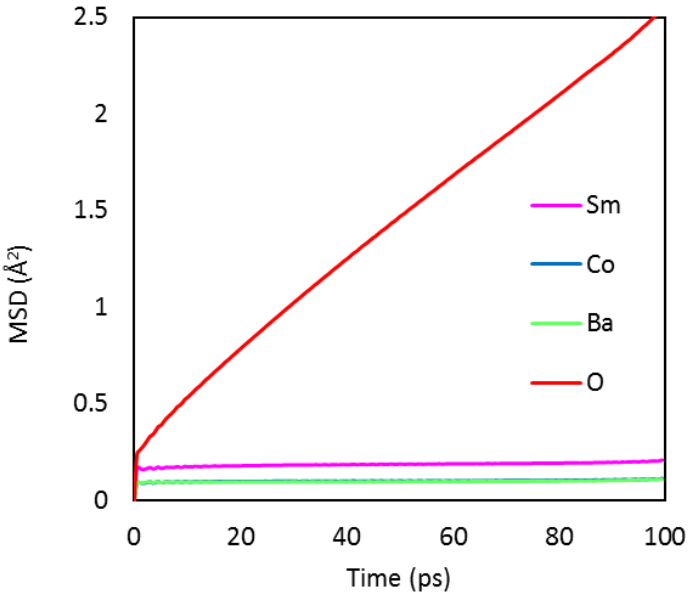

Figure 5.10. Mean square displacement graph for $Sm_{0.75}Ba_{0.25}CoO_{2.88}$ at 1500 K

D_O for oxygen was calculated according to equations 2.45-46, and showed that in general the highest oxygen diffusion is found at temperatures higher than 1000 K, and for $Ca_xSm_{1-x}CoO_{3-x/2}$ at 1500 K. Moreover, all materials show higher oxygen diffusion (even at low temperatures) than the traditional cathode material $La_{0.5}Sr_{0.5}MnO_{3-d}$, which has a experimentally measured D_O of 3×10^{-12} cm^2s^{-1} at 900°C (1173 K), [74] as compared to the calculated value of 2.87×10^{-7} cm^2s^{-1} for $Sm_{0.5}Ca_{0.5}CoO_{2.75}$ at 1200 K (Table 5.5).

Table 5.5. Oxygen diffusion coefficients (D_O) for the different dopant systems, at two dopant concentrations (x), and different temperatures (T).

System	T (K)	$\boldsymbol{D_O}$ (cm^2s^{-1})	
		x=0.25	x=0.50
$Ba_xSm_{1-x}CoO_{3-x/2}$	800	2.06×10^{-8}	5.52×10^{-8}
	1000	6.63×10^{-8}	1.11×10^{-7}
	1200	1.26×10^{-7}	2.08×10^{-7}
	1500	3.69×10^{-7}	4.83×10^{-7}
$Ca_xSm_{1-x}CoO_{3-x/2}$	800	4.27×10^{-8}	6.68×10^{-8}
	1000	1.10×10^{-7}	1.32×10^{-7}
	1200	2.77×10^{-7}	2.49×10^{-7}
	1500	8.40×10^{-7}	7.46×10^{-7}
$Sr_xSm_{1-x}CoO_{3-x/2}$	800	3.84×10^{-8}	7.03×10^{-8}
	1000	9.70×10^{-8}	1.39×10^{-7}
	1200	2.21×10^{-7}	2.87×10^{-7}
	1500	6.80×10^{-7}	7.73×10^{-7}

The highest oxygen diffusion is reached when the system is doped with Ca^{2+}, which can be explained by the fact that Ca^{2+} is also the system with the smallest of the tested dopants. Relating diffusion to activation energy (Figure 5.11 and Table 5.6), E_a decreases with increasing x, indicating that higher dopant concentrations favour oxygen migration, as has previously been reported for Sr-doping of $LaMnO_3$ and $LaCoO_3$. [75]

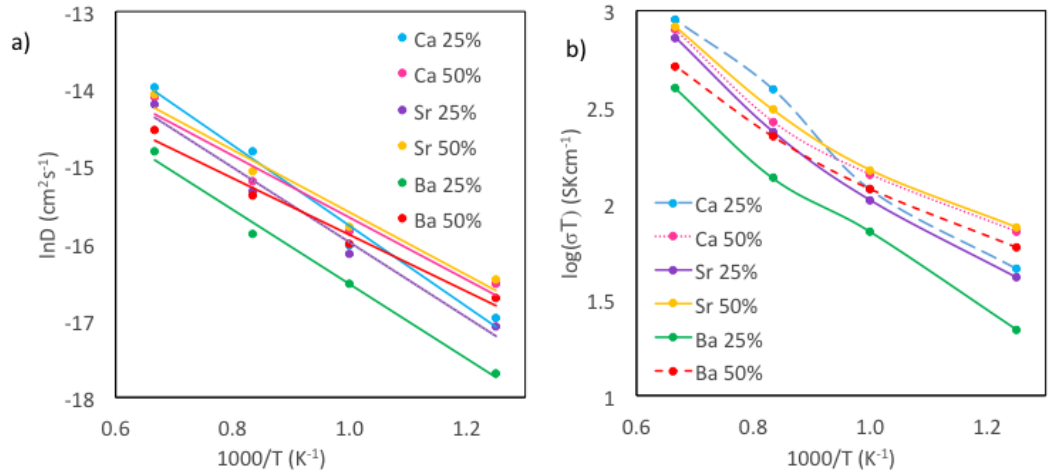

Figure 5.11. a) Arrhenius plots for oxygen diffusion, and b) ionic conductivity for $Ca_xSm_{1-x}CoO_{3-d}$, $Ba_xSm_{1-x}CoO_{3-d}$ and $Sr_xSm_{1-x}CoO_{3-d}$. Temperature range is 800-1500 K.

Table 5.6. Oxygen diffusion activation energies (eV) for temperature range 800-1500 K.

System	E_a , x=0.25 (eV)	E_a , x=0.50 (eV)
$Ba_xSm_{1-x}CoO_{3-d}$	0.42	0.32
$Ca_xSm_{1-x}CoO_{3-d}$	0.45	0.36
$Sr_xSm_{1-x}CoO_{3-d}$	0.42	0.35
$SmCoO_3$	0.93	

Ionic conduction (σ_O) is challenging to measure experimentally since both electronic and ionic conductivities are normally hard to differentiate. [35] Thus, theoretical calculations have proved to be very useful in directly comparing σ_O between different systems. σ_O is calculated from D_O through the Nernst-Einstein equation [35] (eq. 5.9).

$$\sigma_O = \frac{C_O q^2 D_O}{k_B T} \tag{5.9}$$

where C_O is the oxygen concentration, and q the charge of oxygen. The ionic conductivities of the different systems are plotted in Figure 5.11b, which are comparable to experimental studies conducted by Yeh *et al.* on $Sm_{0.5}Sr_{0.5}CoO_{2.75}$, which gave $\log(\sigma_O T)$ between 0 and 2 for a temperature range of 700-1000 K (please note these values have been read from a graph). [35] Furthermore, the ionic conductivities of these materials are close to those of SOFC electrolytes GDC and YSZ, which are excellent oxygen conductors. [35] Thus, all systems investigated here have good oxygen conductivity for SOFC purposes. Specifically, the systems showing highest ionic conductivity at IT-SOFC temperatures are $Sm_{0.5}Sr_{0.5}CoO_{2.75}$, $Sm_{0.5}Ca_{0.5}CoO_{2.75}$ and $Sm_{0.75}Ca_{0.25}CoO_{2.83}$.

5.8 Thermal Expansion Coefficient

In addition to ionic conductivity, another vital property of SOFC cathodes is the thermal expansion coefficient (TEC), calculated from equation 2.47. The cathode requires a TEC that is compatible with the electrolyte, as incompatibility will lead to SOFC cell breakdown. Common SOFC electrolytes include YSZ, LSGM, and GDC, which have TEC of 10.0-12.5×10^{-6} K^{-1}. [32] TEC for $SmCoO_3$ (17.7×10^{-6} K^{-1}) itself is incompatible with these electrolytes, and thus to reduce TEC, doping is vital. [87] DFT+U results showed that the lattice volume increases with increasing x, thus inducing negative chemical pressure, as all dopants have a higher ionic radius than Sm^{3+}; Sm^{3+}(0.96 Å)<Ca^{2+}(1.00 Å)<Sr^{2+}(1.18 Å)<Ba^{2+}(1.35Å). [221] The largest volume increase for all x is seen for Ba^{2+}, and the least for Ca^{2+}, which behaviour has previously been reported in molecular dynamics studies of Sr-doped $SmCoO_3$. [77] The volume expansion in relation to temperature was then

calculated with MD, and the linear thermal expansion coefficient extracted (Table 5.7).

Table 5.7. Linear thermal expansion coefficient. Orthorhombic $SmCoO_3$ has an experimental linear thermal expansion coefficient of 21.7×10^{-6} K^{-1}. [168]

System	TEC, x=0.25 (10^{-6} K^{-1})	TEC, x=0.50 (10^{-6} K^{-1})
$Ca_xSm_{1-x}CoO_{3-d}$	23.3	24.2
$Sr_xSm_{1-x}CoO_{3-d}$	22.7	30.9
$Ba_xSm_{1-x}CoO_{3-d}$	23.7	30.0
	TEC, x=0 (10^{-6} K^{-1})	
$SmCoO_3$	17.1	

The TECs are in alignment with previous results for cobalt-based SOFC cathodes, which normally have higher TEC than SOFC electrolytes. [32] To overcome this incompatibility between these cathodes and traditional electrolytes, Co-site doping with transition metals might be necessary. Such doping has been shown to decrease cathode TEC in for example $La_{1-x}Sr_xCoO_{3-x/2}$. [222]

Comparing all the above calculated properties of $Sm_{1-x}A_xCoO_{3-x/2}$, it can be seen that Ca-doping gives the highest D_O, among the lowest E_a, highest ionic conduction, and more compatible TEC at intermediate temperatures (800-1000 K). Sr-doping, however, gives higher ionic conduction at lower temperature (x=0.50), but due to this composition a much higher TEC. Thus, Ca-doping might be more practical for IT-SOFC cathode applications.

5.9 Chapter Conclusions

The electronic properties and ionic conduction of $Sm_{1-x}A_xCoO_{3-}$ and $Sm_{1-x}A_xCoO_{3-x/2}$ (A=Ca, Sr, Ba, and x=0.25, 0.5) have been modelled using DFT+U and MD calculations. Evaluation of two charge compensation schemes suggests that oxygen vacancy compensation is the more likely for these materials. Furthermore, the change in electronic structure upon doping has been linked directly to distortions in the Co-O bonds. Structural distortions break the octahedral crystal field splitting, which provokes a spin transition in Co that leads to a change in the electronic structure, making the doped $SmCoO_3$ a conductor.

However, we have found that the ionic conductivity in doped $SmCoO_3$ is two times higher at intermediate temperatures than in LSM, with Ca^{2+}, x=0.25, reporting the best results, in agreement with experimental findings. Finally, thermal expansion coefficients were also calculated, and were found to be in the same range as lanthanum-based cathode materials, but still too high for perfect compatibility with the traditional electrolyte materials. One way to overcome this deficiency could be the introduction of additional Co-site dopants, which is the topic of the next chapter.

Chapter 6

Co-site Substitutional Doping of with Fe^{3+}, Mn^{3+}, Ni^{3+}, and Cu^{3+}

Abstract

Doping in the Co-site is suggested to improve the catalytic and electronic properties of $SmCoO_3$, with Fe^{3+}, Mn^{3+}, Ni^{3+}, and Cu^{3+} as proposed dopants. Although some experimental research has been done on these materials, here we present a systematic DFT + U study focused on the electronic, magnetic, and some physical properties for the doped $SmCoO_3$ with these dopants at different concentrations. So far, in the majority of the cases, doping induces distortion in the system, inducing different electron occupations of the Co *d*-orbitals, thus altering the electronic and magnetic structure. From these calculations, the 0 K electronic conductivity (σ_e) was calculated, with $SmMn_xCo_{1-x}O_3$ having highest σ_e, and $SmFe_xCo_{1-x}O_3$ lowest, in line with previous experimental findings. We have also investigated the impact of the doping in the oxygen vacancy formation energy (E_f), which is related to the ionic conductivity (σ_O),and we found that only when $SmCoO_3$ is doped with Cu or Ni, the E_f are lowered, as a consequence of the instability of the +3 valence. Finally, thermal expansion coefficients were calculated through molecular dynamics calculations, with Mn^{3+} doping showing the most decrease at low x, and at x=0.75. From these results, it was reasoned that Mn^{3+} doping at x=0.125, or 0.25, would be most favourable to improve $SmCoO_3$ performance as an IT-SOFC cathode material.

6.1 Introduction

Doping $SmCoO_3$ on the Co-site can increase σ_e by modifying the electronic structure of the perovskite, and transition metal (B) doped samarium oxide perovskites have experimentally shown excellent promise as IT-SOFC cathodes. [87] Fullarton *et al.* discovered already in 1995 that partial substitution on Sm- and/or Co-sites in $SmCoO_3$ greatly improves $\sigma_{O.}$ [18] In combination with this, substitutional Co-site doping of $SmCoO_3$ with B^{3+} could increase σ_e, by making the materials become metallic and magnetic, as well as having an impact in the thermal expansion coefficient by decreasing it. [78,153] For example, Mn-doping of $SmCoO_3$-type cathode materials have been experimentally shown to decrease TEC, alter the catalytic properties, and increase conduction, properties that have also been showed for La-based systems. [73] Fe, Ni, and Cu doping have been suggested to greatly modify the oxygen diffusion, oxygen surface-to-bulk incorporation, and the oxygen reduction catalytic activity of $SmCoO_3$. [18] Ni-doped $SmCoO_3$ has also been shown experimentally to alter the electronic conduction, and are able to accommodate oxygen deficiency. [153] Furthermore, Ni, Fe, and Mn-doping have also been shown to readily reduce TEC $SmCoO_3$-based cathode materials. [29,87]

On the other hand, the full substitution of Co by the dopants leads to completely different types of perovskite materials ($SmBO_3$), on which, compared to $LaBO_3$, not many experimental, and only some theoretical studies, have been conducted. Previous computational research has been focused on $SmFeO_3$ [223–226] and $SmMnO_3$ [227,228] and information on $SmNiO_3$ and $SmCuO_3$ is scarce. Both $SmNiO_3$ and $SmCuO_3$ are thermodynamically unstable, due to the nickel and copper charge state easily reducing from +3 to +2. Thus, these are often found in their oxygen

deficient form. [26,229–232] However, they have both been included here as they have been proposed to readily decrease TEC in La-based cathodes and as possible dopants in $SmCoO_3$. [18,26]

In this chapter, a systematic study of the Co-substitution with Mn, Fe, Ni, and Cu, at different concentrations, as well as the fully substituted $SmBO_3$ pseudo-cubic structures, is presented. Special attention is paid to the influence of dopant concentration on the electronic and magnetic structure, electronic and ionic conductivity, as well as on the thermal expansion coefficients. In addition, the energetics and electronic effect of the oxygen vacancy formation is investigated.

6.2 Computational Details

All calculations in this chapter were performed using the Vienna *ab initio* simulation package, VASP (version 5.3.5). [92–95] We applied the projector-augmented wave method (PAW) to describe the ion-electron interaction, [123] and based on convergence tests, the energy cut-offs for all systems were set to 500 eV. Spin-polarized calculations were executed using the Perdew-Burke-Ernzerhof (PBE) [107,108] functional under electronic (convergence criteria of 10^{-5} eV) and ionic (convergence criteria of 10^{-3} eV·Å^{-1}) self-consistence.

The following valence electrons for the atomic species involved were considered: Sm ($5s^25p^66s^2$), Mn ($3p^63d^64s^1$), Fe ($3p^63d^64s^2$), Co ($4s^23d^7$), Ni ($4s^23d^8$), Cu ($4s^13d^{10}$), and O ($2s^22p^4$). Furthermore, the tetrahedron method with Blöchl corrections for smearing [117] was applied together with a 4x4x4 Γ-centred Monkhorst-Pack grid.

[118] Bader AIM (Atoms in Molecules) charges [130] were calculated using the Henkelman algorithm. [185]

To describe electronic structure, we have used the on-site Coulombic interaction (DFT+U) for the B 3*d*-electrons. Normal exchange correlation functionals (LDA, or GGA) cannot correct the electron self-interaction problem, leading to a metallic description of perovskites or an underestimation of their band gaps. [65,110,111] In this work, we have employed Dudarev's approach, [109] in which an effective Hubbard parameter (U_{eff}) is fitted empirically. The U_{eff}-parameter for B in perovskites have been fitted and tested elsewhere. For Mn U_{eff} = 4 eV [19], for Fe U_{eff} =4.3 eV [212], Co U_{eff} = 3 eV, Ni U_{eff} = 6.4 eV [19], and Cu U_{eff} = 3 eV [233], respectively.

The electronic conductivity is calculated in VASP for the 0 K optimized structures from the frequency dependent dielectric matrix. The electronic conductivity is dependent on relaxation time. Normally, this parameter would be fitted to experimental data, but due to the lack of such data, we have here employed the same relaxation time (0.12 fs) for all calculations. This relaxation time is in line with previous work on electronic conductivity in cobaltates. [234] Thus, the electronic conductivities calculated here should serve as a guide only, until such a point as the validity of this approximation can be verified through corresponding experimental data.

The supercell used throughout this chapter is the 2×2×2 Pm-3m pseudo cubic cell, as this was found to be large enough to model bulk properties and defect structures within computationally reasonable resources. Perovskites normally crystallize in an orthorhombic structure, but under SOFC and IT-SOFC working conditions (*i.e.* high-

temperatures), these materials are found in the pseudocubic structure, and all $SmBO_3$ are isostructural in this respect.

TEC were calculated using molecular dynamics (MD) in the DL_POLY 4 program. [96] A 20x20x20 supercell based on the DFT+U optimized $SmB_xCo_{1-x}O_3$ structures were simulated under NPT conditions, with a Nosé-Hoover thermostat. [139] All statistics were collected after a 10 ps system equilibration, with a 100 ps production phase and a time step of 0.1 fs. To account for electrostatic interactions, Ewald summation was employed, and the Verlet algorithm evaluated the atomic motions. Short-range atomic interactions were calculated with Buckingham potentials (equation 2.41), which are based on the Born model for ionic solids. [75,142,235] To describe the electronic polarization of the atoms (α), the shell model is included, with the interatomic potential library presented in Table 2.2.

6.3 Dopant Configuration

As a first step, the non-equivalent dopant configurations in $SmB_xCo_{1-x}O_3$ were evaluated using the Site-Occupancy Disorder Program (SOD) [214]. The 2×2×2 supercell includes eight Co^{3+} lattice positions, thus a substitution of one Co^{3+} for B^{3+} represents a dopant concentration of x=0.125 (from which only one non-equivalent structure can be found), two Co^{3+} substitutions for x=0.25, four substitutions for x=0.50, and finally in x=0.75 we have two Co^{3+} and six B^{3+}. Three inequivalent configurations for x=0.25 and 0.75 were found, and six for x=0.5, respectively. The different $SmB_xCo_{1-x}O_3$ configurations were optimized with VASP, with their relative energies collected in Table 6.1, whereupon the lowest energy configuration were the ones selected for further study (Figure 6.1).

Table 6.1. Energy difference (in eV) between different dopant configurations. x=0.125, and 1.0 are not included as they only have one possible inequivalent configuration.

	Conf. No.	Mn	Fe	Ni	Cu
x=0.25	1	0.00	0.00	0.00	0.00
	2	0.56	0.43	0.41	0.10
	3	0.97	0.68	0.50	0.38
x=0.50	1	0.00	0.00	0.00	0.00
	2	0.27	0.84	0.43	0.14
	3	0.30	0.85	0.85	0.23
	4	0.30	1.30	0.91	0.32
	5	0.36	1.34	1.15	0.50
	6	0.47	1.59	1.96	1.48
x=0.75	1	0.00	0.00	0.00	0.00
	2	0.11	0.26	1.00	0.40
	3	0.16	0.43	2.23	0.52

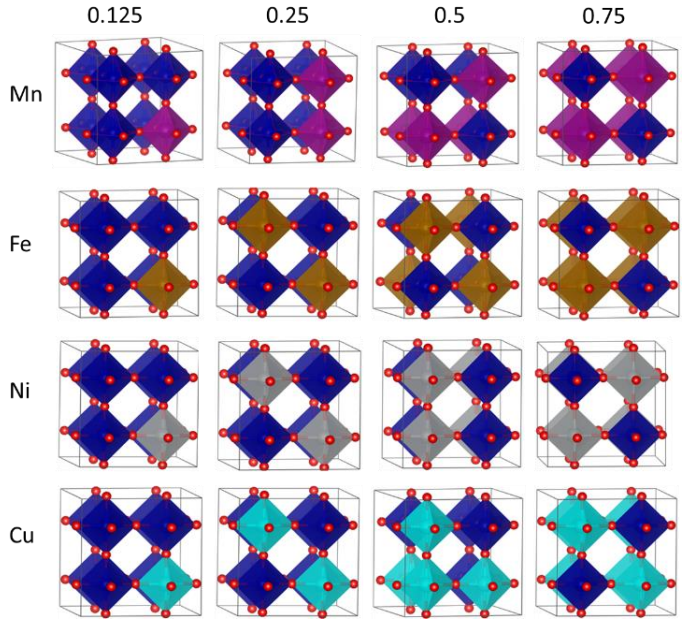

Figure 6.1. Polyhedral representation of the lowest energy dopant configurations. First row is B = Mn^{3+} (purple), second B = Fe^{3+} (brown), third B = Ni^{3+} (grey), and fourth is B = Cu^{3+} (turquoise), with Co represented in dark blue, and red spheres are the oxygen atoms. Sm^{3+} has been omitted for clarity. Columns represent the concentration, which from left to right are x=0.125, 0.25, 0.5, and 0.75 respectively.

In addition, and to further understand the trends in $SmB_xCo_{1-x}O_3$, we also studied the $SmBO_3$ perovskites. Cubic $Sm\mathit{B}O_3$ perovskites are isostructural, with differences in the B-O bond lengths ranging from 0 to 0.6 Å related to the difference in B ionic radii between the materials (Table 6.2) and differences in lattice parameter being observed over the periodic series (Table 6.3). This is to be expected as the nature of B, in terms of ionic radii, and electronegativity will influence the chemistry and physical properties of these materials.

Table 6.2. B-O bond lengths (Å) in SmBxCo1-xO3. Co-O in $SmCoO_3$ is 1.88 Å.

B		**x=0.125**	**x=0.25**	**x=0.5**	**x=0.75**	**x=1.00**
Mn	Mn-O	1.90	1.89, 1.91	1.88, 1.91, 1.93, 1.94	1.90, 1.92, 1.95, 1.96	1.94
	Co-O	1.87, 1.88, 1.89	1.87, 1.89	1.88, 1.90, 1.94, 1.95	1.88, 1.89	
Fe	Fe-O	1.90	1.92, 1.93	1.94	1.90, 1.92, 1.93, 1.95, 1.96, 1.97	1.94
	Co-O	1.86, 1.88, 1.89	1.85, 1.86, 1.88, 1.89, 1.90	1.87	1.88, 1.89	
Ni	Ni-O	1.93	1.93, 1.94	1.91, 1.93	1.84, 1.86, 1.92, 1.93, 1.94	1.88
	Co-O	1.86, 1.88, 1.91, 1.93	1.84, 1.87, 1.88, 1.89, 1.90	1.84, 1.91	1.83, 1.87	
Cu	Cu-O	1.90	1.89, 1.96	1.89, 1.90, 1.94	1.89, 1.90, 1.91, 1.92	1.90
	Co-O	1.86, 1.88	1.85, 1.87, 1.90, 1.93,	1.85, 1.89, 1.90	1.87, 1.90	

6.4 Electronic and magnetic structures

Co^{3+} and B^{3+} can exist in different spin states, depending on the *d*-orbital occupation. Co^{3+} ($3d^6$) has a low spin ground state (LS, $t_{2g}^6 e_g^0$), and thus a negligible magnetic moment (μ) of 0 μ_B. [160] However, upon distortion of the CoO_6-octahedra, the Co^{3+} *d*-orbital occupation can be altered, resulting in different spin states, specifically intermediate (IS, $t_{2g}^5 e_g^1$) or high (HS, $t_{2g}^4 e_g^2$), thus modifying the magnetic properties of the system. In addition, the dopants considered in this work can also present different *d*-orbital occupations (Mn^{3+} ($3d^4$), Fe^{3+} ($3d^5$), Ni^{3+} ($3d^7$), and Cu^{3+} ($3d^8$)), and consequently different spin states. [19,38]

Consequently, the spin arrangement is important as it determines the magnetic structure of the material. Three general magnetic structures are possible: non-magnetic (NM), antiferromagnetic (AFM), and ferromagnetic (FM). Additionally, AFM can be presented in different configurations: C-type, A-type, and G-type, all of them schematically represented in Figure 3.3. We evaluated all the magnetic structures for all dopants and concentrations. Interestingly, almost all $SmB_xCo_{1-x}O_3$ only converged for the FM structure, and no AFM nor NM structures could be converged, with two exceptions. $SmCu_{0.5}Co_{0.5}O_3$ and $SmCu_{0.75}Co_{0.25}O_3$, converged only for the GAFM structure, clearly indicating the preference of these systems for the ferromagnetic structure (Table 6.3).

Table 6.3. Lattice parameter (a) in Å, local magnetic moments (μ) in μ_B for dopant and cobalt, band gap (E_g) in eV, and magnetic ordering in $SmB_xCo_{1-x}O_3$. a for $SmCoO_3$ is 3.75 Å, q_{Co} in $SmCoO_3$ is 1.31 e.

B		x=0.125	x=0.25	x=0.5	x=0.75	x=1.0
Mn	a	3.76	3.78	3.83	3.85	3.87 (3.89) [228]
	μ_{Mn}	3.4	3.5	3.5	3.8	3.9
	μ_{Co}	0.2, 0.06	0.2	2.4, 0.4	0.4	
		FM	FM	FM	FM	FM
	q_{Mn}	1.74	1.74	1.70	1.68	1.71
	q_{Co}	1.28	1.25	1.14, 1.35	1.13	
	E_g	0.78 (α), 0 (β)	0 (α), 0.97 (β)	0 (α), 1.66 (β)	0 (α), 2.16 (β)	0.0 (α), 2.90 (β)
Fe	a	3.78	3.78	3.81	3.85	3.89
	μ_{Fe}	4.2	4.2	4.2	4.3	4.2
	μ_{Co}	0.0, 0.2	0.2	0.3	0.4	
		FM	FM	FM	FM	CAFM
	q_{Fe}	1.70	1.73	1.71	1.68	1.61
	q_{Co}	1.28	1.26	1.17	1.18	
	E_g	0.18 (α), 0.48 (β)	0.46 (α), 0 (β)	2.23 (α), 1.67 (β)	1.04 (α), 1.69 (β)	2.16
Ni	a	3.77	3.81	3.77	3.77	3.78 (3.81) [229]
	μ_{Ni}	1.7	1.7	1.6	1.7, 0.9, 1.6	1.3
	μ_{Co}	0.5, 0.7, 2.9, 3.0	0.01, 1.7, 1.8	1.5	1.3	
		FM	FM	FM	FM	FM
	q_{Ni}	1.17	1.29	1.27	1.33, 1.12	1.21
	q_{Co}	1.17, 1.55	1.21, 1.36	1.35	1.31	
	E_g	1.49 (α), 0 (β)	0 (α), 0.40 (β)	1.12 (α), 0 (β)	0 (α), 1.22 (β)	0.0(α), 2.25 (β)
Cu	a	3.76	3.81	3.80	3.81	3.80
	μ_{Cu}	0.8	0.7	0.6	2.6, 0.7	0.0
	μ_{Co}	0.1, 0.0	1.1, 0.4, 3.0	1.3	0.6	
		FM	FM	GAFM	GAFM	NM
	q_{Cu}	1.32	1.28	1.25	1.18, 1.20	1.15
	q_{Co}	1.30	1.19, 1.30, 1.53	1.34, 1.24	1.40	
	E_g	0.66 (α) 0 (β)	1.02 (α), 0 (β)	0 (α), 0.67 (β)	0.06 (α), 0.21 (β)	0.0

On the other hand, we were able to converge different magnetic structures for $SmBO_3$, whose relative energies can be found in Table 6.4. $SmFeO_3$ was found to

have a CAFM ground state, with GAFM being the second most energetically stable configuration found 0.89 eV higher in energy. For $SmMnO_3$ and $SmNiO_3$, FM are more stable than AFM with a difference in energy with the second most stable magnetic structure larger than 2.00 eV for both cases, which agrees with previous data on cubic phase lanthanide manganate perovskites, and cubic $SmNiO_3$ (which undergoes a insulator to metal transition ~400 K). [153,236] Finally, for $SmCuO_3$ only the FM and NM forms converged, and according to their relative energies, the material is expected to be non-magnetic, with the FM structure at 5.26 eV higher in energy.

Table 6.4. Difference in total energy between different magnetic structures for $SmBO_3$ and their related magnetic moment. Note that $SmNiO_3$ AFM are really ferromagnetic, with different magnetic moments and non-zero total magnetic moment. N/A signifies magnetic structures that were not possible to obtain.

		AAFM	**CAFM**	**FM**	**GAFM**	**NM**
$SmMnO_3$	E_{diff} (eV)	2.20	N/A	0.00	2.60	N/A
	u_B	3.82	N/A	3.93	3.82	N/A
$SmFeO_3$	E_{diff} (eV)	1.78	0.00	2.65	0.89	N/A
	u_B	4.31	4.20	4.40	4.23	N/A
$SmNiO_3$	E_{diff} (eV)	9.57	2.05	0.00	2.65	N/A
	u_B	1.44-6.15	0.33-1.76	2.05	1.06-2.03	N/A
$SmCuO_3$	E_{diff} (eV)	N/A	N/A	5.26	N/A	0.00
	u_B	N/A	N/A	0.88	N/A	0.00

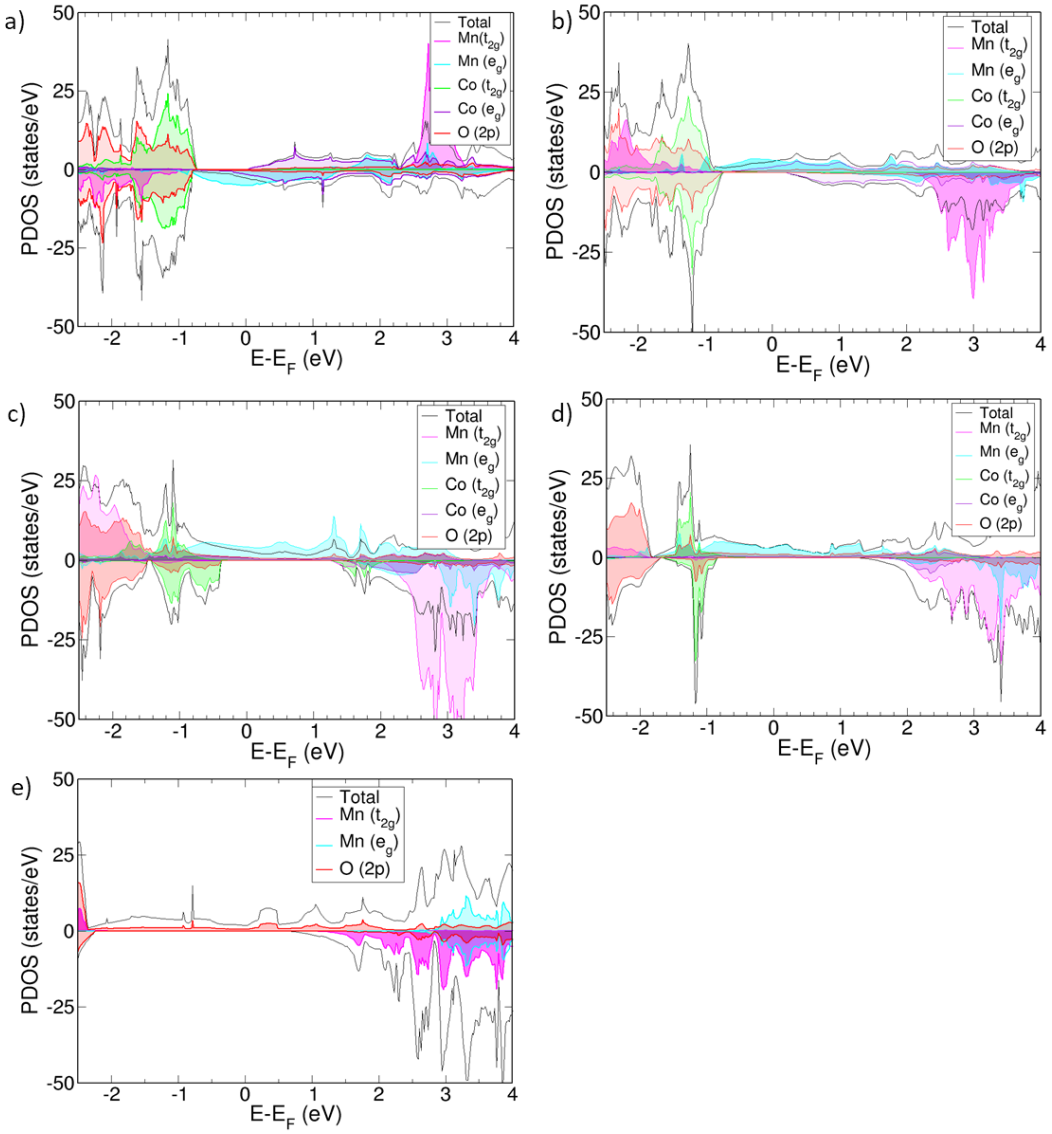

Figure 6.2. PDOS for $SmMn_xCo_{1-x}O_3$, a) x=0.125, b) x=0.25, c) x=0.5, d) x=0.75, e) x=1.0. The Fermi level is at 0 eV, and negative E-E_F represent the occupied bands and positive the virtual bands. Positive PDOS are associated with the α-spin, whereas negative PDOS are associated with β-spin. Please note that the Mn PDOS has been multiplied by 10 for x=0.125, 5 for x=0.25, 0.5, and by 2 for x=0.75. Mn PDOS in e) is not multiplied.

For $SmMn_xCo_{1-x}O_3$ and regardless of the dopant concentration, an overlapping between the Co and Mn e_g-bands (Figure 6.2) is always found at the Fermi level, thus expecting a potentially high electron conductivity to go from Mn^{3+} to Co^{3+}, as high σ_e

has been reported to go through e_g-bands. [218,237] The contribution of each band depends on the dopant concentration, with larger contribution of the Co e_g-bands at lower dopant concentrations, and *vice versa* when the material is heavily doped. Increasing the dopant concentration does not influence the Co t_{2g}/e_g-splitting. We do know from previous publications that the change in the spin state, and thus the occupation of the *d*-orbitals in Co^{3+}, can be directly related to the distortion of the octahedral environment, *i.e.* distortions in the Co-O bonds. Indeed, for x=0.125, 0.25, and 0.75, bonds are only distorted about 0.01 Å with respect to the ideal Co-O bond of 1.88 Å. However, for x=0.50, the range of Co-O bond length is wider (1.88-1.95 Å), thus altering the Co *d*-orbital crystal field splitting, and consequently, the orbital occupation.

This can also be observed in the variation of the cobalt magnetic moment. As shown in Table 6.3, μ_{Co} is almost 0 for all concentrations with the exception of x=0.50, with a μ_{Co} of 2.4, that can be associated to an intermediate spin (IS) state. This is also observed in the PDOS, with the occupation of the Co e_g-orbitals on the one hand, and β-t_{2g}-orbitals at positive energies on the other. Moving through the PDOS with increasing x, it can be seen that this material becomes gradually more like $SmMnO_3$. Looking at the β-band gap, it increases with increasing x, reaching it maximum in $SmMnO_3$. Also noticeable is the magnetic moment of Mn^{3+}, which is found between 3.76 and 3.85, indicating that Mn^{3+} is found in its higher spin state, with the highest Mn magnetic moment observed in $SmMnO_3$.

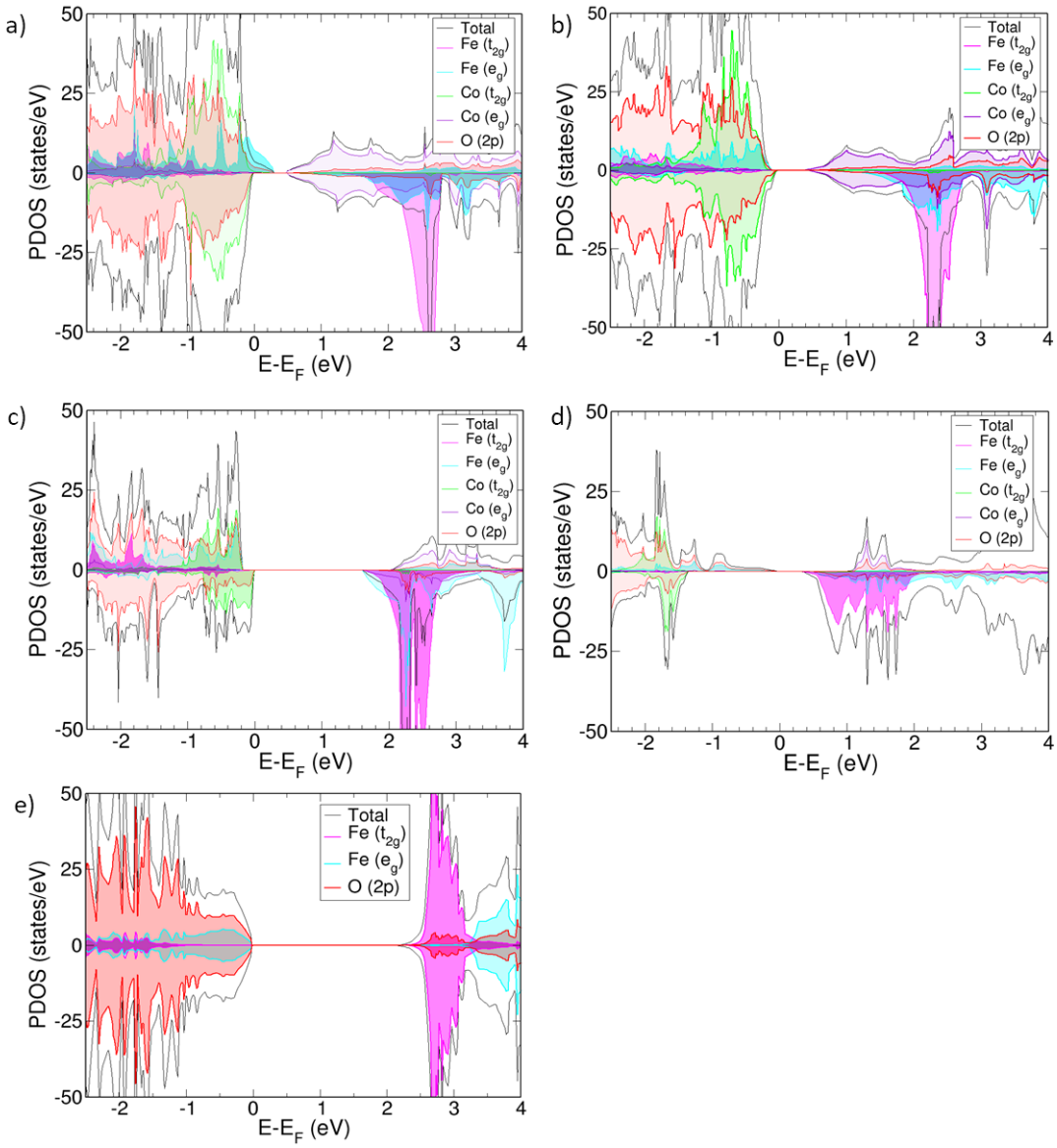

Figure 6.3. PDOS for $SmFe_xCo_{1-x}O_3$, a) x=0.125, b) x=0.25, c) x=0.5, d) x=0.75, e) x=1.0. The Fermi level is at 0 eV, and negative E-E_F represent the occupied bands and positive the virtual bands. Positive PDOS are associated with the α-spin, whereas negative PDOS are associated with β-spin. Please note that the Fe PDOS has been multiplied by 10 for x=0.125, 5 for x=0.25, 0.5, and by 2 for x=0.75. Fe PDOS in e) is not multiplied.

The cobalt crystal field splitting is also constant in $SmFe_xCo_{1-x}O_3$ (Figure 6.3), mainly due to the low distortion degree that the Co-O bonds suffer upon doping, as can be noticed in Table 6.2. At x=0.125, Fe-doped $SmCoO_3$ is metallic, with an overlapping

of Fe e_g- and Co t_{2g}-bands at the Fermi level, thus expecting a relatively large electronic conductivity. However, with increasing dopant concentration, the material becomes a semiconductor first, and then an insulator (x≥0.5), disqualifying it as a good cathode candidate. As it was observed for $SmMn_xCo_{1-x}O_3$, $SmFe_xCo_{1-x}O_3$ gets more $SmFeO_3$ character when increasing x, with the band gap becoming increasingly symmetrical, resulting in pure semiconductor behaviour at x=1.0. The iron magnetic moment remains, on the other hand, mostly constant over the series at 4.2 μ_B, whereas the Co magnetic moments are very low for all the series, oscillating between 0.0 and 0.4 μ_B. In $SmFeO_3$, all Fe-O bond lengths are equal, which results in a symmetrical electronic structure. Worth noting is that all Fe-O bonds are equal for x=0.5 as well, but the Co-O bond lengths, whilst all the same, are different to the Fe-O ones, thus inducing distortions in the lattice and an asymmetric PDOS.

The case of $SmNi_xCo_{1-x}O_3$ (Figure 6.4) and $SmCu_xCo_{1-x}O_3$ (Figure 6.5) is somewhat different to the previous two systems. For $SmNi_xCo_{1-x}O_3$, the Co t_{2g}-bands are not fully occupied whereas the e_g-bands are partially occupied. This can be directly related with a change in the Co spin moment, and thus to the distortions in the Co-O distances (Table 6.2). Interestingly, for x=0.125 the system is a conductor, but conduction occurs only through the Co t_{2g}-bands, and as soon as the dopant concentration increases, the system becomes half-metallic and the conduction is mediated through the nickel e_g-bands. The half-metallic nature is preserved in $SmNiO_3$, thus inferring that Ni-doping, even at low concentrations, induce more $SmNiO_3$ type behaviour than $SmCoO_3$-like. It is worth noting that there is no overlapping between the bands of Co and Ni, which would be indicative of poor electronic conductivity.

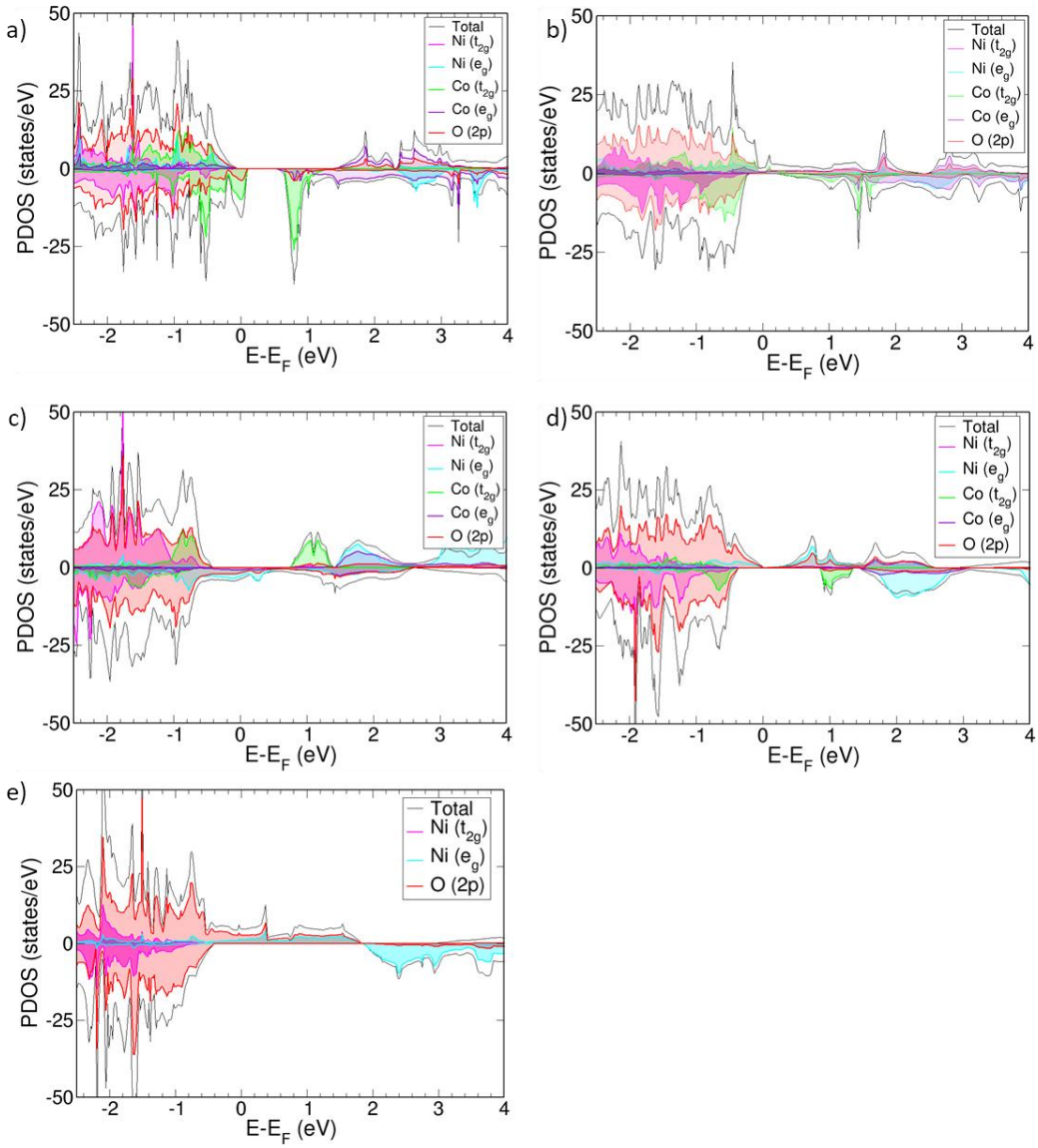

Figure 6.4. PDOS for $SmNi_xCo_{1-x}O_3$, a) x=0.125, b) x=0.25, c) x=0.5, d) x=0.75, e) x=1.0. The Fermi level is at 0 eV, and negative E-E_F represent the occupied bands and positive the virtual bands. Positive PDOS are associated with the α-spin, whereas negative PDOS are associated with β-spin. Please note that the Ni PDOS has been multiplied by 10 for x=0.125, 5 for x=0.25, 0.5, and by 2 for x=0.75. Ni PDOS in e) is not multiplied.

For $SmCu_xCo_{1-x}O_3$ (Figure 6.5), the Cu e_g-bands are partially occupied over the Fermi level for x=0.125, 0.25, and 0.5, indicating that electronic conductivity should be possible. For x=0.75, a change in the electronic structure is seen around the Fermi level, resulting in a tiny band gap, which would suggest a decrease in σ_e. For

$SmCuO_3$, the electronic structure becomes fully metallic and ferromagnetic. Additionally, for all x_{Cu}, the cobalt octahedral environment is distorted, resulting in the Co t_{2g}-levels split over the valence and conduction band. This can be, again, directly related with a change in the cobalt spin moment, and thus to distortions in the Co-O distances, as listed in Table 6.2.

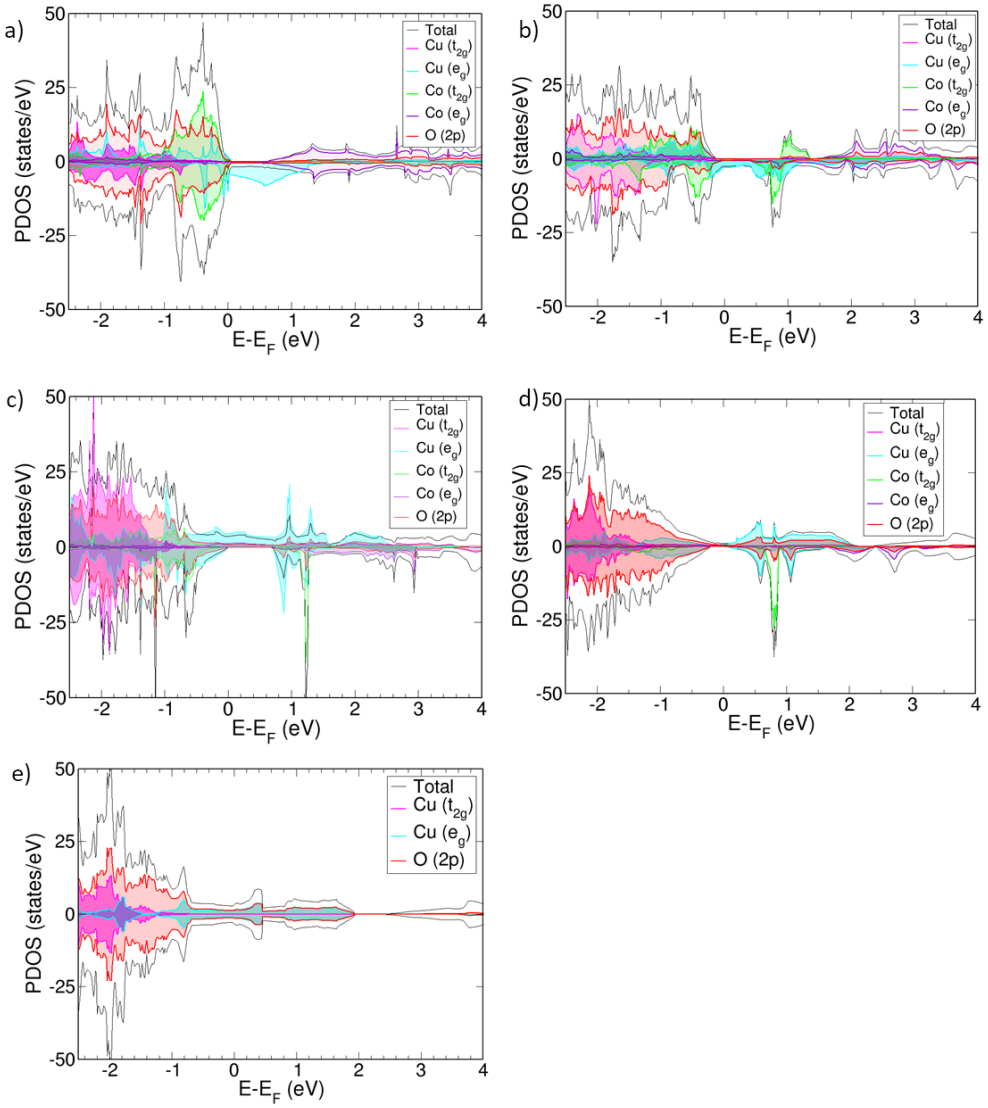

Figure 6.5. PDOS for $SmCu_xCo_{1-x}O_3$, a) x=0.125, b) x=0.25, c) x=0.5, d) x=0.75, e) x=1.0. The Fermi level is at 0 eV, and negative E-E_F represent the occupied bands and positive the virtual bands. Positive PDOS are associated with the α-spin, whereas negative PDOS are associated with β-spin. Please note that the Cu PDOS has been multiplied by 10 for x=0.125, 5 for x=0.25, 0.5, and by 2 for x=0.75. Cu PDOS in e) is not multiplied.

In addition, Bader charges and magnetic moments for cobalt at different concentrations suggest the presence of different mixed valence states, for example when x=0.125. In this situation, Co charges decrease and increase by ~0.2 e with respect to the Co charge in $SmCoO_3$. However, this charge variation is not enough to state that the system has mixed valence states, and neither the magnetic moments nor the electronic structure are clear enough to support this idea. On the other hand, nickel's magnetic moment is around 1.7 for all concentrations, which means that nickel is found in a mixed spin state between high and low spin.

6.5 Electronic Conductivity

It is generally accepted for SOFC that high σ_e is in the region of 100 $S \cdot cm^{-1}$.[238] Here, we have calculated the electronic conductivities (σ_e) for all the aforementioned $SmB_xCo_{1-x}O_3$ at 0 K, not taking into account thermal contributions (Table 6.5 and Figure 6.6). Thermal effects may alter the electronic conduction, but as we here strive to make a comparison between different dopant effects, the 0 K electronic conduction has been deemed to be a suitable approximation. From these results, it is clear that for x> 0.125 in $SmFe_xCo_{1-x}O_3$, σ_e is 0, as expected considering that the PDOS revealed that the material becomes an insulator or semiconductor. It is known from experimental data that Fe-containing perovskites generally have lower σ_e than those containing manganese, [239,240] and that $\sigma_e \neq 0$ Scm^{-1} in Fe-based perovskites at temperatures above 200°C.[78,239] Thus, it is reasonable to believe that at elevated temperatures, σ_e will increase for this material, [239,241] although this increase in σ_e is not expected to be remarkable in comparison to the other systems modelled here. Focusing on those systems that, at least, double σ_e, which are $SmMn_{0.125}Co_{0.875}O_3$,

$SmMn_{0.25}Co_{0.75}O_3$, $SmFe_{0.125}Co_{0.875}O_3$, and $SmNi_{0.25}Co_{0.75}O_3$, it is seen that Cu-doping would not represent a major improvement in terms of σ_e since the maximum σ_e that can be obtained is when x=0.25, with a σ_e of only 120 S cm^{-1}.

Table 6.5. Electrical conductivity, σ_e (Scm^{-1}), for $SmB_xCo_{1-x}O_3$. Relaxation time set to 0.12 fs.

B	x=0.125	x=0.25	x=0.5	x=0.75	x=1.0
Mn	810	120	90	213	70
Fe	320	0	0	0	0
Ni	10	190	41	20	61
Cu	20	120	100	39	23

The largest σ_e are obtained for $SmMn_{0.125}Co_{0.875}O_3$, and $SmFe_{0.125}Co_{0.875}O_3$. These large σ_e can be attributed to the overlapping between the d-bands of Co and the dopants. [183,242] It is further expected that at higher temperatures, these σ_e could be increased. Moreover, all σ_e are in line with general IT-SOFC cathode requirements and experimentally obtained data. [78,86,239]

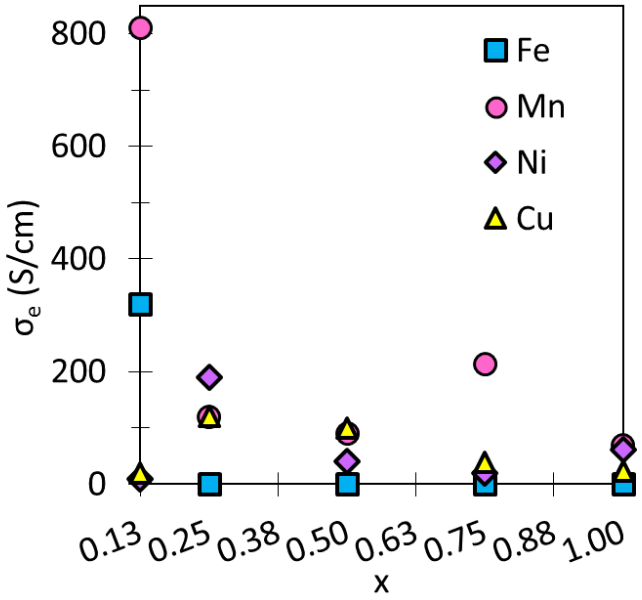

Figure 6.6. σ_e ($S \cdot cm^{-1}$) as a function of x for $SmB_xCo_{1-x}O_3$.

6.6 Oxygen Vacancy Formation Energy

After the dopant configuration in the bulk was optimized, we introduced a single V_O in all systems using SOD, and then optimizing the system using VASP. Oxygen vacancies influence the bulk ionic conduction in SOFC cathode materials, and thus it is important to assess the dopants' influence on the oxygen vacancy formation. The oxygen vacancy formation energy (E_f) is calculated according to equation 4.1. However, firstly it is necessary to evaluate for which $\Delta\mu_O$ these systems are stable. This is assessed through chemical potential phase diagrams, on the construction of which were detailed in Chapter 4. For $SmCoO_3$, it was shown in Chapter 4 that the upper limit to $\Delta\mu_O$ is -0.5 eV. In this chapter, we thus constructed phase diagrams for $SmMnO_3$ and $SmFeO_3$, obtaining that the upper oxygen potential limits for $SmMnO_3$ (based on experimental data from Pawlas-Foryst *et al.* [243]) is $\Delta\mu_O \leq 0$ eV, whereas for $SmFeO_3$ (based on experimental data from Parida *et al.* [244]) is $\Delta\mu_O \leq -0.7$ eV (Figure 6.7).

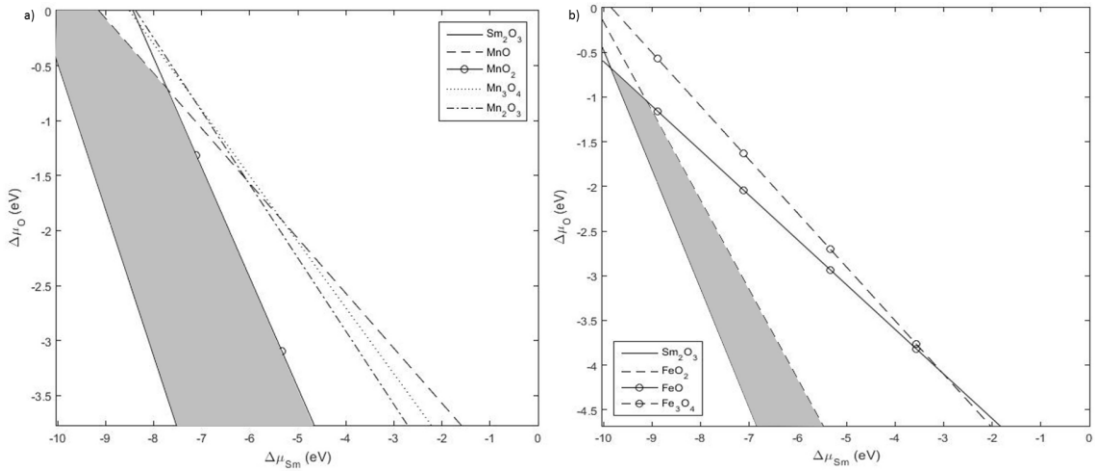

Figure 6.7. $SmMnO_3$ and $SmFeO_3$ chemical potential phase diagrams. Grey area represents area where $SmMnO_3$ and $SmFeO_3$, respectively, are stable. For $SmCoO_3$ phase diagram, see Chapter 4.

The lack of experimental data for $SmCuO_3$ and $SmNiO_3$ resulted in the impossibility of calculating their respective phase diagrams, although it has been reported that both materials are unstable under high partial oxygen pressures. [230–232] According to these results and considering that we want to perform a qualitative and not a quantitative study of E_f, we have decided to use $\Delta\mu_O$ = -0.5 eV for all materials and concentrations, and we assumed that the error that we commit for $SmFeO_3$ is negligible to the purpose of this discussion. [87] However, we have considered $\Delta\mu_O$ = 0 for $SmMn_{0.75}Co_{0.25}O_{3-x}$, since its stoichiometry is closer to $SmMnO_3$ than it is to $SmCoO_3$.

Table 6.6. Oxygen vacancy position and formation energy. N/A signifies no such possible oxygen vacancy position in lattice. Number of vacancy sites are different in each material and is dependent on the dopant configuration from the bulk calculations. Lowest E_f are in bold.

		x=0.125	**x=0.25**	**x=0.5**	**x=0.75**	**x=1.0**
$SmMn_xCo_{1-x}O_3$	Mn-V_O-Mn	N/A	2.73	2.65	2.70, 2.94	2.36
	Mn-V_O-Co	3.71	2.76	2.06, 2.14, 2.36, 2.47, 2.91	3.00, 2.75	N/A
	Co-V_O-Co	2.27, 2.56	2.71, 3.21	2.76	N/A	N/A
$SmFe_xCo_{1-x}O_3$	Fe-V_O-Fe	N/A	2.70	N/A	3.31, 3.43	5.65
	Fe-V_O-Co	2.63	2.94, 2.76	3.53	1.99, 3.32	N/A
	Co-V_O-Co	2.32, 3.05	2.70	N/A	N/A	N/A
$SmNi_xCo_{1-x}O_3$	Ni-V_O-Ni	N/A	1.41	2.48	0.44, 1.43	0.55
	Ni-V_O-Co	2.76	1.57, 1.79	2.39	0.47, 0.57	N/A
	Co-V_O-Co	1.66, 1.84	1.09	2.16	N/A	N/A
$SmCu_xCo_{1-x}O_3$	Cu-V_O-Cu	N/A	1.43	0.93, 0.96, 1.09	0.62, 0.71	0.54
	Cu-V_O-Co	2.19	0.55, 0.70	0.79, 0.81, 0.86, 1.22	0.42, 0.52	N/A
	Co-V_O-Co	2.20, 2.65	0.92	1.29, 1.36, 1.44	N/A	N/A

E_f in Ni- and Cu-doped $SmCoO_3$ are very low (Table 6.6), which means that the oxygen vacancy concentration (C_V) could be expected to be very high, agreeing with the experimental results. [230–232] Nickel and copper can be easily reduced from +3 to +2-charged, with these also being more electronegative than cobalt, [245] thereby readily accommodating the two electrons resulting from the V_O formation, as represented in Kröger-Vink notation by [204]

$$2M_M^X + O_O^X \rightarrow 2M_M' + V_O^{\cdot\cdot} + {}^1/_2\, O_2$$

where M_M^X is B^{3+} or Co^{3+} (depending on V_O position) in the perfect lattice, O_O^X neutral oxygen atom being removed to form $V_O^{\cdot\cdot}$, and M_M' signifying the extra charge present in the system after oxygen removal being localized on the neighboring B- or Co-ions. This is the same equation that was presented in Chapter 4.

Comparing E_f in relation to E_f in $SmCoO_3$ (2.08 eV), Co-site doping with B does not markedly lower the E_f, except at high x_{Cu} and x_{Ni}=0.75. Thus, Co-site does not have a positive influence in improving σ_O. Hence, B-site doping only enhances the formation of oxygen vacancies when doping with Ni^{3+} and Cu^{3+} due to its instability, whereas Fe^{3+} and Mn^{3+} doping have no major impact.

Comparison of E_f in $SmBO_3$ is presented in Figure 6.8. $SmBO_3$ shows a non-linear E_f trend (comparable to $LaBO_3$ [31]), with Fe-based lanthanide oxides having the highest E_f. What is notable in comparison with $LaBO_3$, is that E_f for $SmFeO_3$ is higher with ~1 eV, whereas for $SmMnO_3$ and $SmCoO_3$ E_f is lower. E_f in $SmNiO_3$ and $SmCuO_3$ is very low, as was also seen for $SmCu/Ni_xCo_{1-x}O_3$. This behaviour has previously been seen in experimental studies, and has been related to the relative low energy barriers for reduction of Ni^{3+} to Ni^{2+} and Cu^{3+} to Cu^{2+} discussed above.

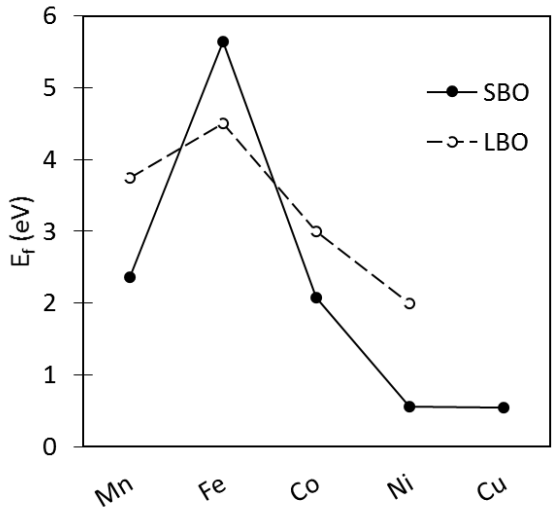

Figure 6.8. E_f for $SmBO_3$ (B=Mn, Fe, Co, Ni, and Cu). SBO is $SmBO_3$, and LBO is $LaBO_3$. Values for $LaBO_3$ taken from Lee *et al.* 2009.[19]

To investigate the validity of the Kröger-Vink model above for $SmBO_3$, we have plotted the change in spin density ($\Delta\rho^{\alpha-\beta}$) upon $V_O^{\cdot\cdot}$ formation (Figure 6.9) as

$$\Delta\rho^{\alpha-\beta} = \rho_{SmBO_{3-x}}^{\alpha-\beta} - \rho_{SmBO_3}^{\alpha-\beta} - \rho_O^{\alpha-\beta}$$

Yellow $\Delta\rho^{\alpha-\beta}$ shows spin gain, and blue spin depletion, whereby at the V_O site a large spin depletion is seen in all systems. $\Delta\rho^{\alpha-\beta}$ shows clearly that in all $SmBO_3$, except $SmFeO_3$, B^{2+}-V_O-B^{2+} clusters are formed, indicated from the gain in $\Delta\rho^{\alpha-\beta}$ on the B-sites. This is most clearly evident in $SmMnO_3$, whereas for $SmNiO_3$ and $SmCuO_3$, some additional $\Delta\rho^{\alpha-\beta}$ is located on the oxygen (in the same plane as V_O) nearest to the reduced copper and nickel ions. For $SmFeO_3$, which is the compound most different in this series and with the highest E_f, the CAFM structure is kept, whereas the lattice is distorted, as well as a general change in spin throughout all Fe-sites. Examining the magnetic moments and Bader charges on the neighboring iron ions,

they have been reduced from μ_{Fe}=4.2 to $\mu_{Fe\ NN\ Vo}$=1.16 and 2.1, which fits with iron going from a d^5-occupancy (Fe^{3+}) to d^4 (Fe^{2+}). This change in iron d-occupancy is unfavourable and have previously been used to describe the high E_f in $LaFeO_3$. [48] A thorough discussion on V_O formation in $SmCoO_3$ was been presented in Chapter 4.

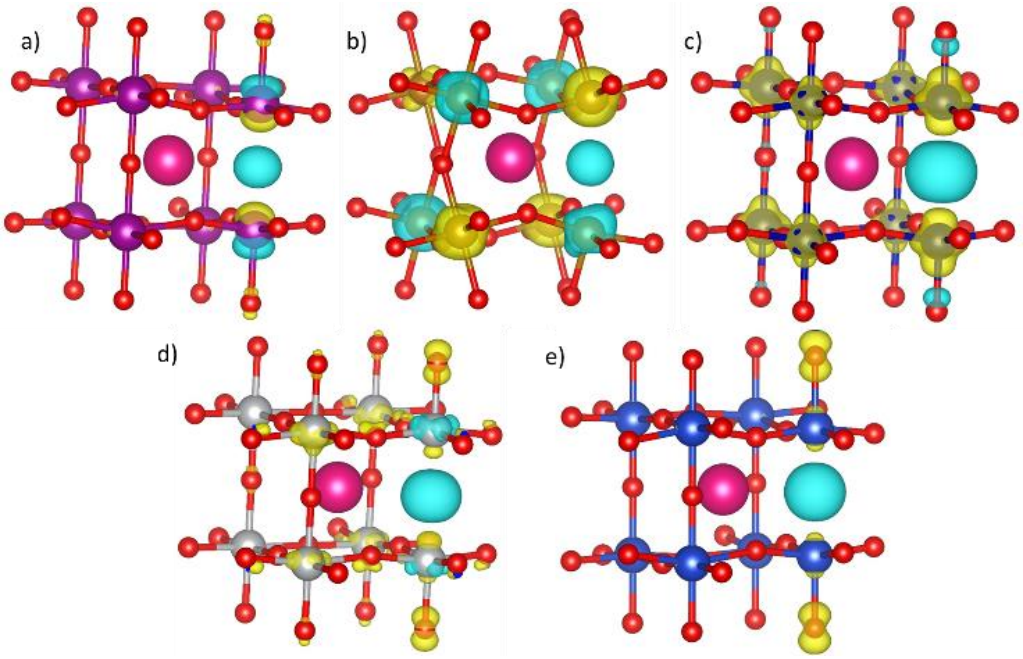

Figure 6.9. Spin density difference ($\Delta\rho^{\alpha-\beta}$) representations of (a) $SmMnO_3$, (b) $SmFeO_3$, c) $SmCoO_3$, d) $SmNiO_3$, and e) $SmCuO_3$ with V_O. Yellow $\Delta\rho^{\alpha-\beta}$ isosurface shows an increase of spin density, whereas blue $\Delta\rho$ isosurface represents a spin density decrease. Isosurface value is set at 0.03. Only one Sm^{3+} has been included in each representation for clarity.

6.7 Thermal Expansion Coefficient

TEC of traditional electrolyte materials are in the region ~10-13×10^{-6} K^{-1}, and cubic $SmCoO_3$ has a calculated TEC of 17.7×10^{-6} K^{-1}. These high TECs are commonplace for cobalt perovskites, and they are known to increase with Sm-site doping, as this increases oxygen vacancy deficiency in the lattice, leading to further lattice volume

expansion upon heating. Co-site doping can decrease TEC, as seen in Figure 6.10 and Table 6.7, which would make the materials more practical as SOFC cathodes. Encouragingly, most systems do have lowered TEC, comparing to $SmCoO_3$, although none is directly in the range of common SOFC electrolytes. Mn-doping is seen to decrease TEC the most, but also varies greatly with x. On the other hand, Fe-doping has barely any influence on the TEC at any x. Doping with copper shows no significant change in TEC at low x, but increases for x=0.5. Finally, Ni-doping shows similar behavior to that of Mn-doping, but does not reduce TEC as readily. Although these results are positive in terms of lowering TEC, they are not sufficient to match an acceptable TEC range.

Table 6.7. Thermal expansion coefficient (TEC) in $\times 10^{-6}$ K^{-1} for $SmB_xCo_{1-x}O_3$. TEC have been calculated over a temperature range of 600-1200 K.

B	**x=0.125**	**x=0.25**	**x=0.5**	**x=0.75**	**x=1.0**
Mn	15.6	16.9	17.7	14.9	15.5
Fe	18.1	17.5	17.0	17.2	16.9
Ni	16.1	17.3	17.6	16.7	16.1
Cu	17.3	17.4	18.6	15.8	14.2

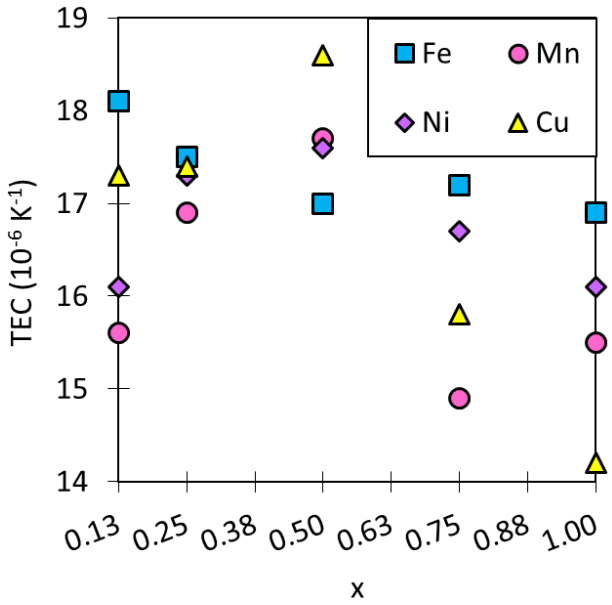

Figure 6.10. The trend in TEC for $SmB_xCo_{1-x}O_3$ calculated over a temperature range of 600-1200 K. TEC for typical SOFC electrolytes are ~10-13×10^{-6} K^{-1}, which is outside the range of this graph.

6.8 Chapter Conclusions

In this chapter, an atomistic study of $SmB_xCo_{1-x}O_3$ with B = Fe^{3+}, Mn^{3+}, Ni^{3+}, and Cu^{3+}, and x = 0.125, 0.25, 0.75, 1.00, utilizing both DFT+U, and MD techniques, was presented. After a complete study of the dopant configurations, the most stable dopant distribution for each dopant and concentration was determined, from which the electronic and magnetic properties, oxygen vacancy formation energy, ionic conductivities and thermal expansion coefficient were calculated.

Regardless of dopant, their inclusion induces a distortion of the Co-O bond that forces different Co *d*-orbital occupations. This in combination with the dopants *d*-orbital occupation explains why the vast majority of the systems become ferromagnetic, with the exception of $SmCu_{0.5}Co_{0.5}O_3$ and $SmCu_{0.75}Co_{0.25}O_3$. The overlap between the e_g-

orbitals of the dopant and cobalt around the Fermi level explained the impressively high electrical conductivity found for $SmMn_{0.125}Co_{0.875}O_3$ in comparison with $SmFe_{0.125}Co_{0.875}O_3$, in which the presence of an electronic band justifies the insignificant electronic conductivity calculated with our methodology. We have also illustrated that doping with Cu and Ni does not significantly improve the electronic conductivity of the perovskite. B-site doping does not either reduce the oxygen vacancy formation energy when B= Mn, Fe, but it does decrease with B=Cu, Ni instead, mainly as a result of the great instability of the +3 valence. In general, the most common V_O configuration was found to be Co-V_O-Co, with cobalt being reduced from Co^{3+} to Co^{2+}. Finally, TEC were calculated, with Mn^{3+}-doping giving lowest TEC at low x, and x=0.75. In conjunction with the DFT+U results, Mn^{3+}-doping at low x, would be most favourable to improve $SmCoO_3$ as an IT-SOFC cathode material. The combination of Mn- and Ca-doping will be the topic of the next chapter.

Chapter 7

$Sm_{0.75}Ca_{0.25}Co_{1-x}Mn_xO_{2.88}$ as IT-SOFC Cathode Material

Abstract

In this chapter, the results from the previous chapters are combined to propose a new and efficient $SmCoO_3$-based cathode material for Intermediate-Temperature Solid Oxide Fuel Cells. $Sm_{0.75}Ca_{0.25}Mn_xCo_{1-x}O_{2.88}$ at two different Mn-concentrations is investigated, and we find that the electronic conductivity in both materials is high, taking into account the limitations inherent in the calculations. Furthermore, the ionic conduction is calculated, with both systems showing excellent oxygen conduction. Calculating thermal expansion coefficients, x=0.25 shows the largest decrease, and is thus concluded to be the most favorable Mn-doping concentration. Thus, we present $Sm_{0.75}Ca_{0.25}Mn_{0.25}Co_{0.75}O_{2.88}$ as offering a significant improvement in performance over the current generation of SOFC cathode.

7.1 Introduction

As stated throughout this work, at IT-SOFC operating temperatures, oxygen reduction in the traditional cathode material $La_{1-x}Sr_xMnO_{3-d}$ (LSM) becomes inefficient and the cathode is no longer able to assist with the oxygen diffusion. [6,7,10,25,69] $SmCoO_3$-based perovskites show higher oxygen reduction efficiency and, unlike LSM, they show excellent oxygen diffusion.[18] For IT-SOFC cathodes, the balance between

both ionic and electronic conductivity is important, and they are inversely related to the oxygen content.[26] Hence, high oxygen content benefits electronic conduction (σ_e), but lowers the ionic conductivity (σ_O), consequently leading to lower oxygen-surface exchange and higher cell polarization resistance.[26] It is also important to highlight that electronic conduction is typically at least two orders of magnitude larger than the ionic conductivity, thus turning the latter into the limiting factor.[26]

Doping $SmCoO_3$ has proven to be an excellent technique to balance both conduction schemes to obtain the best possible performance. From Chapter 5 and 6, it was shown that Ca^{2+}-doped $SmCoO_3$ significantly enhances oxygen diffusion, and that Mn^{3+}-doping increases the electronic conductivity and decreases the thermal expansion coefficient (TEC), making it more compatible with IT-electrolyte materials such as gadolinium-doped ceria (GDC). In this chapter, we confirm that the combination of both dopants in the SCO matrix leads to an outstanding cathode material with impressive oxygen and electron conduction, and low TEC.

7.2 Computational Details

7.2.1 DFT Calculations

We studied the electronic structure of the different systems using DFT calculations by means of the Vienna *ab initio* simulation package, VASP.[92–95] The projector-augmented wave method (PAW) was applied to describe the ion-electron interaction,[123] and the converged kinetic energy cut-off of 500 eV was used. The calculations are spin-polarized with Perdew-Burke-Ernzerhof (PBE)[107,108] functionals and run until electronic and ionic self-consistence, with a convergence

criteria of 10^{-5} eV and 10^{-3} eV·Å^{-1} respectively. For each atomic species, the following valence electrons were considered: Sm ($5s^25p^66s^2$), Ca ($3s^23p^64s^2$), Sr ($4s^24p^65s^2$), La ($5s^25p^66s^25d^1$), Mn ($3p^63d^64s^1$), Co ($4s^23d^7$), and O ($2s^22p^4$).

On-site Coulombic interaction (DFT+U) was used for the Co and Mn 3*d*-electrons to account for the self-interaction error,[65,110,111] by means of Dudarev's approach,[109] with Hubbard parameters (U_{eff}) for Mn and Co of 4 and 3 eV respectively.[19,219]

σ_e was calculated from the frequency dependent dielectric matrix. This calculation is dependent on relaxation time, which should be fitted to experimental electronic conductivity. Since no experimental data is available, and our purpose is to perform a comparative analysis, we have used 0.12 fs for all systems as in Chapter 5 and 6. Finally, the supercell used for the DFT calculations is the 2×2×2 Pm-3m pseudo-cubic cell, with 40 atoms.

7.2.2 MD Calculations

MD simulations were performed with the DL_POLY 4.07 code[96], with a 20×20×20 supercell (39000 atoms) simulated under NPT conditions with a Nosé-Hoover thermostat.[139] With a timestep of 0.5 fs and an equilibration period of 11 ps, statistics were collected after a production run of 100 ps. To account for electrostatic interactions, Ewald summation was employed, with the Verlet algorithm evaluating the atomic motions. Short-range interatomic interactions were simulated using a Buckingham potential, within the Born model for ionic solids.[75,142,235] Electronic polarization was included through the shell model, where ions are modelled as cores with a harmonic spring (*k*) connected to a massless shell with charge *Y*. The

interatomic potentials used here (Table 2.2) are mainly obtained from Cherry *et al.*, which have previously been used to model ionic conductivity (σ_O) in perovskites.[53,147,149,150]

7.3 Dopant Configuration

All the non-equivalent dopant and oxygen vacancy distributions in the materials were evaluated with the Site-Occupancy Disorder program (SOD).[214] We considered a Ca^{2+} concentration of 0.25, equivalent to inserting two Ca^{2+} into our unit cell. According to the Kröger-Vink notation for this dopant scheme, one oxygen vacancy (V_O) is required to ensure the electroneutrality of the system, as seen in Chapter 5.

$$2AO \xrightarrow{SmCoO_3} 2A'_{Sm} + 2O_O^x + V_O^{\cdot\cdot} \tag{7.1}$$

For Mn^{3+}, two different concentrations (x), 0.125 and 0.25, are considered, which are equivalent to substituting one and two Co^{3+} for Mn^{3+}, respectively. Hence, we inserted the Ca^{2+}, Mn^{3+}, and V_O into the $SmCoO_3$ bulk in this order, resulting in 3 different configurations for *x*=0.125, and 23 for *x*=0.25.

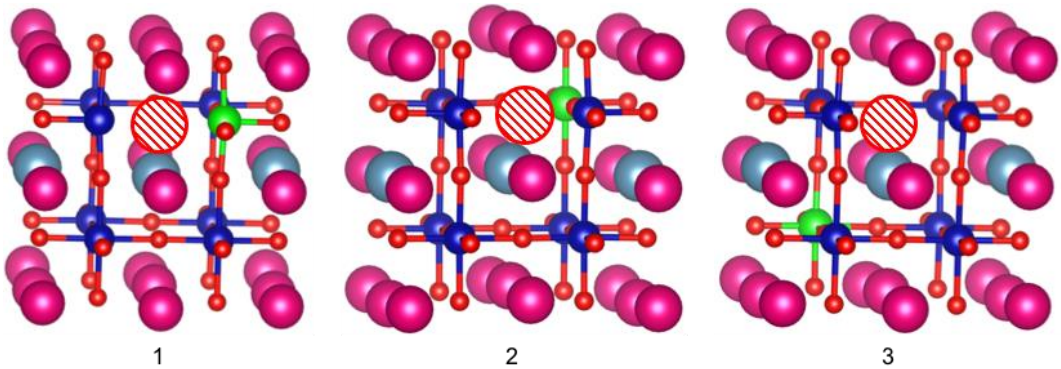

Figure 7.1. The different dopant configurations for $Sm_{0.75}Ca_{0.25}Co_{0.875}Mn_{0.125}O_{2.88}$. Orange sphere indicate vacancy position, and number refers to configuration number in Table 7.1. Sm is pink spheres, Ca grey, O red, Co blue, and Mn green, respectively.

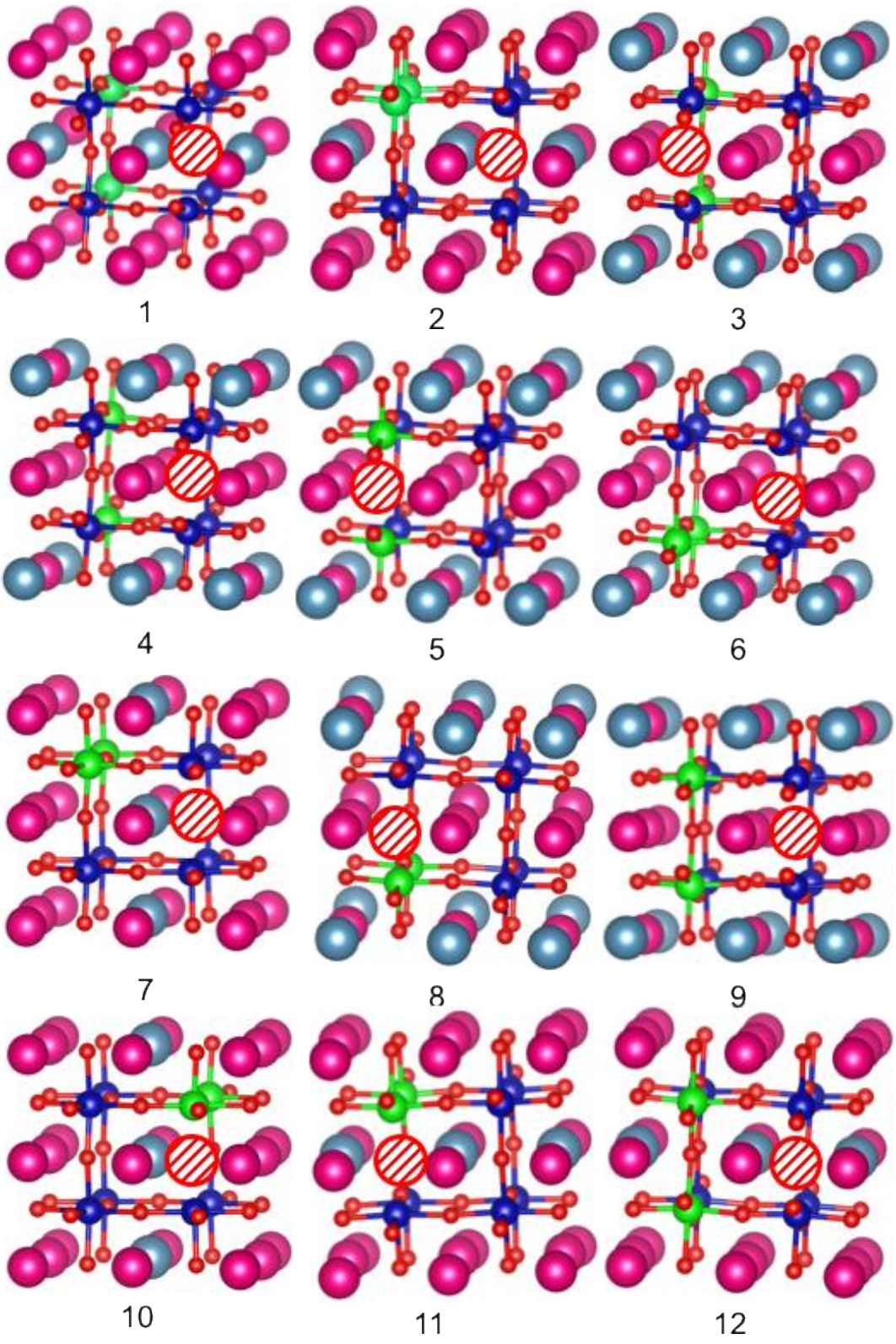
1
2
3
4
5
6
7
8
9
10
11
12

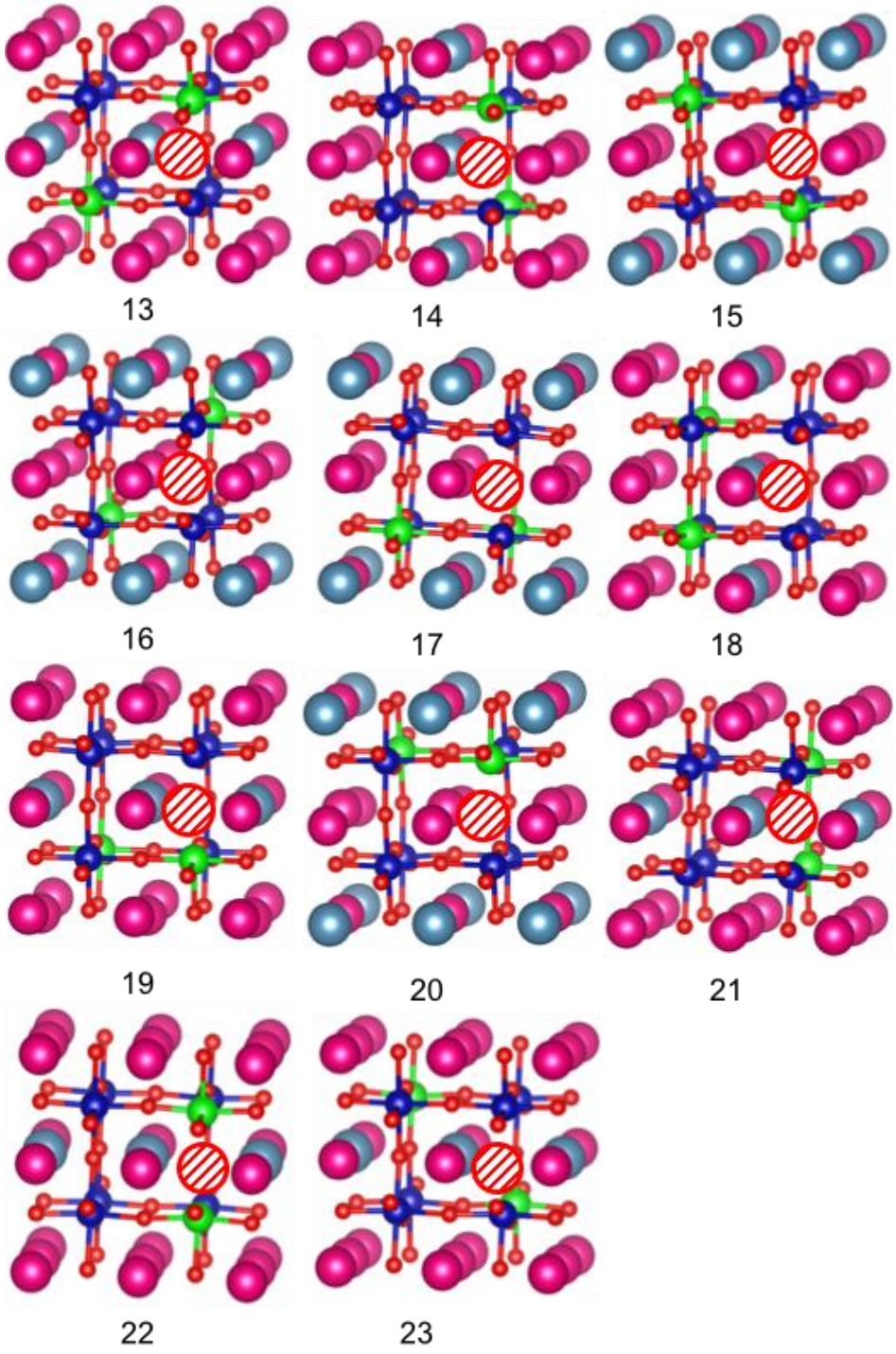

Figure 7.2. Different dopant configurations for $Sm_{0.75}Ca_{0.25}Co_{0.75}Mn_{0.25}O_{2.88}$. Orange sphere indicate vacancy position, and number refers to configuration number in Table 7.1. Sm is pink spheres, Ca grey, O red, Co blue, and Mn green, respectively.

After bulk optimization using DFT+U, we evaluated the relative abundance of each configuration at working temperatures by means of Boltzmann distributions (equation 7.2).[214] Under thermodynamic equilibrium, occurrence probability (P_n) of the different configurations (n) can be calculated, at each temperature T, as[214]

$$P_n = \frac{1}{Z}\exp(-E_n/k_B T) \tag{7.2}$$

$$Z = \sum_{n=1}^{N} P_n E_n \tag{7.3}$$

where Z is the partition function, k_B is Boltzmann's constant, and E_n the energy of configuration n. The resulting distributions are presented in Figure 7.3 below. For x=0.25, configurations 5-23 have been omitted as they have all P<0.0001 at all T.

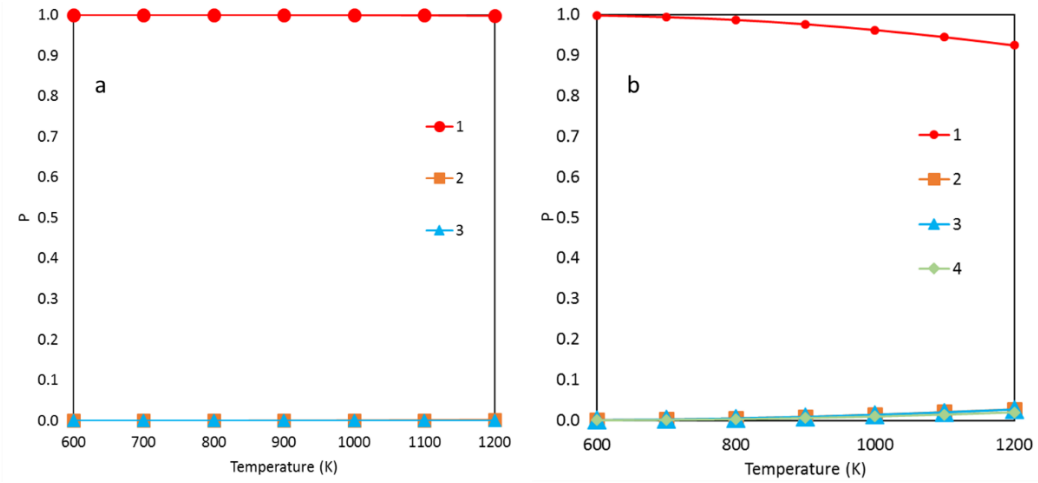

Figure 7.3. Boltzmann distribution of dopant configuration for a) x=0.125 and b) 0.25 as a function of temperature.

From the Boltzmann distributions, it is clear that under equilibrium conditions, only configuration 1 for both x is expected to be found in any abundance. The difference in energy between the different configurations for x=0.125 (0.51 and 0.63 eV,

respectively) was higher than that found between the three most stable configurations for *x*=0.25 (0.36, and 0.37 eV). The full list is included in Table 7.1. Only the most stable configuration at a given concentration was considered to evaluate the electronic structure of the system, whereas we used the three (and four) most stable configurations for calculation of the ionic conductivity and the TEC (see Appendix F).

Table 7.1. All possible configurations and their relative energy (eV) to the lowest energy configuration.

Configuration Number	x=0.125	x=0.25
1	0.00	0.00
2	0.51	0.36
3	0.63	0.37
4		0.40
5		0.77
6		0.79
7		0.82
8		0.95
9		0.98
10		1.04
11		1.14
12		1.20
13		1.28
14		1.50
15		1.57
16		1.62
17		1.66
18		1.67
19		1.71
20		1.84
21		2.64
22		3.06
23		4.00

7.4 Electronic Structure and Electronic Conductivity

From projected density of states plots (Figure 7.4), it is seen that $Sm_{0.75}Ca_{0.25}Mn_xCo_{1-x}O_{2.88}$ is half-metallic with electronic conduction being only possible through the α-channel. For *x*=0.125, this α-channel is mainly described by an overlapping of O(*2p*) and Co t_{2g} and e_g states, but with no contribution of the Mn(3d) orbitals, whereas for *x*=0.25 Mn(3d), both t_{2g} and e_g are also present. The overlapping of the t_{2g} and e_g orbitals in both electronic structures (Figure 7.4), is a result of the loss of the cobalt octahedral environment necessary for an effective octahedral crystal field splitting of the orbitals, evidenced by the distortion of the Co-O bonds relative to the non-doped SCO matrix (Table 7.2). Consequently, this enables different Co *d*-orbital occupations than the expected $t_{2g}^6 e_g^0$), thus leading to low-to-intermediate spin state (LS/IS) and IS spin states, as deduced from Co magnetizations (Table 7.2). From a non-distorted octahedral environment, cobalt magnetic moments (μ_{Co}) are expected to be 0, as described in Chapter 3, but under the presence of distortions, μ_{Co} increase. For *x*=0.125, μ_{Co} ranges from 0.19 to 2.96, whereas for *x*=0.25, all Co show IS state, around 2. Interestingly, for *x*=0.125 Co-O bond distances show less distortion compared to the non-doped SCO matrix than for *x*=0.25, which is unequivocally related to the Co magnetic moments, with the more distorted the system is, the more uniform μ_{Co} are. Distortion, however, does not seem to influence μ_{Mn} as it is high for both concentrations. Another important fact is that different magnetic orderings were calculated, with the ferromagnetic found to be the most stable for all the studied cases. Finally, according to Bader charges, Table 7.2, there is no evidence of charge transfer between any of the metallic species, consistent with the results presented in Chapter 6.

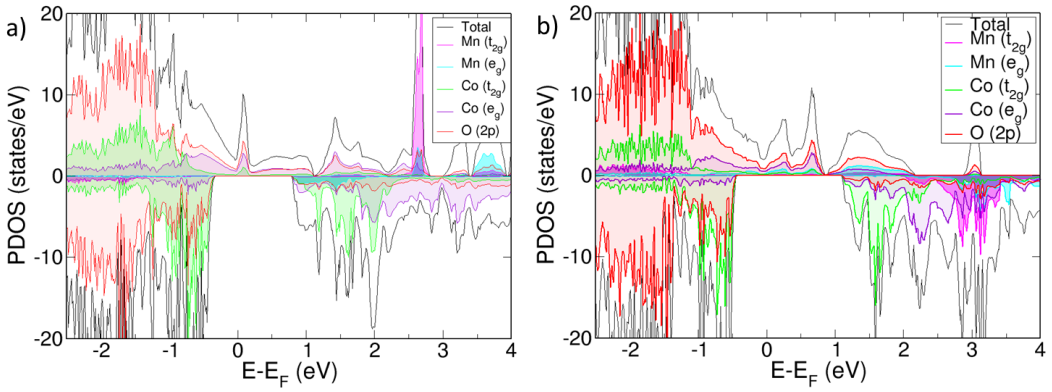

Figure 7.4. Projected Density of States (PDOS) for a) $Sm_{0.75}Ca_{0.25}Mn_{0.125}Co_{0.875}O_{2.88}$ and b) $Sm_{0.75}Ca_{0.25}Mn_{0.25}Co_{0.75}O_{2.88}$. The Fermi level is at 0 eV, and negative E-E_F represent the occupied bands and positive the virtual bands. Positive PDOS are associated with the α-spin, whereas negative PDOS are associated with β-spin.

The calculated σ_e (Table 7.2) show greater electronic conductivity for x=0.25 (30 $S \cdot cm^{-1}$) than for x=0.125 (10 $S \cdot cm^{-1}$), which are in line with experimental work on related SCO perovskites (σ_e<50 Scm^{-1}).[73,86,246] The difference in electronic conductivity between both concentrations is directly associated with the fact that for x=0.125 there is no contribution of both Co and Mn at the Fermi level, whereas they do contribute for x=0.25, making the conduction more effective. If we compare them with $LaMnO_3$-based perovskites, however, σ_e are smaller. We have calculated σ_e for $La_{0.75}Sr_{0.25}MnO_{2.88}$ for comparison reasons, and found that this was 70 Scm^{-1}. Although this could somehow suggest that SCOs would perform worse than LSM, it is important to highlight the following aspects. Firstly, these calculations are performed at 0 K with a general relaxation time and σ_e is known to increase with temperature, [246] which is a variable that unfortunately we cannot include in our calculations. On the other hand, cobalt-containing perovskites are known to have

lower σ_e than LSM, although at IT-SOFC operating temperatures, the limiting factor to IT-SOFC cathode efficiency lies in the ionic conductivity.

Table 7.2. Unique magnetic moments (μ), Bader charges (q), and interatomic distances, and electronic conductivity (σ_e) in $Sm_{0.75}Ca_{0.25}Mn_xCo_{1-x}O_{2.88}$. Co-O distance in $SmCoO_3$ is 1.88 Å.

	x=0.125	*x*=0.25
μ_{Mn} (μ_B)	3.29	3.48
μ_{Co} (μ_B)	0.19, 0.25, 1.89, 2.01, 2.04, 2.41, 2.96	2.03, 2.20, 2.27
q_{Ca}	1.55	1.55
q_{Sm}	2.10	2.12
q_{Co}	1.23, 1.25, 1.31, 1.34	1.28, 1.29, 1.18, 1.19
q_{Mn}	1.71	1.67
q_O	-1.15	-1.16
Co-O (Å)	1.86, 1.87, 1.89, 1.90, 1.91, 1.93, 1.94, 1.95, 1.96, 1.97	1.87, 1.88, 1.91, 1.94, 1.96
Mn-O (Å)	1.87, 1.90, 1.91, 1.98	1.95, 1.96, 1.98, 1.99
σ_e (Scm^{-1})	10	30

7.5 Ionic Conductivity

σ_O and σ_e are difficult to differentiate in experimental measurements, as the former is normally much lower than the latter. Thus, σ_e and σ_O are normally quoted as simply conductivity, with the highest contribution coming from σ_e.[26] As presented previously, σ_O can be calculated from oxygen diffusion coefficients (D_O), obtainable from MD simulations, using the same methodology as in Chapter 5. D_O for $Sm_{0.75}Ca_{0.25}Co_{1-x}Mn_xO_{2.88}$ and E_a are presented in Table 7.3 below, and show good agreement with experimental observations for cobalt perovskites.[18,28,247] D_O for $Sm_{0.75}Ca_{0.25}CoO_{2.88}$ from Chapter 5, and $La_{0.8}Sr_{0.2}MnO_{2.88}$ from Islam *et al.*[75] are included to allow for comparison.

Table 7.3. Oxygen diffusion coefficients (D_O) in 10^8 cm^2s^{-1} at different temperatures, and oxygen migration activation energy (E_a) in eV for $Sm_{0.75}Ca_{0.25}Co_{1-x}Mn_xO_{2.88}$. Data for LSM ($La_{0.8}Sr_{0.2}MnO_{2.88}$) from Islam et al. (1996) has been included for comparison.[75]

T (K)	D_O, x=0.00	D_O, x=0.125	D_O, x=0.25	D_O, LSM
600	1.95	0.759	2.45	
800	4.27	2.93	4.09	1.51
1000	11.0	7.69	9.04	6.23
1200	27.7	23.0	23.8	10.8
1500	84.0	75.9	80.7	42.1
E_a	0.45	0.42	0.44	0.70

All $Sm_{0.75}Ca_{0.25}Mn_xCo_{1-x}O_{2.88}$ show remarkably higher D_O than LSM for the whole range of temperatures, regardless of x, which means that oxygen diffusion is faster in these materials. Furthermore, E_a remains mostly unchanged with increasing x around 0.42 eV, which is in average 0.25 eV less than the one obtained for LSM, describing these materials as excellent oxygen conductors. [35] From these results it is clear that $Sm_{0.75}Ca_{0.25}Mn_xCo_{1-x}O_{2.88}$ presents a distinct improvement on LSM, both in terms of E_a and D_O (Table 2). [75] Additionally, comparing to experimental LSM (D_O=3×10^{-12} cm^2s^{-1} at 900°C (1173 K) [74]), it is clear that D_O is much higher in $Sm_{0.75}Ca_{0.25}Mn_xCo_{1-x}O_{2.88}$. σ_O shows the same trend as observed for D_O (Figure 7.5), with Mn-doping not providing any genuine advantage on σ_O. However, it is clearly seen that at low temperatures, Mn-doping of 0.25 is most advantageous, as it has the highest σ_O.

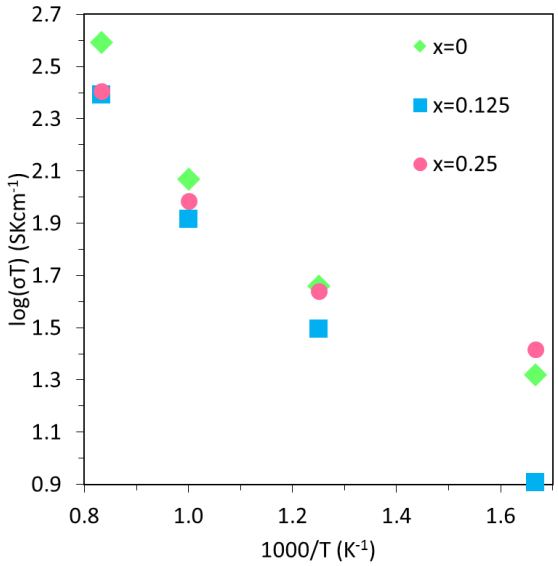

Figure 7.5. Log-plot of ionic conductivity versus 1000/T.

7.6 Thermal Expansion

Lastly, we studied the thermal expansion of $Sm_{0.75}Ca_{0.25}Co_{1-x}Mn_xO_{2.88}$. TEC ($\alpha_T$) is related to the supercell volume, assuming a linear dependence, and was obtained from the MD simulations. [155] For $Sm_{0.75}Ca_{0.25}Co_{1-x}Mn_xO_{2.88}$ to be a viable IT-SOFC cathode material candidate, its TEC needs to be close to that of SOFC electrolyte materials. Common SOFC electrolytes include YSZ, LSGM, and GDC, which have TEC of 10.0-13×10^{-6} K^{-1}, and it is generally accepted that cathodes with TEC smaller than 15×10^{-6} K^{-1} are suitable. [30,32] TEC for x=0.125 is calculated to be 19.5×10^{-6} K^{-1}, and 14.6×10^{-6} K^{-1} for x=0.25, which shows that these materials are suitable for IT-SOFC cathodes, especially at x=0.25 Coupling these results to σ_e and σ_O, Mn-doping with x=0.25, is most suitable for IT-SOFC cathode applications. TEC is greatly decreased for x=0.25, and is approaching the TEC of electrolytes.

7.7 Chapter Conclusions

$Sm_{0.75}Ca_{0.25}Mn_{0.25}Co_{0.75}O_{2.88}$ is the most suitable $SmCoO_3$-based perovskite so far for IT-SOFC cathodes according to our calculations. We have shown that $Sm_{0.75}Ca_{0.25}Co_{0.75}Mn_{0.25}O_{2.88}$ offers a promising electronic conductivity, around 30 Scm^{-1}, occurring *via* both Co and Mn d-orbitals that overlap at the Fermi level. This overlap is a consequence of the distortion induced by the dopants, which at the same time facilitates a different electron occupation in the metal-d orbitals, which in overall results in a ferromagnetic arrangement of the different magnetic moments. In addition, a marked improvement is observed in the ionic conduction, which is the limiting factor in the efficiency of the material. In fact, $Sm_{0.75}Ca_{0.25}Mn_xCo_{1-x}O_{2.88}$ has much higher ionic conductivity, and lower activation energy for oxygen migration than LSM, which ensures faster oxygen diffusion at lower temperatures. Finally, the last bit of the IT-SOFC cathode puzzle is the mechanical coupling between electrolyte and cathode, described in terms of TEC. We show here, that introducing manganese, at x=0.25, into the lattice dramatically decreases TEC, and brings it down to a value close to IT-SOFC electrolytes. Combining all these findings, makes for $Sm_{0.75}Ca_{0.25}Mn_{0.25}Co_{0.75}O_{2.88}$ as a convincing new IT-SOFC cathode material.

Chapter 8

Conclusions and Future Work

8.1 Conclusions

In this thesis, a computational study of bulk $SmCoO_3$-based perovskites has been performed evaluating these materials for use as intermediate temperature Solid Oxide Fuel Cell cathodes. The need for new cathode materials have experimentally identified $SmCoO_3$-based perovskites as promising substitutes to the current state of the art SOFC cathode LSM, which is inefficient at the lowered operating temperatures. Due to the lack of data available on these new cathode materials, we have here conducted a systematic and detailed computational study of $SmCoO_3$-based perovskites focusing on properties that are relevant and important to IT-SOFC cathodes.

Initially, a DFT+U characterization of the magnetic and mechanical properties of both cubic and orthorhombic $SmCoO_3$ was presented in Chapter 3, where focus was on magnetic and mechanical properties. The electronic ground state for both structures is diamagnetic, with all the paramagnetic structures higher in energy at 0 K. As expected from experimental data, the orthorhombic phase was lower in energy than the cubic one. To model the insulator-to-metal spin transition, temperature effects were introduced by mimicking the effect of thermal expansion. From these results, we were able to determine the coexistence of both the CAFM and the DM structures for the orthorhombic phase at high temperatures, and a clear stabilization of the

CAFM structure for the cubic phase around 1100 K. From these calculations we were able to link these experimentally observed transitions to a large increase in the Co spin state, as well as to distortions of the cobalt octahedral environment that allow different Co *d*-orbital occupations. This link between distortions in the Co-O bonds were found to be important throughout the thesis.

Moving on to properties typically connected to SOFC cathode efficiency, we then modelled lattice vacancies within the DFT+U method. At this instance, we took the opportunity to also model lattice vacancies in $LaMnO_3$ to serve as a direct comparison to our $SmCoO_3$ results. As experimental studies have stated that $SmCoO_3$ is not stable at high oxygen pressures and potentials, we calculated the range of chemical potentials in which $SmCoO_3$ and $LaMnO_3$ are stable. We found that the oxygen vacancy formation energy for $LaMnO_3$ is higher than for $SmCoO_3$, but that they are all positive, indicating that the formation of V_O is not spontaneous, except under an oxygen-poor regime. The presence of V_O did not significantly affect the electronic structure of $LaMnO_3$, but it does alter the electronic and magnetic properties of $SmCoO_3$. V_O in $SmCoO_3$ turns this material half-metallic, as a consequence of distortions in the Co-O bonds, in accordance with Chapter 3. Cation vacancy formation energies were also calculated, but it was found that they require very high energies to be formed. Thus, it is expected that these will only exists in very small concentrations, and will have negligible impact on the electronic and ionic conduction in the materials. However, it is evident from Chapter 4 that $SmCoO_3$ in its current form is not suitable as an IT-SOFC cathode material, and thus the rest of the thesis is concerned with doping of $SmCoO_3$.

Firstly, the effect of Sm-site dopants was evaluated in Chapter 5. Since we doped these positions with divalent cations (A=Ca^{2+}, Sr^{2+}, Ba^{2+}) at two different concentrations (x=0.25, 0.5) we studied two potential charge compensation schemes: formation of oxygen vacancies and generation of electronic holes, proving that the former is the predominant charge compensation scheme, with the oxygen vacancy formation energy being negative, whereas the hole formation was positive. The ionic conductivity in $Sm_{1-x}A_xCoO_{3-x/2}$ were found to be higher at intermediate temperatures than in LSM, with Ca^{2+}, x=0.25, reporting the best results. The calculated TEC showed that $Sm_{1-x}A_xCoO_{3-x/2}$ not be compatible with traditional electrolyte materials.

To overcome this, Co-site doping were investigated, and an atomistic study of $SmB_xCo_{1-x}O_3$ (B=Fe^{3+}, Mn^{3+}, Ni^{3+}, and Cu^{3+}) was made. We also calculated the trend in magnetic structure, electronic structure, oxygen formation energy, and thermal expansion over the fully substituted systems $SmBO_3$ for completeness. Mn-doping showed the largest decrease in TEC, with manganese concentrations of 0.125 and 0.25, with a general decrease seen for all B. B are also known to alter the electronic conduction and it was found that $SmMn_xCo_{1-x}O_3$ had the highest σ_e, and $SmFe_xCo_{1-x}O_3$ lowest, in line with previous experimental findings. Calculating E_f for these systems showed no significant difference from $SmCoO_3$, and as such this dopant scheme is not expected to introduce any improvement on ionic conduction.

Combining the findings of Chapter 5 and 6, we investigated $Sm_{0.75}Ca_{0.25}Mn_xCo_{1-x}O_{2.88}$ at two Mn-concentrations using both DFT+U and MD calculations. It was found that $Sm_{0.75}Ca_{0.25}Co_{0.75}Mn_{0.25}O_{2.88}$ shows higher electronic conductivity, 30 Scm^{-1}, than $Sm_{0.75}Ca_{0.25}Co_{0.875}Mn_{0.125}O_{2.88}$, 10 Scm^{-1}. Although being in an acceptable range for IT-SOFC use, and keeping in mind these are 0 K calculations and dependent on

relaxation time, the calculated conductivity for LSM is more than double at 70 Scm^{-1}. However, at IT-SOFC operating conditions, the ionic conductivity is the limiting factor, and needs to be taken into account, together with the thermal expansion coefficient. Ionic conduction and oxygen diffusion was simulated through MD calculations, showing that both systems are good oxygen conductors, with much higher ionic conductivity than LSM at all temperatures. Coupling this to the thermal expansion coefficient, this computational work proposes $Sm_{0.75}Ca_{0.25}Co_{0.75}Mn_{0.25}O_{2.88}$ as a novel IT-SOFC cathode material, which would be an exciting material to bring forward for experimental synthesis.

The research presented in this thesis aims to be a predictive and guiding tool for experimental synthesis, and has systematically and comprehensively modelled bulk properties of $SmCoO_3$-based perovskites, and through the combined findings identified $Sm_{0.75}Ca_{0.25}Mn_{0.25}Co_{0.75}O_{2.88}$ as an IT-SOFC cathode candidate.

8.2 Future Work

Building on the work presented in this thesis, it would be interesting to build surface models of $Sm_{0.75}Ca_{0.25}Mn_{0.25}Co_{0.75}O_{2.88}$ and model the oxygen reduction reaction, which can follow different pathways, and the oxygen surface-bulk exchange. A start on this work has already been made, but issues were encountered. These issues mainly revolve around the surface models where the ORR pathways require the inclusion of oxygen vacancies. We found that introducing an oxygen vacancy at the surface layer required at least a 15 Å×15 Å to contain cubic symmetry. The initial surface models, without oxygen vacancies, had a 7.5 Å×1.5 Å surface area, with 9 surface layers, whereof 5 were fixed bulk layers, and 4 relaxed surface layers. This

resulted in a 96 atom cell, which in its own is computationally expensive. Hence, the larger surface cell required for modelling the oxygen vacancy assisted ORR pathway, was deemed too computationally expensive after test calculations, and remains a challenge for the future.

This surface study could furthermore be combined with an interface study, with $Sm_{0.75}Ca_{0.25}Mn_{0.25}Co_{0.75}O_{2.88}$ and an array of electrolytes making up the interface models. By using MD for the interface studies, it might also be possible to study dopant segregation and to follow the oxygen diffusion from the cathode bulk to electrolyte bulk.

Finally, one of the great issues limiting SOFC performance is cathode chromium poisoning. Thus, modelling the influence of chromium on the ORR, through DFT+U calculations, and ionic conduction (with MD) would be another important area of study.

Bibliography

[1] Jiang X, Xu Q, Shi Y, Li X, Zhou W, Xu H, et al. Synthesis and properties of Sm3+-deficient Sm1−xBaCo2O5+δ perovskite oxides as cathode materials. Int J Hydrogen Energy 2014;39:10817–23. doi:10.1016/j.ijhydene.2014.04.203.

[2] Malavasi L, Fisher CAJ, Islam MS. Oxide-ion and proton conducting electrolyte materials for clean energy applications: structural and mechanistic features. Chem Soc Rev 2010;39:4370–87. doi:10.1039/b915141a.

[3] Haile SM. Fuel cell materials and components. Acta Mater 2003;51:5981–6000. doi:10.1016/j.actamat.2003.08.004.

[4] Doshi R, Richards V, Carter J. Development of Solid- Oxide Fuel Cells That Operate at 500° C. J Electrochem Soc 1999;146:1273–8.

[5] Steele BC, Heinzel A. Materials for fuel-cell technologies. Nature 2001;414:345–52. doi:10.1038/35104620.

[6] Skinner SJ. Recent advances in Perovskite-type materials for solid oxide fuel cell cathodes. Int J Inorg Mater 2001;3:113–21. doi:10.1016/S1466-6049(01)00004-6.

[7] Ormerod RM. Solid oxide fuel cells. Chem Soc Rev 2003;32:17–28. doi:10.1039/b105764m.

[8] Winter M, Brodd RJ. What are batteries, fuel cells, and supercapacitors? Chem Rev 2004;104:4245–69. doi:10.1021/cr020730k.

[9] Minh NQ. Ceramic Fuel Cells. J Am Ceram Soc 1993;76:563–88. doi:10.1111/j.1151-2916.1993.tb03645.x.

[10] Haile SM. Fuel cell materials and components☆☆☆The Golden Jubilee Issue—Selected topics in Materials Science and Engineering: Past, Present and Future, edited by S. Suresh. Acta Mater 2003;51:5981–6000. doi:10.1016/j.actamat.2003.08.004.

[11] Minh N. Solid oxide fuel cell technology - features and applications. Solid State Ionics 2004;174:271–7. doi:10.1016/j.ssi.2004.07.042.

[12] Tao S, Irvine JTS. A redox-stable efficient anode for solid-oxide fuel cells. Nat Mater 2003;2:320–3. doi:10.1038/nmat871.

[13] Cowin PI, Petit CTG, Lan R, Irvine JTS, Tao S. Recent Progress in the Development of Anode Materials for Solid Oxide Fuel Cells. Adv Energy Mater 2011;1:314–32. doi:10.1002/aenm.201100108.

[14] Lo Faro M, La Rosa D, Nicotera I, Antonucci V, Aricò AS. Electrochemical behaviour of propane-fed solid oxide fuel cells based on low Ni content anode catalysts. Electrochim Acta 2009;54:5280–5. doi:10.1016/j.electacta.2009.03.077.

[15] Liu M, Lynch ME, Blinn K, Alamgir FM, Choi Y. Rational SOFC material design: new advances and tools. Mater Today 2011;14:534–46. doi:10.1016/S1369-7021(11)70279-6.

[16] Orera A, Slater PR. New Chemical Systems for Solid Oxide Fuel Cells. Chem Mater 2010;22:675–90. doi:10.1021/cm902687z.

[17] Sun C, Hui R, Roller J. Cathode materials for solid oxide fuel cells: a review. J Solid State Electrochem 2009;14:1125–44. doi:10.1007/s10008-009-0932-0.

[18] Fullarton I, Jacobs J, Benthem H Van. Study of oxygen ion transport in acceptor doped samarium cobalt oxide. Ionics (Kiel) 1995;1:51–8.

[19] Lee Y-L, Kleis J, Rossmeisl J, Morgan D. Ab initio energetics of LaBO3 (001) (B=Mn , Fe, Co, and Ni) for solid oxide fuel cell cathodes. Phys Rev B 2009;80:224101. doi:10.1103/PhysRevB.80.224101.

[20] Koep E, Mebane DS, Das R, Compson C, Liu M. Characteristic Thickness for a Dense La0.8Sr0.2MnOsub Electrode. Electrochem Solid-State Lett 2005;8:A592. doi:10.1149/1.2050607.

[21] Cheng J, Navrotsky A, Zhou X-D, Anderson HU. Enthalpies of Formation of LaMO3 Perovskites (M = Cr, Fe, Co, and Ni). J Mater Res 2005;20:191–200. doi:10.1557/JMR.2005.0018.

[22] Xia C. Sm0.5Sr0.5CoO3 cathodes for low-temperature SOFCs. Solid State Ionics 2002;149:11–9. doi:10.1016/S0167-2738(02)00131-5.

[23] Liu M. Equivalent Circuit Approximation to Porous Mixed- Conducting Oxygen Electrodes in Solid- State Cells. J Electrochem Soc 1998;145:142–54.

[24] Endo A, Ihara M, Komiyama H, Yamada K. Cathodic reaction mechanism for dense Sr-doped lanthanum manganite electrodes. Solid State Ionics 1996;2738.

[25] Van Herle J, McEvoy AJJ, Ravindranathan Thampi K. A study on the La1 − xSrxMnO3 oxygen cathode. Electrochim Acta 1996;41:1447–54. doi:10.1016/0013-4686(95)00393-2.

[26] Pelosato R, Cordaro G, Stucchi D, Cristiani C, Dotelli G. Cobalt based layered perovskites as cathode material for intermediate temperature Solid Oxide Fuel Cells: A brief review. J Power Sources 2015;298:46–67. doi:10.1016/j.jpowsour.2015.08.034.

[27] Lee Y-L, Kleis J, Rossmeisl J, Shao-Horn Y, Morgan D. Prediction of solid oxide fuel cell cathode activity with first-principles descriptors. Energy Environ Sci 2011;4:3966. doi:10.1039/c1ee02032c.

[28] Yamamoto O. Solid oxide fuel cells: fundamental aspects and prospects. Electrochim Acta 2000;45:2423–35. doi:10.1016/S0013-4686(00)00330-3.

[29] Ullmann H, Trofimenko N, Tietz F, Stöver D, Ahmad-Khanlou A. Correlation between thermal expansion and oxide ion transport in mixed conducting perovskite-type oxides for SOFC cathodes. Solid State Ionics 2000;138:79–90. doi:10.1016/S0167-2738(00)00770-0.

[30] Gao Z, Mogni LV, Miller EC, Railsback JG, Barnett SA. A perspective on low-temperature solid oxide fuel cells. Energy Environ Sci 2016;9:1602–44. doi:10.1039/C5EE03858H.

[31] Pavone M, Ritzmann AM, Carter EA. Quantum-mechanics-based design principles for solid oxide fuel cell cathode materials. Energy Environ Sci 2011;4:4933. doi:10.1039/c1ee02377b.

[32] Kilner JA, Burriel M. Materials for Intermediate-Temperature Solid-Oxide Fuel Cells. Annu Rev Mater Res 2014;44:365–93. doi:10.1146/annurev-matsci-070813-113426.

[33] Gaur NK, Thakur R. Thermal and Mechanical Properties of ACoO3 (R = Sm, Tb, Dy, Ho, and Er). Metall Mater Trans A 2013;44:5876–83. doi:10.1007/s11661-013-1942-1.

[34] Koponen MJ, Suvanto M, Kallinen K, Kinnunen T-JJ, Härkönen M, Pakkanen TA. Structural transformations in cubic structure of Mn/Co perovskites in reducing and oxidizing atmospheres. Solid State Sci 2006;8:450–6. doi:10.1016/j.solidstatesciences.2005.11.008.

[35] Yeh TC, Routbort JL, Mason TO. Oxygen transport and surface exchange properties of Sr0.5Sm0.5CoO3−δ. Solid State Ionics 2013;232:138–43. doi:10.1016/j.ssi.2012.11.024.

[36] Thursfield A, Metcalfe IS. Air separation using a catalytically modified mixed conducting ceramic hollow fibre membrane module. J Memb Sci 2007;288:175–87. doi:10.1016/j.memsci.2006.11.015.

[37] Dine El Hannani M, Rached D, Rabah M, Khenata R, Benayad N, Hichour M, et al. First-principles investigations of structural, electronic and magnetic properties of cubic LaMnO3. Mater Sci Semicond Process 2008;11:81–6. doi:10.1016/j.mssp.2009.04.002.

[38] Arima T, Tokura Y. Optical Study of Electronic Structure in Perovskite-Type RMO3 (R= La, Y; M= Sc, Ti, V, Cr, Mn, Fe, Co, Ni, Cu). J Phys Soc Japan 1995;64:2488–501.

[39] Arima T, Tokura Y, Torrance J. Variation of optical gaps in perovskite-type 3d transition-metal oxides. Phys Rev B 1993;48:15–8.

[40] Woodley SM, Gale JD, Battle PD, Catlow CRA. Oxygen ion migration in orthorhombic LaMnO3−δ. J Chem Phys 2003;119:9737. doi:10.1063/1.1615759.

[41] Smart LE, Moore AE. Solid State Chemistry: An Introduction. 4th ed. CRC Press; 2012.

[42] Goldschmidt VM. Die Gesetze der Krystallochemie. Naturwissenschaften 1926;14:477–85. doi:10.1007/BF01507527.

[43] Liu XC, Hong R, Tian C. Tolerance factor and the stability discussion of ABO3-

type ilmenite. J Mater Sci Mater Electron 2009;20:323–7. doi:10.1007/s10854-008-9728-8.

[44] Johnsson M, Lemmens P. Crystallography and Chemistry of Perovskites. John Wiley Sons, Ltd, New York 2007:11. doi:10.1002/9780470022184.hmm411.

[45] Lufaso MW, Woodward PM. Jahn-Teller distortions, cation ordering and octahedral tilting in perovskites. Acta Crystallogr B 2004;60:10–20. doi:10.1107/S0108768103026661.

[46] Chen XG, Fu JB, Yun C, Zhao H, Yang YB, Du HL, et al. Magnetic and transport properties of cobalt doped La0.7Sr0.3MnO3. J Appl Phys 2014;116:103907. doi:10.1063/1.4894713.

[47] Zhao BC, Song WH, Ma YQ, Zhang RL, Yang J, Sheng ZG, et al. Magnetic and transport properties of the Co-doped manganite La0.7Sr0.3Mn1-xCoxO3 (0≤x≤0.5). Phys Status Solidi 2005;242:1719–27. doi:10.1002/pssb.200440052.

[48] Ritzmann AM, Muñoz-García AB. Ab Initio DFT+U Analysis of Oxygen Vacancy Formation and Migration in La1-xSrxFeO3-δ (x= 0, 0.25, 0.50). Chem Mater 2013;25:3011–9. doi:10.1021/cm401052w.

[49] Malavasi L, Ritter C, Cristina Mozzati M, Tealdi C, Saiful Islam M, Bruno Azzoni C, et al. Effects of cation vacancy distribution in doped LaMnO3+ δ perovskites. J Solid State Chem 2005;178:2042–9. doi:10.1016/j.jssc.2005.04.019.

[50] Chroneos A, Yildiz B, Tarancón A, Parfitt D, Kilner JA. Oxygen diffusion in solid oxide fuel cell cathode and electrolyte materials: mechanistic insights from atomistic simulations. Energy Environ Sci 2011;4:2774. doi:10.1039/c0ee00717j.

[51] Aparicio-Anglès X, Roldan A, de Leeuw NH. Gadolinium-Vacancy Clusters in the (111) Surface of Gadolinium-Doped Ceria: A Density Functional Theory Study. Chem Mater 2015;27:7910–7. doi:10.1021/acs.chemmater.5b02861.

[52] Jones A, Islam MS. Atomic-scale insight into LaFeO3 perovskite: Defect nanoclusters and ion migration. J Phys Chem C 2008;112:4455–62.

doi:10.1021/jp710463x.

[53] Cherry M, Islam MS, Catlow CRA. Oxygen ion migration in perovskite-type oxides. J Solid State Chem 1995;118:125–32.

[54] Mastrikov YA, Heifets E, Kotomin EA, Maier J. Atomic, electronic and thermodynamic properties of cubic and orthorhombic LaMnO3 surfaces. Surf Sci 2009;603:326–35. doi:10.1016/j.susc.2008.11.034.

[55] Peña MA, Fierro JL. Chemical structures and performance of perovskite oxides. Chem Rev 2001;101:1981–2017.

[56] Manthiram A, Kim J-H, Kim YN, Lee K-T. Crystal chemistry and properties of mixed ionic-electronic conductors. J Electroceramics 2011;27:93–107. doi:10.1007/s10832-011-9635-x.

[57] Niu Y, Sunarso J, Liang F, Zhou W, Zhu Z, Shao Z. A Comparative Study of Oxygen Reduction Reaction on Bi- and La-Doped SrFeO[sub 3−δ] Perovskite Cathodes. J Electrochem Soc 2011;158:B132. doi:10.1149/1.3521316.

[58] Porras-Vazquez JM, Pike T, Hancock C a., Marco JF, Berry FJ, Slater PR. Investigation into the effect of Si doping on the performance of SrFeO3−δ SOFC electrode materials. J Mater Chem A 2013;1:11834. doi:10.1039/c3ta12113e.

[59] De Souza RA, Islam MS, Ivers-Tiffée E. Formation and migration of cation defects in the perovskite oxide LaMnO3. J Mater Chem 1999;9:1621–7. doi:10.1039/a901512d.

[60] Arbuzova TI, Voronin VI, Gizhevskiĭ B a., Naumov S V., Arbuzov VL. An inhomogeneous paramagnetic state of the LaMnO3 + δ nanoceramics prepared by shock-wave loading. Phys Solid State 2010;52:1217–26. doi:10.1134/S1063783410060168.

[61] Jena H, Kutty KVG. Studies on the structural and ionic transport properties at elevated temperatures of La 1− x MnO 3± δ synthesized by a wet chemical method. J Alloys Compd 2003;350:102–12.

[62] Chukalkin YG, Teplykh a. E. Structure and magnetism of the manganite LaMnO3 with defects. Phys Solid State 2006;48:2310–6.

doi:10.1134/S1063783406120110.

[63] Fita I, Szymczak R, Baran M, Markovich V, Puzniak R, Wisniewski a., et al. Evolution of ferromagnetic order in LaMnO3.05 single crystals: Common origin of both pressure and self-doping effects. Phys Rev B 2003;68:14436. doi:10.1103/PhysRevB.68.014436.

[64] Solovyev I, Hamada N, Terakura K. Crucial role of the lattice distortion in the magnetism of LaMnO3. Phys Rev Lett 1996;76:4825–8.

[65] Ravindran P, Kjekshus A, Fjellvåg H, Delin A, Eriksson O. Ground-state and excited-state properties of LaMnO3 from full-potential calculations. Phys Rev B 2002;65:64445. doi:10.1103/PhysRevB.65.064445.

[66] Choi Y, Mebane DS, Lin MC, Liu M. Oxygen Reduction on LaMnO 3 -Based Cathode Materials in Solid Oxide Fuel Cells. Chem Mater 2007;19:1690–9. doi:10.1021/cm062616e.

[67] Choi Y, Lin MC, Liu M. Rational design of novel cathode materials in solid oxide fuel cells using first-principles simulations. J Power Sources 2010;195:1441–5. doi:10.1016/j.jpowsour.2009.09.017.

[68] Ahmad E, Liborio L, Kramer D, Mallia G. Thermodynamic stability of LaMnO 3 and its competing oxides: A hybrid density functional study of an alkaline fuel cell catalyst. Phys Rev B 2011:1–20.

[69] De Souza RA, Kilner JA, Walker JF. A SIMS study of oxygen tracer diffusion and surface exchange in La0.8Sr0.2MnO3+δ. Mater Lett 2000;43:43–52. doi:10.1016/S0167-577X(99)00228-1.

[70] Huang Y, Vohs JM, Gorte RJ. An Examination of LSM-LSCo Mixtures for Use in SOFC Cathodes. J Electrochem Soc 2006;153:A951. doi:10.1149/1.2186183.

[71] Xia C, Rauch W, Chen F, Liu M. Sm0.5Sr0.5CoO3 cathodes for low-temperature SOFCs. Solid State Ionics 2002;149:11–9. doi:10.1016/S0167-2738(02)00131-5.

[72] Singh P, Minh NQ. Solid Oxide Fuel Cells: Technology Status. Int J Appl

Ceram Technol 2005;1:5–15. doi:10.1111/j.1744-7402.2004.tb00149.x.

[73] Wang Y, Zhao X, Lü S, Meng X, Zhang Y, Yu B, et al. Synthesis and characterization of SmSrCo2−xMnxO5+δ (x=0.0, 0.2, 0.4, 0.6, 0.8, 1.0) cathode materials for intermediate-temperature solid-oxide fuel cells. Ceram Int 2014;40:11343–50. doi:10.1016/j.ceramint.2014.03.113.

[74] Jiang SP. Development of lanthanum strontium manganite perovskite cathode materials of solid oxide fuel cells: A review. J Mater Sci 2008;43:6799–833. doi:10.1007/s10853-008-2966-6.

[75] Islam MS, Cherry M, Catlow CRA. Oxygen Diffusion in LaMnO3and LaCoO3Perovskite-Type Oxides: A Molecular Dynamics Study. J Solid State Chem 1996;124:230–7.

[76] Ishihara T. Intermediate Temperature Solid Oxide Fuel Cells Using a New LaGaO3 Based Oxide Ion Conductor. J Electrochem Soc 1998;145:3177. doi:10.1149/1.1838783.

[77] Farhan MA, Akhtar MJ. Negative pressure driven phase transformation in Sr doped $SmCoO_3$. J Phys Condens Matter 2010;22:75402. doi:10.1088/0953-8984/22/7/075402.

[78] Jung KH, Choi S, Park H-H, Seo W-S. High temperature thermoelectric properties of Sr and Fe doped SmCoO3 perovskite structure. Curr Appl Phys 2011;11:S260–5. doi:10.1016/j.cap.2010.12.032.

[79] Pearce MC, Thangadurai V. Structural and electrochemical characterization of Ce0.85Ca0.05Sm0.1O1.9 oxide ion electrolyte with Sr-doped LaMnO3 and SmCoO3 cathodes. Ionics (Kiel) 2008;14:483–9. doi:10.1007/s11581-008-0240-1.

[80] Fleig J. SOLID OXIDE FUEL CELL CATHODES: Polarization Mechanisms and Modeling of the Electrochemical Performance. Annu Rev Mater Res 2003;33:361–82. doi:10.1146/annurev.matsci.33.022802.093258.

[81] Tu H, Takeda Y. Ln(1-x) SrxCo03 (Ln= Sm, Dy) FOR THE ELECTRODE OF SOLID OXIDE FUEL CELLS. Solid State Ionics 1997;100:283–8.

[82] Pawar S, Shinde K. Studies on Electric and Dielectric Properties of Porous Sm

0.5 Sr 0.5 CoO 3− δ. J Mater 2013;2013:6.

[83] Skinner SJ, Laguna-Bercero MA. Advanced Inorganic Materials for Solid Oxide Fuel Cells. Energy Mater., Chichester, UK: John Wiley & Sons, Ltd; 2011, p. 33–94. doi:10.1002/9780470977798.ch2.

[84] Ju Y-W, Inagaki T, Ida S, Ishihara T. Sm(Sr)CoO3 Cone Cathode on LaGaO3 Thin Film Electrolyte for IT-SOFC with High Power Density. J Electrochem Soc 2011;158:B825. doi:10.1149/1.3592427.

[85] Jirák Z, Hejtmánek J, Knížek K, Novák P, Šantavá E, Fujishiro H. Magnetism of perovskite cobaltites with Kramers rare-earth ions. J Appl Phys 2014;115:17E118. doi:10.1063/1.4862946.

[86] Scurtu R, Somacescu S, Calderon-Moreno JM, Culita D, Bulimestru I, Popa N, et al. Nanocrystalline Sm0.5Sr0.5CoO3−δ synthesized using a chelating route for use in IT-SOFC cathodes: Microstructure, surface chemistry and electrical conductivity. J Solid State Chem 2014;210:53–9. doi:10.1016/j.jssc.2013.10.044.

[87] Baek SW, Kim JH, Bae J. Characteristics of ABO3 and A2BO4 (A=Sm, Sr; B=Co, Fe, Ni) samarium oxide system as cathode materials for intermediate temperature-operating solid oxide fuel cell. Solid State Ionics 2008;179:1570–4. doi:10.1016/j.ssi.2007.12.010.

[88] Ivanova NB, Kazak N V., Michel CR, Balaev a. D, Ovchinnikov SG. Low-temperature magnetic behavior of the rare-earth cobaltites GdCoO3 and SmCoO3. Phys Solid State 2007;49:2126–31. doi:10.1134/S1063783407110182.

[89] Knížek K, Jirák Z, Hejtmánek J, Veverka M, Maryško M, Maris G, et al. Structural anomalies associated with the electronic and spin transitions in LnCoO3. Eur Phys J B 2005;47:213–20. doi:10.1140/epjb/e2005-00320-3.

[90] Xiang P-H, Asanuma S, Yamada H, Sato H, Inoue IH, Akoh H, et al. Electrolyte-gated SmCoO3 thin-film transistors exhibiting thickness-dependent large switching ratio at room temperature. Adv Mater 2013;25:2158–61. doi:10.1002/adma.201204505.

[91] Cramer CJ, Truhlar DG. Density functional theory for transition metals and transition metal chemistry. Phys Chem Chem Phys 2009;11:10757–816. doi:10.1039/b907148b.

[92] Kresse G, Furthmüller J. Efficiency of ab-initio total energy calculations for metals and semiconductors using a plane-wave basis set. Comput Mater Sci 1996;6:15–50.

[93] Kresse G, Hafner J. Ab initio molecular-dynamics simulation of the liquid-metal–amorphous-semiconductor transition in germanium. Phys Rev B 1994;49:14251.

[94] Kresse G, Hafner J. Ab initio molecular dynamics for liquid metals. Phys Rev B 1993;47:558.

[95] Kresse G, Furthmüller J. Efficient iterative schemes for ab initio total-energy calculations using a plane-wave basis set. Phys Rev B Condens Matter 1996;54:11169–86.

[96] Todorov IT, Smith W, Trachenko K, Dove MT. DL_POLY. J Mater Chem 2006;16:1911–8.

[97] Gale JD. GULP: Capabilities and prospects. Zeitschrift Fur Krist 2005;220:552–4. doi:10.1524/zkri.220.5.552.65070.

[98] Gale JD. GULP: A computer program for the symmetry-adapted simulation of solids. J Chem Soc, Faraday Trans 1997;93:629–37.

[99] Gale JD, Rohl AL. The General Utility Lattice Program (GULP). Mol Simul 2003;29:291–341. doi:10.1080/0892702031000104887.

[100] Born M, Oppenheimer R. Zur Quantentheorie der Molekeln. Ann Phys 1927;389:457–84. doi:10.1002/andp.19273892002.

[101] Hohenberg P, Kohn W. Inhomogeneous electron gas. Phys Rev 1964;155.

[102] Kohn W, Sham L. Self-consistent equations including exchange and correlation effects. Phys Rev 1965;385.

[103] Janotti A, Van de Walle CG. LDA + U and Hybrid Functional Calculations for Defects in ZnO, SnO2, and TiO2. Adv Calc Defects Mater Electron Struct

Methods 2011:155–64. doi:10.1002/9783527638529.ch9.

[104] Sousa SF, Fernandes PA, Ramos MJ. General performance of density functionals. J Phys Chem A 2007;111:10439–52. doi:10.1021/jp0734474.

[105] Perdew J, Zunger A. Self-interaction correction to density-functional approximations for many-electron systems. Phys Rev B 1981;23.

[106] Ernzerhof M, Scuseria GE. Assessment of the Perdew–Burke–Ernzerhof exchange-correlation functional. J Chem Phys 1999;110:5029. doi:10.1063/1.478401.

[107] Perdew J, Burke K, Ernzerhof M. Errata: Generalized Gradient Approximation Made Simple. Phys Rev Lett 1997;78:1396.

[108] Perdew J, Burke K, Ernzerhof M. Generalized Gradient Approximation Made Simple. Phys Rev Lett 1996;77:3865–8.

[109] Dudarev S, Botton G, Savrasov S. Electron-energy-loss spectra and the structural stability of nickel oxide: An LSDA+ U study. Phys Rev B 1998;57:1505–9.

[110] Geng T, Han Z, Zhuang S. Effective Coulomb interaction in LaMnO3. Phys B Condens Matter 2010;405:3714–6. doi:10.1016/j.physb.2010.05.072.

[111] Ravindran P, Vidya R, Fjellvåg H, Kjekshus A. Electronic Structure and Excited-state Properties of Perovskite-like Oxides. J Cryst Growth 2004;268:554–9. doi:10.1016/j.jcrysgro.2004.04.090.

[112] Zhou F, Cococcioni M, Marianetti C, Morgan D, Ceder G. First-principles prediction of redox potentials in transition-metal compounds with LDA+U. Phys Rev B 2004;70:235121. doi:10.1103/PhysRevB.70.235121.

[113] Ritzmann AM, Pavone M, Muñoz-García AB, Keith JA, Carter EA. Ab initio DFT+U analysis of oxygen transport in LaCoO3: the effect of Co3+ magnetic states. J Mater Chem A 2014;2:8060–74. doi:10.1039/c4ta00801d.

[114] Zhang S, Han N, Tan X. Density functional theory calculations of atomic, electronic and thermodynamic properties of cubic LaCoO3 and La1_xSrxCoO3 surfaces. RSC Adv 2015;5:760. doi:10.1039/c4ra12563k.

[115] Kresse G, Furthmüller J, Marsman M. VASP the Guide. Comput Physics, Faculaty Physics, Vienna Univ Technol Austria 2012.

[116] Bloch F. Über die Quantenmechanik der Elektronen in Kristallgittern. Zeitschrift Für Phys 1929;52:555–600. doi:10.1007/BF01339455.

[117] Blöchl PE, Jepsen O, Andersen OK. Improved tetrahedron method for Brillouin-zone integrations. Phys Rev B 1994;49:16223–33. doi:10.1103/PhysRevB.49.16223.

[118] Monkhorst HJ, Pack JD. Special points for Brillouin-zone integrations. Phys Rev B 1976;13:5188–92.

[119] Hellmann H. Einführung in die Quantenchemie. Franz Deutsche; 1937. doi:10.1002/ange.19410541109.

[120] Feynman RP. Forces in molecules. Phys Rev 1939;56:340–3. doi:10.1103/PhysRev.56.340.

[121] Hamann D, Schlüter M, Chiang C. Norm-Conserving Pseudopotentials. Phys Rev Lett 1979;43:1494–7. doi:10.1103/PhysRevLett.43.1494.

[122] Vanderbilt D. Soft self-consistent pseudopotentials in a generalized eigenvalue formalism. Phys Rev B 1990;41:7892–5. doi:10.1103/PhysRevB.41.7892.

[123] Blöchl PE. Projector augmented-wave method. Phys Rev B 1994;50:17953.

[124] Andersen OK. Linear methods in band theory. Phys Rev A 1975;12:3060–83. doi:10.1080/00431672.1975.9931783.

[125] Kresse G, Joubert J. From ultrasoft pseudopotentials to the projector augmented wave method. Phys Rev B 1999;59:1758.

[126] Gill PE, Murray W, Wright MH. Practical optimization. Academic Press; 1981.

[127] Francis GP, Payne MC. Finite basis set corrections to total energy pseudopotential calculations. J Phys Condens Matter 1990;2:4395–404. doi:10.1088/0953-8984/2/19/007.

[128] Bader RFW, Popelier PLA, Keith TA. Theoretical Definition of a Functional Group and the Molecular Orbital Paradigm. Angew Chemie Int Ed English 1994;33:620–31. doi:10.1002/anie.199406201.

[129] Bader RFW. Principle of stationary action and the definition of a proper open system. Phys Rev B 1994;49:13348–56. doi:10.1103/PhysRevB.49.13348.

[130] Bader RFW. Atoms in Molecules: A Quantum Theory. Oxford: Oxford University Press; 1990.

[131] Bader RFW, Gillespie RJ, MacDougall PJ. A physical basis for the VSEPR model of molecular geometry. J Am Chem Soc 1988;110:7329–36. doi:10.1021/ja00230a009.

[132] Ángyán JG, Jansen G, Loss M, Hättig C, Heß BA. Distributed polarizabilities using the topological theory of atoms in molecules. Chem Phys Lett 1994;219:267–73. doi:10.1016/0009-2614(94)87056-X.

[133] De Proft F, Van Alsenoy C, Peeters A, Langenaeker W, Geerlings P. Atomic charges, dipole moments, and Fukui functions using the Hirshfeld partitioning of the electron density. J Comput Chem 2002;23:1198–209. doi:10.1002/jcc.10067.

[134] Wiberg KB, Rablen PR. Comparison of atomic charges derived via different procedures. J Comput Chem 1993;14:1504–18. doi:10.1002/jcc.540141213.

[135] Allen MP, Tildesley DJ. Computer simulation of liquids. Oxford: Oxford University Press; 1989. doi:10.1016/j.cpc.2008.01.029.

[136] Leach A. Molecular Modelling - Principles and Applications. 2nd ed. Prentice Hall; 2001.

[137] Berendsen HJC, Postma JPM, van Gunsteren WF, DiNola A, Haak JR. Molecular dynamics with coupling to an external bath. J Chem Phys 1984;81:3684–90. doi:10.1063/1.448118.

[138] Hünenberger PH. Thermostat algorithms for molecular dynamics simulations. Adv Polym Sci 2005;173:105–47. doi:10.1007/b99427.

[139] Hoover WG. Canonical dynamics: Equilibrium phase-space distributions. Phys Rev A 1985;31:1695–7. doi:10.1103/PhysRevA.31.1695.

[140] Buehler MJ. Atomistic modeling of materials failure. At Model Mater Fail 2008:1–488. doi:10.1007/978-0-387-76426-9.

[141] Nosé S. A unified formulation of the constant temperature molecular dynamics methods. J Chem Phys 1984;81:511. doi:10.1063/1.447334.

[142] Born M, Mayer J. Lattice theory of ionic solids. Phys B-CONDENSED MATTER 1932;75:1–18.

[143] Ewald PP. Die Berechnung optischer und elektrostatischer Gitterpotentiale. Ann Phys 1921;369:253–87. doi:10.1002/andp.19213690304.

[144] Essmann U, Perera L, Berkowitz ML, Darden T, Lee H, Pedersen LG. A smooth particle mesh Ewald method. J Chem Phys 1995;103:8577–93. doi:10.1063/1.470117.

[145] Islam MS. Computer modelling of defects and transport in perovskite oxides. Solid State Ionics 2002;154–155:75–85. doi:10.1016/S0167-2738(02)00466-6.

[146] Catlow CRA, Dixon M, Mackrodt WC. Computer Simulation of Solids. vol. 166. Berlin/Heidelberg: Springer-Verlag; 1982. doi:10.1007/BFb0017927.

[147] Bush TS, Gale JD, Catlow CRA, Battle PD. Self-consistent interatomic potentials for the simulation of binary and ternary oxides. J Mater Chem 1994;4:831. doi:10.1039/jm9940400831.

[148] Dick Jr. BG, Overhauser AW. Theory of the Dielectric Constants of Alkali Halide Crystals. Phys Rev 1958;112:90–103. doi:10.1103/PhysRev.112.90.

[149] Read MSD, Islam MS, Watson GW, King F, Hancock FE. Defect chemistry and surface properties of LaCoO3. J Mater Chem 2000;10:2298–305. doi:10.1039/b002168g.

[150] Lewis G V, Catlow CRA. Potential models for ionic oxides. J Phys C Solid State Phys 1985;18:1149–61. doi:10.1088/0022-3719/18/6/010.

[151] Gale JD. Empirical potential derivation for ionic materials. Philos Mag Part B 1996;73:3–19. doi:10.1080/13642819608239107.

[152] Wold A, Ward R. Perowskite-type oxides of cobalt, chromium and vanadium with some rare earth elements. J Am Chem Soc 1954;76:1029.

[153] Perez-Cacho J, Blasco J, Garcia J, Sanchez R. Relationships between

Structure and Physical Properties in SmNi1-xCoxO3. J Solid State Chem 2000;150:145–53. doi:10.1006/jssc.1999.8570.

[154] Wyckoff RWG. The second edition supplement of the Structure of Crystals. Crystallogr Open Database - 5910020 1931;254.

[155] Orlovskaya N, Lugovy M, Pathak S, Steinmetz D, Lloyd J, Fegely L, et al. Thermal and mechanical properties of LaCoO3 and La0.8Ca0.2CoO3 perovskites. J Power Sources 2008;182:230–9. doi:10.1016/j.jpowsour.2008.03.072.

[156] Sahu SK, Tanasescu S, Scherrer B, Marinescu C, Navrotsky A. Energetics of lanthanide cobalt perovskites: LnCoO 3−δ (Ln = La, Nd, Sm, Gd). J Mater Chem A 2015;3:19490–6. doi:10.1039/C5TA03655K.

[157] Capon F, Boileau A, Carteret C, Martin N, Boulet P, Pierson JF. Cation size effect on the thermochromic properties of rare earth cobaltites RECoO3 (RE: La, Nd, Sm). J Appl Phys 2013;114:113510. doi:10.1063/1.4821884.

[158] Sathyamoorthy B, Md Gazzali PM, Murugesan C, Chandrasekaran G. Electrical properties of samarium cobaltite nanoparticles synthesized using Sol–Gel autocombustion route. Mater Res Bull 2014;53:169–76. doi:10.1016/j.materresbull.2014.02.009.

[159] Tachibana M, Yoshida T, Kawaji H, Atake T, Takayama-Muromachi E. Evolution of electronic states in RCoO3 (R=rare earth): Heat capacity measurements. Phys Rev B 2008;77:94402. doi:10.1103/PhysRevB.77.094402.

[160] Vasil'chikova TN, Kuz'mova TG, Kamenev AA, Kaul' AR, Vasil'ev AN. Spin states of cobalt and the thermodynamics of Sm1 − x Ca x CoO3 − δ solid solutions. JETP Lett 2013;97:34–7. doi:10.1134/S002136401301013X.

[161] Malzbender J, Steinbrech RW, Singheiser L. Determination of the interfacial fracture energies of cathodes and glass ceramic sealants in a planar solid-oxide fuel cell design. J Mater Res 2003;18:929–34. doi:10.1557/JMR.2003.0127.

[162] Roldan A, Santos-Carballal D, de Leeuw NH. A comparative DFT study of the

mechanical and electronic properties of greigite Fe3S4 and magnetite Fe3O4. J Chem Phys 2013;138:204712. doi:10.1063/1.4807614.

[163] Michel CR, Delgado E, Santillán G, Martínez AH, Chávez-Chávez A. An alternative gas sensor material: Synthesis and electrical characterization of SmCoO3. Mater Res Bull 2007;42:84–93. doi:10.1016/j.materresbull.2006.05.008.

[164] Alifanti M, Bueno G, Parvulescu V, Parvulescu VI, Cortés Corberán V. Oxidation of ethane on high specific surface SmCoO3 and PrCoO3 perovskites. Catal Today 2009;143:309–14. doi:10.1016/j.cattod.2009.02.026.

[165] Zhu H, Zhang G, Wu X. Injection of spin polarization into Si from the heterostructure LaMnO3/Si interface. Appl Phys Express 2014;93003.

[166] Hamdad N, Rozale H, Lakdja a., Chahed a., Benhelal O. New theoretical investigation on the electronic structure and magnetic interaction for both cubic SrFeO3 and CaFeO3 oxides: Comparison between GGA and GGA+U approaches. Superlattices Microstruct 2013;63:182–96. doi:10.1016/j.spmi.2013.08.002.

[167] Saitoh T, Mizokawa T, Fujimori A, Abbate M. Electronic structure and temperature-induced paramagnetism in LaCoO 3. Phys Rev B 1997;55:4257–66.

[168] Liu R, Xu D, Li S, Lü Z, Xue Y, Wang D, et al. Solid-state synthesis and properties of SmCoO3. Front Chem China 2006;1:398–401. doi:10.1007/s11458-006-0065-2.

[169] Shein IR, Kozhevnikov VL, Ivanovskii AL. First-principles calculations of the elastic and electronic properties of the cubic perovskites SrMO3 (M=Ti, V, Zr and Nb) in comparison with SrSnO3. Solid State Sci 2008;10:217–25. doi:10.1016/j.solidstatesciences.2007.09.013.

[170] Le Page Y, Saxe P. Symmetry-general least-squares extraction of elastic data for strained materials from ab initio calculations of stress. Phys Rev B 2002;65:1–14. doi:10.1103/PhysRevB.65.104104.

[171] Wu Y, Hu W. Elastic and brittle properties of the B2-MgRE (RE = Sc, Y, Ce,

Pr, Nd, Gd, Tb, Dy, Ho, Er) intermetallics. Eur Phys J B 2007;60:75–81. doi:10.1140/epjb/e2007-00323-0.

[172] Lei M, Ledbetter H, Xie Y. Elastic constants of a material with orthorhombic symmetry: An alternative measurement approach. J Appl Phys 1994;76:2738–41. doi:10.1063/1.357577.

[173] Jiang C, Srinivasan SG, Caro A, Maloy S a. Structural, elastic, and electronic properties of Fe3C from first principles. J Appl Phys 2008;103:43502. doi:10.1063/1.2884529.

[174] Li JH, Dai Y, Dai XD. Long-range n-body potential and applied to atomistic modeling the formation of ternary metallic glasses. Intermetallics 2012;31:292–320. doi:10.1016/j.intermet.2012.05.018.

[175] Johnson R. Relationship between Two-Body Interatomic Potentials in a Lattice Model and Elastic Constants. Phys Rev B 1972;6:2094–100. doi:10.1103/PhysRevB.6.2094.

[176] Askeland D, Fulay P. Essentials of Materials Science & Engineering - SI Version. 2nd ed. Cengage Learning; 2009.

[177] Friák M, Hickel T, Grabowski B, Lymperakis L, Udyansky A, Dick A, et al. Methodological challenges in combining quantum-mechanical and continuum approaches for materials science applications. Eur Phys J Plus 2011;126:101. doi:10.1140/epjp/i2011-11101-2.

[178] Zhou J-S, Goodenough JB, Yan J. Bulk modulus anomaly in RCoO3 (R=La, Pr, and Nd). Phys Rev B 2005;71:220103. doi:10.1103/PhysRevB.76.144116.

[179] Gogotsi G, Galenko V, Ozerskii B, Orlovskaya N. the Mechanical Behavior of Lanthanum Cobaltite-Based At Different Temperatures. Refract Ind Ceram 2001;42:341–6.

[180] Kuo JH, Anderson HU. Oxidation-Reduction Nonstoichiometry Behavior of Undoped and Defect Structure and Sr-Doped LaMnO. J Solid State Chem 1989;83:52–60. doi:10.1016/0022-4596(89)90053-4.

[181] Nowotny J, Rekas M. Defect chemistry of (La, Sr) MnO3. J Am Ceram Soc

1998;80:67–80.

[182] Leontiou AA, Ladavos AK, Bakas T V, Vaimakis TC, Pomonis PJ. Reverse uptake of oxygen from La1−xSrx (Fe3+/Fe4+)O3±δ perovskite-type mixed oxides (x = 0.00, 0.15, 0.30, 0.40, 0.60, 0.70, 0.80, 0.90). Appl Catal A Gen 2003;241:143–54. doi:S0926860X02004581.

[183] Mizusaki J, Mori N, Takai H, Yonemura Y. Oxygen nonstoichiometry and defect equilibrium in the perovskite-type oxides La1− xSrxMnO3+d. Solid State Ionics 2000;129:163–77.

[184] Poulsen FW. Defect chemistry modelling of oxygen-stoichiometry , vacancy concentrations , and conductivity of (La 1 2 x Sr x) y MnO 3 6d q. Solid State Ionics 2000;129:145–62. doi:10.1016/S0167-2738(99)00322-7.

[185] Henkelman G, Arnaldsson A, Jónsson H. A fast and robust algorithm for Bader decomposition of charge density. Comput Mater Sci 2006;36:354–60.

[186] Alahmed Z, Fu H. First-principles determination of chemical potentials and vacancy formation energies in PbTiO3 and BaTiO3. Phys Rev B 2007;76:224101. doi:10.1103/PhysRevB.76.224101.

[187] Heifets E, Piskunov S, Kotomin EA, Zhukovskii YF, Ellis DE. Electronic structure and thermodynamic stability of double-layered SrTiO3(001) surfaces: Ab initio simulations. Phys Rev B 2007;75:115417. doi:10.1103/PhysRevB.75.115417.

[188] Sundell PG, Björketun ME, Wahnström G. Thermodynamics of doping and vacancy formation in BaZrO3 perovskite oxide from density functional calculations. Phys Rev B 2006;73:104112. doi:10.1103/PhysRevB.73.104112.

[189] Raebiger H, Lany S, Zunger A. Origins of the p-type nature and cation deficiency in Cu2 O and related materials. Phys Rev B 2007;76:45209. doi:10.1103/PhysRevB.76.045209.

[190] Tanaka T, Matsunaga K, Ikuhara Y, Yamamoto T. First-principles study on structures and energetics of intrinsic vacancies in SrTiO3. Phys Rev B 2003;68:205213. doi:10.1103/PhysRevB.68.205213.

[191] Van De Walle CG, Neugebauer J. First-principles calculations for defects and

impurities: Applications to III-nitrides. J Appl Phys 2004;95:3851–79. doi:10.1063/1.1682673.

[192] Scanlon DO, Buckeridge J, Catlow CRA, Watson GW. Understanding doping anomalies in degenerate p-type semiconductor LaCuOSe. J Mater Chem C 2014;2:3429–38. doi:10.1039/c4tc00096j.

[193] Freysoldt C, Grabowski B, Hickel T, Neugebauer J, Kresse G, Janotti A, et al. First-principles calculations for point defects in solids. Rev Mod Phys 2014;86:253–305. doi:10.1103/RevModPhys.86.253.

[194] Pacchioni G. Modeling doped and defective oxides in catalysis with density functional theory methods: room for improvements. J Chem Phys 2008;128:182505. doi:10.1063/1.2819245.

[195] Komsa H-P, Rantala TT, Pasquarello A. Finite-size supercell correction schemes for charged defect calculations. Phys Rev B 2012;86:45112. doi:10.1103/PhysRevB.86.045112.

[196] Torpo L, Marlo M. Comprehensive ab initio study of properties of monovacancies and antisites in 4H-SiC. J Phys Condens Matter 2001;13:6203–31.

[197] Buckeridge J, Scanlon DO, Walsh A, Catlow CRA. Automated procedure to determine the thermodynamic stability of a material and the range of chemical potentials necessary for its formation relative to competing phases and compounds. Comput Phys Commun 2014;185:330–8. doi:10.1016/j.cpc.2013.08.026.

[198] Zhang S, Han N, Tan X. Supporting information Density functional theory calculations of atomic , electronic and thermodynamic properties of cubic LaCoO 3 and La 1 − x Sr x CoO 3 surfaces. RSC Adv 2014;5.

[199] Ahmad EA, Liborio L, Kramer D, Mallia G, Kucernak AR, Harrison NM. Thermodynamic stability of LaMnO <math display=“inline”> <msub> <mrow/> <mn>3</mn> </msub> </math> and its competing oxides: A hybrid density functional study of an alkaline fuel cell catalyst. Phys Rev B 2011;84:85137. doi:10.1103/PhysRevB.84.085137.

[200] Jacob KT, Attaluri M. Refinement of thermodynamic data for LaMnO3. J Mater Chem 2003;13:934–42. doi:10.1039/b208550j.

[201] STANDARD THERMODYNAMIC PROPERTIES OF CHEMICAL SUBSTANCES. CRC Handb Chem Phys 2012;13:5.4-5.41.

[202] Kaibicheva EA, Rudnyi EB, Sidorov LN, Sorokin ID. Determination of Enthalpies of CoO2-Ion and NiO2-Ion Formation by the Ion-Molecular Equilibrium Method. Zh Fiz Khim SSSR 1991;65:919.

[203] Chase MW. NIST-JANAF Thermochemical Tables. American Chemical Society; 1998.

[204] Kröger FA, Vink HJ. Relations between the Concentrations of Imperfections in Crystalline Solids. Solid State Phys 1956;3:307–435. doi:10.1016/S0081-1947(08)60135-6.

[205] Persson C, Zhao YJ, Lany S, Zunger A. n-Type doping of CuInSe2 and CuGaSe2. Phys Rev B - Condens Matter Mater Phys 2005;72:1–14. doi:10.1103/PhysRevB.72.035211.

[206] Alkauskas A, Broqvist P, Pasquarello A. Defect levels through hybrid density functionals: Insights and applications. Phys Status Solidi Basic Res 2011;248:775–89. doi:10.1002/pssb.201046195.

[207] Kim JH, Cassidy M, Irvine JTS, Bae J. Advanced Electrochemical Properties of LnBa0.5Sr0.5Co2O5+δ (Ln=Pr, Sm, and Gd) as Cathode Materials for IT-SOFC. J Electrochem Soc 2009;156:B682. doi:10.1149/1.3110989.

[208] Shimada H, Yamaguchi T, Suzuki T, Sumi H, Hamamoto K, Fujishiro Y. High power density cell using nanostructured Sr-doped SmCoO3 and Sm-doped CeO2 composite powder synthesized by spray pyrolysis. J Power Sources 2016;302:308–14. doi:10.1016/j.jpowsour.2015.10.082.

[209] Fukunaga H, Koyama M, Takahashi N, Wen C, Yamada K. Reaction model of dense Sm0.5Sr0.5CoO3 as SOFC cathode. Solid State Ionics 2000;132:279–85. doi:10.1016/S0167-2738(00)00642-1.

[210] Wei B, Chen K, Wang CC, Lü Z, Jiang SP. Performance degradation of SmBaCo2O5+δ cathode induced by chromium deposition for solid oxide fuel

cells. Electrochim Acta 2015;174:327–31. doi:10.1016/j.electacta.2015.06.019.

[211] Deml AM, Stevanović V, Muhich CL, Musgrave CB, O'Hayre R. Oxide enthalpy of formation and band gap energy as accurate descriptors of oxygen vacancy formation energetics. Energy Environ Sci 2014;7:1996. doi:10.1039/c3ee43874k.

[212] Ritzmann AM, Dieterich JM, Carter EA. DFT+U analysis of the electronic structure and defect chemistry of LSCF. Phys Chem Chem Phys 2016;18:12260–9. doi:10.1039/C6CP01720G.

[213] Kuklja MM, Kotomin EA, Merkle R, Mastrikov YA, Maier J. Combined theoretical and experimental analysis of processes determining cathode performance in solid oxide fuel cells. Phys Chem Chem Phys 2013;15:5443–71. doi:10.1039/c3cp44363a.

[214] Grau-Crespo R, Hamad S, Catlow CRA, de Leeuw NH. Symmetry-adapted configurational modelling of fractional site occupancy in solids. J Phys Condens Matter 2007;19:256201. doi:10.1088/0953-8984/19/25/256201.

[215] Orikasa Y, Ina T, Nakao T, Mineshige A, Amezawa K, Oishi M, et al. X-ray Absorption Spectroscopic Study on La 0.6 Sr 0.4 CoO 3−δ Cathode Materials Related with Oxygen Vacancy Formation. J Phys Chem C 2011;115:16433–8. doi:10.1021/jp2029642.

[216] Shluger AL, McKenna KP, Sushko P V, Ramo DM, Kimmel A V. Modelling of electron and hole trapping in oxides. Model Simul Mater Sci Eng 2009;17:84004. doi:10.1088/0965-0393/17/8/084004.

[217] Kotomin EA, Eglitis RI, Postnikov A V., Borstel G, Christensen NE. First-principles and semiempirical calculations for bound-hole polarons in KNbO3. Phys Rev B 1999;60:11–5.

[218] Pavone M, Muñoz-Garcia AB, Ritzmann AM, Carter EA. First-Principles Study of Lanthanum Strontium Manganite: New Insights into Electronic Structure and Oxygen Vacancy Formation. J Phys Chem C 2014;118:13346–56.

[219] Olsson E, Aparicio-Anglès X, de Leeuw NH. Ab initio study of vacancy

formation in cubic LaMnO3 and SmCoO3 as cathode materials in solid oxide fuel cells. J Chem Phys 2016;145:14703. doi:10.1063/1.4954939.

[220] Marthinsen A, Faber C, Aschauer U, Spaldin NA, Selbach SM. Coupling and competition between ferroelectricity , magnetism , strain and oxygen vacancies in AMnO 3 perovskites. MRS Commun 2016:1–26. doi:10.1557/mrc.2016.30.

[221] Shannon RD. Revised effective ionic radii and systematic studies of interatomic distances in halides and chalcogenides. Acta Crystallogr Sect A 1976;32:751–67. doi:10.1107/S0567739476001551.

[222] Kim JH, Baek S-W, Lee C, Park K, Bae J. Performance analysis of cobalt-based cathode materials for solid oxide fuel cell. Solid State Ionics 2008;179:1490–6. doi:10.1016/j.ssi.2008.01.086.

[223] Sun Y, Ren W, Cao S, Zhou H, Zhao HJ, Xu H. Hydrostatic pressure driven spin, volume and band gap collapses in SmFeO3: a GGA+U study. Philos Mag 2016;96:1613–22. doi:10.1080/14786435.2016.1170223.

[224] Zhao HJ, Ren W, Yang Y, Chen XM, Bellaiche L. Effect of chemical and hydrostatic pressures on structural and magnetic properties of rare-earth orthoferrites: a first-principles study. J Phys Condens Matter 2013;25:466002. doi:10.1088/0953-8984/25/46/466002.

[225] Sahoo S, Mahapatra PK, Choudhary RNP. The structural, electrical and magnetoelectric properties of soft-chemically-synthesized $SmFeO_3$ ceramics. J Phys D Appl Phys 2016;49:35302. doi:10.1088/0022-3727/49/3/035302.

[226] Ciambelli P, Cimino S, De Rossi S, Lisi L, Minelli G, Porta P, et al. AFeO3 (A = La, Nd, Sm) and LaFe1-xMgxO3 perovskites as methane combustion and CO oxidation catalysts: Structural, redox and catalytic properties. Appl Catal B Environ 2001;29:239–50. doi:10.1016/S0926-3373(00)00215-0.

[227] Choithrani R, Gaur NK, Singh RK. Thermodynamic properties of $SmMnO_3$, $Sm_{0.55}Sr_{0.45}MnO_3$ and $Ca_{0.85}Sm_{0.15}MnO_3$. J Phys Condens Matter 2008;20:415201. doi:10.1088/0953-8984/20/41/415201.

[228] Lee W, Han JW, Chen Y, Cai Z, Yildiz B. Cation size mismatch and charge interactions drive dopant segregation at the surfaces of manganite perovskites.

J Am Chem Soc 2013;135:7909–25. doi:10.1021/ja3125349.

[229] Shukla N, Joshi T, Dasgupta S, Borisov P, Lederman D, Datta S. Electrically induced insulator to metal transition in epitaxial SmNiO3 thin films. Appl Phys Lett 2014;105:2012–7. doi:10.1063/1.4890329.

[230] Nikulin I V., Novojilov MA, Kaul AR, Mudretsova SN, Kondrashov S V. Oxygen nonstoichiometry of NdNiO3-d and SmNiO3-d. Mater Res Bull 2004;39:775–91. doi:10.1016/j.materresbull.2004.02.005.

[231] Karppinen M, Yamauchi H, Suematsu H, Isawa K, Nagano M, Itti R, et al. Control on the Copper Valence and Properties by Oxygen Content Adjustment in the LaCuO3−ySystem (0≤y≤0.5). J Solid State Chem 1997;130:213–22. doi:10.1006/jssc.1997.7296.

[232] Karppinen M, Yamauchi H, Ito T, Suematsu H, Fukunaga O. High-pressure synthesis and thermal decomposition of LaCuO3. Mater Sci Eng B 1996;41:59–62. doi:10.1016/S0921-5107(96)01624-8.

[233] Vázquez S, Suescun L, Faccio R. Effect of Cu doping on Ba0.5Sr0.5Fe1−xCuxO3−δ perovskites for solid oxide fuel cells: A first-principles study. J Power Sources 2016;311:13–20. doi:10.1016/j.jpowsour.2016.02.028.

[234] Baran JD, Molinari M, Kulwongwit N, Azough F, Freer R, Kepaptsoglou D, et al. Tuning Thermoelectric Properties of Misfit Layered Cobaltites by Chemically Induced Strain. J Phys Chem C 2015;119:21818–27. doi:10.1021/acs.jpcc.5b05583.

[235] Mayer JE. Dispersion and Polarizability and the van der Waals Potential in the Alkali Halides. J Chem Phys 1933;1:270–9. doi:10.1063/1.1749283.

[236] Lee HY, Huang K, Goodenough JB. Sr- and Ni-Doped LaCoO3 and LaFeO3 Perovskites. J Electrochem Soc 1998;145:3220–7. doi:10.1149/1.1838789.

[237] Loa I, Adler P, Grzechnik A, Syassen K, Schwarz U, Hanfland M, et al. Pressure-induced quenching of the Jahn-Teller distortion and insulator-to-metal transition in LaMnO3. Phys Rev Lett 2001;87:125501/1-125501/4. doi:10.1103/PhysRevLett.87.125501.

[238] Zhou W, Ran R, Shao Z. Progress in understanding and development of Ba0.5Sr0.5Co0.8Fe0.2O3−δ-based cathodes for intermediate-temperature solid-oxide fuel cells: A review. J Power Sources 2009;192:231–46. doi:10.1016/j.jpowsour.2009.02.069.

[239] Tai LW, Nasrallah MM, Anderson HU, Sparlin DM, Sehlin SR. Structure and electrical properties of La1 - xSrxCo1 - yFeyO3. Part 2. The system La1 - xSrxCo0.2Fe0.8O3. Solid State Ionics 1995;76:273–83. doi:10.1016/0167-2738(94)00245-N.

[240] Richter J, Holtappels P, Graule T, Nakamura T, Gauckler LJ. Materials design for perovskite SOFC cathodes. Monatshefte Fur Chemie 2009;140:985–99. doi:10.1007/s00706-009-0153-3.

[241] Tai LW, Nasrallah MM, Anderson HU, Sparlin DM, Sehlin SR. Structure and electrical properties of La1-xSrxCo1-yFeyO3. Part 1. The system La0.8Sr0.2Co1-yFeyO3. Solid State Ionics 1995;76:259–71. doi:10.1016/0167-2738(94)00244-M.

[242] Mizusaki J, Miwa Y. Nonstoichiometry of the Perovskite-Type Oxides La1-xSrxCoO3-d. J Solid State Chem 1989;80:102–11. doi:10.1016/j.infsof.2008.09.005.

[243] Pawlas-Foryst E, Jacob KT, Fitzner K. Thermodynamics of SmMnO3 and SmMn2O5 Phases Dtermined by the E.M.F. Method. Arch Metall Mater 2006;51:253–60.

[244] Parida SC, Venugopal V, Jacob KT. Thermodynamic properties of SmFeO3(s) and Sm3Fe5O12(s). J Phase Equilibria 2003;24:431–40. doi:10.1361/105497103770330082.

[245] Volkova NE, Kolotygin VA, Gavrilova LY, Kharton V V, Cherepanov VA. Nonstoichiometry, thermal expansion and oxygen permeability of SmBaCo2 − xCuxO6 − δ. Solid State Ionics 2014;260:15–20. doi:http://dx.doi.org/10.1016/j.ssi.2014.03.003.

[246] Cvejin K, Manjakkal L, Kulawik J, Zaraska K, Szwagierczak D. Characterization and applicability of Sm0.9Sr0.1CoO3-δ in oxygen sensors.

Microelectron Int 2014;31:154–7. doi:10.1108/MI-11-2013-0075.

[247] Carter S, Selcuk A, Chater RJ, Kajda J, Kilner JA, Steele BCH. Oxygen transport in selected nonstoichiometric perovskite-structure oxides. Solid State Ionics 1992;53–56:597–605. doi:10.1016/0167-2738(92)90435-R.

[248] Makov G, Payne M. Periodic boundary conditions in ab initio calculations. Phys Rev B 1995;51:4014–22. doi:10.1103/PhysRevB.51.4014.

[249] Lany S, Zunger A. Assessment of correction methods for the band-gap problem and for finite-size effects in supercell defect calculations: Case studies for ZnO and GaAs. Phys Rev B - Condens Matter Mater Phys 2008;78:17–20. doi:10.1103/PhysRevB.78.235104.

[250] Murphy ST, Hine NDM. Anisotropic charge screening and supercell size convergence of defect formation energies. Phys Rev B - Condens Matter Mater Phys 2013;87:1–18. doi:10.1103/PhysRevB.87.094111.

Appendix A

Goldschmidt Factors

Table A.1. Goldschmidt tolerance factor for different dopants in $SmCoO_3$.

Dopant	*t* (Sm-site)	*t* (Co-site)	Favourable Dopant Site
Ca	0.94	0.65	Sm
Sr	1.01	0.65	Sm
Ba	1.07	0.61	Sm
Mn	0.75	0.93	Co
Fe	0.80	0.87	Co
Ni	0.71	0.97	Co
Cu	0.77	0.90	Co

Appendix B

Mechanical Properties from MD

Table B.1. Mechanical properties calculated using the interatomic potential set from Chapter 2.

	Cubic	Orthorhombic
B (GPa)	266.67	259.44
G (GPa)	158.91	140.46
E (GPa)	366.28	288.53
$\boldsymbol{\sigma}$	0.27	0.26

Appendix C

$SmCoO_3$ Density of States

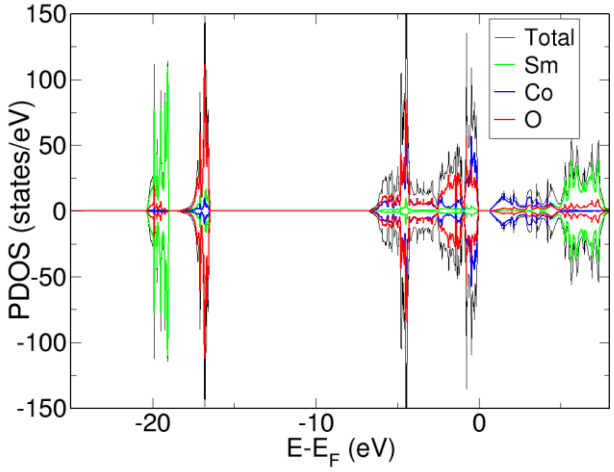

Figure C.1. Density of state for cubic $SmCoO_3$ ground state. The Fermi level is at 0 eV, and negative E-E_F represent the occupied bands and positive the virtual bands. Positive PDOS are associated with the α-spin, whereas negative PDOS are associated with β-spin.

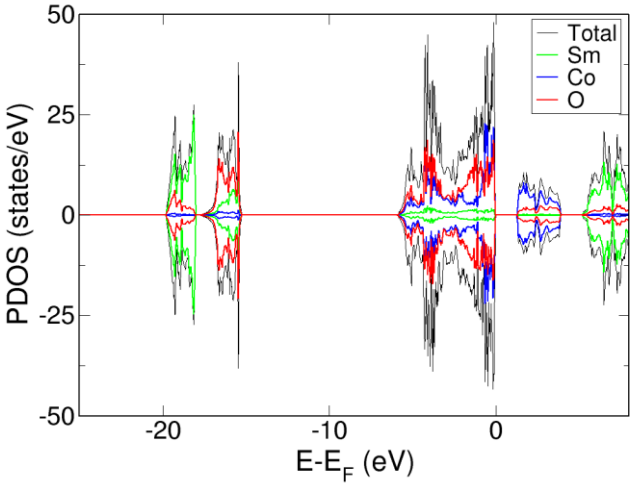

Figure C.2. Density of states for orthorhombic $SmCoO_3$ ground state. The Fermi level is at 0 eV, and negative E-E_F represent the occupied bands and positive the virtual bands. Positive PDOS are associated with the α-spin, whereas negative PDOS are associated with β-spin.

Appendix D

Finite-Charge Correction Schemes

As discussed in Chapter 4, charge corrections can be taken into account when modelling non-neutral systems. When modelling non-zero charge systems, two major errors can arise as a result of using periodic boundary conditions; image-charge interactions, and differences in the reference electrostatic potential. To correct these, numerous correction schemes have been developed. [195] In this appendix, only a few of the most commonly used finite-charge correction schemes will be addressed, but further information can be found in the literature.

The simplest form of a finite-charge correction scheme was presented by Makov and Payne (MP) [195,248], which is a Madelung potential correction scheme derived from the screened Coulomb interaction between two point charges. The MP method is the most common method to correct the image-charge interaction, and takes the form

$$\Delta E_{MP} = \frac{q^2 \alpha_M}{2\epsilon L} + \frac{2\pi q Q_s}{3\epsilon L^3}, \qquad (D.1)$$

where ΔE_{MP} is the MP correction (which would be applied to equation 4.1), q is the charge, α_M is the Madelung constant of the supercell, ϵ is the dielectric constant of the material, Q_s the second radial moment of the charge density, and L is the cell length. This scheme has been shown to work well for molecular systems, but

unfortunately overestimates the correction magnitude in solids. The overestimation has been attributed to Q_s, which does not consider dielectric screening response.

Hence, another correction scheme was proposed by Lany and Zunger (LZ) [249], which has established itself as the standard correction method for image-charge interactions. The LZ correction term (ΔE_{LZ}) is calculated from equation D.2.

$$\Delta E_{LZ} = [1 + C_{sh}(1 - \epsilon^{-1})]\frac{q^2\alpha_M}{2\epsilon L}, \qquad (D.2)$$

C_{sh} is the shape factor, which is dependent only upon the shape of the supercell and the dielectric of the material. The dielectric tensor is further dependent on cell shape, with cubic systems having constant dielectric tensors in all lattice directions, whereas for orthorhombic systems there will be anisotropy due to the non-equal lattice parameters. For orthorhombic systems, this can be taken into account by using the method developed by Murphy and Hines. [250] However, with large dielectric constants, the magnitude of ΔE_{LZ} decreases and becomes negligible in relation to the other terms in equation 4.1.

Appendix E

Electronic Structures of $SmCoO_3$ and $LaMnO_3$ with Cation Vacancies

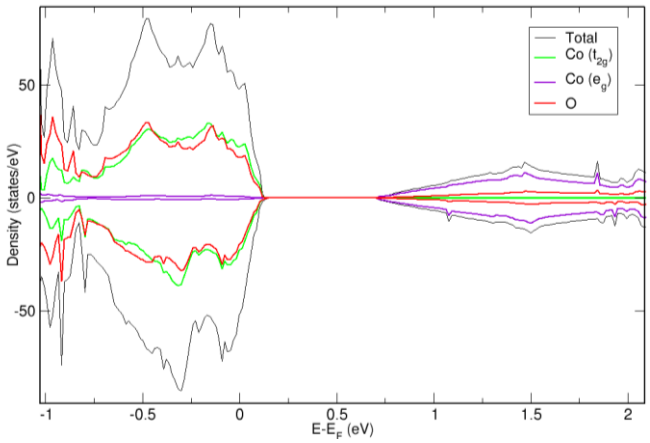

Figure E.1. PDOS for $SmCoO_3$ with Sm vacancy. The Fermi level is at 0 eV, and negative E-E_F represent the occupied bands and positive the virtual bands. Positive PDOS are associated with the α-spin, whereas negative PDOS are associated with β-spin.

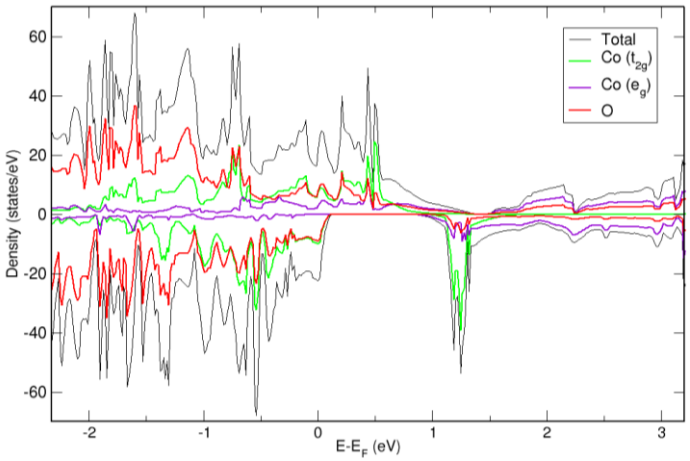

Figure E.2. PDOS for the $SmCoO_3$ with cobalt vacancy. The Fermi level is at 0 eV, and negative E-E_F represent the occupied bands and positive the virtual bands. Positive PDOS are associated with the α-spin, whereas negative PDOS are associated with β-spin.

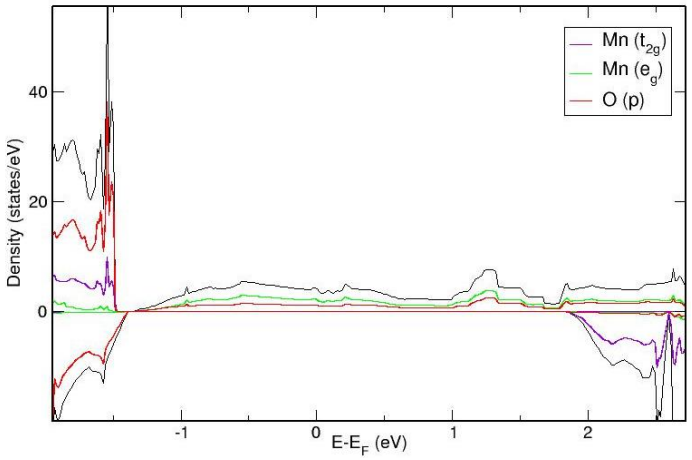

Figure E.3. PDOS for $LaMnO_3$ with a lanthanum vacancy. The Fermi level is at 0 eV, and negative E-E_F represent the occupied bands and positive the virtual bands. Positive PDOS are associated with the α-spin, whereas negative PDOS are associated with β-spin.

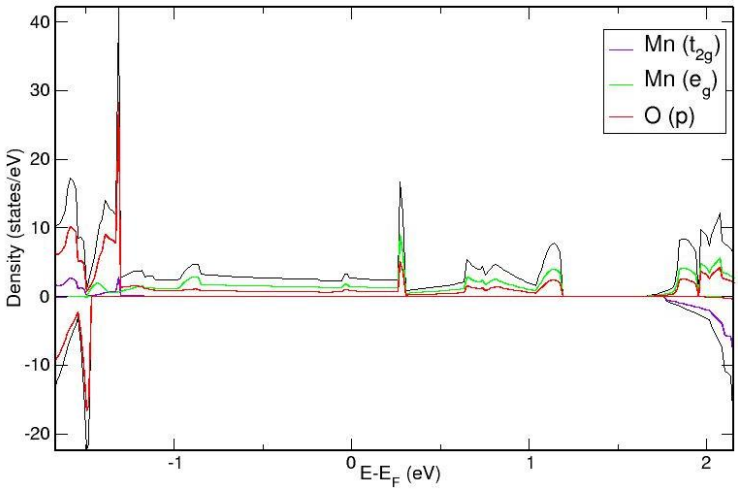

Figure E.4. PDOS for $LaMnO_3$ with Mn-vacancy. The Fermi level is at 0 eV, and negative E-E_F represent the occupied bands and positive the virtual bands. Positive PDOS are associated with the α-spin, whereas negative PDOS are associated with β-spin.

Appendix F

MD Results for the Most Stable Configurations in Chapter 7

Table F.1. Oxygen Diffusion coefficients ($\times 10^{-8}$ cm^2s^{-1}) for x=0.125, and 0.25, for configurations 1-3 and 1-4 respectively in Table 7.1.

	x=0.125			x=0.25			
T (K)	conf 1	conf 2	conf 3	conf 1	conf 2	conf 3	conf 4
600	0.759	3.67	2.17	2.45	2.30	1.68	2.47
800	2.93	5.83	4.33	4.09	3.42	2.33	3.52
1000	7.69	9.83	7.83	9.04	6.71	5.41	5.58
1200	23.0	21.3	22.5	23.8	13.5	11.9	12.4
1500	75.9	74.7	74.2	80.7	56.9	55.7	54.5

Table F.2. Oxygen Migration Activation Energy (eV) for x_{Mn}=0.125, and 0.25, for configurations 1-3 and 1-4 respectively in Table 7.1.

conf	**x=0.125**	**x=0.25**
1	0.42	0.44
2	0.37	0.40
3	0.42	0.45
4		0.39

Table F.3. Ionic conductivity (σ_O) at different temperatures for $Sm_{0.75}Ca_{0.25}Co_{1-x}Mn_xO_{2.88}$ for configuration 1-3 and 1-4 respectively in Table 7.1.

	σ_O (Scm^{-1}), **x=0.125**			**σ_O** (Scm^{-1}), **x=0.25**			
T (K)	conf 1	conf 2	conf 3	conf 1	conf 2	conf 3	conf 4
600	0.014	0.065	0.039	0.044	0.041	0.030	0.044
800	0.039	0.078	0.058	0.055	0.046	0.031	0.047
1000	0.082	0.105	0.084	0.096	0.072	0.058	0.060
1200	0.205	0.190	0.200	0.212	0.120	0.106	0.110
1500	0.540	0.531	0.528	0.575	0.405	0.397	0.388

Table F.4. Thermal expansion coefficients ($\times 10^{-6}$ K^{-1}) for x_{Mn}=0.125, and 0.25, for configurations 1-3 and 1-4 respectively in Table 7.1.

conf	**x=0.125**	**x=0.25**
1	19.5	14.6
2	16.6	17.1
3	20.3	16.0
4		16.6